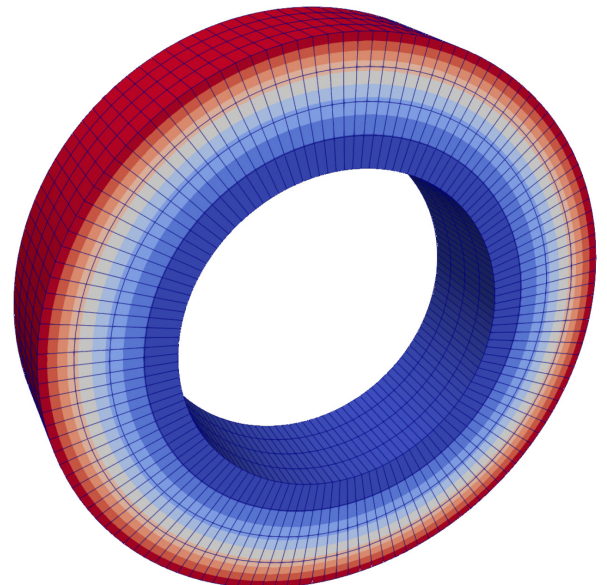
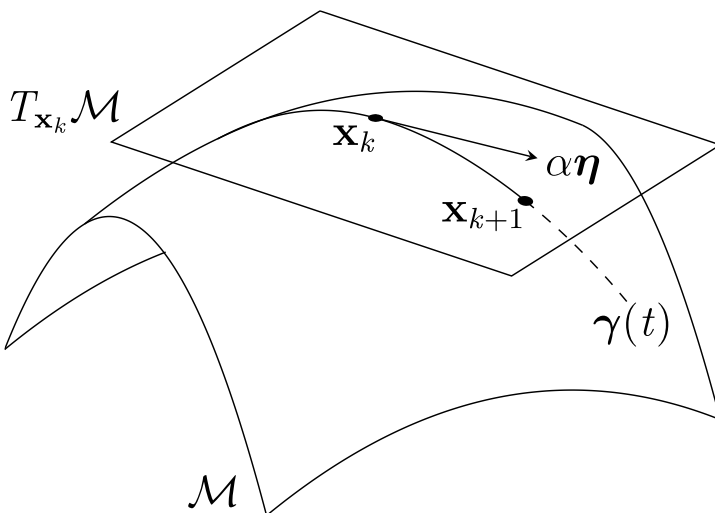


# Differential Geometry and the Geometrically Non-linear Reissner-Mindlin Shell Model

Alexander Müller





# Differential Geometry and the Geometrically Non-linear Reissner-Mindlin Shell Model

von

**Alexander Müller**

Bericht Nr. 77

Institut für Baustatik und Baudynamik der Universität Stuttgart

Professor Dr.-Ing. habil. M. Bischoff

2024



© Alexander Müller

*Berichte können bezogen werden über:*  
Institut für Baustatik und Baudynamik  
Universität Stuttgart  
Pfaffenwaldring 7  
70550 Stuttgart

Tel.: 0711 - 685 66123  
Fax: 0711 - 685 66130  
E-Mail: sekretariat@ibb.uni-stuttgart.de  
<http://www.ibb.uni-stuttgart.de/>

*Alle Rechte, insbesondere das der Übersetzung in andere Sprachen, vorbehalten. Ohne Genehmigung des Autors ist es nicht gestattet, diesen Bericht ganz oder teilweise auf photomechanischem, elektronischem oder sonstigem Wege zu kommerziellen Zwecken zu vervielfältigen.*

D 93 - Dissertation an der Universität Stuttgart  
ISBN 978-3-00-078095-0

# Differential Geometry and the Geometrically Non-linear Reissner-Mindlin Shell Model

Von der Fakultät Bau- und Umweltingenieurwissenschaften  
der Universität Stuttgart zur Erlangung der Würde eines  
Doktor-Ingenieurs (Dr.-Ing.) genehmigte Abhandlung

vorgelegt von

**Alexander Müller**

aus Göppingen

Hauptberichter: Prof. Dr.-Ing. habil. Manfred Bischoff, Stuttgart

Mitberichter: Prof. Ignacio Romero, PhD, Madrid

Mitberichter: Prof. Dr. Oliver Sander, Dresden

Tag der mündlichen Prüfung: 20. Oktober 2023

Institut für Baustatik und Baudynamik der Universität Stuttgart

2024



## Kurzfassung

Dünnwandige Strukturen üben seit jeher eine große Faszination auf den Menschen aus. Diese Faszination rührt daher, dass die dünnwandigen Strukturen zwar zerbrechlich wirken, aber dennoch in der Lage sind, hohe Lasten zu tragen. Die Vorteile der hohen Tragfähigkeit und des geringen Materialeinsatzes sind nicht selbstverständlich, da diese guten Eigenschaften mit einem hohen Beulrisiko einhergehen. Der Ingenieur, der die Tragfähigkeit von Schalenstrukturen untersucht, muss daher immer auch die Wahrscheinlichkeit des Versagens berücksichtigen.

Um dieses potenziell katastrophale Versagen vorhersagen zu können, kommen seit jeher Strukturmodelle zum Einsatz. Computersimulationen, verwenden numerische Lösungsverfahren, die aus diesen Strukturmodellen abgeleitet werden. Diese numerischen Lösungsverfahren müssen einerseits korrekte Ergebnisse liefern und andererseits robust und effizient sein. Die vorliegende Arbeit befasst sich mit diesen numerischen Lösungsverfahren und macht Vorschläge um jede der drei genannten Eigenschaften zu verbessern. Dies geschieht im Rahmen des Reissner-Mindlin-Schalen-Modells.

Die vorliegende Arbeit zielt darauf ab, das Reissner-Mindlin-Schalen-Modell und seine Finite-Elemente-Formulierung durch theoretische und numerische Untersuchungen weiterzuentwickeln. Dabei wird ein breites Themenspektrum abgedeckt: die exakte Herleitung der Schnittgrößen der Schale, die Untersuchung der Reissner-Mindlin-Annahmen, korrekte Linearisierungsverfahren für eine konsistente und symmetrische Steifigkeitsmatrix, Eigenschaften geeigneter Direktor-Interpolationsverfahren, die numerische Durchsetzung der Annahme verschwindender Normalspannungen und die Funktionsanalyse in nichtlinearen Funktionsräumen.

Um diese Ziele zu erreichen, legt diese Arbeit großen Wert auf die Grundlagen der Differentialgeometrie, um eine solide mathematische Basis für das Schalenmodell und die Formulierung zu schaffen. Dabei wird vor allem die Optimierung auf Mannigfaltigkeiten verwendet, um den korrekten Linearisierungsprozess für eine Reissner-Mindlin-Schalenformulierung herzuleiten. Durch die Interpretation der Einheitslängen-Nebenbedingung als ein Optimierungsproblem in einem beschränkten Raum, ergibt sich eine Formulierung mit fünf Freiheitsgraden pro Knoten. Dies stellt die optimale Anzahl von Freiheitsgraden für diese Schalen-Formulierung dar und übertrifft traditionelle Ansätze wie die Lagrange-Multiplikator-Methode oder die Penalty-Methode, die beide zu einer höheren Anzahl von Freiheitsgraden führen.

Die Differentialgeometrie auf Mannigfaltigkeiten wird verwendet, um die korrekten Schnittgrößen im Detail herzuleiten. Diese werden dann verwendet, um die Bewegungsgleichungen des Schalenmodells aufzustellen. Darüber hinaus trägt die Differentialgeometrie zum Verständnis des speziellen Direktorfeldes im Reissner-Mindlin-Schalenmodell bei. Durch die gründliche Analyse dieses speziellen Direktorfeldes und seiner Auswirkungen

liefert die Arbeit ein umfassendes Verständnis mechanischer Modelle mit Nebenbedingungen. Deshalb kann die vorliegende Abhandlung als Grundstein für Finite-Elemente-Formulierungen anderer Strukturmodelle dienen.

Die Annahme der verschwindenden Normalspannung und ihre numerische Umsetzung werden ebenfalls untersucht, und es wird ein neuer, vielversprechender Ansatz vorgeschlagen, der die bestehenden Methoden übertrifft. Dies wird wiederum durch die konsequente Anwendung der Optimierung auf Mannigfaltigkeiten erreicht, die in den Methoden aus der Literatur fehlt. Daraus wird ein effizientes und robustes numerisches Verfahren entwickelt, das auch auf andere Modelle mit Spannungsnebenbedingungen anwendbar ist. Die Leistungsfähigkeit wird anhand eines einfachen Modellproblems und einer geometrischen und materiellen nichtlinearen Schalensimulation untersucht.

Die Symmetrie der Steifigkeitsmatrix wird auf zwei Arten behandelt. Zunächst wird ein konsistenter Linearisierungsprozess für die Reissner-Mindlin-Schalenformulierung angegeben, der eine symmetrische Steifigkeitsmatrix ergibt. Dies steht im Gegensatz zu Linearisierungsverfahren, die in der Literatur zu finden sind und die die Steifigkeitsmatrix ad hoc symmetrisieren oder eine unsymmetrische Steifigkeitsmatrix verwenden, die nur im Gleichgewicht symmetrisch ist. Zweitens wird gezeigt, dass die Symmetrie der Steifigkeitsmatrix direkt aus der Symmetrie der Riemannschen Hesse-Matrix abgeleitet werden kann. Dies steht im Gegensatz zur fehleranfälligen und möglicherweise unsymmetrischen zweiten Variation, die in der Literatur verwendet wird. Diese Ergebnisse gelten auch wiederum für andere Strukturmodelle, die Freiheitsgrade auf Mannigfaltigkeiten einbeziehen.

Finite-Elemente-Formulierungen aus der Literatur für das Reissner-Mindlin-Schalenmodell diskretisieren das Direktorfeld auf unterschiedliche Art und Weise. Diese haben ihre jeweiligen Vor- und Nachteile, die in dieser Arbeit diskutiert werden. Aus dieser Diskussion geht hervor, dass die direkte Interpolation auf Mannigfaltigkeiten die einzige Möglichkeit ist, verschiedene Nachteile zu vermeiden. Im Gegensatz zur Interpolation in Vektorräumen, in denen eine kanonische Interpolationsregel existiert, gibt es bei der Interpolation auf Mannigfaltigkeiten verschiedene Möglichkeiten. Diese Möglichkeiten werden verglichen und hinsichtlich ihrer Konvergenzrate und ihres Einflusses auf Locking-Phänomene analysiert. Dies geschieht durch den Vergleich der Finite-Elemente-Lösungen mit der analytischen Lösung für ein geometrisch nichtlineares Problem. Die Untersuchung wird für lineare Lagrange'sche Ansatzfunktionen und B-Splines-Ansatzfunktionen höherer Ordnung durchgeführt.

All diese Untersuchungen führen zu einer statischen Schalenformulierung, die mehrere wünschenswerte Eigenschaften aufweist, die denen bestehender Formulierungen überlegen sind. Dazu gehören Objektivität, die Fähigkeit, unbegrenzte Gesamtrotationen richtig abzubilden, die Erfüllung der Längeneinheitsbeschränkung für interpolierte Direktoren, keine künstliche Pfadabhängigkeit, Vermeidung von Singularitäten und das Erreichen optimaler Konvergenzordnungen. Darüber hinaus sind die resultierenden Elementvektoren und -matrizen unabhängig von der Nummerierung der Finite-Elemente-Knoten. Die konsistente Aktualisierung der Knotendirektoren ermöglicht in Verbindung mit



dem konsistenten Linearisierungsprozess eine Formulierung, die hinsichtlich der erforderlichen Lastinkremente und der Anzahl der erforderlichen Iterationen besser abschneidet als bestehende Formulierungen. Diese Vorteile wurden durch die Untersuchung der mathematischen Literatur auf dem Gebiet der Optimierung und der Interpolation auf Mannigfaltigkeiten möglich gemacht.

Zusammenfassend kann gesagt werden, dass die vorliegende Arbeit offene Fragen des geometrisch nichtlinearen Reissner-Mindlin-Schalenmodells und seiner Finite-Elemente-Formulierung aufgreift und behandelt. Sie liefert Analysen und schlägt Lösungen vor. Durch eine strenge Herleitung des Reissner-Mindlin-Schalenmodells in Verbindung mit einer soliden mathematischen Grundlage im Bereich der Differentialgeometrie versucht die vorliegende Arbeit einen Fortschritt auf dem Gebiet der Strukturmechanik zu erzielen. Die Analysen und Lösungen, die in dieser Studie vorgestellt werden, verbessern nicht nur das Verständnis und die Verfeinerung des Reissner-Mindlin-Schalenmodells und seiner Finite-Elemente-Formulierung, sondern können auch Auswirkungen auf die Verbesserung der Genauigkeit, der Effizienz und der Zuverlässigkeit von Lösungsverfahren für die numerische Behandlung anderer Strukturmodelle.



## Abstract

Thin-walled structures have always fascinated mankind. This fascination stems from the fact that, although thin-walled structures look fragile, they can carry high loads. The advantages of the high load-bearing capacity and low material input cannot be taken for granted, as these good properties come with a high risk of buckling. The engineer designing these structures for their load-bearing capacity must always keep the probability of failure in mind.

Structural models have always been used to predict this potentially catastrophic failure. Computer simulations designed to predict it, use numerical solution procedures derived from these structural models. These numerical solution methods must provide correct results on the one hand and be robust and efficient on the other hand. The present work deals with these numerical solution methods, by improving each of the two properties mentioned. This is done within the framework of the Reissner-Mindlin shell model.

Thus, the aim of the present work is to advance the finite element formulation for the geometrically non-linear Reissner-Mindlin shell model through theoretical and numerical investigations. The work covers a wide range of topics, including the exact derivation of the shell's stress resultants, the investigation of the Reissner-Mindlin assumptions, correct linearization procedures for a consistent and symmetric stiffness matrix, properties of suitable director interpolation schemes, the influence of locking phenomena, the enforcement of the zero normal stress assumption, and functional analysis in non-linear function spaces.

In order to achieve these goals, this thesis places significant emphasis on the fundamentals of differential geometry to provide a solid mathematical basis for the shell model and formulation. In particular, optimization on manifolds is used to derive the correct linearization process for a Reissner-Mindlin shell formulation. By interpreting the unit-length constraint of the shell's director as an unconstrained optimization problem in a constrained space, a formulation with five degrees of freedom per node is obtained. This is the optimal number of degrees of freedom for this shell formulation and outperforms traditional approaches, such as the Lagrange multiplier method or the penalty method, which result in higher numbers of degrees of freedom.

Differential geometry of manifolds is used to revisit and derive the correct stress resultants in detail. These are then used to formulate the differential equations of the shell model, the balance of linear and angular momentum. Additionally, differential geometry guides the understanding of the unit-length constraint for the director field in the Reissner-Mindlin shell model. By thoroughly analyzing this constraint and its implications, the thesis provides a comprehensive understanding of constraints in mechanical models in general, thus serving as a cornerstone for future studies.

The zero normal stress assumption and its numerical realization are investigated, and a novel and promising approach is proposed that outperforms existing methods. This is done again by rigorously applying the notion of optimization on manifolds, which is missing

in the methods proposed in the literature. In comparison to these methods found in the literature, this results in fewer iterations and a more robust numerical procedure. This applies also to other models with zero stress constraints. The performance is investigated by studying a small model problem and a fully geometrically and materially non-linear shell simulation.

The symmetry of the stiffness matrix is investigated in two ways. First, the consistent linearization process is stated for the Reissner-Mindlin shell formulation, which yields an unconditionally symmetric stiffness matrix. This is in contrast to the linearization procedures found in the literature, which symmetrize the stiffness matrix ad hoc or use an unsymmetric stiffness matrix, which is symmetric only at equilibrium. Second, it is shown that the symmetry of the stiffness matrix is directly derived from the symmetry of the Riemannian Hessian. This contrasts with the error-prone and potentially unsymmetric second variation, which is used in literature. These results also apply to other structural models involving degrees of freedom on manifolds.

Finite element formulations for the Reissner-Mindlin shell model from the literature discretize the director field in different ways. These have their respective advantages and disadvantages, which are discussed in this thesis. From this discussion, it appears that direct interpolation on manifolds is the only way to avoid the various drawbacks. Unlike interpolation in vector spaces, where a canonical interpolation rule exists, there are several options for interpolation on manifolds. These options are compared and analyzed in the context of the rate of convergence and their influence on locking phenomena. This is done by comparing the finite element solutions with the analytical solution for a highly geometrically non-linear problem. The investigation is carried out for linear Lagrangian ansatz functions and higher-order B-spline ansatz functions.

All of these key questions and their answers lead to a static shell formulation, that achieves several desirable features, superior to those of existing formulations. These include objectivity, the ability to accommodate unlimited magnitudes of rotations, the satisfaction of the unit length constraint for interpolated directors, no artificial path dependence, the avoidance of singularities, and the achievement of higher convergence orders. In addition, the resultant element vectors and matrices are independent of the numbering of nodes. The consistency of the update of the nodal directors enables, in conjunction with the consistency of the linearization process, a formulation that outperforms existing formulations in terms of required load increments and the number of required iterations. These achievements were made possible by investigating the mathematical literature in the field of optimization on manifolds and interpolation on manifolds.

In summary, the present work revisits and addresses open questions in the geometrically non-linear Reissner-Mindlin shell model and its finite element formulation, providing comprehensive analyses and proposing solutions. By providing a rigorous derivation of the Reissner-Mindlin shell model and its finite element formulation, coupled with a solid mathematical foundation in the realm of differential geometry, this research proposes an advance in the field of structural mechanics. The comprehensive analyses and solutions

presented in this study do not only enhance the understanding and refinement of the Reissner-Mindlin shell model and its finite element formulation but also have implications for improving the accuracy, efficiency, and reliability of various other structural models, thus contributing to the broader field of structural mechanics.



## Danksagung

Diese Arbeit entstand im Rahmen meiner Tätigkeit als wissenschaftlicher Mitarbeiter am Institut für Baustatik und Baudynamik (IBB) der Universität Stuttgart. An dieser Stelle möchte ich mich bei allen beteiligten Personen bedanken, die mich bei der Anfertigung meiner Dissertation unterstützt haben.

Mein besonderer Dank gilt meinem Doktorvater Prof. Dr.-Ing. habil. Manfred Bischoff für die Möglichkeit, diese Arbeit durchführen zu können. Sein Vertrauen in meine Arbeit und meine Arbeitsweise bildete die Grundlage für die Entstehung dieser Arbeit. Der von ihm gewährte Freiraum, insbesondere in Form einer Landesstelle, ermöglichte es mir, die Arbeit in der vorliegenden Fassung zu verfassen. Er hat mich in allen Phasen meiner Dissertation uneingeschränkt unterstützt, aber besonders hervorzuheben ist seine Geduld, mit der er meine ausführlichen, verschachtelten und gelegentlich unnötig komplexen Sätze, welche auch hin und wieder grammatikalisch falsch waren, aber insbesondere diejenigen, bei denen man bis zum Ende auf das Verb wartet, ertragen hat.

Des Weiteren möchte ich Prof. Dr.-Ing. Ekkehard Ramm danken, der mich dazu ermutigte, an diesem klassischen und bereits intensiv erforschten Thema dranzubleiben.

Ein besonderer Dank gilt auch Prof. Ignacio Romero, PhD, für sein Interesse an meinem Thema und die Übernahme und schnelle Erstellung des Mitberichts.

Besondere Erwähnung verdient die Unterstützung von Prof. Dr. Oliver Sander, bei dem ich als Gastwissenschaftler in Dresden eine äußerst bereichernde Zeit erlebte. Sein Interesse an meinem Thema und auch seine konstruktive Kritik haben mir sehr geholfen und mich auch motiviert, zu versuchen, die vorliegende Arbeit in einer mathematisch sauberen Form zu präsentieren. Seine mathematische und programmiertechnische Herangehensweise an Probleme hat mich nachhaltig geprägt.

Ein herzliches Dankeschön gilt auch meinen derzeitigen und ehemaligen Kolleginnen und Kollegen am IBB und in Dresden, die mich in den letzten Jahren unterstützt haben. Vielen Dank für den privaten und fachlichen Austausch mit euch. Aus Kolleginnen und Kollegen sind über die Jahre hinweg Freunde geworden, was mich sehr freut.

Abschließend möchte ich mich von ganzem Herzen bei meinen Freunden und meiner Familie, meiner Mutter Ilse bedanken, die mich während meines Studiums und meiner Promotion unterstützt haben. Ein besonderer Dank gilt auch meiner Frau Kristin, die mich in den letzten Jahren in jeder Hinsicht unterstützt und ermutigt, aber auch meine Launen ertragen, hat. Ich danke euch allen dafür, dass ihr in den letzten Jahren immer an meiner Seite wart.

Stuttgart, im Februar 2024

Alexander Müller





---

# Contents

<b>List of Figures</b>	<b>xv</b>
<b>List of Tables</b>	<b>xix</b>
<b>Abbreviations and Nomenclature</b>	<b>xxi</b>
<b>1 Introduction</b>	<b>1</b>
1.1 Motivation . . . . .	1
1.2 State of the Art . . . . .	3
1.2.1 Historical Overview . . . . .	3
1.2.2 The Reissner-Mindlin Shell Model . . . . .	5
1.2.3 Linearization of Finite Elements for Non-linear Fields . . . . .	7
1.3 Scope of This Work . . . . .	9
1.4 Overview . . . . .	11
<b>2 First-Order Differential Geometry</b>	<b>13</b>
2.1 Manifolds, Charts, Atlases and Parameterization . . . . .	13
2.2 Differential Topology . . . . .	15
2.3 Embeddings and Submanifolds . . . . .	17
2.4 Directional Derivatives, Tangents and Cotangents . . . . .	20
2.4.1 Abstract Manifolds . . . . .	20
2.4.2 Embedded Submanifolds . . . . .	21
2.4.3 Tangent Space and Tangent Bundle . . . . .	23
2.4.4 Covectors and Cotangent Bundle . . . . .	25
2.4.5 Tangent vectors as Derivations . . . . .	26
2.5 Tensors . . . . .	28
2.6 Retractions . . . . .	33
2.7 Riemannian Manifolds . . . . .	35
2.7.1 Riemannian Metric . . . . .	35

2.7.2	Musical Isomorphisms . . . . .	36
2.7.3	Riemannian Gradient . . . . .	38
2.7.4	Riemannian Submanifolds . . . . .	39
2.8	Alternating Tensors and Volume Forms . . . . .	42
2.8.1	Wedge Product . . . . .	42
2.8.2	Riemannian Volume Form . . . . .	43
2.8.3	Cross Product . . . . .	44
2.8.4	Determinant of a Tensor . . . . .	45
2.8.5	Piola Transform . . . . .	47
<b>3</b>	<b>Second-Order Differential Geometry</b>	<b>51</b>
3.1	Affine Connections . . . . .	51
3.2	Parallel Transport . . . . .	55
3.3	Geodesics . . . . .	57
3.4	Riemannian Exponential Map . . . . .	60
3.5	Riemannian Hessian . . . . .	61
<b>4</b>	<b>Foundations of Finite Elasticity</b>	<b>67</b>
4.1	Kinematics . . . . .	67
4.1.1	Configuration, Motion and Deformation . . . . .	67
4.1.2	Deformation Gradient . . . . .	71
4.1.3	Strain . . . . .	74
4.2	Traction and Stress . . . . .	77
4.3	Balance Principles . . . . .	80
4.3.1	Conservation of Mass . . . . .	80
4.3.2	Balance of Linear and Angular Momentum . . . . .	82
4.4	Elastic Constitutive Theory . . . . .	83
4.5	Potential Energy and Weak Form . . . . .	86
4.6	Objectivity . . . . .	88
<b>5</b>	<b>The Non-linear Reissner-Mindlin Shell Model</b>	<b>91</b>
5.1	Geometry and Kinematics . . . . .	92
5.1.1	Motion, Configuration and Deformation . . . . .	92
5.1.2	Tangent Space Mappings . . . . .	94
5.1.3	Shell Shifter and Transformation of Integrals . . . . .	96
5.1.4	Strain . . . . .	99
5.2	Stress Resultants . . . . .	101
5.2.1	Cauchy Stress Resultants . . . . .	101
5.2.2	Stress Resultant Components . . . . .	104
5.2.3	Pulled-back Quantities . . . . .	110

5.2.4	Calculations in a Local Cartesian Frame . . . . .	110
5.3	Balance Principles . . . . .	112
5.3.1	Conservation of Mass . . . . .	112
5.3.2	Balance of Linear Momentum . . . . .	114
5.3.3	Balance of Angular Momentum . . . . .	117
5.3.4	The Reissner-Mindlin Assumptions . . . . .	121
5.4	Stress Normal Constraint for Non-trivial Material Laws . . . . .	124
5.4.1	Existing Algorithm . . . . .	125
5.4.2	Proposed Algorithm . . . . .	126
5.4.3	Model Problem . . . . .	129
5.4.4	Conclusion . . . . .	131
5.5	Variation, Linearization and Discretization . . . . .	132
5.5.1	Euclidean Variation and Linearization of the Continuous Energy .	132
5.5.2	Discretization . . . . .	137
5.6	Element Vectors and Matrices . . . . .	140
5.6.1	Internal Forces and Material Stiffness Matrix . . . . .	140
5.6.2	Geometric Stiffness Matrix . . . . .	141
<b>6</b>	<b>Idiosyncrasies of Finite Elements for Non-linear Fields</b>	<b>149</b>
6.1	From Functional Analysis to System Matrices . . . . .	149
6.1.1	Historical Overview and Remarks . . . . .	150
6.1.2	The Linear Case . . . . .	151
6.1.3	The Non-linear Case . . . . .	153
6.2	Symmetry of the Tangent Operator . . . . .	161
6.2.1	Historical Overview and Remarks . . . . .	161
6.2.2	Point of Departure . . . . .	162
6.2.3	Compact Lie Groups . . . . .	164
6.2.4	The Unit Sphere . . . . .	165
6.2.5	Conclusion . . . . .	166
6.3	Discretization and Interpolation . . . . .	167
6.3.1	Historical Overview and Remarks . . . . .	167
6.3.2	Interpolation on Manifolds . . . . .	169
<b>7</b>	<b>Numerical Experiments</b>	<b>175</b>
7.1	Point of Departure . . . . .	175
7.2	Plastic Deformation of a Free-Form Surface . . . . .	176
7.3	Pure Bending of Straight Beam . . . . .	179
7.3.1	Analytical Solution . . . . .	181
7.3.2	Exemplary Finite Element Solution . . . . .	183
7.3.3	Q1 Elements with Assumed Natural Strain . . . . .	185

7.3.4	Higher-order NURBS Elements . . . . .	190
7.3.5	Conclusion . . . . .	194
<b>8</b>	<b>Summary and Outlook</b>	<b>197</b>
<b>A</b>	<b>Appendix</b>	<b>201</b>
A.1	Transformation Rule of Christoffel Symbols . . . . .	201
A.2	Divergence of a Tensor . . . . .	201
A.3	Derivatives of the Projector . . . . .	202
A.4	Covariant Derivative for Compact Lie Groups . . . . .	202
A.5	The Inextensible Director Derivatives . . . . .	203
A.6	The Shifter Tensor Components in the Midsurface Basis . . . . .	204
A.7	The Determinant of the Shifter Tensor . . . . .	205
A.8	Derivation of Local Shell Angular Momentum From Local Three-Dimensional Angular Momentum . . . . .	206
A.9	The Potential Energy Given by Midsurface Quantities . . . . .	207
A.10	Solving the Local GFE Minimization Problem . . . . .	207
A.11	Assumed Natural Strain for Transverse Shear . . . . .	210

---

# List of Figures

2.1	Commutative diagram of Eq. (2.2). . . . .	14
2.2	Charts and change of coordinates. Figure adapted from [Abs08, Fig. 3.1].	15
2.3	Mapping of coordinate representation of a function mapping between manifolds. . . . .	16
2.4	The inclusion map . . . . .	18
2.5	Klein's bottle immersed but not embedded into $\mathbb{R}^3$ . . . . .	19
2.6	Mapping rationale for $\tilde{f}$ and $f$ of Eq. (2.8) . . . . .	21
2.7	A coordinate grid. Figure Inspired by [Lee03]. . . . .	23
2.8	Tangent bundle $T\mathcal{S}^1$ of the circle $\mathcal{S}^1$ as embedded into $\mathbb{R}^2$ . . . . .	24
2.9	The action of a covector onto a vector. Inspired by [Mis73, Box 10.3]. . .	26
2.10	Push forward of a function mapping between manifolds. . . . .	31
2.11	Line search in a vector space and on a manifold . . . . .	34
2.12	Commutative diagram between musical isomorphisms and pull-back and push-forward operations . . . . .	37
2.13	Decomposition of a vector into components tangent and normal to a manifold. . . . .	40
3.1	Illustration of Eq. (3.13). . . . .	56
3.2	Visual representation of Eq. (3.14) . . . . .	57
3.3	A geodesic curve on the manifold defined by the parameterization $\sin x + \sin y$	59
3.4	Prestressed string clamped between two shells. . . . .	60
4.1	Motion, configuration and deformation of a body $\mathcal{B}$ . . . . .	68
4.2	The spatial and material velocities and accelerations. . . . .	71
4.3	Motion, configuration and the coordinate frames. . . . .	72
4.4	Commutative diagram between metric tensors and pull-back and push-forward of the deformation gradient. . . . .	73
4.5	Commutative diagrams between metric tensors and pulled-back and pushed-forward metrics. . . . .	75

4.6	Traction vectors and normals of cut through the body of the reference and current configuration. . . . .	78
5.1	Kinematics of the shell. Reference and current configuration. . . . .	93
5.2	Linear and non-linear commutative mapping diagram of the shell's body and the shell midsurface. . . . .	97
5.3	Push-forward operation of the normal of the cut in the parameter space to the current configuration. . . . .	102
5.4	Decomposition of the stress resultant $\mathbf{n}^1$ . . . . .	105
5.5	Decomposition of the stress resultant $\mathbf{m}^1$ and $\hat{\mathbf{m}}^1$ . . . . .	106
5.6	Decomposition of the stress resultant $\mathbf{l}$ . . . . .	107
5.7	Number of iterations needed to reach $ S^{33}  < 1e-10$ . . . . .	130
5.8	The function $S^{33}(C_{33})$ in black and its linearization in dashed black. . . .	131
6.1	General solution process of the manifold-valued PDE or potential functionals. In red dash-dotted unfeasible paths to derive a consistent formulation.	154
6.2	Spatial relation of different function spaces in a vector space and for manifolds. . . . .	155
6.3	The unit sphere $\mathcal{S}^2$ with a unit vector $\mathbf{t}$ and the corresponding tangent space $\mathbf{\Lambda} = [\mathbf{t}^1 \mathbf{t}^2]$ . . . . .	159
6.4	Graphical comparison of interpolation between two nodal directors interpolations. . . . .	172
7.1	Structural system and boundary conditions of the free-form surface. . . .	177
7.2	Graphical representation and description of the load function $\lambda(t)$ . . . .	177
7.3	The undeformed midsurface and deformed midsurface after unloading are shown on the left. The undeformed surface is slightly translated in negative Y-direction for better visualization. On the right, the displacement of point A in Y-direction is shown. . . . .	178
7.4	Deformed and undeformed midsurface configuration of the bending of a straight beam, including boundary conditions and parameters. . . . .	180
7.5	The Cauchy stress components $\sigma^{11}$ (left) and $\sigma^{13}$ (right). . . . .	184
7.6	Stress resultants and displacement error for pure bending with a thickness of $h = 1$ cm. . . . .	185
7.7	Illustration of displacement error and bending moment error. . . . .	187
7.8	Illustration of the shear forces error (a), the membrane forces error (b), and the corresponding energies. . . . .	188
7.9	Pure bending configuration of an element with linear ansatz functions and NFE (left) or PBFEE/GFE (right) as director interpolation. . . . .	189
7.10	Illustration of a part of the deformed configuration with four elements. .	189

7.11	Illustration of displacement error (a) and bending moment error (b) for varying element sizes $h$ .	190
7.12	The shear forces error (a), membrane forces error (b), and the corresponding energies.	192
7.13	Displacement error and bending moment error are shown for varying slenderness.	193
7.14	Shear and membrane energies fractions.	194
A.1	Assumed natural strain collocation points A, B, C and D	211





---

# List of Tables

5.1	Summary of different tensorial mappings in the shell body and on the shell's midsurface . . . . .	98
5.2	Summary of important stress resultant formulas . . . . .	109
5.3	Effective stress resultant components . . . . .	109
7.1	Average iterations necessary to solve the vanishing normal stress constraint per quadrature point. . . . .	178



---

# Abbreviations and Nomenclature

## Abbreviations

ANS	.....	Assumed natural strains
GFE	.....	Geodesic finite elements
IGA	.....	Isogeometric analysis
NFE	.....	Nodal finite elements
PBFE	.....	Projection-based finite elements
PDE	.....	Partial differential equation

## Mathematical notation

$A \cong B$	.....	$A$ is isomorphic to $B$
$\mathbf{A} : \mathbf{B}$	.....	Scalar product between two second-order tensors, contracting both basis vectors
$\mathbf{AB}$	.....	Matrix product
$\mathbf{A} \cdot \mathbf{B}$	.....	Tensor product between two second-order tensors contracting one basis vector
$\mathbf{a} \cdot \mathbf{b}$	.....	Dot product between two basis vectors
$\mathbf{a} \times \mathbf{b}$	.....	Cross product between two vectors
$\Theta, \theta$	.....	point in $\mathbb{R}^n$
$\mathcal{M}, \mathcal{N}$	.....	manifolds or sets
$\langle \mathbf{a}, \mathbf{b} \rangle$	.....	Inner product between two basis vectors
$\mathbf{x}$	.....	point in a manifold $\mathcal{M}$
$N_{\mathbf{x}}\mathcal{M}$	.....	Normal space of $\mathcal{M}$ at the point $\mathbf{x}$ (orthogonal complement of $T_{\mathbf{x}}\mathcal{M}$ )
$T\mathcal{M}$	.....	Tangent bundle of $\mathcal{M}$
$T_{\mathbf{x}}\mathcal{M}$	.....	Tangent space of $\mathcal{M}$ at the point $\mathbf{x}$
$\delta_i^j$	.....	The <i>Kronecker delta</i> . One for $i = j$ and 0 otherwise

$\mathbf{d}\mathbf{v}$ .....	Riemannian volume form, i.e., $\mathbf{d}\mathbf{v} = \sqrt{\det(g_{ab})} dx^1 \wedge \dots \wedge dx^n$
$\mathcal{D}(\mathcal{M})$ .....	Space of function on $\mathcal{M}$
$I$ .....	A scalar interval, usually $I \subset \mathbb{R}$
$\text{Sym}_n$ .....	Space of symmetric matrices of size $n$ .
$\mathfrak{X}(\mathcal{M})$ .....	Space of vector fields on $\mathcal{M}$
$\mathcal{E}, \mathcal{V}, \mathcal{W}$ .....	Vector spaces, usually $\mathbb{R}^n$
$\phi$ .....	coordinate chart
$\mathbf{v}$ .....	Vector or tangent vector in a vector space $\mathcal{E}$
$\xi, \eta, \zeta$ .....	tangent vector fields on a manifold
$\xi_{\mathbf{x}}, \eta_{\mathbf{x}}, \zeta_{\mathbf{x}}$ ...	tangent vectors on a manifold at position $\mathbf{x}$
$D$ .....	subsets of a set that resembles a vector space $\mathcal{E}$
$\mathcal{U}, \mathcal{V}$ .....	subsets of a set that resembles a manifold $\mathcal{M}$
$\iota$ .....	inclusion map
$f$ .....	a function that maps onto $\mathbb{R}$
$\mathbf{f}$ .....	a function that maps onto $\mathbb{R}^n$

**Greek letters**

$\alpha, \beta, \dots$ .....	Indices of curvilinear coordinates
$\Gamma_{IK}^J, \gamma_{ik}^j$ .....	Christoffel symbols or coefficients of an affine connection
$\nabla$ .....	Affine connection on a manifold

**Derivatives**

$\frac{\partial(\bullet)}{\partial t}$ .....	partial derivative of $(\bullet)$ w.r.t. $t$
$\frac{d(\bullet)}{dt}$ .....	total derivative of $(\bullet)$ w.r.t. $t$
$D_{\mathbf{v}}\boldsymbol{\eta}$ .....	Directional derivative of $\boldsymbol{\eta}$ in direction $\mathbf{v}$
$\frac{D}{dt}\boldsymbol{\eta}$ .....	Covariant derivative of vector field $\boldsymbol{\eta}$ along a scalar direction $t$ stemming from a curve $\gamma$
$\nabla_{\mathbf{v}}\boldsymbol{\eta}$ .....	Covariant directional derivative of $\boldsymbol{\eta}$ in direction $\mathbf{v}$

# 1

---

## Introduction

Life as we perceive it is fundamentally influenced by various forces. The study of mechanical behavior has a tradition dating back thousands of years. This is mainly because mechanics can be *experienced*. Displacements can be measured. Dents in cars can be repaired. Ships can be sunk by collisions with icebergs. Galaxies collide. People die. Everything in our environment screams *mechanics*.

Some things are disturbing, while others are simply fascinating. Among the latter are shell structures that seem to defy gravity as if by magic. These include leaves, seashells, eggs, jet fighters, and those big gymnastics balls that, when bounced while sitting on them, help our blood flow and train our muscles and coordination. All these shell structures have one thing in common: As three-dimensional objects, they have two dimensions that are significantly larger than the remaining direction. For this reason, shell structures are also called thin-walled structures. In addition to the geometric description, shells can also be described based on their mechanical load-carrying behavior. For example, there are flat plates that are loaded transversely or membranes that have practically no bending stiffness, such as trash bags. All these shells, from trash bags to watermelons to the International Space Station, have a high stiffness-to-material ratio in addition to their geometric commonality.

### 1.1 Motivation

Starting from nature, shells have always been an inspiration for people to overcome their challenges. One example is the Pantheon in Rome as a prominent representative of historical buildings, whereas hollow nanomaterials in drug delivery systems are modern applications of shell structures. Thus, our environment often does not scream *mechanics* but *structural mechanics* at us. Research in structural mechanics is still largely motivated

by the need to simulate thin-walled structures in a variety of fields, including civil engineering, mechanical engineering, aerospace, shipbuilding, and biology. This is motivated by the fact that simulation can be used to make predictions about real behavior. This is especially important because the benefits of shells are accompanied by being always close to a very rapid, unannounced and catastrophic failure. Thus, these limits have to be predicted as accurately as possible. These characteristics are summed up in the sentence stated by Ramm et al. [Ram02]: “The shell is the prima donna among structures. Capable of maximum performance, but temperamental and sensitive if not properly treated.” (cf. p. 29). Another fitting quote is “God made the bulk; the surface was invented by the devil.” by the physicist Wolfgang Pauli, as quoted in Jamtveit and Meakin [JM99]. These quotes are an excellent overview of the issues of shell simulations because the requirement to handle the design of thin-walled structures with great care also carries over to the simulation of these structures. As a result, simulating thin-walled constructions is not only difficult because the thin direction is only geometrically small, but this translates to challenging mechanical behavior. As computer use has increased since the mid-1970s, many researchers have tackled this problem by developing finite element formulations. Geometrically non-linear shell models and their finite element formulations have a bumpy and eventful history dating back to the 1940s. In particular, the theoretical and numerical work has helped to make Reissner-Mindlin shell formulations the workhorse of modern simulation software involving shell simulations. However, there are still some inconsistencies in deriving a correct formulation to allow a computer to make predictions about the structural behavior. There are also some blind spots in the theoretical derivations.

The present work deals with both the improvement of the theoretical basis of the geometrically non-linear Reissner-Mindlin shell model and the improvement of the numerical formulation to make the computer predictions better, faster, and more reliable.

Accordingly, the present work represents a comprehensive advancement that significantly enhances the geometrically non-linear Reissner-Mindlin shell model, improving its theoretical and numerical foundations on all fronts.

The driver for shell theories is, from the beginning, a fundamental understanding of differential geometry. However, the negotiations over which shell theory is best are not solely driven by purely geometric reasoning; The interaction between forces and the shell also plays a crucial role. This is especially true in dynamic scenarios, where the design space for modeling inertia effects is quite large. As a result, there is ample room for assumptions and approximations in order to develop a computationally efficient model for the specific scenario of interest. Consequently, deriving a perfect shell model is impossible, partly due to the varying interpretations of “perfection” in different contexts. Therefore, the only viable solution is to establish a hierarchy of models, each tailored to address a particular type of problem. In this hierarchy, two classic shell models are named after

Kirchhoff [Kir50] and Love [Lov88] and after Reissner [Rei45] and Mindlin [Min51]. These models are not only useful because they are more computationally efficient than a full three-dimensional formulation but also for enhancing our understanding of underlying physical effects and facilitating informed assumptions about structural behavior—a feat that a fully three-dimensional theory cannot accomplish. Consequently, this work places equal emphasis on achieving consistent and efficient numerical behavior, as well as understanding the underlying theory.

Shell models are primarily concerned with simplifying the mechanical behavior of thin-walled structures along the thin direction. In addition to the approximations provided by a shell model, various numerical formulations to solve the underlying equations with the finite element method may also incorporate approximations. The nature of these approximations can lead to erroneous numerical results, ranging from intentional to inadvertent.

As opposed to the past, shell formulations suitable for deformations that result in small displacements are no longer the subject of heated debate. The controversy regarding shell formulations capable of predicting large displacement persists to this day. This is notably true for so-called Reissner-Mindlin shell formulations that are *geometrically non-linear*.

In conclusion, the research at hand addresses the unresolved theoretical and practical issues related to the geometrically non-linear Reissner-Mindlin shell model. The core aim of this work is the development of a consistent Reissner-Mindlin shell formulation while striking a balance between computational efficiency and accuracy. It focuses on identifying and addressing the pitfalls and approximations associated with shell models and numerical formulations. These pitfalls are studied in detail to also give future researchers a better understanding of the underlying issues. By doing so, the study aims to contribute to a better understanding of the behavior of thin-walled structures and improve the prediction quality of Reissner-Mindlin shell formulations. This is done by rigorously defining the underlying foundations of differential geometry and continuum mechanics to derive a consistent and efficient formulation of the geometrically non-linear Reissner-Mindlin shell model.

## 1.2 State of the Art

### 1.2.1 Historical Overview

In the following, some historical milestones in the development of (non-linear) shell theories are presented. Classical shell models can be grouped into *Kirchhoff-Love*-type and *Reissner-Mindlin*-type models. The former rely on a kinematic description that is

based only on the midsurface position, while the latter incorporate independent rotations of the director field, thus taking into account transverse shear deformation. Here, the director field is usually associated with the material fibers in the normal direction in the undeformed configuration. Despite Koiter's opinion that Love's shell model was perfect<sup>1</sup>, with the advent of computers, it became clear, that shell formulations based on the Kirchhoff-Love model have several drawbacks. Due to the underlying fourth-order differential equation, one needs special finite elements, which are equipped with a continuous derivative of the displacements at the element boundaries. Furthermore, the lack of rotational degrees of freedom makes the application of boundary conditions challenging. Both problems do not occur in Reissner-Mindlin shell formulations, at the price of more degrees of freedom due to the independent director field. Unfortunately, the director field introduces new problems. These stem from the fact that the director field is assumed to be *inextensional*. This yields a theory that has to deal with non-linear configuration spaces since the director field lives on the unit sphere.

The derivation of these shell theories has been accomplished by considering different approaches. Love's shell theory [Lov88] was developed by reducing the three-dimensional body to a two-dimensional surface called the *midsurface*. In this derivation, several geometric assumptions and mechanical assumptions for the stresses are made to arrive at the Kirchhoff-Love shell model. In contrast to this, the brothers E. and F. Cosserat [CC09] developed a shell model, by directly assuming a two-dimensional surface and stating the equilibrium using stress resultants. The mathematical description of the surface is done not only by describing the midsurface, but also by introducing independent director fields. These are then coupled with the stress resultants to yield the equilibrium equations. This method of directly assuming a two-dimensional surface is called the *direct approach*. A major contribution to this approach is the paper series by Simo and coworkers [Sim89; SF89; Sim90a; Sim90b; SK92; Sim92b]. This direct approach yields so-called *geometrically exact* shell models. A third method, introduced in Ahmad et al. [Ahm68], is the *degenerated solid approach*, where the three-dimensional body is discretized and into these discrete equations, shell assumptions are plugged in.

All these derivations can lead to the same differential equation if equivalent assumptions are made. Especially, the equivalence of the direct approach and the degenerated solid approach was shown in Büchter [Büc92].

A fixed set of assumptions can be a limiting factor. Consequently, these restrictions can also be made optional, through a power series expansion of the displacement field in the thickness direction as done in Naghdi [Nag73]. By using an infinite number of terms, this approach yields the three-dimensional response.

---

<sup>1</sup>Koiter gave a talk, titled "All you need is Love" in the 1960s [Cam99].



Much more can be said about the historical development of shell models in general, but the reader is referred to the following works: The origins of geometrically non-linear shell formulations can be traced back to Chien [Chi44]. For a historical review of non-linear shell theory, the reader is referred to Seidel [Sei73], Waltersdorf [Wal71], and Bischoff [Bis99]. For a concise summary of geometrically exact shell formulation using stress resultants, see Zienkiewicz et al. [Zie14].

### 1.2.2 The Reissner-Mindlin Shell Model

In the following, the historical developments of the geometrically non-linear Reissner-Mindlin model will be described, along with the disadvantages that still exist or have been overcome in the past. Especially, the treatment of the unit director field is the focus of this section.

Initially, director rotations in shell formulations were represented by angle pairs in linear spaces [Ram76]. This linearity naturally results in a symmetric stiffness matrix. Unfortunately, this straightforward approach is flawed because it contains singularities, which may cause convergence issues and limit the rotation's magnitude [IT02; Bet98; Ram76; BR92]. This can be explained by the so-called *hairy ball theorem* [Bro12, §2], which proves that no parameterization exists, that yields a smooth non-degenerate tangent vector field for the unit sphere. Hence, addressing the singularity necessitates a transition between parameterizations in its vicinity [Ram76]. Moreover, these formulations require the evaluation of trigonometric functions for the residual vector and the stiffness matrix. A similar history can be observed for Kirchhoff-Love rods, starting with Antman [Ant74], where Euler angles are used to rotate the cross-section frame. Similarly, it has been common to tackle the problem by allowing only moderately large rotations, e.g., Argyris [Arg82] proposed to include the Taylor expansion of the rotations up to the quadratic term, which leads to a formulation, that actually allows moderate rotations but non-objective results. A solution to the problem is to avoid parameterization of the unit sphere at all.

To address the singularities inherent in a parameterization, Hughes and Liu [HL81] employed direct interpolation of the director. This formulation leads to an objective and path-independent approach. An alternative approach was proposed by Simo and co-workers for Timoshenko beams [Sim85] and Reissner-Mindlin shells [SF89]. There, the authors exploited the manifold structure of  $\mathcal{SO}(3)$  and  $\mathcal{S}^2$ . The Riemannian manifold  $\mathcal{SO}(3)$  is a compact three-dimensional Lie Group called the special orthogonal group and the Riemannian manifold  $\mathcal{S}^2$  is the two-dimensional unit sphere. These manifolds can be defined as  $\mathcal{SO}(3) = \{\mathbf{X} \in \mathbb{R}^3 \times \mathbb{R}^3 \mid \mathbf{X}^T \mathbf{X} = \mathbf{I} \wedge \det \mathbf{X} = 1\}$  and  $\mathcal{S}^2 = \{\mathbf{x} \in \mathbb{R}^3 \mid \mathbf{x}^T \mathbf{x} = 1\}$ .

Nevertheless, these formulations are artificial *path-dependent* and *non-objective* due to the interpolation of rotation increments. Moreover, it is necessary to keep track of history variables at each quadrature point. Crisfield and Jelenić [CJ99] pointed out these shortcomings and presented a remedy for the case of a non-linear Timoshenko beam formulation. In this formulation, the nodal quantities living in  $\mathcal{SO}(3)$  are interpolated, in contrast to the erroneous interpolation of quantities in the tangent bundle  $T\mathcal{SO}(3)$ . This approach yields an objective and path-independent formulation. The proposed formula is well-known in computer graphics and is called SLERP (Spherical Linear intERPolation), see Romero and Arnold [RA17]. In Crisfield and Jelenić [CJ99, Ch. 5b], this concept is extended to higher-order polynomials, but it is still restricted to one-dimensional spaces. Therefore, it is only useful for beams. For a summary of several interpolation schemes for beams and their drawbacks, refer to Romero [Rom04].

For the two-dimensional representation in the context of shells, the generalization of SLERP does not lead to a satisfactory concept. For example, the formulation proposed in Areias et al. [Are13] generalizes SLERP and leads to an objective and path-independent approach, but it suffers from a spurious dependence of the computational results on the node numbering. Furthermore, since the nodal director components are arguments inside trigonometric functions, evaluation, and linearization are expensive. Additionally, the formulation is only applicable to states, where the nodal directors are not parallel, which is not desirable.

Recently proposed formulations limit the transverse shear to be geometrically linear, thus avoiding the treatment of large rotations. The approach by Benson et al. [Ben10] inherits this property directly from the formulations of Belytschko et al. [Bel84] and Belytschko et al. [Bel92]. Furthermore, in Oesterle et al. [Oes17] and Long et al. [Lon12], the ansatz space must be  $C^1$ -continuous between elements due to the presence of second derivatives in the weak form. This requirement is inherited from the Kirchhoff-Love model since the shear deformation is hierarchically added to the Kirchhoff-Love formulation. This continuity constraint can be fulfilled by using splines as shape functions. Nevertheless, the needed  $C^1$ -continuity may compromise the elegance of this hierarchic approach and needs special attention [Kie10]. Nevertheless, the formulations from Oesterle et al. [Oes17] and Long et al. [Lon12] are path-independent and objective.

An isogeometric approach that includes the director rotation has been proposed by Dornisch et al. [Dor16]. It is based on the formulation of [Sim90a] and thus suffers from similar shortcomings, such as path dependence and non-objectivity, inherited from the history fields at each integration point, see [Dor16, Table A.2].

Finally, the formulation of Sander et al. [San16b] must be mentioned, which inherits objectivity and path independence from the continuous model at the cost of solving a small non-linear minimization problem at each integration point to obtain the interpolated

value. The formulation is not derived from the Reissner-Mindlin model, but due to its importance for the subsequent chapters, it is included here. This formulation is constructed from a Cosserat-type shell model with drilling rotations, which requires interpolation in  $\mathcal{SO}(3)$ . The resulting finite elements are called geodesic finite elements, which use tools of interpolation on manifolds to obtain a consistent formulation.

### 1.2.3 Linearization of Finite Elements for Non-linear Fields

The solution of the algebraic equations derived from the differential equation is usually obtained by a Newton-Raphson scheme. This is the work-horse for non-linear problems in structural mechanics, even though it is not guaranteed to converge. Nevertheless, it is widely used and provides a good balance between accuracy and efficiency. The Newton-Raphson scheme requires the solution of a linearized problem at each iteration step, whereas the linearized problem is stated with the tangent stiffness matrix. To at least guarantee the best possible convergence behavior, the tangent stiffness matrix needs to be derived by *consistent linearization*. The foundations of a consistent linearization can be found in the works Hughes and Pister [HP78], Marsden and Hughes [MH94], Simo and Marsden [SM84], and Wriggers [Wri88]. Historically, the linearization of complex material behavior has been a major issue in the development of finite element formulations. The correct linearization was often difficult to obtain, but in several cases, it was very beneficial for the convergence behavior of the Newton-Raphson scheme. Impressive consistent linearizations are, for example, in the context of geometrically linear but materially non-linear problems, the consistent linearization of Simo and Taylor [ST85] and for geometrically non-linear contact problems Wriggers and Simo [WS85].

Unfortunately, almost 50 years later, most of the Reissner-Mindlin shell formulations still suffer from a lack of consistent linearization, which leads to several problems such as poor convergence behavior. This usually necessitates introducing small load steps, which is not desirable. In contrast to consistent linearization in the context of material non-linearity or non-linearity from contact problems, the non-linearity coming from non-linear solution fields is still not well understood. This applies to geometrically non-linear Reissner-Mindlin shells, to geometrically non-linear three-dimensional beams, as well as to geometrically non-linear Cosserat-type shells.

In [Sim85], Simo derived a tangent operator in the context of beams that may be unsymmetric, *away from equilibrium* for a potential taking values from  $\mathcal{SO}(3)$ . This is a result of using the *second variation* as a tool to construct the tangent operator.

Later, Simo [Sim92a] concluded that the *Hessian* — specifically, the *Riemannian Hessian* — can be obtained by symmetrizing the unsymmetric second variation. This procedure

is only valid for manifolds that can be classified as *compact Lie Groups*, which does not apply to the two-dimensional unit sphere. In Makowski and Stumpf [MS95], these results of [Sim92a] were revisited. There, the authors stated that an unsymmetric tangent operator can result from the second variation, but it lacks a well-defined nature. Therefore, they concluded that the Riemannian Hessian is the appropriate and well-defined tensorial quantity to be used as a tangent operator. For this Hessian, several works concluded that it needs to be symmetric for a torsion-free connection [Mis73; dC92; Sim92a; MS95; Rom05; Abs08; Ste15; RA17]. The present work explores the second variation as well as the Riemannian Hessian as candidates for the tangent operator on a theoretical level and also provides the quantities needed for implementing the latter. Nevertheless, the symmetry of the tangent operator is still controversially discussed in, e.g., Suetake et al. [Sue03]. For a historical reference, a short note on the history of unsymmetric tangent operators can be found in Ray [Ray15, Ch. 1.7].

## 1.3 Scope of This Work

This work aims to rigorously present the structural-mechanical fundamentals of the Reissner-Mindlin shell model and shell formulation in order to gain knowledge for both theory and numerical simulation.

In summary, this thesis deals with the following topics in the context of the Reissner-Mindlin shell model:

- Exact derivation of the shell stress resultants.
- Investigation of the Reissner-Mindlin assumptions.
- Consistent linearization procedure for a consistent and symmetric stiffness matrix.
- Properties of suitable director interpolation schemes to obtain a path-independent and objective formulation.
- The influence of locking on the correct choice of the director interpolation.
- Enforcement of the zero normal stress assumption.
- Functional analysis in non-linear function spaces from an engineering perspective.

From the conglomerate of these derivations, a shell formulation can be distilled that has the following features:

- It inherits the objectivity of the continuous shell model.
- The magnitude of total rotations is not limited.
- The unit length constraint of the interpolated director is satisfied in the domain.
- Since no history fields are introduced at the integration points, the interpolation of the director is path-independent.
- Singularities are avoided by not parametrizing the unit sphere.
- The stiffness matrix is symmetric without neglecting any terms and without applying symmetrization procedures.
- The resulting element vectors and matrices are invariant to node numbering.
- Fewer load steps and iterations are needed in comparison to formulations found in the literature.
- Convergence orders are not artificially decreased.

While individual features of the proposed formulation can be found in various shell formulations in the literature, it is worth noting that, to the author’s knowledge, there is currently no Reissner-Mindlin shell formulation that encompasses *all* of these features simultaneously, except for the author’s contribution [MB22]. These conclusions led to the shell formulation from Müller and Bischoff [MB22]. Specifically, this means that it works for Lagrangian finite elements with arbitrary polynomial order, as well as for isogeometric finite elements, which also incorporate higher polynomial orders as ansatz functions. Additionally, the underlying geometrically non-linear shell model is revisited and the derivations of the balance laws, stress resultants, and the Reissner-Mindlin assumptions are discussed.

Furthermore, the present work aims to answer questions concerning the consistent linearization of the Reissner-Mindlin shell model. By using the notion of optimization on manifolds, the correct linearization process is derived. To achieve this, the notion of optimization on manifolds is used to derive the correct linearization process. A key aspect of this approach is to interpret the unit-length constraint as a problem of *unconstrained optimization on a constrained space* rather than a problem of *constrained optimization on an unconstrained space*. The foundations of algebraic optimization on manifolds, which form the basis for this interpretation, are summarized in the works by Absil et al. [Abs08] and Boumal [Bou23]. By adopting this perspective, a formulation with five degrees of freedom per node is obtained, which represents the optimal number. It is worth noting that this optimal number of degrees of freedom cannot be achieved by using approaches such as the *Lagrange multiplier method* or the *penalty method*, which are commonly used to handle constraints. These methods would result in seven or six degrees of freedom per node, respectively, which is more than the optimal number. Despite their suboptimal nature, these approaches are still widely used in the literature, as seen in works by Weeger et al. [Wee19], Betsch and Janz [BJ16], and Harsch et al. [Har21], among others.

Thus, covering all these given aspects, the result yields a geometrically non-linear Reissner-Mindlin shell formulation, which is an improvement in several directions.

## 1.4 Overview

**Chapter 2** and **Chapter 3** introduce the mathematical foundations of differential geometry, which are necessary to fully investigate the Reissner-Mindlin shell model in later chapters. In particular, the concept of manifolds, tangent spaces, vector fields, differential forms, and the Riemannian metric are introduced, while simultaneously defining the notation used throughout this work.

**Chapter 4** describes the foundation of elasticity in the context of continuum mechanics, which is used as a starting point for the derivation of the shell model and the shell formulation.

**Chapter 5** is the heart of this thesis and describes the Reissner-Mindlin shell model from kinematics, stress resultants, and balance laws up to the aspects of implementation of the residual vector and stiffness matrix in the finite element context. Additionally, the numerical enforcement of the vanishing normal stress assumption is discussed.

**Chapter 6** describes various aspects and pitfalls that arise in the context of solving partial differential equations on manifolds. In particular, the role of functional analysis and the symmetry of the tangent operator is examined. Furthermore, the requirements and possibilities for a consistent director interpolation are discussed.

**Chapter 7** presents numerical experiments that demonstrate and compare the properties of the proposed shell formulation. This is done in the context of various director interpolations and various locking prevention techniques.





# 2

---

## First-Order Differential Geometry

Several definitions of differential geometry are used throughout this thesis. They lay the foundations for understanding the developments in the rest of the thesis, i.e., the later defined Reissner-Mindlin shell model and the numerical methods. This chapter introduces some fundamental concepts, such as the notion of manifolds, tangent spaces, Riemannian manifolds, Riemannian metric, and differentiation.

First, the abstract notion of manifolds is established, and then more geometric structure is added to it. In terms of differential geometry, the chapter is based on Absil et al. [Abs08], Boumal [Bou23], Marsden and Hughes [MH94], Abraham et al. [Abr84], do Carmo [dC92], Lee [Lee03], O’Neill [ONe83], Steenrod [Ste99], and Misner et al. [Mis73]. See Munkres [Mun00] for more information on topology. For details on the historical context of differential geometry, the reader is referred to Reich [Rei13].

### 2.1 Manifolds, Charts, Atlases and Parameterization

A manifold’s abstract definition is based on the concepts of *charts* and *atlases*. As these terms suggest, a manifold can be imagined as the Earth’s surface with two-dimensional charts and an atlas as a collection of these charts that covers the whole Earth. Let  $\mathcal{M}$  be a set. A bijection  $\phi$ , that maps a subset  $\mathcal{U}$  of  $\mathcal{M}$  onto an open subset  $D$  of  $\mathbb{R}^m$  is then a chart of the set  $\mathcal{M}$  with dimension  $m$ . This chart can be identified by the pair  $(\mathcal{U}, \phi)$ .

**Definition 1.** The pair  $(\mathcal{U}, \phi)$  is called a ( $m$ -dimensional) *chart* on the set  $\mathcal{M}$ , if the mapping

$$\phi : \begin{cases} \mathcal{U} \rightarrow D, \\ \mathbf{x} \mapsto (\phi^1(\mathbf{x}), \dots, \phi^m(\mathbf{x})), \end{cases} \quad (2.1)$$

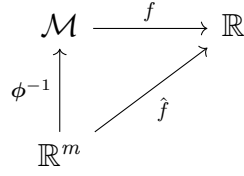


**Figure 2.1:** Commutative diagram of Eq. (2.2).

is continuous, maps to an open set  $D \subset \mathbb{R}^m$  and has a continuous inverse  $\phi^{-1}$ . The number  $\phi^i(\mathbf{x})$  is called the  $i$ -th *coordinate* of the point  $\mathbf{x}$  in the chart  $\phi$ . The inverse mapping  $\phi^{-1} : D \rightarrow \mathcal{U}$  is called (*local*) *parameterization* of  $\mathcal{M}$ .

In the following, if  $\mathcal{U}$  is clear from the context, we use  $\phi$  as a shortcut for a chart. Charts can be used to study the set  $\mathcal{U}$  by transforming them to  $D = \phi(\mathcal{U})$ , which is a subset of  $\mathbb{R}^m$ , where the usual linear analysis rules apply. Particularly, a function  $f$  taking arguments from  $\mathcal{U}$  can be studied using the function

$$\hat{f} = f \circ \phi^{-1} : \begin{cases} \phi(\mathcal{U}) \rightarrow D \subset \mathbb{R}^m, \\ \theta \mapsto \hat{f}(\theta), \end{cases} \quad (2.2)$$

as shown in Fig. 2.1. The quantity  $\hat{f}$  is referred to as the *coordinate representative* of  $f$ . Additionally, it maps from an Euclidean space, which simplifies the study of  $f$ .

A family of charts  $(\mathcal{U}_i, \phi_i)$  is needed to study  $\mathcal{M}$ , as a single chart  $(\mathcal{U}, \phi)$  does not necessarily cover each point of  $\mathcal{M}$ . If a family of charts covers every point of  $\mathcal{M}$ , it is called an *atlas* of  $\mathcal{M}$ , i.e.,  $\cup_i \mathcal{U}_i = \mathcal{M}$ .

**Definition 2.** A set  $\mathcal{M}$  is called a (*topological*) *manifold*<sup>1</sup>, if there exists an atlas of it.

Following that, we refine the concept of manifolds by limiting the set of possible charts on  $\mathcal{M}$ . Particularly, if two charts  $(\mathcal{U}_1, \phi_1)$  and  $(\mathcal{U}_2, \phi_2)$  map the same point  $\mathbf{x} \in \mathcal{U}_1 \cap \mathcal{U}_2$ , these two mappings should be compatible, see Fig. 2.2. Therein, two charts are defined on the set  $\mathcal{M}$  and these charts map the dashed regions. Then, where the two charts map the same subset, i.e., the intersection of the two charts  $\phi(\mathcal{U}_a \cap \mathcal{U}_b)$ , these mappings of the two charts should be compatible. This means a coordinate change from one chart to the other should be smooth to some degree. This requirement leads to a refined definition of an atlas of  $\mathcal{M}$ .

**Definition 3.** A  $C^l$ -*atlas*  $\mathcal{A}$  of the set  $\mathcal{M}$  is a collection of charts  $(\mathcal{U}_i, \phi_i)$  such that

1.  $\cup_i \mathcal{U}_i = \mathcal{M}$ ,

---

<sup>1</sup>We have omitted the fact that the set  $\mathcal{M}$  must be a Hausdorff space and second countable. See [Mun00] for topological details.

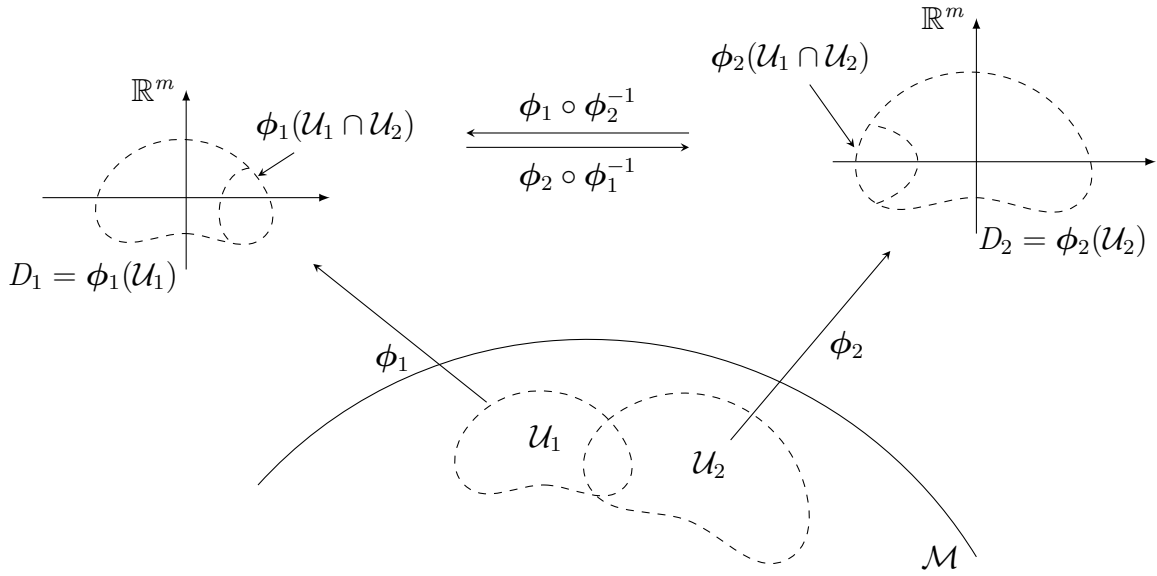


**Figure 2.2:** Charts and change of coordinates. Figure adapted from [Abs08, Fig. 3.1].

2. for all  $(\mathcal{U}_a, \phi_a)$  and  $(\mathcal{U}_b, \phi_b)$  with  $\mathcal{U}_a \cap \mathcal{U}_b \neq \emptyset$ , where the change of coordinates

$$\phi_b \circ \phi_a^{-1} : \begin{cases} \phi(\mathcal{U}_a \cap \mathcal{U}_b) \rightarrow \phi(\mathcal{U}_a \cap \mathcal{U}_b), \\ \theta \mapsto \phi_b(\phi_a^{-1}(\theta)), \end{cases} \quad (2.3)$$

is  $C^l$ -smooth.

If a manifold admits such an atlas, it is a differentiable manifold.

**Definition 4.** A (topological) manifold  $(\mathcal{M}, \mathcal{A})$  is called  $C^l$ -differentiable manifold, if there exists a  $C^l$ -atlas of it.

In the following, a manifold is referred not by the pair  $(\mathcal{M}, \mathcal{A})$ , but simply by  $\mathcal{M}$ , and it is assumed that the differentiability is clear from the context or is unimportant. This also refers to the topologies defined on the manifold induced by the atlas.

## 2.2 Differential Topology

Similar to Eq. (2.2) where a function  $f$  maps from a manifold  $\mathcal{M}$  to  $\mathbb{R}$ , consider a function  $\mathbf{f}$  that maps from manifold  $\mathcal{M}$  of dimension  $m$  onto another manifold  $\mathcal{N}$  of dimension  $n$ . This abstract definition is used later, to define functions between the reference configuration and the current configuration in the context of continuum mechanics.

One special class of such functions is the class of homeomorphisms.

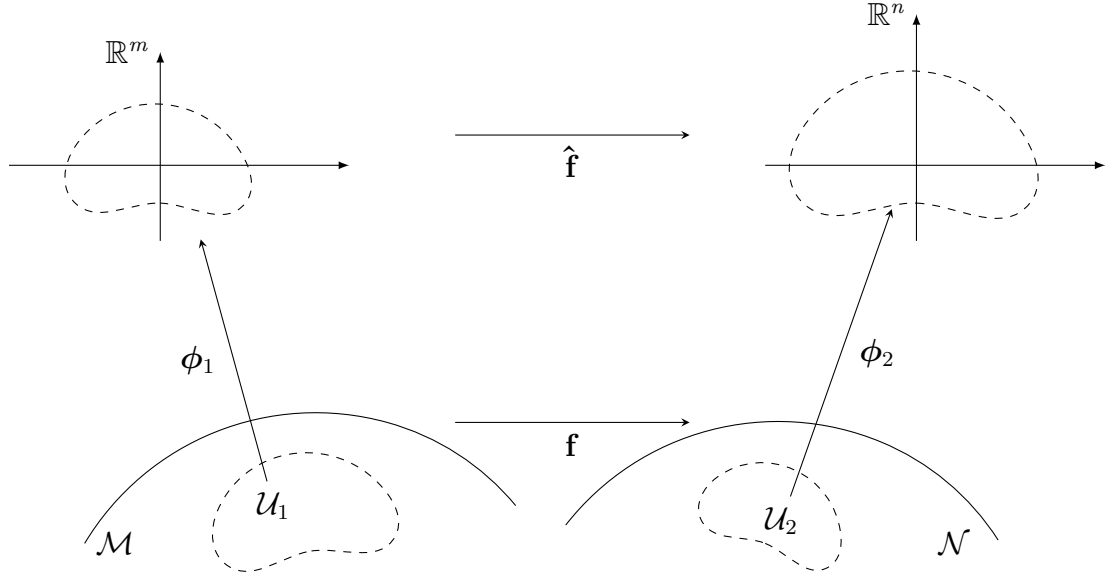


**Figure 2.3:** Mapping of coordinate representation of a function mapping between manifolds.

**Definition 5.** A *homeomorphism*  $\mathbf{f} : \mathcal{M} \rightarrow \mathcal{N}$  is a bijection where,  $\mathbf{f}$  and its inverse  $\mathbf{f}^{-1}$  are continuous. Two manifolds  $\mathcal{M}$  and  $\mathcal{N}$  are homeomorphic, if there exists a homeomorphism between them.

Hence, homeomorphisms preserve topological invariants, or vice versa topological invariants are defined as properties that are preserved by homeomorphisms. Moreover, because the charts  $\phi_i$  in an atlas define homeomorphisms from each subset  $\mathcal{U}_i$  to a subset of  $\mathbb{R}^m$ , a (topological) manifold may also be conceptualized as follows: A manifold is a set in which, for any point  $\mathbf{x}$ , there exists a neighborhood that is homeomorphic to a subset of  $\mathbb{R}^m$ . This leads to the sloppy definition: “A manifold is a space that resembles Euclidean space locally.”

If we want to study the derivatives of the function  $\mathbf{f}$  in a convenient way, we can use a coordinate representative, as in Eq. (2.2). This can be done by introducing a chart  $\phi_1$  in the neighborhood of  $x \in \mathcal{M}$  and a chart  $\phi_2$  in the neighborhood of  $\mathbf{f}(x) \in \mathcal{N}$ . Then, the coordinate representation of  $\mathbf{f}$  is given by

$$\hat{\mathbf{f}} = \phi_2 \circ \mathbf{f} \circ \phi_1^{-1} : \begin{cases} \mathbb{R}^m & \rightarrow \mathbb{R}^n, \\ \boldsymbol{\theta} & \mapsto \phi_2(\mathbf{f}(\phi_1^{-1}(\boldsymbol{\theta}))), \end{cases} \quad (2.4)$$

where the mapping is visualized in Fig. 2.3. Since  $\hat{\mathbf{f}}$  is a mapping from a Euclidean space to a Euclidean space with  $\hat{\mathbf{f}}$ . Defining a directional derivative is trivial. Additionally, since the notion of tangent vectors or embeddings is not yet introduced, the only possibility to

define the directional derivative of  $\mathbf{f}$  in direction  $\mathbf{v}$  “through the charts” ([Abs08, Ch. 3.2, p. 24])  $\phi_1$  and  $\phi_2$ . Thus, the directional derivative of  $\mathbf{f}$  in direction  $\mathbf{v}$  is defined, through the charts, as

$$D\hat{\mathbf{f}}(\boldsymbol{\theta}) : \begin{cases} \mathbb{R}^m & \rightarrow \mathbb{R}^n, \\ \mathbf{v} & \mapsto D_{\mathbf{v}}\hat{\mathbf{f}}(\boldsymbol{\theta}) = D\hat{\mathbf{f}}(\boldsymbol{\theta})[\mathbf{v}] \end{cases}, \quad (2.5)$$

with  $\mathbf{v} \in \mathbb{R}^m$ . This also defines the notation of directional derivatives in Euclidean spaces as  $D_{\mathbf{v}}\mathbf{f}(\boldsymbol{\theta}) = D\mathbf{f}(\boldsymbol{\theta})[\mathbf{v}]$ . Here, the first one achieves a compact notation. The second emphasizes that the directional derivative (of  $\mathbf{f}$ ) is a *machine*<sup>2</sup> with two *slots*<sup>2</sup> into which the position  $\mathbf{x}$  and the direction  $\mathbf{v}$  are inserted.

Since the concept of derivation is available, also differentiability can be defined. The function  $\mathbf{f}$  is differentiable of class  $C^l$ , if  $\hat{\mathbf{f}}$  is. This can be used to define *diffeomorphisms*.

**Definition 6.** A  $C^l$ -*diffeomorphism*  $\mathbf{f} : \mathcal{M} \rightarrow \mathcal{N}$  is a bijection where,  $\mathbf{f}$  and its inverse  $\mathbf{f}^{-1}$  are  $C^l$ -continuous. Two manifolds  $\mathcal{M}$  and  $\mathcal{N}$  are  $C^l$ -diffeomorphic, if there exists a diffeomorphism between them. Hence, every  $C^l$ -diffeomorphism is a homeomorphism but the *vice versa* is not true.

## 2.3 Embeddings and Submanifolds

Some functions between manifolds can be categorized as *immersions*, *inclusions*, and *embeddings*. This allows the definition of *embedded submanifolds*, which is the main use of these concepts here. Consider once again the function  $\mathbf{f} : \mathcal{M} \rightarrow \mathcal{N}$  and its coordinate representation  $\hat{\mathbf{f}}$ , as described in Eq. (2.4). Again, the dimensions of  $\mathcal{M}$  and  $\mathcal{N}$  are  $m$  and  $n$ , respectively. If  $\mathbf{f}$  is injective at every  $\mathbf{x} \in \mathcal{M}$ , it is referred to as an immersion. When  $\mathbf{f}$  is surjective, it is referred to as a submersion. Using the differential  $D\hat{\mathbf{f}}(\boldsymbol{\theta})[\bullet] : \mathbb{R}^m \rightarrow \mathbb{R}^n$ , a comparable classification can be obtained. Let the rank of  $\hat{\mathbf{f}}$  denote the dimension of its differential image. If the rank of  $\hat{\mathbf{f}}$  is  $m$ , it is an immersion at each point and  $m \leq n$ . In contrast, if the rank is  $n$ , it is a submersion at each point and  $m \geq n$ . Using these definitions, the concept of embeddings can be defined.

**Definition 7.** An *embedding*  $\mathbf{f}$  of a manifold  $\mathcal{M}$  in a manifold  $\mathcal{N}$  is an immersion, which is a homeomorphism between  $\mathcal{M}$  and its image  $\mathbf{f}(\mathcal{M}) \subset \mathcal{N}$ .

For the notion of an embedded submanifold, we need the notion of *inclusions*. An *inclusion* is a function  $\iota$  that maps an element  $\mathbf{x}$  of a subset to  $\mathbf{x}$ , but as an element of the superset. For visualization, see Fig. 2.4. Therein, the inclusion map sends all elements of the subset

<sup>2</sup>This wording is taken from [Mis73].

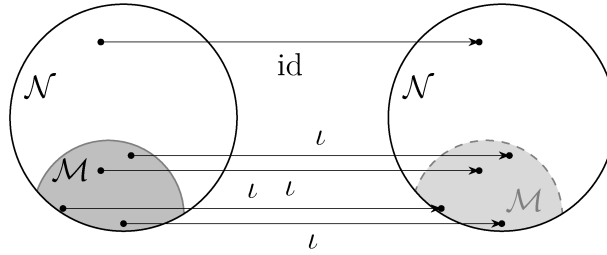


**Figure 2.4:** The inclusion map  $\iota$  sends a point  $x$  as an element from the set  $\mathcal{M} \subset \mathcal{N}$  to the same point  $x$  but represented as an element of  $\mathcal{N}$ . The identity map  $\text{id}$  maps elements from  $\mathcal{N}$  to  $\mathcal{N}$ .

$\mathcal{M}$  to the same element but as an element in the super set  $\mathcal{N}$ . Formally, an inclusion  $\iota$  is a mapping

$$\iota : \begin{cases} \mathcal{M} \rightarrow \mathcal{N}, \\ \mathbf{x} \mapsto \iota(\mathbf{x}). \end{cases} \quad (2.6)$$

Since these functions are defined between different manifolds, two special manifold categories can be defined.

**Definition 8.** Let  $(\mathcal{M}, \mathcal{A})$  and  $(\mathcal{N}, \mathcal{B})$  be manifolds such that  $\mathcal{M} \subset \mathcal{N}$ .  $\mathcal{A}$  and  $\mathcal{B}$  denote the corresponding atlases. An *immersed submanifold*  $(\mathcal{M}, \mathcal{A})$  of a manifold  $(\mathcal{N}, \mathcal{B})$  is a manifold, where the inclusion map is an immersion.

**Definition 9.** Let  $(\mathcal{M}, \mathcal{A})$  and  $(\mathcal{N}, \mathcal{B})$  be manifolds such that  $\mathcal{M} \subset \mathcal{N}$ .  $\mathcal{A}$  and  $\mathcal{B}$  denote the corresponding atlases. An *embedded submanifold*  $(\mathcal{M}, \mathcal{A})$  of a manifold  $(\mathcal{N}, \mathcal{B})$  is a manifold, where the inclusion map is an embedding, see Definition 7. The space  $\mathcal{N}$  is then called *embedding space*.

**EXAMPLE 1** (Klein’s bottle). Klein’s bottle can be immersed into  $\mathbb{R}^3$  as shown in Fig. 2.5, via a map  $\mathbf{f} : \mathbb{R}^2 \rightarrow \mathbb{R}^3$ . Since the inclusion map is an immersion it is an immersed submanifold of  $\mathbb{R}^3$ . It cannot be embedded into  $\mathbb{R}^3$ , since the map  $\mathbf{f}$  is not everywhere invertible due to self-intersections. Therefore, it is not homeomorphic.

**EXAMPLE 2** (The circle and  $\mathbb{R}$ ). The circle  $\mathcal{S}^1 = \{\mathbf{x} \in \mathbb{R}^2 \mid \mathbf{x} \cdot \mathbf{x} = 1\}$  cannot be embedded onto the real line, since a map  $\mathbf{f}$  would necessarily cut the circle open and then invertibility is lost. In topology, the result that no homeomorphism exists can also be seen by comparing topological invariants. The circle is compact and the real number line is not. Since homeomorphisms preserve topological invariants, and compactness is such an invariant, no homeomorphism can exist.

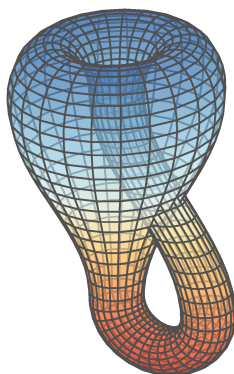


**Figure 2.5:** Klein's bottle immersed but not embedded into  $\mathbb{R}^3$ .

EXAMPLE 3 (The circle and  $\mathbb{R}^2$ ). The circle can be embedded using the inclusion map  $\iota : S^1 \rightarrow \mathbb{R}^2$ . Since the inclusion map is an embedding, it is an embedded submanifold of  $\mathbb{R}^2$ .

EXAMPLE 4 ( $\mathbb{R}^n$  into  $\mathbb{R}^{n+k}$ ). An embedding is represented by the inclusion map  $\mathbb{R}^n \rightarrow \mathbb{R}^{n+k}$ , which is obtained by mapping  $(x^1, \dots, x^n)$  to  $(x^1, \dots, x^n, 0, \dots, 0)$ .

## 2.4 Directional Derivatives, Tangents and Cotangents

Understanding the local behavior of manifolds requires a firm understanding of tangent vectors and direction derivatives. They also allow the concept of the local change of a function. In addition, they allow for the approximation of manifolds via linear subspaces known as tangent spaces.

### 2.4.1 Abstract Manifolds

Consider a real-valued function  $f : \mathbb{R}^n \rightarrow \mathbb{R}$ . The *Euclidean directional derivative* of  $f$  in direction  $\mathbf{v} \in \mathbb{R}^n$  at  $\mathbf{x} \in \mathbb{R}^n$  is defined as

$$D_{\mathbf{v}}f(\mathbf{x}) = Df(\mathbf{x})[\mathbf{v}] = \lim_{t \rightarrow 0} \frac{f(\mathbf{x} + t\mathbf{v}) - f(\mathbf{x})}{t}. \quad (2.7)$$

In order to generalize this for an abstract manifold — that is not embedded in an ambient space

in a vector space. This problem can be circumvented, again, through the aid of charts. Consider a function  $\gamma : \mathbb{R} \rightarrow \mathcal{M}; t \mapsto \gamma(t)$ . This definition of  $\gamma$ , can be used to define the function

$$\tilde{f} = f \circ \gamma : \begin{cases} \mathbb{R} \rightarrow \mathbb{R}, \\ t \mapsto f(\gamma(t)) \end{cases}. \quad (2.8)$$

Now, the manifold-valued function  $f$  is replaced by the simpler real-valued function  $\tilde{f}$ . See Fig. 2.6 for a visual representation of the situation. Since we are now searching for a function that maps from  $\mathbb{R}$  to  $\mathbb{R}$ , which can be found by a classical vector space derivative, the complexity of the problem has been drastically reduced. This yields

$$\dot{\gamma}(0)[f] = \left. \frac{d(f(\gamma(t)))}{dt} \right|_{t=0} = \lim_{t \rightarrow 0} \frac{f(\gamma(t)) - f(\gamma(0))}{t}, \quad (2.9)$$

but this unusual notation needs some explanation. In this abstract setting, where there is no embedding space, tangent vectors have no visual meaning. The mapping  $\dot{\gamma}(0)[\bullet]$  nevertheless accepts a function  $f \in \mathcal{D}(\mathcal{M})$  and maps it to a scalar. It is the derivative in the direction  $\dot{\gamma}(0)$  of the function  $f$ . Thus,  $\dot{\gamma}(0)$  is the *tangent vector*. It should not be interpreted as a time derivative of  $\gamma$ , despite the notation, because the difference quotient  $\lim_{t \rightarrow 0} (\gamma(t) - \gamma(0))/t$  is not defined. The tangent vector  $\dot{\gamma}(0)$  is only implicitly defined by Eq. (2.9).



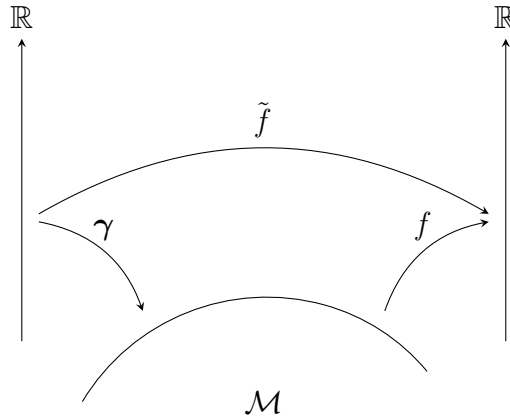


**Figure 2.6:** Mapping rationale for  $\tilde{f}$  and  $f$  of Eq. (2.8)

**Definition 10.** A *tangent vector*  $\xi_{\mathbf{x}}$  is defined at a specific point  $\mathbf{x}$  of a manifold  $\mathcal{M}$ . Consider a mapping from  $\mathcal{D}(\mathcal{M})$  to  $\mathbb{R}$  such that there exists a curve  $\gamma$  on  $\mathcal{M}$  with  $\gamma(0) = \mathbf{x}$ . This curve should satisfy

$$\xi_{\mathbf{x}}[f] = \dot{\gamma}(0)[f] = \left. \frac{d(f(\gamma(t)))}{dt} \right|_{t=0}, \quad \forall f \in \mathcal{D}(\mathcal{M}). \quad (2.10)$$

This curve  $\gamma$  is said to *realize* the tangent vector  $\xi_{\mathbf{x}}$  [Abs08].

This also defines now a directional derivative as follows

$$D_{\xi}f(\mathbf{x}) = \left. \frac{d(f(\gamma(t)))}{dt} \right|_{t=0}, \quad (2.11)$$

where  $\gamma(t)$  again realizes  $\xi$  at  $\mathbf{x}$ . However, the question arises as to how to define the curve  $\gamma$  so that it realizes  $\xi_{\mathbf{x}}$ . In particular, this means informally “ $\frac{\partial}{\partial t}\gamma(t)|_{t=0} = \xi_{\mathbf{x}}$ ”. The presence of such a curve is assumed for the time being. The construction of such a curve will be discussed in Section 2.6 on page 33. However, we return first to tangent vectors and provide a graphical intuition for them.

## 2.4.2 Embedded Submanifolds

Consider the manifold  $\mathcal{M}$  as being embedded into a vector space  $\mathcal{E}$ ; hence, the tangent vector of the curve  $\gamma$  on  $\mathcal{M}$  can be determined as

$$\gamma'(0) = \lim_{t \rightarrow 0} \frac{\iota(\gamma(t)) - \iota(\gamma(0))}{t}, \quad (2.12)$$

where  $\iota$  is the inclusion map that sends an element from  $\mathcal{M}$  to the same element in  $\mathcal{E}$ . Now the difference in Eq. (2.12) is well-defined since  $\mathcal{E}$  is a vector space. In particular, the tangent vector  $\gamma'(0)$  is now an element of  $T_{\mathbf{x}}\mathcal{E} \cong \mathcal{E}$ , where  $T_{\mathbf{x}}\mathcal{E}$  is the tangent space at  $\mathbf{x}$  of  $\mathcal{E}$ . Given that  $\mathcal{E}$  is considered to be a vector space,  $T_{\mathbf{x}}\mathcal{E}$  is isomorphic to the space itself. In particular, this means  $T_{\mathbf{x}}\mathcal{E} \cong \mathcal{E}$ .

The following relationship between  $\gamma'$  and  $\dot{\gamma}$  may now be constructed from Definition 10. Consider a function  $f : \mathcal{M} \rightarrow \mathbb{R}$  and again  $\gamma(0) = \mathbf{x}$ , the relationship reads

$$\dot{\gamma}(0)[f] = D_{\gamma'}\bar{f}(\gamma(0)), \quad (2.13)$$

where  $\bar{f}$  is the extension of  $f$  into a neighborhood  $\mathcal{U}$  of  $\mathbf{x}$  in  $\mathcal{E}$ .

In an abuse of notation,  $\gamma'$  and  $\dot{\gamma}$  are used interchangeably. Additionally, we can now relate the directional derivative of the embedding space and the directional derivative on the manifold by

$$Df(\mathbf{x})[\boldsymbol{\xi}] = \left. \frac{d(f(\gamma(t)))}{dt} \right|_{t=0} = \left. \frac{d(\bar{f}(\gamma(t)))}{dt} \right|_{t=0} = D\bar{f}(\mathbf{x})[\boldsymbol{\xi}], \quad (2.14)$$

where  $\gamma(t)$  again realizes  $\boldsymbol{\xi}$  at  $\mathbf{x}$  and  $\boldsymbol{\xi} \in T\mathcal{E}$ . Thus  $\mathcal{E}$  is viewed as an element of the embedding space.

**Tangent vectors From Local Parameterization** The concept of tangent vectors was previously abstract. Now a more geometric way is presented. Consider a local parameterization, as described in Definition 1 on page 14, such that

$$\varphi : \begin{cases} \mathbb{R}^m \rightarrow \mathcal{U}, \\ \boldsymbol{\theta} \mapsto \varphi(\boldsymbol{\theta}). \end{cases} \quad (2.15)$$

This parameterization maps from the Euclidean space  $\mathbb{R}^m$  to a neighborhood  $\mathcal{U} \subset \mathcal{M}$  as indicated in Fig. 2.7. Let  $\mathcal{M}$  be embedded into  $\mathbb{R}^M$ . Consider  $\{\hat{\mathbf{e}}_i\}$  as the standard basis of  $\mathbb{R}^M$  and  $\{\mathbf{e}_i\}$  as the standard basis of  $\mathbb{R}^m$ . Then, the parameterization can be written as  $\varphi(\boldsymbol{\theta}) = \varphi^i(\boldsymbol{\theta})\hat{\mathbf{e}}_i$ . Consequently,

$$\mathbf{g}_j(\boldsymbol{\theta}) = \frac{\partial \varphi^i(\boldsymbol{\theta})}{\partial \theta^j} \hat{\mathbf{e}}_i \quad (2.16)$$

defines a tangent vector on the manifold  $\mathcal{M}$  and is represented as a vector of  $\mathbb{R}^M$ . These tangent vectors  $\{\mathbf{g}_j(\boldsymbol{\theta})\}$  define a basis for  $T_{\varphi(\boldsymbol{\theta})}\mathcal{M}$  embedded into  $\mathbb{R}^M$ . This basis is usually called *holonomic basis* or *coordinate basis*. The scalars  $\theta^1, \dots, \theta^n$  are called *curvilinear coordinates*. If we keep all coordinates constant, except one, we get *coordinate curves*

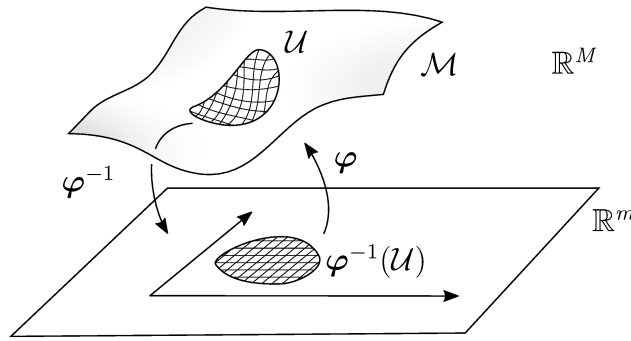


**Figure 2.7:** A coordinate grid. Figure Inspired by [Lee03].

on the manifold, i.e. the thin lines in  $\mathcal{U}$  in Fig. 2.7. These base vectors  $\mathbf{g}_j(\boldsymbol{\theta})$  and the corresponding coordinates  $\theta^i$  define a *curvilinear coordinate system*.

### 2.4.3 Tangent Space and Tangent Bundle

A collection of tangent vectors can be presented in two ways, namely as tangent spaces or as tangent bundles. All possible tangent vectors at a single position  $\mathbf{x}$  can be collected. This set admits a vector space structure and is called *tangent space*. The tangent space of  $\mathcal{M}$  at point  $\mathbf{x}$  is denoted by  $T_{\mathbf{x}}\mathcal{M}$ . It can be stated formally as

$$T_{\mathbf{x}}\mathcal{M} = \{\gamma'(0) : \gamma \in \mathcal{D}(\mathcal{M}), \gamma(0) = \mathbf{x}\}, \quad (2.17)$$

which underlines the fact that it consists of all possible tangents at  $\mathbf{x}$ . Additionally, if  $\mathcal{M}$  is defined by a level set of a constant rank function  $\mathbf{f} : \mathcal{E} \rightarrow \mathbb{R}^m$  then

$$T_{\mathbf{x}}\mathcal{M} = \ker(\mathbf{Df}[\bullet]), \quad (2.18)$$

where the notation  $\mathbf{Df}[\bullet]$  means that the directional derivative is applied to the function  $\mathbf{f}$  in all directions by keeping the direction slot empty. This basically means that all directions  $\mathbf{v} \in \mathcal{E}$ , that yield  $\mathbf{Df}[\mathbf{v}] = 0$ , span the tangent space. Thus,  $\mathbf{Df}[\mathbf{v}] = 0$  means that  $\mathbf{f}$  stays zero in the direction  $\mathbf{v}$ , which means remaining up to the first order on the manifold. This can be interpreted as the very definition of the tangent space.

The tangent space can be interpreted as a local linear approximation of a non-linear manifold.

**EXAMPLE 5** (Tangent space of the sphere). Consider the sphere  $\mathcal{S}^{n-1} = \{\mathbf{x} \in \mathbb{R}^n \mid \mathbf{x}^T \mathbf{x} = 1\}$ . The corresponding level set function would be  $f : \mathbb{R}^n \rightarrow \mathbb{R}, \mathbf{x} \mapsto \mathbf{x}^T \mathbf{x} - 1$ . The

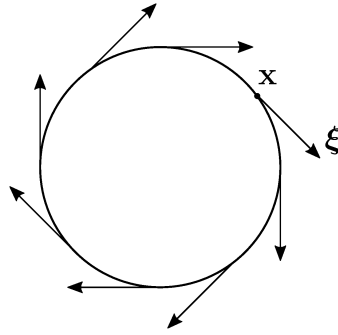


**Figure 2.8:** Tangent bundle  $TS^1$  of the circle  $S^1$  as embedded into  $\mathbb{R}^2$ .

directional derivative  $Df[\mathbf{v}] = 2\mathbf{v}^T \mathbf{x}$  yields the tangent space  $T_{\mathbf{x}}\mathcal{S}^{n-1} = \ker(Df) = \{\mathbf{v} \in \mathbb{R}^n \mid \mathbf{v}^T \mathbf{x} = 0\}$ .

---

This *linearization* of the manifold will be frequently used in later derivations.

The other concept involving tangent vectors is the set of pairs of points  $\mathbf{x}$  and their tangent vectors. It is defined as the disjoint union of all tangent spaces. This set is called *tangent bundle* and defined as

$$T\mathcal{M} = \bigsqcup_{\mathbf{x} \in \mathcal{M}} T_{\mathbf{x}}\mathcal{M} = \{(\mathbf{x}, \boldsymbol{\xi}) : \mathbf{x} \in \mathcal{M} \wedge \boldsymbol{\xi} \in T_{\mathbf{x}}\mathcal{M}\}. \quad (2.19)$$

The tangent bundle can be endowed with its own distinct manifold structure, see [Lee03]. In fact, if  $\mathcal{M}$  is an embedded submanifold in  $\mathcal{E}$  then  $T\mathcal{M}$  is an embedded submanifold of  $\mathcal{E} \times \mathcal{E}$  with dimension  $2(\dim \mathcal{M})$ . There exists a natural projection

$$\pi \begin{cases} T\mathcal{M} \rightarrow \mathcal{M}, \\ (\mathbf{x}, \boldsymbol{\xi}) \mapsto \pi_{\mathbf{x}}(\boldsymbol{\xi}) = \mathbf{x}. \end{cases} \quad (2.20)$$

Thus,  $\pi_{\mathbf{x}}(\boldsymbol{\xi}) = \mathbf{x}$  is called the foot of  $\boldsymbol{\xi}$ . For a visualization see Fig. 2.8. Here the tangent bundle of the circle is shown, there are several tangent vectors  $\boldsymbol{\xi}$  with different feet  $\mathbf{x}$ .

**Tangent Vector Fields** A tangent vector field is a *section* of the tangent bundle  $T\mathcal{M}$ . Thus, a tangent vector field assigns to each point  $\mathbf{x} \in \mathcal{M}$  a tangent vector. Therefore, this yields

$$\boldsymbol{\eta} : \begin{cases} \mathcal{M} \rightarrow T_{\mathbf{x}}\mathcal{M}, \\ \mathbf{x} \mapsto \boldsymbol{\eta}_{\mathbf{x}}. \end{cases} \quad (2.21)$$

Consequently,  $\boldsymbol{\eta}$  is used to denote a vector field, and  $\boldsymbol{\eta}_{\mathbf{x}}$  denotes a specific tangent vector at  $\mathbf{x}$ .

### 2.4.4 Covectors and Cotangent Bundle

Covectors are defined as linear functionals acting in the tangent space  $T_{\mathbf{x}}\mathcal{M}$  at a point  $\mathbf{x} \in \mathcal{M}$ . A covector takes a vector and returns a real number. Thus, a covector is a linear map

$$\boldsymbol{\omega}_{\mathbf{x}} : \begin{cases} T_{\mathbf{x}}\mathcal{M} \rightarrow \mathbb{R}, \\ \boldsymbol{\eta} \mapsto \boldsymbol{\omega}_{\mathbf{x}}(\boldsymbol{\eta}). \end{cases} \quad (2.22)$$

This space of linear functionals acting on  $T_{\mathbf{x}}\mathcal{M}$  is called  $T_{\mathbf{x}}^*\mathcal{M}$ . It is also called the *dual space* of  $T_{\mathbf{x}}\mathcal{M}$ . This notation is also used for other vector spaces  $V$  and its dual space  $V^*$ . For this dual space, a basis can be defined, which is the content of the next definition.

**Definition 11** (Dual basis). Let  $V$  be a finite-dimensional vector space with a basis  $\mathbf{g}_1, \dots, \mathbf{g}_n$ . The covectors  $\mathbf{g}^1, \dots, \mathbf{g}^n$  that satisfy

$$\mathbf{g}^i(\mathbf{g}_j) = \delta_j^i, \quad (2.23)$$

define a basis for  $V^*$  and this basis is called *dual basis* to  $\mathbf{g}_1, \dots, \mathbf{g}_n$ . The object  $\delta_j^i$  is called *Kronecker delta*.<sup>3</sup>

Using this dual basis it is apparent that each covector  $\boldsymbol{\omega} \in V^*$  can be written as

$$\boldsymbol{\omega} = \omega_i \mathbf{g}^i, \quad (2.24)$$

where the components  $\omega_i$  can be calculated by  $\omega_i = \boldsymbol{\omega}(\mathbf{g}_i)$ . Index notation always uses the *Einstein summation convention*, which neglects the summation sign over repeating indices. Therefore, the action of a covector  $\boldsymbol{\omega} = \omega_i \mathbf{g}^i$  on a vector  $\boldsymbol{\eta} = \eta^i \mathbf{g}_i$  is

$$\boldsymbol{\omega}(\boldsymbol{\eta}) = \omega_i \eta^i. \quad (2.25)$$

This can be graphically interpreted as seen in Fig. 2.9. A covector can be represented as the collection of level sets, i.e. as parallel planes. The longer the covector is, the closer these planes are to each other. A vector can be graphically represented as an arrow. Thus, the action of a covector onto a vector is the measurement of how often the vector *pierces* through the level sets of the covector. Since the vector  $\boldsymbol{\eta}$  in Fig. 2.9 pierces through the

<sup>3</sup>Named after Leopold Kronecker, who used it in Kronecker, Leopold [Kro95, Ch. Über Systeme von Functionen mehrer Variablen, p. 216].

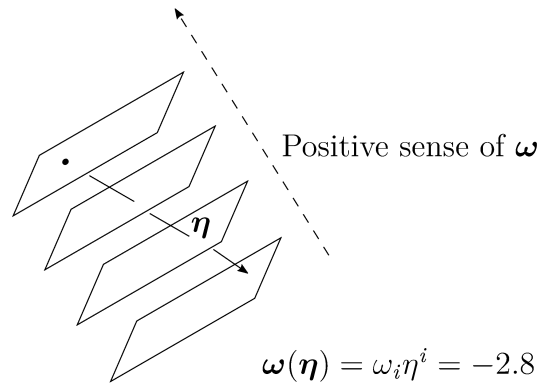


**Figure 2.9:** The action of a covector onto a vector. Inspired by [Mis73, Box 10.3].

planes of the covector  $\omega$  2.8 times and the positive sense of  $\omega$  is in the other direction, the action of the covector onto the vector is  $w_i \eta^i = -2.8$ .

**Cotangent Bundle** A *cotangent bundle* can be defined analogously to Eq. (2.19) as

$$T^*\mathcal{M} = \bigsqcup_{\mathbf{x} \in \mathcal{M}} T_{\mathbf{x}}^*\mathcal{M} = \{(\mathbf{x}, \boldsymbol{\xi}) : \mathbf{x} \in \mathcal{M} \wedge \boldsymbol{\xi} \in T_{\mathbf{x}}^*\mathcal{M}\}. \quad (2.26)$$

Again, analogous to the case of the tangent bundle, a *covector field* is a section of the cotangent bundle  $T^*\mathcal{M}$ . Consequently, we denote a covector field as  $\omega = \omega_i \mathbf{g}^i$  and the corresponding covector at  $\mathbf{x}$  as  $\omega_{\mathbf{x}} = (\omega_i \mathbf{g}^i) \Big|_{\mathbf{x}}$ . Furthermore, covector fields are often denoted as *one-forms*.

**EXAMPLE 6** (Covectors in Euclidean space). Consider a Euclidean space  $\mathbb{R}^n$  with a basis  $(\mathbf{e}_1, \dots, \mathbf{e}_n)$ . The dual basis is denoted by  $(\mathbf{e}^1, \dots, \mathbf{e}^n)$ . These basis covectors are defined by

$$\mathbf{e}^j(\mathbf{v}) = \mathbf{e}^j(v^1, \dots, v^n) = v^j. \quad (2.27)$$

Thus, the action of the base covector  $\mathbf{e}^j$  onto vectors in Euclidean space is the extraction of the  $j$ -th component of the vector.

### 2.4.5 Tangent vectors as Derivations

Tangent vectors can be identified as *derivations*. As motivation consider the directional derivative of a function  $f : \mathcal{M} \rightarrow \mathbb{R}$ , where  $\mathcal{M}$  can be considered to be embedded in  $\mathbb{R}^m$

with the basis  $\mathbf{e}_i$  and coordinates  $x^i$ ,

$$D_{\mathbf{v}}f = v^a \frac{\partial f}{\partial x^a} = v^a \frac{\partial}{\partial x^a} f. \quad (2.28)$$

Therefore, it is common to write  $\mathbf{v}f$  as shorthand for  $D_{\mathbf{v}}f$  by identifying  $\mathbf{v} \equiv v^a \frac{\partial}{\partial x^a}$ . This notation is not often used in the work at hand but in some appropriate places in the context of base vectors. Considering the derivative in the direction of a base vector, this yields

$$D_{\mathbf{e}_i}f = \frac{\partial f}{\partial x^i} = \frac{\partial}{\partial x^i} f, \quad (2.29)$$

which leads to

$$\mathbf{e}_i \equiv \frac{\partial}{\partial x^i}, \quad (2.30)$$

where the partial symbol is bold to indicate the vector nature of the object. The same is done for the dual basis as

$$\mathbf{e}^i \equiv \mathbf{d}x^i. \quad (2.31)$$

Therefore, by definition of the dual basis, we also have

$$\mathbf{e}^i \left( \frac{\partial}{\partial x^j} \right) = \delta^i_j. \quad (2.32)$$

For a more elaborate reasoning, see Misner et al. [Mis73], Marsden and Hughes [MH94], and Lee [Lee03].

## 2.5 Tensors

Tensors generalize the notion of vectors and covectors. According to Reich [Rei13], the term *tensor* can be traced back to the works of Voigt [Voi98]. Tensors can be defined as follows. Covectors are linear functionals that can be generalized to multilinear functionals. Consider the finite-dimensional vector spaces  $V_1, \dots, V_n$  and  $W$ . A map  $\mathbf{T} : V_1 \times \dots \times V_n \rightarrow W$  is said to be multilinear, if it is linear for each function separately. In particular, this requirement can be stated as

$$\mathbf{T}(\mathbf{v}_1, \dots, a\mathbf{v}_i + b\tilde{\mathbf{v}}_i, \dots, \mathbf{v}_n) = a\mathbf{T}(\mathbf{v}_1, \dots, \mathbf{v}_i, \dots, \mathbf{v}_n) + b\mathbf{T}(\mathbf{v}_1, \dots, \tilde{\mathbf{v}}_i, \dots, \mathbf{v}_n). \quad (2.33)$$

Then, a covariant  $k$ -tensor is a multilinear map

$$\mathbf{T} : \underbrace{V \times \dots \times V}_{k \text{ times}} \rightarrow \mathbb{R}, \quad (2.34)$$

and a contravariant  $k$ -tensor is defined as

$$\mathbf{T} : \underbrace{V^* \times \dots \times V^*}_{k \text{ times}} \rightarrow \mathbb{R}. \quad (2.35)$$

For a mixed tensor of type  $(k, l)$  it holds

$$\mathbf{T} : \underbrace{V^* \times \dots \times V^*}_{k \text{ times}} \times \underbrace{V \times \dots \times V}_{l \text{ times}} \rightarrow \mathbb{R}. \quad (2.36)$$

In the following, the order of the covariant and contravariant slots of a mixed tensor may differ. However, it is commonly denoted as being of type  $(k, l)$ . The *rank* of a tensor refers to the number of slots, where covariant or contravariant vectors can be inserted, effectively determining the number of arguments it accepts. Therefore, a tensor of type  $(k, l)$  has rank  $k + l$ .

The space of tensors on  $V$ , is denoted by

$$\begin{aligned} T^k(V^*) &= \{\text{covariant } k\text{-tensors on } V\}, \\ T^k(V) &= \{\text{contravariant } k\text{-tensors on } V\}, \\ T^{(k,l)}(V) &= \{\text{mixed } (k,l)\text{-tensors on } V\}. \end{aligned} \quad (2.37)$$

Consider again a basis  $\mathbf{g}_i, \dots, \mathbf{g}_n$  for  $V$  and the dual basis  $\mathbf{g}^i, \dots, \mathbf{g}^n$  for  $V^*$ , the basis for the space  $T^{(k,l)}(V)$  is given by

$$\mathbf{g}_{i_1} \otimes \dots \otimes \mathbf{g}_{i_k} \otimes \mathbf{g}^{j_1} \otimes \dots \otimes \mathbf{g}^{j_l}, \quad (2.38)$$



where  $(\otimes)$  denotes the *tensor product*, *outer product* or *dyadic product*. For two tensors  $\mathbf{A} = A_i^j \mathbf{g}^i \otimes \mathbf{g}_j$  and  $\mathbf{B} = B_{kl} \mathbf{g}^k \otimes \mathbf{g}^l$ , the tensor product is defined as

$$\mathbf{C} = \mathbf{A} \otimes \mathbf{B} = A_i^j B_{kl} \mathbf{g}^i \otimes \mathbf{g}_j \otimes \mathbf{g}^k \otimes \mathbf{g}^l = C_{ijkl} \mathbf{g}^i \otimes \mathbf{g}_j \otimes \mathbf{g}^k \otimes \mathbf{g}^l, \quad (2.39)$$

which yields a fourth-order  $(1, 3)$ -tensor. Then, a multiplication of this  $(1, 1)$ -tensor and a  $(0, 2)$ -tensor can be defined by the *contraction* of indices as follows

$$\mathbf{C} = \text{contract}(\mathbf{A} \otimes \mathbf{B}) = \mathbf{A} \cdot \mathbf{B} = A_i^j B_{kl} \mathbf{g}_j \cdot \mathbf{g}^k \mathbf{g}^i \otimes \mathbf{g}^l \quad (2.40)$$

$$= A_i^j B_{kl} \delta_j^k \mathbf{g}^i \otimes \mathbf{g}^l = A_i^j B_{jl} \mathbf{g}^i \otimes \mathbf{g}^l = C_{il} \mathbf{g}^i \otimes \mathbf{g}^l, \quad (2.41)$$

which yields a new  $(2, 0)$ -tensor. The contraction of purely covariant or contravariant indices is not possible without the definition of a Riemannian metric, which will be defined in Section 2.7.1. First, further operations on tensors that do not need the definition of a metric are defined.

### Push-Forward and Pull-Back

Due to their multilinear nature, tensors can be transformed so that they accept arguments from a different vector space. These actions are denoted by push-forward and pull-back. As a means to do this, functions between manifolds are revisited, which were stated in Section 2.2 on page 15. First, we already witnessed several versions of pull-back of functions. For example, consider the functions  $\mathbf{f} : \mathcal{M} \rightarrow \mathcal{N}$  and  $g : \mathcal{N} \rightarrow \mathbb{R}$ . Then, the *pull-back* of  $g$  under  $\mathbf{f}$  is the map  $\mathbf{f}^*(g) : \mathcal{M} \rightarrow \mathbb{R}$  simply defined by

$$\mathbf{f}^*(g) = g \circ \mathbf{f}. \quad (2.42)$$

Despite this being trivial it enables the following definition for vectors.

**Definition 12** (Push-forward). Let  $\mathcal{M}$  and  $\mathcal{N}$  be smooth manifolds and  $\mathbf{f} : \mathcal{M} \rightarrow \mathcal{N}$  a smooth map. Additionally, let  $\gamma : \mathbb{R} \rightarrow \mathcal{M}$  be a function from a  $C^1$ -function space  $\mathcal{D}(\mathcal{M})$  and  $\dot{\gamma}'(0)$  is tangent vector at  $\mathbf{x} = \mathbf{0}$  as defined in Definition 10 on page 21. Then, the action

$$\mathbf{f}_* : \begin{cases} T_{\mathbf{x}}\mathcal{M} \rightarrow T_{\mathbf{f}(\mathbf{x})}\mathcal{N}, \\ \dot{\gamma}(0) \mapsto \mathbf{f}_*(\dot{\gamma}(0)) = (\mathbf{f} \circ \gamma)'(0) = \overline{\dot{\gamma}^*}(\mathbf{f})(0), \end{cases} \quad (2.43)$$

is called the *push-forward* of  $\dot{\gamma}(0)$  to  $T_{\mathbf{f}(\mathbf{x})}\mathcal{N}$ .

Let us shortly interpret this in coordinates by introducing two charts  $\phi$  and  $\psi$  around  $\mathbf{x}$  and  $\mathbf{f}(\mathbf{x})$ , respectively. Then, we get, similar to Eq. (2.4) on page 16, a function  $\hat{\mathbf{f}} : \mathbb{R}^m \rightarrow \mathbb{R}^n$ , defined by  $\psi \circ \hat{\mathbf{f}} \circ \phi$ . Thus, we can — similar to Eq. (2.4) on page 16

— use partial derivatives. Consider  $\{\mathbf{E}_i\}$  as basis for  $\mathbb{R}^m$  with the coordinates  $X^i$  and the function  $\hat{\gamma} : \mathbb{R} \rightarrow \mathbb{R}^m$  as coordinate representative of  $\gamma : \mathbb{R} \rightarrow \mathcal{M}$ . Again we have  $\gamma(0) = \mathbf{x}$ . The coordinate representative of  $\mathbf{x}$  is denoted by  $\hat{\mathbf{x}} = \phi(\mathbf{x})$ . Furthermore, denote  $\{\mathbf{e}_j\}$  as basis for  $\mathbb{R}^n$  with the coordinates  $x^j$ . Then, the push-forward of the vector  $\hat{\gamma}'(0) = \frac{\partial \hat{\gamma}^i}{\partial t} \Big|_{t=0} \mathbf{E}_i = \mathbf{v} = v^i \mathbf{E}_i$  reads

$$\hat{\mathbf{f}}_*(\mathbf{v}) = \frac{\partial \hat{\mathbf{f}}(\hat{\gamma}(t))}{\partial t} \Big|_{t=0} = \frac{\partial \hat{f}^i(\hat{\gamma}(t))}{\partial t} \Big|_{t=0} \mathbf{e}_i = \frac{\partial \hat{f}^i}{\partial X^j} \Big|_{\hat{\mathbf{x}}} \frac{\partial \hat{\gamma}^j}{\partial t} \Big|_{t=0} \mathbf{e}_i = \frac{\partial \hat{f}^i}{\partial X^j} \Big|_{\hat{\mathbf{x}}} v^j \mathbf{e}_i. \quad (2.44)$$

Therefore, if we write  $\mathbf{w} = \hat{\mathbf{f}}_*(\mathbf{v}) = w^i \mathbf{e}_i$  and  $\hat{\mathbf{F}} = \frac{\partial \hat{f}^i}{\partial X^j} \Big|_{\hat{\mathbf{x}}} \mathbf{e}_i \otimes \mathbf{E}^j = \hat{F}^i_j \mathbf{e}_i \otimes \mathbf{E}^j$ , then the components of the pushed vector read

$$w^i = \hat{F}^i_j v^j. \quad (2.45)$$

Consequently, tangent vectors are pushed forward simply by the *Jacobian* of the function under which the pushing takes place. This Jacobian can be written using two charts and the corresponding bases as  $\hat{\mathbf{F}} = \hat{F}^i_j \mathbf{e}_i \otimes \mathbf{E}^j$ . Often, such tensors are called *two-point tensors*, since they are defined w.r.t. two different coordinate systems. In tensor notation, Eq. (2.45) reads

$$\mathbf{w} = w^i \mathbf{e}_i = \hat{\mathbf{F}} \cdot \mathbf{v}, \quad (2.46)$$

or without coordinate representatives  $\boldsymbol{\zeta} = \mathbf{F} \cdot \boldsymbol{\eta}$ , which will be possible, if an embedding space is employed. Thus, if an embedding space exists, we can use the notion of tangent vectors as vectors in the embedding space as in Eq. (2.12). The explicit functional dependence of this inclusion mapping as defined in Eq. (2.6) is discarded to simplify the notation and now  $\mathbf{f} : \mathcal{M} \rightarrow \mathcal{N}$  should be read as  $\mathbf{f} : \mathbb{R}^M \rightarrow \mathbb{R}^N$ . Thus, the embedding space of  $\mathcal{M}$  is  $\mathbb{R}^M$ . Consider  $\{\hat{\mathbf{E}}_i\}$  as the Euclidean standard basis with coordinates  $Z^i$  in  $\mathbb{R}^M$ , and similar for  $\mathcal{N}$ , where the embedding space is  $\mathbb{R}^N$  with the Euclidean standard basis  $\{\hat{\mathbf{e}}_i\}$  and the coordinates  $z^i$ . Therefore, we can use chain rule and get

$$\begin{aligned} \hat{\mathbf{f}}_*(\mathbf{v}) &= \frac{\partial \hat{\mathbf{f}}(\hat{\gamma}(t))}{\partial t} \Big|_{t=0} = \frac{\partial (\boldsymbol{\psi}(\mathbf{f}(\phi^{-1}(\hat{\gamma}(t)))))}{\partial t} \Big|_{t=0} \\ &= \frac{\partial \psi^i}{\partial z^j} \frac{\partial f^j}{\partial Z^k} \frac{\partial (\phi^{-1})^k}{\partial X^l} \frac{\partial \hat{\gamma}^l}{\partial t} \Big|_{t=0} \mathbf{e}_i \\ &= \frac{\partial \psi^i}{\partial z^j} \frac{\partial f^j}{\partial Z^k} \frac{\partial (\phi^{-1})^k}{\partial X^l} \Big|_{\hat{\mathbf{x}}} v^l \mathbf{e}_i, \end{aligned} \quad (2.47)$$

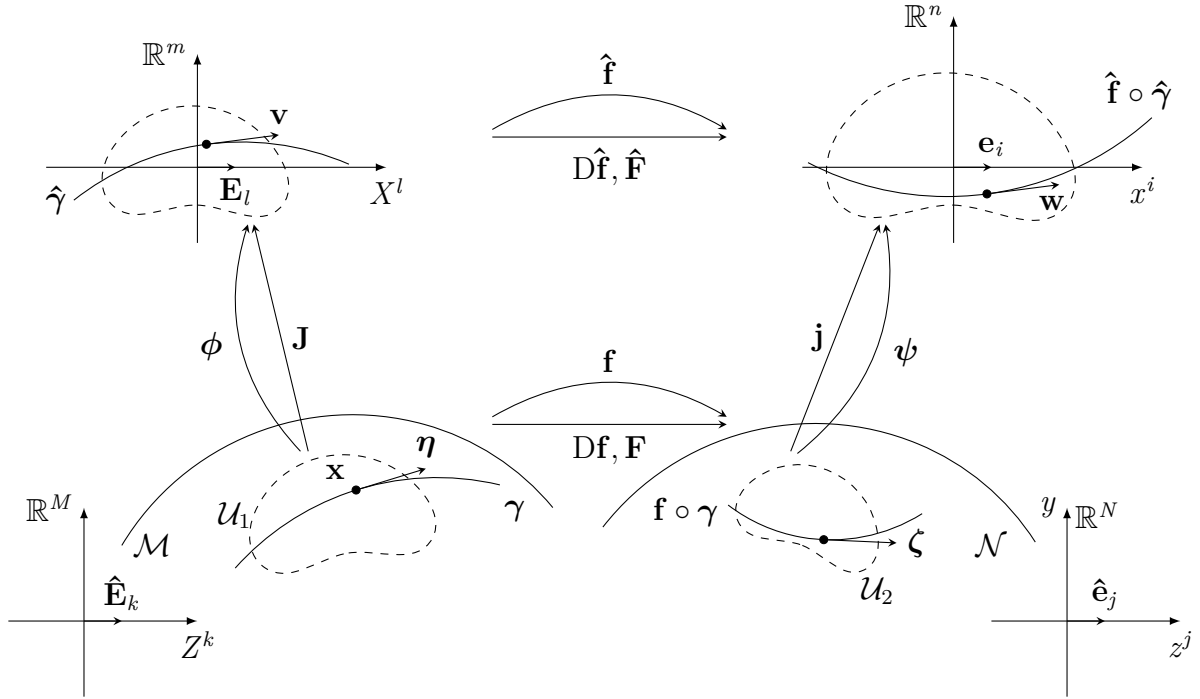


**Figure 2.10:** Push forward of a function mapping between manifolds.

where again the inclusion maps  $\iota$  and the extension of  $\mathbf{f} : \mathcal{M} \rightarrow \mathcal{N}$  to  $\mathbb{R}^M \rightarrow \mathbb{R}^N$  are neglected. These definitions are also visualized in Fig. 2.10. In this figure, the commutative nature of the discussed quantities is shown. In the lower left corner the curve  $\gamma$  with the tangent vector  $\boldsymbol{\eta}$  is shown, which is mapped to the curve  $\mathbf{f} \circ \gamma$  with the tangent vector  $\boldsymbol{\zeta}$  on the lower right corner. If we go through the charts, the path goes first up and  $\boldsymbol{\eta}$  becomes  $\mathbf{v} = \mathbf{J} \cdot \boldsymbol{\eta}$ , from there, using the differential  $D\hat{\mathbf{f}}$  it becomes  $\mathbf{w} = D\hat{\mathbf{f}} \cdot \mathbf{J} \cdot \boldsymbol{\eta}$  ending up in the top right corner and finally it becomes  $\boldsymbol{\zeta} = \mathbf{j}^{-1} \cdot D\hat{\mathbf{f}} \cdot \mathbf{J} \cdot \boldsymbol{\eta}$  and we are back in the lower right corner.

This, yields a bouquet of possible identifications, since Eq. (2.47) is a chain of several push-forwards from  $\mathbb{R}^m$  to  $T_{\mathbf{x}}\mathcal{M}$  to  $T_{f(\mathbf{x})}\mathcal{N}$  to  $\mathbb{R}^n$ . We can identify

$$\begin{aligned}
 \mathbf{J}^{-1} &= \left. \frac{\partial(\phi^{-1})^k}{\partial X^l} \right|_{\hat{\mathbf{x}}} \hat{\mathbf{E}}_k \otimes \mathbf{E}^l = (J^{-1})^k_l \hat{\mathbf{E}}_k \otimes \mathbf{E}^l, \\
 D\mathbf{f} &= \left. \frac{\partial f^j}{\partial Z^k} \right|_{\mathbf{x}} \hat{\mathbf{e}}_j \otimes \hat{\mathbf{E}}^k = (Df)^j_k \hat{\mathbf{e}}_j \otimes \hat{\mathbf{E}}^k, \\
 \mathbf{j} &= \left. \frac{\partial \psi^i}{\partial z^j} \right|_{f(\mathbf{x})} \mathbf{e}_i \otimes \hat{\mathbf{e}}^j = j^i_j \mathbf{e}_i \otimes \hat{\mathbf{e}}^j.
 \end{aligned} \tag{2.48}$$

This allows the creation of several intermediate pushed vectors and vector components as follows

$$\begin{aligned}
 \boldsymbol{\eta} &= \eta^k \hat{\mathbf{E}}_k = \mathbf{J}^{-1} \cdot \mathbf{v}, & \eta^k &= (J^{-1})^k_l v^l, \\
 \boldsymbol{\zeta} &= \zeta^j \hat{\mathbf{e}}_j = \mathbf{Df} \cdot \mathbf{J}^{-1} \cdot \mathbf{v}, & \zeta^j &= (\mathbf{Df})^j_k (J^{-1})^k_l v^l, \\
 \mathbf{w} &= w^i \mathbf{e}_i = \mathbf{j} \cdot \mathbf{Df} \cdot \mathbf{J}^{-1} \cdot \mathbf{v}, & w^i &= j^i_j (\mathbf{Df})^j_k (J^{-1})^k_l v^l.
 \end{aligned} \tag{2.49}$$

This is also connected to the coordinate base vectors in Eq. (2.16). The charts  $\boldsymbol{\psi}$  and  $\boldsymbol{\phi}$  or their inverses define (local) parameterizations, which define coordinate base vectors. Thus, we have

$$\begin{aligned}
 \mathbf{G}_i &= G^k_i \hat{\mathbf{E}}_k, & G^k_i &= (J^{-1})^k_l \delta^l_i, \\
 \mathbf{g}_i &= g^k_i \hat{\mathbf{e}}_k, & g^j_i &= (\mathbf{Df})^j_k G^k_i.
 \end{aligned} \tag{2.50}$$

The quantity  $\mathbf{G}_i$  is the tangent vector at  $\mathbf{x}$  represented as an element of the embedding space. It can be interpreted as the pushed-forward vector of  $\mathbf{E}_i$ . Sloppily,  $\mathbf{G}_i$  can furthermore be simply interpreted as columns of  $\mathbf{J}^{-1}$ . For example, the vector  $\boldsymbol{\eta}$  can now also be defined with components in the basis  $\mathbf{G}_i$ . Thus, this yields

$$\boldsymbol{\eta} = \eta^j \hat{\mathbf{E}}_j = \hat{\eta}^\alpha \mathbf{G}_\alpha, \tag{2.51}$$

where Greek superscripts and subscripts are used to denote the indices of the components in the curvilinear coordinate system.

The push-forward also induces its dual concept as follows.

**Definition 13** (Pull-back). Let  $\mathcal{M}$  and  $\mathcal{N}$  be smooth manifolds and  $\mathbf{f} : \mathcal{M} \rightarrow \mathcal{N}$  a smooth map. Additionally, let  $\boldsymbol{\omega} \in T_{\mathbf{f}(\mathbf{x})}^* \mathcal{N}$  be a tangent covector on  $\mathcal{N}$  at  $\mathbf{f}(\mathbf{x})$  and  $\boldsymbol{\eta} \in T_{\mathbf{x}} \mathcal{M}$  be a tangent vector on  $\mathcal{M}$  at  $\mathbf{x}$ . Then, the action

$$\mathbf{f}^* : T_{\mathbf{f}(\mathbf{x})}^* \mathcal{N} \rightarrow T_{\mathbf{x}}^* \mathcal{M}, \tag{2.52}$$

which can be characterized by

$$\mathbf{f}^*(\boldsymbol{\omega})(\boldsymbol{\eta}) = \boldsymbol{\omega}(\mathbf{f}_*(\boldsymbol{\eta})), \tag{2.53}$$

is called the *pull-back* of  $\boldsymbol{\omega}$  to  $T_{\mathbf{x}}^* \mathcal{M}$ .

Let us also interpret this in coordinates by introducing two charts  $\boldsymbol{\phi}$  and  $\boldsymbol{\psi}$  around  $\mathbf{x}$  and  $\mathbf{f}(\mathbf{x})$  and the coordinate representative  $\hat{\mathbf{f}} : \mathbb{R}^m \rightarrow \mathbb{R}^n$ , defined by  $\boldsymbol{\psi} \circ \hat{\mathbf{f}} \circ \boldsymbol{\phi}$ . Consider  $\{\mathbf{E}_i\}$  as basis for  $\mathbb{R}^m$  with the coordinates  $X^i$  and the coordinate representative of  $\mathbf{x}$  given by  $\hat{\mathbf{x}} = \boldsymbol{\phi}(\mathbf{x})$ . Furthermore,  $\{\mathbf{e}_j\}$  denotes the basis of  $\mathbb{R}^n$  with the coordinates  $x^j$ .

Consider the coordinate representative of  $\boldsymbol{\omega}$  by  $\hat{\boldsymbol{\omega}} = \hat{\omega}_j \mathbf{e}^j$ . Furthermore, let  $\hat{\boldsymbol{\chi}} = \hat{\omega}_j \mathbf{E}^j$  be the coordinate representative of the pull-back of  $\hat{\boldsymbol{\omega}}$ . Finally, again let the coordinate representative of  $\boldsymbol{\eta}$  be again  $\mathbf{v} = v^i \mathbf{e}_i$ . Then, using Eq. (2.45), the pull-back Eq. (2.53) of  $\hat{\boldsymbol{\omega}} = \hat{\omega}_j \mathbf{e}_j$  in the basis  $\{\mathbf{E}_j\}$  reads

$$\hat{\chi}_i v^j = \hat{\omega}_i \hat{F}^i_j v^j. \quad (2.54)$$

Comparing coefficients yields the pull-back of the coefficients

$$\hat{\chi}_i = \hat{\omega}_i \hat{F}^i_j, \quad (2.55)$$

which would be written in tensor notation as  $\hat{\boldsymbol{\chi}} = \hat{\mathbf{F}}^T \cdot \hat{\boldsymbol{\omega}}$  or without coordinate representatives as  $\boldsymbol{\chi} = \mathbf{F}^T \cdot \boldsymbol{\omega}$ . Thus, the transpose of the Jacobian of the mapping can be used to pull back covectors. Again, if we assume an embedding space exists, as before for vectors, similar results of intermediate pulled covectors would apply.

## 2.6 Retractions

The following tool can be motivated by the desire to extend line search from a vector space to non-linear manifolds. Consider the function  $f : \mathbb{R}^n \rightarrow \mathbb{R}$ , which is supposed to be minimized. In such a vector space, line search can be stated as follows

$$\mathbf{x}_{k+1} = \mathbf{x}_k + \alpha \mathbf{v}, \quad \text{with } \alpha = \arg \min_t f(\mathbf{x}_k + t\mathbf{v}) \quad (2.56)$$

where  $\mathbf{x}_{k+1}, \mathbf{x}_k, \mathbf{v} \in \mathbb{R}^n$  and  $\alpha \in \mathbb{R}_+$ . Here,  $\mathbf{v}$  is the search direction, which is the negative gradient in the gradient descent method. This search direction can then be used to parameterize the line of search as  $\boldsymbol{\gamma}(t) = \mathbf{x}_k + t\mathbf{v}$  as shown on the left in Fig. 2.11. The step size  $\alpha \in \mathbb{R}_+$  is calculated by solving  $\alpha = \arg \min_t f(\boldsymbol{\gamma}(t))$  approximately. The *straight* line  $\boldsymbol{\gamma}(t)$  is then the search space for the minimization problem at the current position  $\mathbf{x}_k$  in the direction  $\mathbf{v}$  as depicted in Fig. 2.11. This procedure is then repeated until a convergence criterion is met.

Consider now the manifold-valued function  $f : \mathcal{M} \rightarrow \mathbb{R}$  and the manifold as shown on the right-hand side in Fig. 2.11. If the line search is generalized for manifolds, the only reasonable choice of a search direction  $\mathbf{v}$  is a tangent vector  $\boldsymbol{\eta} \in T_{\mathbf{x}_k} \mathcal{M}$  at the current position  $\mathbf{x}_k$ . This does not help, since now a search direction is chosen, but the position  $\mathbf{x}_k \in \mathcal{M}$  and the search direction  $\boldsymbol{\eta}$ , do not stem from the same space. In a vector space, this identification is trivial since  $T_{\mathbf{x}_k} \mathbb{R}^n$  is isomorphic to  $\mathbb{R}^n$  itself and the addition  $\mathbf{x} + \alpha \mathbf{v}$  is well-defined.

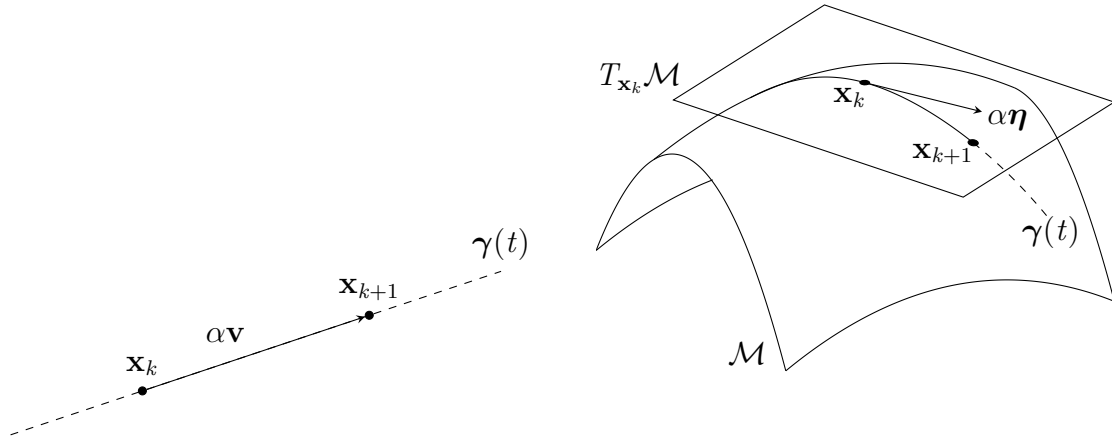


**Figure 2.11:** Line search in a vector space and on a manifold

This problem can be resolved by so-called *retractions*, which generalize the notion of straight lines to manifolds.<sup>4</sup> A retraction describes motion in the direction of a tangent vector while remaining on the manifold. Therefore, a retraction  $\mathbf{R}_x$  is a mapping that takes a tangent vector of  $T_x\mathcal{M}$  and returns a point on the manifold. In Fig. 2.11 the result of the retraction would then be the new point  $\mathbf{x}_{k+1} = \mathbf{R}_x(\alpha\boldsymbol{\eta})$ .

**Definition 14** (Retraction). A *retraction* on a manifold  $\mathcal{M}$  is a smooth mapping  $\mathbf{R}$  from the tangent bundle  $T\mathcal{M}$  to  $\mathcal{M}$ , with the following properties. Let  $\mathbf{x} \in \mathcal{M}$  and let  $\mathbf{R}_x$  be the restriction of  $\mathbf{R}$  to  $T_x\mathcal{M}$ , then

- $\mathbf{R}(\mathbf{0}) = \mathbf{x}$ , where  $\mathbf{0}$  denotes the zero element of  $T_x\mathcal{M}$  and
- the curve  $\boldsymbol{\gamma}_\eta : t \mapsto \mathbf{R}_x(t\boldsymbol{\eta})$  satisfies  $\dot{\boldsymbol{\gamma}}_\eta(0) = \boldsymbol{\eta}$ .

A canonical example of a retraction is the Riemannian exponential mapping, which will be defined in Section 3.4 on page 60.

For embedded submanifolds, as defined in Section 2.4.2 on page 21, there is a natural retraction described as follows.

1. Move in the linear embedding space to  $\mathbf{x} + \boldsymbol{\eta}$ .
2. Project back onto the manifold by finding the closest point to  $\mathbf{x} + \boldsymbol{\eta}$  on the manifold.

The most obvious example is the unit sphere  $\mathcal{S}^{n-1} \subset \mathbb{R}^n$ , for which the closest point projection is given by the *radial return normalization*

$$\mathbf{R}_x(\boldsymbol{\eta}) = \frac{\mathbf{x} + \boldsymbol{\eta}}{\|\mathbf{x} + \boldsymbol{\eta}\|}. \tag{2.57}$$

---

<sup>4</sup>This is usually attributed to geodesic curves, but these were not introduced yet, therefore this property is attributed to the more general concept of retractions.

## 2.7 Riemannian Manifolds

For a short historical overview of Riemannian geometry, the reader is referred to do Carmo [dC92, Ch. 1.1]. For the interested reader of the biographies of Gauss and Riemann, the reader is referred to Bell [Bel37].

A Riemannian manifold is a manifold endowed with additional geometric structure. The notions of tangent vectors and directional derivatives, which do not depend on a metric, were defined in Section 2.4. For our goal to do structural mechanics, it is important to measure angles, length, and deviation of angles or length. This is the job of Riemannian metrics.

### 2.7.1 Riemannian Metric

Every tangent space  $T_{\mathbf{x}}\mathcal{M}$  of a manifold  $\mathcal{M}$  can be equipped with an *inner product*  $\langle \cdot, \cdot \rangle_{\mathbf{x}}$ . This inner product is a symmetric, bilinear positive-definite form and therefore induces the norm  $\|\boldsymbol{\eta}_{\mathbf{x}}\|_{\mathbf{x}} = \sqrt{\langle \boldsymbol{\eta}_{\mathbf{x}}, \boldsymbol{\eta}_{\mathbf{x}} \rangle_{\mathbf{x}}}$ .

**Definition 15.** A Riemannian metric  $g$  of a smooth manifold  $\mathcal{M}$  assigns to each point  $\mathbf{x}$  an inner product  $\langle \cdot, \cdot \rangle_{\mathbf{x}}$  on the corresponding tangent space  $T_{\mathbf{x}}\mathcal{M}$ . This yields a smooth map

$$g_{\mathbf{x}} : \begin{cases} T_{\mathbf{x}}\mathcal{M} \times T_{\mathbf{x}}\mathcal{M} \rightarrow \mathbb{R}, \\ (\boldsymbol{\eta}, \boldsymbol{\zeta}) \mapsto g_{\mathbf{x}}(\boldsymbol{\eta}, \boldsymbol{\zeta}) = g(\boldsymbol{\eta}, \boldsymbol{\zeta}) = \langle \boldsymbol{\eta}, \boldsymbol{\zeta} \rangle. \end{cases} \quad (2.58)$$

A *Riemannian manifold* is thus a pair  $(\mathcal{M}, g)$ , where  $\mathcal{M}$  is a manifold and  $g$  is the Riemannian metric on  $\mathcal{M}$ .

If coordinate vector fields  $\mathbf{g}_i$  are introduced, the *components* of the Riemannian metric  $g_{ij}$  can be calculated as

$$g_{ij} = g(\mathbf{g}_i, \mathbf{g}_j) = \langle \mathbf{g}_i, \mathbf{g}_j \rangle_{\mathbf{x}}. \quad (2.59)$$

Additionally, this induces the definition of the metric tensor, which defines a (0,2)-tensor field. It is given by

$$\mathbf{g} = g_{ij} \mathbf{g}_i \otimes \mathbf{g}_j. \quad (2.60)$$

With these definitions, the inner product of the vectors  $\boldsymbol{\eta} = \eta^i \mathbf{g}_i$  and  $\boldsymbol{\zeta} = \zeta^j \mathbf{g}_j$  can be stated as

$$g(\boldsymbol{\eta}, \boldsymbol{\zeta}) = \langle \boldsymbol{\eta}, \boldsymbol{\zeta} \rangle_{\mathbf{x}} = \boldsymbol{\eta}^T \tilde{\mathbf{g}} \boldsymbol{\zeta} = \boldsymbol{\eta} \cdot \mathbf{g} \cdot \boldsymbol{\zeta} = \eta^i \zeta^j g_{ij}, \quad (2.61)$$

where the second term emphasizes the fact that the metric tensor stems from an inner product; the third, fourth, and fifth terms represent the same results but in *matrix*, *direct*<sup>5</sup> or *index*<sup>6</sup> notation, respectively. The matrix  $\tilde{\mathbf{g}}$  simply contains the coefficients  $g_{ij}$ . With an abuse of notation, the tilde ornaments are dropped and also refer to this matrix  $\tilde{\mathbf{g}}$  by  $\mathbf{g}$ .

EXAMPLE 7 (Euclidean space). The space  $\mathbb{R}^m$  has as basis  $\mathbf{e}_i = (0, \dots, 1, \dots, 0)$ . The canonical metric is therefore,  $\langle \mathbf{e}_i, \mathbf{e}_j \rangle = \delta_{ij}$ . Here, the inner product  $\langle \mathbf{e}_i, \mathbf{e}_j \rangle_{\mathbf{x}}$  is the simple *dot product*  $\mathbf{e}_i \cdot \mathbf{e}_j$ .

## 2.7.2 Musical Isomorphisms

The definition of covectors in Section 2.4.4 on page 25 does not need the definition of a Riemannian metric. However, if a Riemannian metric is given, covectors can be transformed into vectors and vice versa. Consider a map  $\mathbf{h} : T_{\mathbf{x}}\mathcal{M} \rightarrow T_{\mathbf{x}}^*\mathcal{M}$  with the vectors at  $\mathbf{x}$ ,  $\boldsymbol{\eta} = \eta^i \mathbf{g}_i$  and  $\boldsymbol{\zeta} = \zeta^j \mathbf{g}_j$  as

$$\mathbf{h}(\boldsymbol{\eta})(\boldsymbol{\zeta}) = \langle \boldsymbol{\eta}, \boldsymbol{\zeta} \rangle, \quad (2.62)$$

and in coordinates

$$\mathbf{h}(\boldsymbol{\eta})(\boldsymbol{\zeta}) = g_{ij} \eta^j \zeta^i. \quad (2.63)$$

This implies that the covector  $\mathbf{h}(\boldsymbol{\eta})$  can be written as

$$\mathbf{h}(\boldsymbol{\eta}) = g_{ij} \eta^j \mathbf{g}^i. \quad (2.64)$$

As a shorthand, the following definition is used

$$\eta_i = g_{ij} \eta^j. \quad (2.65)$$

This procedure is usually named *lowering the indices*, since  $\mathbf{h}(\boldsymbol{\eta})$  is obtained by lowering the index of  $\boldsymbol{\eta}$ .

---

<sup>5</sup>Alternatively called *vector* notation

<sup>6</sup>Alternatively called *subscript* notation and *suffix* notation



$$\begin{array}{ccc}
 T_{\mathbf{x}}^* \mathcal{M} & \xleftarrow{\mathbf{f}^*} & T_{\mathbf{f}(\mathbf{x})}^* \mathcal{N} \\
 \mathbf{G} \uparrow & & \uparrow \mathbf{g} \\
 T_{\mathbf{x}} \mathcal{M} & \xrightarrow{\mathbf{f}_*} & T_{\mathbf{f}(\mathbf{x})} \mathcal{N}
 \end{array}$$

**Figure 2.12:** Commutative diagram between musical isomorphisms and pull-back and push-forward operations

Analogously, we can define, using the inverse mapping  $\mathbf{h}^{-1} : T_{\mathbf{x}}^* \mathcal{M} \rightarrow T \mathcal{M}$ , which can be represented by the inverse matrix of  $\{g_{ij}\}$ . These matrix coefficients are denoted by  $g^{ij}$  such that

$$g_{ij} g^{jk} = \delta_i^k. \quad (2.66)$$

Therefore,  $\mathbf{h}^{-1}$  or  $g^{ij}$  can be used for *raising the indices* of a covector  $\boldsymbol{\omega} = \omega_i \mathbf{g}^i$  such that

$$\omega^i = g^{ij} \omega_j. \quad (2.67)$$

This also defines a relation between the covariant and contravariant base vectors, namely

$$\mathbf{g}^i = g^{ij} \mathbf{g}_j \quad \text{and} \quad \mathbf{g}_i = g_{ij} \mathbf{g}^j. \quad (2.68)$$

Consequently,  $\mathbf{h}$  and its inverse define isomorphisms between  $T_{\mathbf{x}}^* \mathcal{M}$  and  $T_{\mathbf{x}} \mathcal{M}$ . Formally, these isomorphisms are defined as

$$\mathbf{g} : \begin{cases} T_{\mathbf{x}} \mathcal{M} \rightarrow T_{\mathbf{x}}^* \mathcal{M}, \\ \boldsymbol{\eta} \mapsto \boldsymbol{\eta}^\flat = \mathbf{g} \cdot \boldsymbol{\eta}, \text{ and} \end{cases} \quad \mathbf{g}^{-1} : \begin{cases} T_{\mathbf{x}}^* \mathcal{M} \rightarrow T_{\mathbf{x}} \mathcal{M}, \\ \boldsymbol{\eta} \mapsto \boldsymbol{\eta}^\sharp = \mathbf{g}^{-1} \cdot \boldsymbol{\eta}. \end{cases} \quad (2.69)$$

A vector representation of a covector  $\boldsymbol{\omega}$  is often denoted by  $\boldsymbol{\omega}^\sharp$ , and similarly, the covector representation of a vector  $\boldsymbol{\eta}$  is often denoted by  $\boldsymbol{\eta}^\flat$ . These musical symbols are motivated by the fact that in musical notation, flat and sharp mean lowering and raising the pitch. Therefore, these isomorphisms are called *musical isomorphisms*. The musical isomorphisms close the commuting diagram in Fig. 2.12 along with the push-forward and pull-back operations. These isomorphisms can also be used to define the *transpose* of a tensor. Consider a tensor  $\mathbf{C} = C^i_j \mathbf{g}_i \otimes \mathbf{g}^j$ . The components of the *metric transpose*  $\mathbf{C}^T$  are defined as

$$(\mathbf{C}^T)^l_k = g_{ki} C^i_j g^{lj}, \quad (2.70)$$

see also Marsden and Hughes [MH94, 3.4 Proposition (ii)] or Federico [Fed15]. It can be derived via the statement involving the metric  $\langle \mathbf{w}, \mathbf{C} \cdot \mathbf{v} \rangle_{\mathbf{x}} = \langle \mathbf{C}^T \cdot \mathbf{w}, \mathbf{v} \rangle_{\mathbf{x}}$ . This is in general not identical to the *algebraic transpose* or dual to  $C_j^i$ , which can be stated as  $(\mathbf{C}^t)_j^i$ .<sup>7</sup> The metric transpose and algebraic transpose are related via

$$(\mathbf{C}^T)^l_k = g_{ki} C_j^i g^{lj} = g_{ki} (\mathbf{C}^t)_j^i g^{lj}. \quad (2.71)$$

### 2.7.3 Riemannian Gradient

Let  $f : \mathcal{M} \rightarrow \mathbb{R}$  be a function defined on a manifold  $(\mathcal{M}, g)$ . The directional derivative of  $f$  in the direction of the tangent vector  $\boldsymbol{\eta}$  is defined as  $D_{\boldsymbol{\eta}} f(\mathbf{x})$  since an embedding space is assumed. The Riemannian gradient of  $f$  is defined as follows:

**Definition 16.** Let  $f : \mathcal{M} \rightarrow \mathbb{R}$  be a function defined on a manifold  $(\mathcal{M}, g)$ . The *Riemannian gradient* is the vector field defined by

$$D_{\boldsymbol{\eta}} f(\mathbf{x}) = g_{\mathbf{x}}(\boldsymbol{\eta}, \text{grad } f(\mathbf{x})) = \langle \boldsymbol{\eta}, \text{grad } f(\mathbf{x}) \rangle_{\mathbf{x}}. \quad (2.72)$$

Therefore, in contrast to the directional derivative, the Riemannian gradient directly depends on the definition of the chosen Riemannian metric.

Consider  $\mathcal{M}$  embedded into  $\mathbb{R}^M$  with basis vector  $\hat{\mathbf{E}}_i$  with the coordinates  $Z^i$ . Also, consider a parameterization  $\boldsymbol{\varphi} : \mathbb{R}^m \rightarrow \mathcal{U} \subset \mathcal{M}$  as given by Eq. (2.15) and the corresponding base vectors  $\mathbf{g}_j(\boldsymbol{\theta}) = \frac{\partial \boldsymbol{\varphi}^i(\boldsymbol{\theta})}{\partial \theta^j} \hat{\mathbf{E}}_i$  as introduced in Eq. (2.16). This parameterization defines the function  $\tilde{f} = f \circ \boldsymbol{\varphi} : \mathbb{R}^m \rightarrow \mathbb{R}$ . The directional derivative can then be stated as

$$D_{\tilde{\mathbf{x}}} \tilde{f}(\boldsymbol{\theta}) = \frac{\partial \tilde{f}}{\partial \theta^j} \mathbf{g}^j, \quad (2.73)$$

where  $\mathbf{g}^j$  can be written as in Eq. (2.68). Considering  $\boldsymbol{\eta} = v^i \mathbf{g}_i$ , Eq. (2.72) reads

$$\frac{\partial \tilde{f}}{\partial \theta^i} v^i = v^i g_{ij}(\boldsymbol{\theta}) (\widetilde{\text{grad } f}(\boldsymbol{\theta}))^j. \quad (2.74)$$

The notation  $\widetilde{\text{grad } f}$  denotes the components of  $\text{grad } f$  in the basis  $\mathbf{g}_i$  and  $\boldsymbol{\theta}$  contains the coordinates in this chart of the point  $\mathbf{x}$  as before. The coordinate representation of the

---

<sup>7</sup>This is also used in [Fed15], where  $(\cdot)^t$  and  $(\cdot)^T$  are swapped to the notation used here. The algebraic transpose has also been named the dual of  $\mathbf{C}$  in [MH94].

gradient then reads

$$\widetilde{(\text{grad } f(\boldsymbol{\theta}))}^i = g^{ij} \frac{\partial \tilde{f}}{\partial \theta^j}, \quad (2.75)$$

due to the arbitrariness of  $\eta^i$ . This also underlines the dependence on the Riemannian metric through the metric coefficients  $g^{ij}$ . Furthermore, the Riemannian gradient can be expressed in a coordinate-free way as  $\text{grad } f(\mathbf{x}) = (Df)^\sharp$  using musical isomorphisms from Section 2.7.2.

In Euclidean spaces, e.g.,  $\mathbb{R}^n$ , the Riemannian gradient boils down to

$$\text{grad } f(\mathbf{x}) = \begin{bmatrix} \frac{\partial f}{\partial x^1} \\ \vdots \\ \frac{\partial f}{\partial x^n} \end{bmatrix} \mathbf{E}^i. \quad (2.76)$$

#### 2.7.4 Riemannian Submanifolds

Riemannian submanifolds have several nice properties, that make the later optimization problem for the Reissner-Mindlin shell formulation convenient. This realization is also a main contribution of this thesis. This is elaborated on in Section 6.1.3 on page 153.

Let  $\mathcal{M}$  be an embedded submanifold of  $\overline{\mathcal{M}}$ . Since the tangent space  $T_{\mathbf{x}}\mathcal{M}$  can be seen as a subspace  $T_{\mathbf{x}}\overline{\mathcal{M}}$ , the Riemannian metric  $\bar{g}$  of  $\overline{\mathcal{M}}$  induces a metric  $g$  on  $\mathcal{M}$  as

$$g_{\mathbf{x}}(\boldsymbol{\eta}, \boldsymbol{\zeta}) = \bar{g}_{\mathbf{x}}(\boldsymbol{\eta}, \boldsymbol{\zeta}), \quad (2.77)$$

where  $\boldsymbol{\eta}$  and  $\boldsymbol{\zeta}$  are viewed as elements of  $T_{\mathbf{x}}\mathcal{M}$  or  $T_{\mathbf{x}}\overline{\mathcal{M}}$ . This metric turns  $\mathcal{M}$  into a Riemannian manifold. If the metric is chosen in such a way that it is compatible with the embedding space, then the manifold  $\mathcal{M}$  is called *Riemannian submanifold*. Additionally, such a metric is called an *induced metric*. Conversely, if  $\mathcal{M}$  is embedded into  $\overline{\mathcal{M}}$ , but we choose a different metric, it is *not* a Riemannian submanifold but merely a Riemannian manifold.

Additionally, the embedding admits the orthogonal complement to the tangent space. If  $\mathcal{M}$  is embedded into  $\mathbb{R}^m$ , the one-dimensional *normal space* is

$$N_{\mathbf{x}}\mathcal{M} = \{\mathbf{v} \in \mathbb{R}^m : \bar{g}_{\mathbf{x}}(\mathbf{v}, \boldsymbol{\eta}) = 0 \quad \forall \boldsymbol{\eta} \in T_{\mathbf{x}}\mathcal{M}\}. \quad (2.78)$$

Since the definition of the normal space needs the notion of orthogonality, a metric is needed. Therefore, the normal space can only be defined, if a Riemannian metric is chosen.

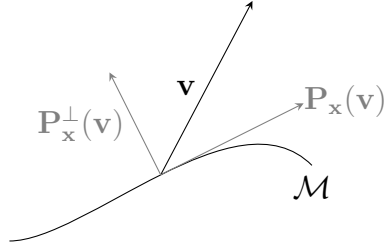


**Figure 2.13:** Decomposition of a vector into components tangent and normal to a manifold.

In contrast to this, the tangent space was defined by directional derivatives without the need for a metric. Furthermore, an embedding space needs to be available.

### Projection of Vector Fields

The definition of normal space and tangent space can be used to decompose elements of the embedding space. Consider a vector  $\mathbf{v} \in \mathbb{R}^m$ , that can be decomposed as

$$\mathbf{v} = \mathbf{P}_x(\mathbf{v}) + \mathbf{P}_x^\perp(\mathbf{v}), \quad (2.79)$$

where  $\mathbf{P}_x$  denotes the orthogonal projection onto  $T_x \mathcal{M}$  and  $\mathbf{P}_x^\perp$  the orthogonal projection onto  $N_x \mathcal{M}$  as depicted in Fig. 2.13. This decomposition gives rise to a convenient construction of the Riemannian gradient. Consider a function  $f : \mathcal{M} \rightarrow \mathbb{R}$  and its extension  $\bar{f} : \mathbb{R}^m \rightarrow \mathbb{R}$ . From Definition 16 and Eq. (2.14), the following holds for the Riemannian gradient of  $f$

$$g_x(\boldsymbol{\eta}, \text{grad } f(\mathbf{x})) = D_{\boldsymbol{\eta}} f(\mathbf{x}) = D_{\boldsymbol{\eta}} \bar{f}(\mathbf{x}) = \bar{g}_x(\boldsymbol{\eta}, \text{grad } \bar{f}(\mathbf{x})), \quad \boldsymbol{\eta} \in T_x \mathcal{M}. \quad (2.80)$$

The right-hand side can then be decomposed into the normal and tangent parts as follows

$$\text{grad } \bar{f}(\mathbf{x}) = \text{grad } \bar{f}(\mathbf{x})_{\parallel} + \text{grad } \bar{f}(\mathbf{x})_{\perp}. \quad (2.81)$$

Inserting this into Eq. (2.80) gives

$$g_x(\boldsymbol{\eta}, \text{grad } f(\mathbf{x})) = \bar{g}_x(\boldsymbol{\eta}, \text{grad } \bar{f}(\mathbf{x})_{\parallel} + \text{grad } \bar{f}(\mathbf{x})_{\perp}) = \bar{g}_x(\boldsymbol{\eta}, \text{grad } \bar{f}(\mathbf{x})_{\parallel}), \quad (2.82)$$

where the normal part of the gradient vanishes, since  $\boldsymbol{\eta} \in T_x \mathcal{M}$  and  $\text{grad } \bar{f}(\mathbf{x})_{\perp} \in N_x \mathcal{M}$ . Since the metrics  $g$  and  $\bar{g}$  can be identified through Eq. (2.77), we have  $\text{grad } f(\mathbf{x}) = \text{grad } \bar{f}(\mathbf{x})_{\parallel}$ . The usage of the projection operators from Eq. (2.79) yields

$$\text{grad } f(\mathbf{x}) = \mathbf{P}_x(\text{grad } \bar{f}(\mathbf{x})). \quad (2.83)$$

This results in a very convenient representation of the Riemannian gradient represented as a vector in the embedding space, since the gradient in Euclidean spaces is simply given by Eq. (2.76). A smooth extension of a function  $f$  needs to be differentiated in the linear embedding space — which is trivial — and the intermediate quantity needs to be orthogonally projected onto the tangent space. As an additional remark, this projection method of gradients is not new. It can be traced back at least to Rosen [Ros60], and the subsequent article [Ros61]. For the case of the unit sphere, where the tangent space projection is simply  $\mathbf{P}_{\mathbf{x}} = \mathbf{I} - \mathbf{x} \otimes \mathbf{x}$ , this yields the Riemannian Gradient as

$$\text{grad } f(\mathbf{x}) = (\mathbf{I} - \mathbf{x} \otimes \mathbf{x}) \text{grad } \bar{f}(\mathbf{x}) = \text{grad } \bar{f}(\mathbf{x}) - \mathbf{x}(\mathbf{x} \cdot \text{grad } \bar{f}(\mathbf{x})), \quad (2.84)$$

which simply uses the Euclidean gradient from the embedding space and subtracts the component in the direction of  $\mathbf{x}$ , namely in the direction of the normal space.

## 2.8 Alternating Tensors and Volume Forms

Alternating tensors are needed to generalize the notion of the volume map from Cartesian coordinates. These are needed to correctly integrate stress resultants and the energy on the shell's midsurface.

Consider a permutation  $\sigma$  and its sign as  $\text{sgn } \sigma$ , where  $\text{sgn } \sigma$  is 1 or  $-1$ , depending on whether the permutation  $\sigma$  is even or odd, respectively. For any vectors  $\mathbf{v}_1, \dots, \mathbf{v}_n$  of the vector space  $V$ , alternating tensors can be defined by

$$\mathbf{T}(\mathbf{v}^{\sigma(1)}, \dots, \mathbf{v}^{\sigma(n)}) = \text{sgn } \sigma \mathbf{T}(\mathbf{v}^1, \dots, \mathbf{v}^n). \quad (2.85)$$

Thus, we have, e.g.,  $\mathbf{T}(\mathbf{v}^1, \mathbf{v}^2) = -\mathbf{T}(\mathbf{v}^2, \mathbf{v}^1)$ . Equivalently, an alternating 2-tensor is simply a skew-symmetric bilinear form on  $V$ . Additionally, if two elements are repeated, then an alternating tensor is zero. Alternating tensors are also called  $k$ -forms since they are constructed from  $k$  covectors. Like a one-form,  $k$ -forms map  $k$  vectors to a scalar. Their construction can be defined via the definition of the *wedge product*.

### 2.8.1 Wedge Product

The wedge product is the antisymmetric tensor product as follows

$$\boldsymbol{\omega} \wedge \boldsymbol{\chi} = \boldsymbol{\omega} \otimes \boldsymbol{\chi} - \boldsymbol{\chi} \otimes \boldsymbol{\omega}. \quad (2.86)$$

Therefore, like the tensor product ( $\otimes$ ), the wedge product  $\wedge$  creates a second-order tensor, i.e., a two-form from two first-order tensors. If  $\boldsymbol{\omega}$  and  $\boldsymbol{\chi}$  are vectors,  $\boldsymbol{\omega} \wedge \boldsymbol{\chi}$  is called *bivector* and if  $\boldsymbol{\omega}$  and  $\boldsymbol{\chi}$  are one-forms, the result is a two-form.

Three vectors combined with the wedge product yield a *trivector* or three-form as

$$\begin{aligned} \boldsymbol{\omega} \wedge \boldsymbol{\chi} \wedge \boldsymbol{\varphi} &= \boldsymbol{\omega} \wedge (\boldsymbol{\chi} \wedge \boldsymbol{\varphi}) = \boldsymbol{\omega} \wedge (\boldsymbol{\chi} \wedge \boldsymbol{\varphi}) \\ &= \boldsymbol{\omega} \otimes \boldsymbol{\chi} \otimes \boldsymbol{\varphi} + \boldsymbol{\chi} \otimes \boldsymbol{\varphi} \otimes \boldsymbol{\omega} + \boldsymbol{\varphi} \otimes \boldsymbol{\omega} \otimes \boldsymbol{\chi} \\ &\quad - \boldsymbol{\chi} \otimes \boldsymbol{\omega} \otimes \boldsymbol{\varphi} - \boldsymbol{\omega} \otimes \boldsymbol{\varphi} \otimes \boldsymbol{\chi} - \boldsymbol{\varphi} \otimes \boldsymbol{\chi} \otimes \boldsymbol{\omega}. \end{aligned} \quad (2.87)$$

Consider an alternating tensor  $\mathbf{T} = \boldsymbol{\omega}_1 \wedge \dots \wedge \boldsymbol{\omega}_k$ . The full contraction with  $k$  vectors to a scalar can be written as

$$\mathbf{T}(\mathbf{v}^1, \dots, \mathbf{v}^k) = \boldsymbol{\omega}_1 \wedge \dots \wedge \boldsymbol{\omega}_k(\mathbf{v}^1, \dots, \mathbf{v}^k) = \det([\boldsymbol{\omega}_i(\mathbf{v}^j)]), \quad (2.88)$$

where  $\det : \mathbb{R}^{k \times k} \rightarrow \mathbb{R}$  is the usual determinant function of a square matrix.

## 2.8.2 Riemannian Volume Form

Using the definition of alternating tensors, the quantities to integrate volumes on manifolds can be defined. Consider a Cartesian basis  $\{\mathbf{e}_i\}$  of  $V$  and a basis  $\{\mathbf{e}^i\}$  of  $V^*$ . The special tensor

$$\tilde{\boldsymbol{\varepsilon}} = \mathbf{e}^1 \wedge \cdots \wedge \mathbf{e}^k = \varepsilon_{a_1 \dots a_k} \mathbf{e}^{a_1} \otimes \cdots \otimes \mathbf{e}^{a_k} \quad (2.89)$$

is called *Levi-Civita tensor*. The values  $\varepsilon_{a_1 \dots a_k}$  are sometimes called *Levi-Civita symbols*. They can be derived as being 1 or  $-1$ , if the permutation of the indices  $a_1 \dots a_k$  is even or odd, respectively. Consider the restriction to  $k = 3$  and the three vectors  $\mathbf{v}^1, \mathbf{v}^2$  and  $\mathbf{v}^3$  defined as  $\mathbf{v}^i = v^{ij} \mathbf{e}_j$ . Then, the Levi-Civita tensor can be used to compute the volume of the parallelepiped  $P$  spanned by the vectors  $\mathbf{v}^1, \mathbf{v}^2$  and  $\mathbf{v}^3$ , which is defined as

$$P = \{t_1 \mathbf{v}^1 + t_2 \mathbf{v}^2 + t_3 \mathbf{v}^3 \mid 0 \leq t_i \leq 1\}. \quad (2.90)$$

The volume can then be computed as

$$\begin{aligned} \text{Vol}(P) &= \tilde{\boldsymbol{\varepsilon}}(\mathbf{v}_1, \mathbf{v}_2, \mathbf{v}_3) = \varepsilon_{ijk} v^{1i} v^{2j} v^{3k} = \det([\mathbf{e}^i(\mathbf{v}_j)]) = \det([\delta_j^i]) \det([v^{ij}]) \\ &= \det([v^{ij}]), \end{aligned} \quad (2.91)$$

where  $[v^{ij}]$  is a matrix with the components  $v^{ij}$ .

The identity  $\det([\mathbf{e}^i(\mathbf{v}_j)]) = \det([\delta_j^i]) \det([v^{ij}])$  can be derived by revisiting Ex. 6 on page 26.

In a general curvilinear coordinate system with the basis  $\{\mathbf{g}_i\}$  and the dual basis  $\{\mathbf{g}^i\}$  the *covariant Levi-Civita tensor* and *contravariant Levi-Civita tensor* read

$$\begin{aligned} \boldsymbol{\varepsilon} &= \sqrt{\det([g_{ab}])} \mathbf{g}^i \wedge \mathbf{g}^j \wedge \mathbf{g}^k = \sqrt{\det([g_{ab}])} \varepsilon_{ijk} \mathbf{g}^i \otimes \mathbf{g}^j \otimes \mathbf{g}^k, \\ \boldsymbol{\varepsilon}^\sharp &= \sqrt{\det([g^{ab}])} \mathbf{g}_i \wedge \mathbf{g}_j \wedge \mathbf{g}_k = \sqrt{\det([g^{ab}])} \varepsilon^{ijk} \mathbf{g}_i \otimes \mathbf{g}_j \otimes \mathbf{g}_k, \end{aligned} \quad (2.92)$$

which are now tensors since they now transform like one. The symbols  $\varepsilon^{ijk}$  can be derived via the identity  $\varepsilon^{ijk} \varepsilon_{ijk} = 1$ . For more details on the correct definition, see [Car19, Sec. 2.8] and [Lee03, Sec. 10.35]. Since  $\boldsymbol{\varepsilon}$  is central to computing the volume of manifolds, it is also called *Riemannian volume form*.

Consider again the vectors  $\mathbf{v}^i = v^{ij} \mathbf{g}_j$ , now defined in the curvilinear basis, which span the volume of  $P$ . This volume can now be calculated as follows:

$$\begin{aligned} \text{Vol}(P) &= \boldsymbol{\varepsilon}(\mathbf{v}^1, \mathbf{v}^2, \mathbf{v}^3) = \sqrt{\det([g_{ab}])} \det(\mathbf{g}^i(\mathbf{v}_j)) = \sqrt{\det([g_{ab}])} \det(\mathbf{g}^i(\mathbf{g}_j)) \det([v^{ij}]) \\ &= \sqrt{\det([g_{ab}])} \det([\delta_j^i]) \det([v^{ij}]) = \sqrt{\det([g_{ab}])} \det([v^{ij}]). \end{aligned} \quad (2.93)$$

Since the measure also depends on the orientation and length of  $\mathbf{g}_i$ , it is crucial to multiply by  $\sqrt{\det([g_{ab}])}$  to get the true volume. The quantity  $\sqrt{\det([g_{ab}])}$  is the volume of the parallelepiped spanned by the base vectors  $\mathbf{g}_i = q_{ij}\mathbf{E}_j$ . This can be seen by calculating it with Eq. (2.91), which results in  $\det[q_{ij}] = \sqrt{\det([g_{ab}])}$ .

Using these results, a coordinate-independent integration on a manifold can be defined. In the spirit of Section 2.4.5 on page 26, this is done by defining the differential volume element as

$$\mathbf{d}\mathbf{v} = \varepsilon(\mathbf{e}^1, \mathbf{e}^2, \mathbf{e}^3) = \sqrt{\det([g_{ab}])} \mathbf{d}x^1 \wedge \mathbf{d}x^2 \wedge \mathbf{d}x^3 = \sqrt{\det([g_{ab}])} dv, \quad (2.94)$$

see [Lee03]. Thus, the total volume of a manifold  $\mathcal{M}$  is

$$\text{Vol}(\mathcal{M}) = \int_{\mathcal{M}} \mathbf{d}\mathbf{v} = \int_{\mathcal{M}} \sqrt{\det([g_{ab}])} dv. \quad (2.95)$$

In the following derivations, the Riemannian volume form is indicated with a bold symbol  $\mathbf{d}\mathbf{v}$  to make the dependence on the metric explicit. The usual infinitesimal volume element is denoted with  $dv$ .

### 2.8.3 Cross Product

The covariant Levi-Civita tensor is also related to the cross product of two vectors. Consider two three-dimensional vectors  $\mathbf{v} = v^i\mathbf{e}_i$  and  $\mathbf{w} = w^i\mathbf{e}_i$  from a vector space  $V$  with the Cartesian basis  $\{\mathbf{e}_i\}$ . The wedge product of these two vectors results in the bivector

$$\begin{aligned} \mathbf{v} \wedge \mathbf{w} &= v^i w^j \mathbf{e}_i \wedge \mathbf{e}_j \\ &= (v^1 w^2 - v^2 w^1) \mathbf{e}_1 \wedge \mathbf{e}_2 + (v^1 w^3 - v^3 w^1) \mathbf{e}_1 \wedge \mathbf{e}_3 + (v^2 w^3 - v^3 w^2) \mathbf{e}_2 \wedge \mathbf{e}_3. \end{aligned} \quad (2.96)$$

If we identify  $\mathbf{e}_1 \wedge \mathbf{e}_2 \rightarrow \mathbf{e}_3$ ,  $\mathbf{e}_1 \wedge \mathbf{e}_3 \rightarrow -\mathbf{e}_2$  and  $\mathbf{e}_2 \wedge \mathbf{e}_3 \rightarrow \mathbf{e}_1$ , the usual definition of the cross product  $\mathbf{v} \times \mathbf{w}$  is obtained. This process of transformation is called the *Hodge star operator*, which produces the Hodge dual. In three dimensions this yields the identification  $\mathbf{v} \times \mathbf{w} = \star(\mathbf{v} \wedge \mathbf{w})$ .

In a curvilinear coordinate system, these relations are more complicated. The cross product  $\mathbf{v} \times \mathbf{w}$  of two three-dimensional vectors  $\mathbf{v} = v^i\mathbf{g}_i$ ,  $\mathbf{w} = w^i\mathbf{g}_i$ , now defined in the curvilinear basis  $\{\mathbf{g}_i\}$  cannot be defined via

$$\mathbf{v} \times \mathbf{w} = v^i w^j \mathbf{g}_k (v^1 w^2 - v^2 w^1) \mathbf{g}_3 - (v^1 w^3 - v^3 w^1) \mathbf{g}_2 + (v^2 w^3 - v^3 w^2) \mathbf{g}_1, \quad (2.97)$$



and the identification  $\mathbf{g}_1 \wedge \mathbf{g}_2 \rightarrow \mathbf{g}_3$ ,  $\mathbf{g}_1 \wedge \mathbf{g}_3 \rightarrow -\mathbf{g}_2$  and  $\mathbf{g}_2 \wedge \mathbf{g}_3 \rightarrow \mathbf{g}_1$ . The right-hand side would not transform correctly since it is artificially linear in the base vectors and a transformation would therefore also only appear to be linear. In contrast to this, the left-hand side  $\mathbf{v} \times \mathbf{w} = (v^i \mathbf{g}_i) \times (w^j \mathbf{g}_j)$ , transforms with two transformation matrices. Thus, the cross product produces only a so-called *pseudovector*.

The coordinate-independent version of the cross product is given via the covariant Levi-Civita tensor from Eq. (2.92) as

$$\boldsymbol{\omega} = \mathbf{v} \times \mathbf{w} = \sqrt{\det([g_{ab}])} \varepsilon_{ijk} v^i w^j \mathbf{g}^k = \omega_k \mathbf{g}^k, \quad (2.98)$$

which yields a covector. This is the definition of the cross product, that is used in the present work. To obtain a vector from the cross product, the musical isomorphisms from Section 2.7.2 can be used to raise the index. This yields

$$\mathbf{u} = (\mathbf{v} \times \mathbf{w})^\sharp = \sqrt{\det([g_{ab}])} \varepsilon_{ijk} g^{kl} v^i w^j \mathbf{g}_l = u^l \mathbf{g}_l, \quad (2.99)$$

which yields a vector.

## 2.8.4 Determinant of a Tensor

The textbook definition of the determinant of a mapping  $\Phi : V \rightarrow V$  relies on the property that the mapping is an *endomorphism*. An endomorphism is a mapping that maps to the same space, from which the input is taken. This is only given for mixed tensors. E.g. for a mixed tensor  $\mathbf{A} : T_{\mathbf{x}}\mathcal{M} \rightarrow T_{\mathbf{x}}\mathcal{M}$ , which defines an endomorphism, we have  $\mathbf{A} = A^i_j \mathbf{g}_i \otimes \mathbf{g}^j$ , in the basis  $\{\mathbf{g}_i\}$  and its dual basis  $\{\mathbf{g}^i\}$ . Using the covariant Levi-Civita tensor, we get the general expression of the determinant

$$\sqrt{\det([g_{ab}])} \varepsilon_{lmn} \det \mathbf{A} = \sqrt{\det([g_{ab}])} \varepsilon_{ijk} \mathbf{A}^i_l \mathbf{A}^j_m \mathbf{A}^k_n, \quad (2.100)$$

which can be simplified by multiplying by  $\sqrt{\det([g^{ab}])} \varepsilon^{lmn}$  from the right as

$$\begin{aligned} \det \mathbf{A} &= \varepsilon_{ijk} \mathbf{A}^i_l \mathbf{A}^j_m \mathbf{A}^k_n \varepsilon^{lmn}, \\ \det \mathbf{A} &= \varepsilon_{ijk} \mathbf{A}^i_1 \mathbf{A}^j_2 \mathbf{A}^k_3 = \det([A^i_j]), \end{aligned} \quad (2.101)$$

which resembles the usual determinant equation. The tensor determinant for second-order mixed tensors coincides with the determinant of its components. Only these mixed tensors define endomorphisms. Therefore, purely covariant or contravariant tensors can be modified by raising or lowering the indices. Then  $\mathbf{B} : T_{\mathbf{x}}\mathcal{M} \rightarrow T_{\mathbf{x}}^*\mathcal{M}$  and

$\mathbf{C} : T_{\mathbf{x}}^* \mathcal{M} \rightarrow T_{\mathbf{x}} \mathcal{M}$  have the determinants

$$\begin{aligned} \det \mathbf{B} &= \det([g^{ab} B_{bc}]) = \det([g^{ab}]) \det(B_{bc}), \\ \det \mathbf{C} &= \det([g_{ab} C^{bc}]) = \det([g_{ab}]) \det(C^{bc}). \end{aligned} \quad (2.102)$$

Therefore, for purely covariant or contravariant second-order tensors, the tensor determinant does *not* coincide with the determinant of its components. This can also be used to interpret the determinant of the metric tensor. Despite the fact that  $\det([g_{ab}])$  is in general not equal to one,  $\det \mathbf{g} = \det([g_{ab} g^{bc}]) = \det([\delta_a^b]) = 1$ . For a three-dimensional manifold, this also replicates the common result

$$\begin{aligned} \varepsilon(\mathbf{g}_1, \mathbf{g}_2, \mathbf{g}_3) &= \mathbf{g}_1 \cdot (\mathbf{g}_2 \times \mathbf{g}_3) = \sqrt{\det([g_{ab}])} \\ \varepsilon(\mathbf{g}^1, \mathbf{g}^2, \mathbf{g}^3) &= \mathbf{g}^1 \cdot (\mathbf{g}^2 \times \mathbf{g}^3) = \frac{1}{\sqrt{\det([g_{ab}])}}. \end{aligned} \quad (2.103)$$

or

$$\mathbf{g}_i \times \mathbf{g}_j = \sqrt{\det([g_{ab}])} \varepsilon_{ijk} \mathbf{g}^k, \quad \text{and} \quad \mathbf{g}^i \times \mathbf{g}^j = \frac{\varepsilon^{ijk}}{\sqrt{\det([g_{ab}])}} \mathbf{g}_k, \quad (2.104)$$

This result for purely covariant or contravariant tensors works since they are simply recast to mixed tensors, which again define an endomorphism. Consider a mapping between two manifolds, i.e., a two-point mixed tensor. The problem gets again more involved, as described in the following. For a two-point tensor  $\mathbf{F} : T_{\mathbf{x}} \mathcal{M} \rightarrow T_{\mathbf{f}(\mathbf{x})} \mathcal{N}$ , like the deformation gradient, the endomorphism needed for the determinant calculation, can be defined in two ways. First, by exploiting the fact, that the product  $\mathbf{F}^T \cdot \mathbf{F}$  results in a tensor that defines an endomorphism, the determinant of  $\mathbf{F}$  can be derived as follows [Fed15]. Consider  $\{\mathbf{g}_i\}$  as the basis of  $T_{\mathbf{f}(\mathbf{x})} \mathcal{N}$  with the metric  $\mathbf{g} = g_{ab} \mathbf{g}^a \otimes \mathbf{g}^b$ , and for  $T_{\mathbf{x}} \mathcal{M}$ , the basis  $\{\mathbf{G}_i\}$  with the metric  $\mathbf{G} = g_{AB} \mathbf{G}^A \otimes \mathbf{G}^B$ . This yields the following result

$$\begin{aligned} \det \mathbf{F} &= \sqrt{\det(\mathbf{F}^T \cdot \mathbf{F})} = \sqrt{\det([\mathbf{F}^T]^A_a F^a_B]} = \sqrt{\det([g_{ab} F^b_B G^{AB} F^a_B])}, \\ &= \sqrt{\det([g_{ab}])} \sqrt{\det([G^{AB}])} \det([F^b_B]) = \frac{\sqrt{\det([g_{ab}])}}{\sqrt{\det([G_{AB}])}} \det([F^b_B]), \end{aligned} \quad (2.105)$$

where the definition of the tensor transpose of Eq. (2.70) was used. Furthermore, the fact that transposing a tensor does not change the determinant was also employed. This is also the result defined in [MH94, Prop. 5.3]. The second way, used in Marsden and Hughes [MH94], is by introducing two local charts, which results again in an endomorphism, and then yielding the same result of Eq. (2.105). Alternatively, if we interpret  $\mathbf{dV}$  from

Eq. (2.94) as the volume form of  $\mathcal{M}$  it reads

$$\mathbf{dV} = \varepsilon_{\mathbf{G}}(\mathbf{G}^1, \mathbf{G}^2, \mathbf{G}^3) = \sqrt{\det([G_{ab}])} \mathbf{dX}^1 \wedge \mathbf{dX}^2 \wedge \mathbf{dX}^3 = \sqrt{\det([G_{ab}])} dV, \quad (2.106)$$

and  $\mathbf{dv}$  as the volume form of  $\mathcal{N}$

$$\mathbf{dv} = \varepsilon_{\mathbf{g}}(\mathbf{g}^1, \mathbf{g}^2, \mathbf{g}^3) = \sqrt{\det([g_{ab}])} \mathbf{dx}^1 \wedge \mathbf{dx}^2 \wedge \mathbf{dx}^3 = \sqrt{\det([g_{ab}])} dv. \quad (2.107)$$

Here,  $\varepsilon_{\mathbf{G}}$  and  $\varepsilon_{\mathbf{g}}$  denote the Levi-Civita tensor on  $\mathcal{M}$  and  $\mathcal{N}$ , respectively.

Thus, in curvilinear coordinates, it is crucial to correctly derive the volume element or determinant of a tensor, since they depend on the metric.

### 2.8.5 Piola Transform

From the former expressions, the question of how volume elements transform under a function between manifolds was answered. Now, the question arises, how do areas transform? This can be answered by relating the area element on  $\mathcal{M}$  to its volume element. Consider  $\mathbf{da}$  as the area element of  $\partial\mathcal{N}$ ,  $\mathbf{N}$  as a unit normal covector field also on  $\partial\mathcal{N}$ , which is assumed to be the plane  $X^1 = 0$ , and  $\mathbf{w}$  as a vector field on  $\mathcal{N}$ . Without loss of generality, a three-dimensional manifold is considered. Then, the area element and volume element are related via

$$\mathbf{w} \cdot \mathbf{da} = \mathbf{w} \cdot \mathbf{N} da = \varepsilon_{\mathbf{g}}(\mathbf{w}, \mathbf{g}^2, \mathbf{g}^3) = \mathbf{w} \cdot (\mathbf{g}_2 \times \mathbf{g}_3) dv = \mathbf{w} \cdot (\mathbf{g}_2 \times \mathbf{g}_3) dadx^1, \quad (2.108)$$

where using the latter cross-product identification yields  $\mathbf{da} = \mathbf{N} da = (\mathbf{g}_2 \times \mathbf{g}_3) da = \sqrt{\det([g_{ab}])} \mathbf{g}^1 da$ . This yields also the result on  $\mathcal{M}$  as  $\mathbf{dA} = \sqrt{\det([G_{AB}])} \mathbf{G}^1 dA$

The pull-back  $\mathbf{da}$  to  $\mathcal{M}$  is not as simple as before, since the one-form does not only depend on the base vector but also on the metric tensor itself. The pull-back of  $\mathbf{g}^1$  can be done via Eq. (2.55) on page 33 and the pull-back of  $\sqrt{\det([g_{ab}])}$ . This yields the relation

$$(\mathbf{da})_a = \det \mathbf{F} (F^{-1})^A_a (\mathbf{dA})_A, \quad (2.109)$$

which is sometimes called *Nanson's formula*.

Consider again the example from Eq. (2.108), the transformation reads

$$(\sqrt{\det([g_{ab})}] \mathbf{g}^1 da)_a = \det \mathbf{F} (F^{-1})^A{}_a \sqrt{\det([G_{AB})]} (\mathbf{G}^1)_A dA \quad (2.110)$$

$$= \frac{\sqrt{\det([g_{ab})]}}{\sqrt{\det([G_{AB})]}} \det([F^b{}_B]) (F^{-1})^A{}_a \sqrt{\det([G_{AB})]} (\mathbf{G}^1)_A dA \quad (2.111)$$

$$= \sqrt{\det([g_{ab})]} \det([F^b{}_B]) (F^{-1})^A{}_a (\mathbf{G}^1)_A dA. \quad (2.112)$$

The general case, not related to area differential elements as in Eq. (2.109), but to *normals* instead, is called *Piola transform*. The notion of normals is defined now as one-forms that are defined via the cross-product Eq. (2.98) or simply by stating that the object transforms as given in Eq. (2.109). Thus, given a normal field  $\mathbf{N}$  on  $\mathcal{M}$ , the Piola transform reads

$$\mathbf{n} = J \mathbf{F}^{-T} \cdot \mathbf{N}, \quad (2.113)$$

which yields a normal vector field  $\mathbf{n}$  defined on  $\mathcal{N}$ .

Since the determinant and volume form transformations are non-standard in the way they are presented, one example is provided, in which the mapping properties of Eqs. (2.105) and (2.107) are shown.

**EXAMPLE 8** (Deformation of quadrilateral with curved edges). Consider a quadrilateral  $\mathcal{M}$  with curved edges with the parameterization

$$\mathbf{R}(\theta^1, \theta^2) = \begin{bmatrix} X \\ Y \end{bmatrix} = \begin{bmatrix} 2\theta^2 \\ 2(\theta^2)^2 + \theta^1 \end{bmatrix}, \quad (2.114)$$

which results in the base vectors  $\mathbf{G}_1 = \frac{\partial \mathbf{R}(\theta^1, \theta^2)}{\partial \theta^1} = [0, 1]$  and  $\mathbf{G}_2 = \frac{\partial \mathbf{R}(\theta^1, \theta^2)}{\partial \theta^2} = [2, 4\theta^2]$ . This yields for the determinant of the metric coefficients  $\sqrt{\det([G_{AB})]} = 2$ . Consider for both quadrilaterals the ranges  $\theta^1 = [0, 1]$  and  $\theta^2 = [0, 2]$  of the parameterization coordinates. Integrating the area yields

$$\text{Vol}(\mathcal{M}) = \int_{\mathcal{M}} \mathbf{dV} = \int_{\mathcal{M}} \sqrt{\det([G_{AB})]} dV = \int_0^1 \int_0^2 2 d\theta^1 d\theta^2 = 4. \quad (2.115)$$

Consider another quadrilateral  $\mathcal{N}$  with curved edges with the parameterization

$$\mathbf{r}(\theta^1, \theta^2) = \begin{bmatrix} x \\ y \end{bmatrix} = \begin{bmatrix} 4(\theta^2)^2 \\ 4(\theta^2)^3 + 2\theta^1 \end{bmatrix}, \quad (2.116)$$

with the curvilinear base vectors  $\mathbf{g}_1 = \frac{\partial \mathbf{r}(\theta^1, \theta^2)}{\partial \theta^1} = [0, 2]$  and  $\mathbf{g}_2 = \frac{\partial \mathbf{r}(\theta^1, \theta^2)}{\partial \theta^2} = [8\theta^2, 12(\theta^2)^2]$ . This yields for the determinant of the metric coefficients  $\sqrt{\det([g_{ab}])} = 16\theta^2$ . Integrating the area yields

$$\text{Vol}(\mathcal{N}) = \int_{\mathcal{N}} \mathbf{d}\mathbf{v} = \int_{\mathcal{N}} \sqrt{\det([g_{ab}])} \, dv = \int_0^1 \int_0^2 16\theta^2 \, d\theta^1 \, d\theta^2 = 16. \quad (2.117)$$

The map  $\Phi : \mathcal{M} \rightarrow \mathcal{N}$  that deforms  $\mathcal{M}$  to  $\mathcal{N}$  can be constructed via

$$\Phi(X, Y) = \mathbf{r}(\mathbf{R}^{-1}(X, Y)) = \begin{bmatrix} X^2 \\ \frac{1}{2}X^3 - X^2 + 2Y \end{bmatrix}. \quad (2.118)$$

The Jacobian w.r.t.  $X, Y$  of  $\Phi$ , later called the deformation gradient of this map in Cartesian coordinates  $X$  and  $Y$  with the base vectors  $\mathbf{E}_1$  and  $\mathbf{E}_2$  reads,

$$\mathbf{F}(X, Y) = \begin{bmatrix} 2X & 0 \\ \frac{3}{2}X^2 - 2X & 2 \end{bmatrix} \mathbf{E}_a \otimes \mathbf{E}^A. \quad (2.119)$$

Since this is defined in the Cartesian coordinate system, it defines an endomorphism  $\mathbb{R}^2 \rightarrow \mathbb{R}^2$  and its determinant is  $\det \mathbf{F} = \det([F^a_A]) = 4X$ . This can be used to integrate the deformed area via an integration on the undeformed manifold by integrating

$$\text{Vol}(\mathcal{N}) = \int_{\mathcal{N}} \mathbf{d}\mathbf{v} = \int_{\mathcal{M}} \det \mathbf{F} \, \mathbf{d}\mathbf{V} = \int_0^2 \int_{X^2/2}^{X^2/2+2} 4X \, dY \, dX = 16, \quad (2.120)$$

as expected. It can also be derived similarly the other way around. The undeformed area can be integrated on the deformed manifold as

$$\text{Vol}(\mathcal{M}) = \int_{\mathcal{M}} \mathbf{d}\mathbf{V} = \int_{\mathcal{N}} 1/\det \mathbf{F}(\Phi^{-1}(x, y)) \, \mathbf{d}\mathbf{v} = \int_0^4 \int_{x^{3/2}/2}^{x^{3/2}/2+4} 4\sqrt{x} \, dy \, dx = 4. \quad (2.121)$$

If  $\mathbf{F}$  is defined in the coordinates  $\theta^i$ , we get

$$\mathbf{F}(\mathbf{R}(\theta^1, \theta^2)) = \delta^a_A \mathbf{g}_a \otimes \mathbf{G}^A. \quad (2.122)$$

Now, by repeating Eq. (2.120), we get with Eq. (2.105)

$$\text{Vol}(\mathcal{N}) = \int_{\mathcal{N}} \mathbf{d}\mathbf{v} = \int_{\mathcal{M}} \det \mathbf{F} \mathbf{d}\mathbf{V} = \int_{\mathcal{M}} \frac{\sqrt{\det([g_{ab}]})}{\sqrt{\det([G_{AB}]})} \det([\delta^b_B]) \sqrt{\det([G_{AB}]}) dV \quad (2.123)$$

$$= \int_0^1 \int_0^2 16\theta^2 d\theta^1 d\theta^2 = 16, \quad (2.124)$$

as expected.

# 3

---

## Second-Order Differential Geometry

Second-order geometry information is the natural additional information that can be added to a Riemannian manifold. The metric allows the notion of comparing quantities *within* a single tangent space and allows the definition of length and angles on the manifold. Second-order information is needed to compare quantities between *different* tangent spaces. This boils down to the notion of *parallel transport* or *covariant derivatives*, which enable the definition of *curvature*. Thus, second-order information is needed to capture the *curvature* information of the manifold. This can be used to derive curvature information of a physical body or curvature information of the manifold, where our degrees of freedom later live in for the Reissner-Mindlin shell formulation. This chapter is mainly based on Absil et al. [Abs08], Boumal [Bou23], do Carmo [dC92], and Lee [Lee03]. These books present a formal approach to the topic and alternatively the reader is referred to Misner et al. [Mis73] and Needham [Nee21] for a visual approach.

### 3.1 Affine Connections

We started with topological information in Section 2.2, followed by directional derivatives and the definition of tangent spaces. Afterward, a Riemannian metric enabled the measurement of length and angles on the manifold in Section 2.7. Finally, the definition of alternating tensors in Section 2.8 allowed the integration on manifolds. Now this geometric toolbox is filled with affine connections. An affine connection on a Riemannian manifold is another geometric structure that can be added to a manifold.

An affine connection  $\nabla$  solves the problem of obtaining intrinsic derivatives of tangent vector fields on a manifold. There are infinite possibilities to define an affine connection on a manifold, but the benefits of the *Riemannian connection* or *Levi-Civita connection* stand out in contrast to other conceivable affine connections. One benefit is that the

resulting Riemannian Hessian is a symmetric bilinear form and that it is invariant with respect to the metric. Otherwise, this could lead to an unsymmetric form, see [MS95; Rom05; Ray15].

**Definition 17.** An *affine connection* is a mapping as follows

$$\nabla : \begin{cases} \mathfrak{X}(\mathcal{M}) \times \mathfrak{X}(\mathcal{M}) \rightarrow \mathfrak{X}(\mathcal{M}), \\ (\boldsymbol{\xi}, \boldsymbol{\eta}) \mapsto \nabla_{\boldsymbol{\xi}}\boldsymbol{\eta}, \end{cases} \quad (3.1)$$

where  $\mathfrak{X}(\mathcal{M})$  denotes an arbitrary vector field defined in  $\mathcal{M}$  in contrast to  $\mathcal{D}(\mathcal{M})$  which denotes a scalar field defined in  $\mathcal{M}$ . Therefore, the connection  $\nabla$  takes two vector fields as arguments and the result is a vector field. Consider  $a, b \in \mathbb{R}$ ,  $f, g \in \mathcal{D}(\mathcal{M})$  and  $\boldsymbol{\xi}, \boldsymbol{\eta}, \boldsymbol{\zeta} \in \mathfrak{X}(\mathcal{M})$ . Then, an affine connection  $\nabla_{\boldsymbol{\xi}}\boldsymbol{\eta}$  satisfies the following properties, see [Abs08, p. 94] or [dC92, Definition 2.1]:

- $\mathcal{D}(\mathcal{M})$ -linearity in  $\boldsymbol{\eta}$ :  $\nabla_{f\boldsymbol{\eta}+g\boldsymbol{\zeta}}\boldsymbol{\xi} = f\nabla_{\boldsymbol{\eta}}\boldsymbol{\xi} + g\nabla_{\boldsymbol{\zeta}}\boldsymbol{\xi}$
- $\mathbb{R}$ -linearity in  $\boldsymbol{\xi}$ :  $\nabla_{\boldsymbol{\eta}}(a\boldsymbol{\xi} + b\boldsymbol{\zeta}) = a\nabla_{\boldsymbol{\eta}}\boldsymbol{\xi} + b\nabla_{\boldsymbol{\eta}}\boldsymbol{\zeta}$
- Product rule:  $\nabla_{\boldsymbol{\eta}}(f\boldsymbol{\xi}) = (D_{\boldsymbol{\eta}}f)\boldsymbol{\xi} + f\nabla_{\boldsymbol{\eta}}\boldsymbol{\xi}$

Based on these definitions, by considering a tangent vector  $\boldsymbol{\xi}$  defined along a curve  $\mathbf{c} : I \rightarrow \mathcal{M}$ , the *covariant derivative* along  $\mathbf{c}$  can be defined as

$$\frac{D\boldsymbol{\xi}(\mathbf{c}(t))}{dt} = \nabla_{\partial_t\mathbf{c}}\boldsymbol{\xi}. \quad (3.2)$$

This relationship directly connects the affine connection to the concept of a covariant derivative. Consequently, the covariant derivative is the outcome of equipping an affine connection  $\nabla$  with a derivative direction and a vector field, the change of which is of interest.

Consider two tangent vector fields

$$\boldsymbol{\eta} = \eta^i \mathbf{g}_i, \text{ and } \boldsymbol{\xi} = \xi^i \mathbf{g}_i, \quad (3.3)$$

defined in a coordinate basis  $\{\mathbf{g}_i(\theta^j)\}$  with curvilinear coordinates  $\theta^i$  as given by Eqs. (2.15) and (2.16) on page 22. The dependence on  $\theta^i$  is not denoted in the following for a shorter notation. The covariant derivative of  $\boldsymbol{\eta}$  in direction  $\boldsymbol{\xi}$ , using the product rule, reads

$$\nabla_{\boldsymbol{\xi}}\boldsymbol{\eta} = \xi^i \nabla_{\mathbf{g}_i}(\eta^j \mathbf{g}_j) = \xi^i (D_{\mathbf{g}_i}\eta^j \mathbf{g}_j + \eta^j \nabla_{\mathbf{g}_i}\mathbf{g}_j) = \xi^i \left( \frac{\partial \eta^j}{\partial \theta^i} \mathbf{g}_j + \eta^j \nabla_{\mathbf{g}_i}\mathbf{g}_j \right). \quad (3.4)$$



If the shortcut  $\nabla_{\mathbf{g}_i} \mathbf{g}_j = \Gamma_{ij}^k \mathbf{g}_k$  is introduced, Eq. (3.4) can be grouped together and this yields

$$\nabla_{\xi} \boldsymbol{\eta} = \xi^i \left( \frac{\partial \eta^k}{\partial \theta^i} + \eta^j \Gamma_{ij}^k \right) \mathbf{g}_k. \quad (3.5)$$

The numbers  $\Gamma_{ij}^k$  are denoted in this case as *coefficients of the connection*  $\nabla$ , since these coefficients fully define the connection and vice versa.

Similarly, for a one-form  $\boldsymbol{\omega} = \omega_i \mathbf{g}^i$ , it is possible to derive the analog of Eq. (3.5) as

$$\nabla_{\xi} \boldsymbol{\omega} = \xi^i \left( \frac{\partial \omega_k}{\partial \theta^i} - \omega_j \Gamma_{ik}^j \right) \mathbf{g}^k. \quad (3.6)$$

The coefficients of the connection  $\Gamma_{ij}^k$  are not necessarily symmetric in the lower indices  $i$  and  $j$ .

**EXAMPLE 9.** As a motivation, consider a curve  $\mathcal{C}$  in  $\mathbb{R}^2$  with the parameterization  $\mathbf{c} : I \rightarrow \mathbb{R}^2$ . The tangent vector of this curve's parameterization is  $\mathbf{v}(t) = \frac{d\mathbf{c}}{dt}(t)$ , which is always in the tangent space  $T_{\mathbf{c}(t)}\mathcal{C}$ . Then, the “derivative”  $\frac{d\mathbf{v}}{dt}(t)$  does not belong to the tangent bundle, since it has components in the normal direction of the curve. Thus, this notion of such a derivative is not *intrinsic* to the manifold  $\mathcal{C}$ .

To fix this inconsistency of Example 9, one can consider, as in Section 2.7.4 on page 40, the wrong quantity as a quantity in the embedding space and then obtain the correct one by projecting the result on the tangent space in the covariant derivative. Consequently, the covariant derivative is constructed as follows: first, by computing a simple partial derivative that yields a quantity no longer residing in the tangent space, as illustrated in Example 9. Subsequently, this deviation is rectified by incorporating the coefficients of the connection, resulting in a quantity that once again resides in the embedded tangent space.

A usual shortcut for the covariant derivative of the components of Eq. (3.5) is given by

$$\eta^k{}_{|i} = \frac{\partial \eta^k}{\partial \theta^i} + \eta^j \Gamma_{ij}^k. \quad (3.7)$$

## Levi-Civita Connection

Up to this point, the connection  $\nabla$  or its coefficients can be chosen freely to satisfy the requirements of Definition 17. The satisfaction of these requirements does not yield

a unique connection. If the manifold  $\mathcal{M}$  is restricted to be a Riemannian manifold  $(\mathcal{M}, g)$ , i.e. equipped with a Riemannian metric  $g$ , then this singles out a well-defined and unique connection. This connection is called the Levi-Civita connection or Riemannian connection.

**Definition 18.** The *Levi-Civita connection* is an affine connection, which satisfies the following additional properties

1. It is invariant w.r.t. the metric:  $\nabla_{\eta}\langle\xi, \zeta\rangle = \langle\nabla_{\eta}\xi, \zeta\rangle + \langle\xi, \nabla_{\eta}\zeta\rangle$ ,
2. and symmetric in the sense  $\nabla_{\eta}\xi - \nabla_{\xi}\eta = [\eta, \xi]$ ,

where  $[\xi, \eta]$  is the Lie bracket and defined as

$$[\xi, \eta] = \frac{\partial \xi^i}{\partial \theta^j} \eta^j - \frac{\partial \eta^i}{\partial \theta^j} \xi^j. \quad (3.8)$$

The fact that this connection exists and is unique is important enough to have its own name: the *fundamental theorem of Riemannian geometry*. As mentioned, both requirements result in a unique connection. The symmetry requirement property can be further interpreted as follows:

$$\begin{aligned} \nabla_{\eta}\xi - \nabla_{\xi}\eta &= \frac{\partial \xi^i}{\partial \theta^j} \eta^j + \xi^k \Gamma^i_{kj} \eta^j - \frac{\partial \eta^i}{\partial \theta^j} \xi^j - \eta^k \Gamma^i_{kj} \eta^j \\ &= \frac{\partial \xi^i}{\partial \theta^j} \eta^j + \xi^k \Gamma^i_{kj} \eta^j - \frac{\partial \eta^i}{\partial \theta^j} \xi^j - \eta^j \Gamma^i_{jk} \xi^k \\ &= \frac{\partial \xi^i}{\partial \theta^j} \eta^j - \frac{\partial \eta^i}{\partial \theta^j} \xi^j + \xi^k (\Gamma^i_{kj} - \Gamma^i_{jk}) \eta^j, \end{aligned} \quad (3.9)$$

where it is apparent that  $\nabla_{\eta}\xi - \nabla_{\xi}\eta = [\xi, \eta]$  implies the symmetry of the coefficients of the connection symbols  $\Gamma^i_{kj} = \Gamma^i_{jk}$ . Connections that have symmetric coefficients are called *symmetric* or *torsion-free*.

**Koszul's formula** The requirements in Definition 18 can be recast into a single equation, which has the name *Koszul's formula*. An affine connection must satisfy the so-called *Koszul's formula* to be the unique Levi-Civita connection. This formula can be constructed from the requirements mentioned in Definition 18. It reads

$$\begin{aligned} 2\langle\nabla_{\xi}\eta, \zeta\rangle &= \langle[\xi, \eta], \zeta\rangle - \langle[\xi, \zeta], \eta\rangle - \langle[\eta, \zeta], \xi\rangle \\ &\quad + D_{\xi}\langle\eta, \zeta\rangle + D_{\eta}\langle\xi, \zeta\rangle - D_{\zeta}\langle\xi, \eta\rangle, \end{aligned} \quad (3.10)$$

with  $\xi, \eta, \zeta \in T\mathcal{M}$ . In coordinates, in the case of a holonomic basis as defined in Eq. (2.16) on page 22, the Lie bracket of the coordinate base vectors vanishes. This means  $[\mathbf{g}_i, \mathbf{g}_j] = \mathbf{0}$ , which results in

$$\Gamma_{ij}^k = \frac{1}{2}g^{kl} \left( \frac{\partial g_{jl}}{\partial \theta_i} + \frac{\partial g_{il}}{\partial \theta_j} - \frac{\partial g_{ij}}{\partial \theta_l} \right) = \frac{1}{2}g^{kl} (g_{jl,i} + g_{il,j} - g_{ij,l}). \quad (3.11)$$

These coefficients of the connection, named *Christoffel symbols of the second kind*, are attributed to Elwin Bruno Christoffel, who first defined them in [Chr69, p. 48]. For a non-holonomic basis, additional components arise in Eq. (3.11), see Misner et al. [Mis73].

For Euclidean spaces, i.e.,  $\mathbb{R}^m$  equipped with the trivial metric  $g(\mathbf{u}, \mathbf{v}) = \mathbf{u} \cdot \mathbf{v}$ . The connection simply boils down to the usual directional derivative. Formally, we have  $\nabla_{\mathbf{u}} \mathbf{v} = D_{\mathbf{u}} \mathbf{v}$ .

## 3.2 Parallel Transport

From the very definition of the covariant derivative, it is apparent to ask what denotes a vanishing derivative. Consider a vector field  $\mathbf{w} : \mathbb{R}^n \rightarrow \mathbb{R}^n$ . In Euclidean space, the directional derivative of  $\mathbf{w}$  in a direction  $\mathbf{v} \in \mathbb{R}^n$  at position  $\mathbf{x} \in \mathbb{R}^n$  reduces to

$$D_{\mathbf{v}} \mathbf{w}(\mathbf{x}) = \lim_{\varepsilon \rightarrow 0} \frac{\mathbf{w}(\mathbf{x} + \varepsilon \mathbf{v}) - \mathbf{w}(\mathbf{x})}{\varepsilon}, \quad (3.12)$$

which can be read as the change of the vector field  $\mathbf{w}$  at position  $\mathbf{x}$  in direction  $\mathbf{v}$ . Therefore, this derivative vanishes, if  $\mathbf{w}$  evaluated at  $\mathbf{x} + \varepsilon \mathbf{v}$  is parallel to, and has the same length as,  $\mathbf{w}(\mathbf{x})$ .

If this is generalized to manifolds, two pitfalls arise. First, the line  $\mathbf{x} + \varepsilon \mathbf{v}$  has to be replaced by a curve  $\gamma$  that realizes the tangent vector  $\xi$  as in Definition 10 on page 21. Otherwise, the point  $\mathbf{x} + \varepsilon \mathbf{v}$  is adrift, having departed from the manifold. Thus, using the curve  $\gamma$  and its tangent vector  $\xi$  yields

$$D_{\xi} \boldsymbol{\eta}(\mathbf{x}) = \lim_{\varepsilon \rightarrow 0} \frac{\boldsymbol{\eta}_{\gamma(\varepsilon)} - \boldsymbol{\eta}_{\gamma(0)}}{\varepsilon}, \quad (3.13)$$

with  $\gamma(0) = \mathbf{x}$ . As shown in Fig. 3.1, this is still not a proper definition, since the difference is still not well-defined. This results from the fact that no well-defined concept exists to define differences (and sums) between different tangent spaces, namely  $T_{\gamma(\varepsilon)}\mathcal{M}$  and  $T_{\gamma(0)}\mathcal{M}$ . Consequently,  $\boldsymbol{\eta}_{\gamma(\varepsilon)}$  lives in  $T_{\gamma(\varepsilon)}\mathcal{M}$  and  $\boldsymbol{\eta}_{\gamma(0)}$  in  $T_{\gamma(0)}\mathcal{M}$  indicated by the quadrilaterals in the figure.

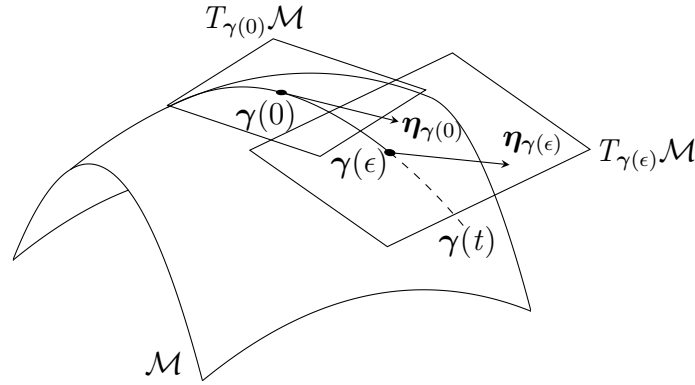


**Figure 3.1:** Illustration of Eq. (3.13). The vectors  $\boldsymbol{\eta}_{\gamma(\epsilon)}$  and  $\boldsymbol{\eta}_{\gamma(0)}$  live in different tangent spaces. Thus, the difference in Eq. (3.13) can not be well-defined, since the vectors are defined through different base vectors.

To fix this inconsistency, the vector  $\boldsymbol{\eta}(\gamma(\epsilon))$  at  $T_{\gamma(\epsilon)}\mathcal{M}$  has to be transported back to  $T_{\gamma(0)}\mathcal{M}$ . Then, both vectors are defined in the same tangent space and differences make sense again. The transportation of  $\boldsymbol{\eta}(\gamma(\epsilon))$  should not change the basic properties of the vector. This process is called *parallel transport*.<sup>1</sup> The name parallel transport can be easily understood with the linear example from Eq. (3.12), since the movement from  $\mathbf{x} + \epsilon\mathbf{v}$  to  $\mathbf{x}$  was merely shifting the vector  $\mathbf{w}$ . This allows the definition

$$\nabla_{\boldsymbol{\xi}}\boldsymbol{\eta}(\mathbf{x}) = \lim_{\epsilon \rightarrow 0} \frac{\boldsymbol{\eta}_{\gamma(\epsilon)|\gamma(0)} - \boldsymbol{\eta}_{\gamma(0)}}{\epsilon}, \quad (3.14)$$

where  $\boldsymbol{\eta}_{\gamma(\epsilon)|\gamma(0)}$  denotes the parallel transport of the vector from  $\gamma(\epsilon)$  to  $\gamma(0)$ . For a visualization, refer to Fig. 3.2. Therein, the vector field  $\boldsymbol{\eta}$  is evaluated at  $t = 0$  and  $t = \epsilon$ . This gives the vectors  $\boldsymbol{\eta}_{\gamma(0)}$  and  $\boldsymbol{\eta}_{\gamma(\epsilon)}$ . Then, the vector  $\boldsymbol{\eta}_{\gamma(\epsilon)}$  is parallel transported back to  $\gamma(0)$ , which is denoted by  $\boldsymbol{\eta}_{\gamma(\epsilon)|\gamma(0)}$ , and the difference is taken. This difference is  $d\boldsymbol{\eta}$ . Taking the limit  $\epsilon \rightarrow 0$  yields the covariant derivative  $\nabla_{\boldsymbol{\xi}}\boldsymbol{\eta}(\mathbf{x})$ . Parallel transport can also be used for different algorithms and not only for interpreting the covariant derivative. This is also indicated in Fig. 3.2, where  $\boldsymbol{\eta}_{\gamma(\epsilon)}$  can also be parallel transported to  $\gamma(1)$  or  $\gamma(2)$ . In Euclidean spaces with the standard metric, this means no change at all. In the non-linear case, parallel transportation can be defined by requiring that the covariant derivative of the parallel transported vector vanishes, indicating that indeed it is parallel transported.

**Definition 19.** Consider a vector  $\hat{\boldsymbol{\eta}}$  defined at position  $t_1$  of a curve  $\gamma : \mathbb{R} \rightarrow \mathcal{M}; t \mapsto \gamma(t)$ . Let  $\boldsymbol{\xi}$  be the tangent vector field of  $\gamma$ . Then, the vector field  $\boldsymbol{\eta}$  that corresponds to the

<sup>1</sup>The notion of parallelism can be traced back to Levi-Civita [Lev16], who is referring to Riemann [Rie76], even though they used Christoffel symbols for their derivation of the earlier work Christoffel [Chr69].

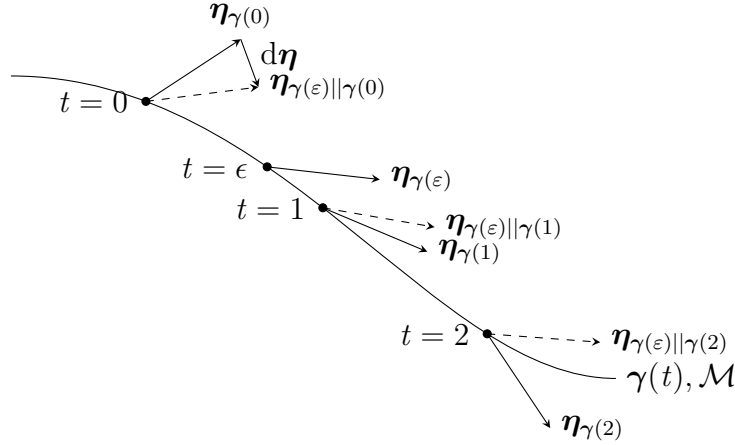


**Figure 3.2:** Visual representation of Eq. (3.14). The solid arrows denote snapshots of the vector field  $\boldsymbol{\eta}$ . The dashed arrows represent the vector field stemming from the parallel transported vector  $\boldsymbol{\eta}_{\gamma(\epsilon)}$ . Since the Levi-Civita connection is used, this corresponds to simply rotating  $\boldsymbol{\eta}_{\gamma(\epsilon)}$  along the curve, such that the angle w.r.t. the tangent vector of the curve  $\boldsymbol{\gamma}$  persists. At  $t = 0$ , the covariant derivative can be taken by  $D_{\boldsymbol{\xi}}\boldsymbol{\eta} = \lim_{\epsilon \rightarrow 0} \frac{d\boldsymbol{\eta}}{\epsilon} = \lim_{\epsilon \rightarrow 0} \frac{\boldsymbol{\eta}_{\gamma(\epsilon)} \parallel \boldsymbol{\gamma}(0) - \boldsymbol{\eta}_{\gamma(0)}}{\epsilon}$ . The tangent vector  $\boldsymbol{\xi}$  of the curve  $\boldsymbol{\gamma}$  is not shown.

*parallel transported* vector  $\hat{\boldsymbol{\eta}}$  is defined through the first-order differential equation

$$\nabla_{\boldsymbol{\xi}}\boldsymbol{\eta} = \mathbf{0} \quad \Longleftrightarrow \quad \xi^i \left( \frac{\partial \eta^k}{\partial \theta^i} + \eta^j \Gamma_{ij}^k \right) \mathbf{g}_k = \xi^i \eta^k_{|i} \mathbf{g}_k = 0, \quad (3.15)$$

with the initial condition  $\boldsymbol{\eta}(t_1) = \hat{\boldsymbol{\eta}}$ . Thus,  $\boldsymbol{\eta}$  is the *parallel transportation* of  $\hat{\boldsymbol{\eta}}$ . If  $\mathcal{M}$  is a Riemannian manifold and  $\nabla$  is the Levi-Civita connection, the parallel translation generated by  $\nabla$  is an isometry. This is also depicted in Fig. 3.2

Thus, a given parallel transport can be used to define the connection  $\nabla$ , since Eq. (3.15) can be solved for the coefficients of the connection. Consequently, the knowledge of the covariant derivative, parallel transport, or the connection itself can be used to define each other. In other words, if one of them is known, the other two can be derived. Parallel transportation denotes the process of moving a vector from one point to another with the least change possible, while simultaneously staying in the tangent space. What least change means is dictated by the metric and the given affine connection.

### 3.3 Geodesics

Geodesic curves recover the notion of straight lines from Euclidean spaces. This straightness of lines carries over to manifolds through the definition of the covariant derivative

and its notion of *no change*. Straight lines can be characterized by the fact that their underlying direction does not change. Thus, if a line  $\gamma : \mathbb{R} \rightarrow \mathbb{R}^n$  has the parameterization  $\gamma(t) = \mathbf{x} + t\mathbf{v}$ , with  $\mathbf{x}, \mathbf{v} \in \mathbb{R}^n$ , then the derivative yields  $\frac{\partial \gamma}{\partial t} = \mathbf{v}$ . This is a constant, and thus the straight-line parameterization has no acceleration. The construction of straight-line parameterization with non-zero acceleration is possible but does not change the shape. Similarly, geodesic curves can be stated via the requirement of no acceleration. The intrinsic definition of no acceleration can be provided by the covariant derivative of the velocity vector of a curve. Consider a curve  $\gamma : \mathbb{R} \rightarrow \mathcal{M}$  and its velocity vector  $\mathbf{v} = \frac{\partial \gamma}{\partial t}$ . This yields the defining equation

$$\nabla_{\mathbf{v}} \mathbf{v} = 0, \tag{3.16}$$

which can also be stated informally as “geodesics are curves, that parallel transport their own velocity vector”.

Again, using a chart  $\phi$  with coordinates  $x^i$ ,  $\hat{\gamma}$  can be given as  $(\hat{\gamma}^1(t), \dots, \hat{\gamma}^n(t)) = \phi(\gamma(t))$ . Then, Eq. (3.16) reads in components

$$\frac{\partial^2 \hat{\gamma}^k}{\partial t^2} + \Gamma_{ij}^k(\gamma) \frac{\partial \hat{\gamma}^i}{\partial t} \frac{\partial \hat{\gamma}^j}{\partial t} = 0, \tag{3.17}$$

where  $\Gamma_{ij}^k(\gamma)$  are the Christoffel symbols in the chart  $\varphi$ . Thus, finding geodesics curves involves the solution of an ordinary second-order differential equation with a given initial point  $\gamma(0)$  and velocity (direction)  $\frac{\partial \gamma(t)}{\partial t}|_{t=0}$ , which is the unique geodesic originating at  $\gamma(0)$  and starting in direction  $\frac{\partial \gamma(t)}{\partial t}|_{t=0}$ . The solvability of this differential equation depends highly on the nature of  $\Gamma_{ij}^k(\gamma)$  and on the initial conditions. Even for simple parameterization of a manifold, the geodesic curve can get quite complicated, see Fig. 3.3. This dependence usually yields a numerically as well as analytically daunting task.

In the next section, we revisit the geodesic curve from a different viewpoint, but first, some examples are given, to provide a physical and geometrical insight into geodesic curves.

**EXAMPLE 10 (Roller coaster).** Consider a roller-coaster ride with constant speed and with the quantities as introduced in Example 9 on page 53. The curve is denoted by  $\mathcal{C}$ . If we ride along this roller coaster with constant velocity, we are tracing out the one-dimensional geodesic curve on this one-dimensional manifold  $\mathcal{C}$ . Then, the covariant derivative of the velocity  $\mathbf{v}$  gives  $\nabla_{\mathbf{v}} \mathbf{v} = \mathbf{0}$ . Thus, there seems to be no acceleration. In this example, this last statement is false, which can be shown with roller coaster passengers with sensitive stomachs. The misconception stems from the notion of intrinsic and extrinsic quantities. The intrinsic acceleration  $\nabla_{\mathbf{v}} \mathbf{v}$  *along the path* is exactly zero but the extrinsic is not. The extrinsic acceleration is then merely, as in Example 9, the

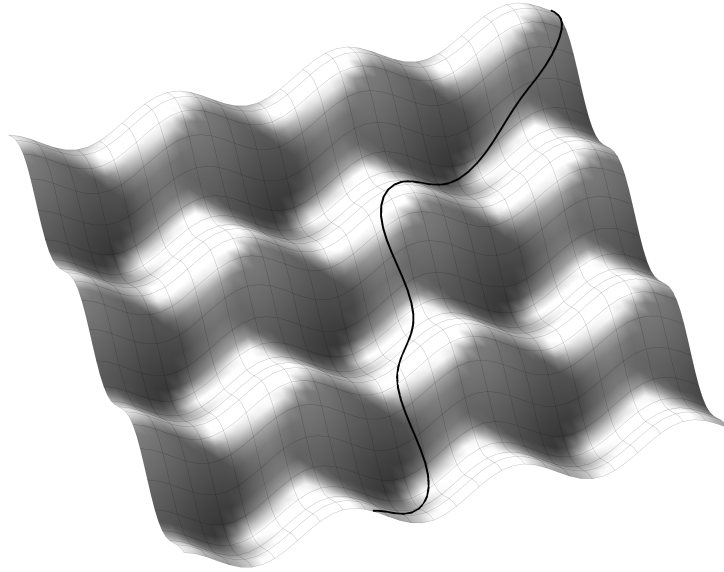


**Figure 3.3:** A geodesic curve on the manifold defined by the parameterization  $\sin x + \sin y$

second derivative of the parameterization. Since the intrinsic acceleration (the tangential part) is zero for geodesics, the extrinsic acceleration vector is an element of the normal space. Therefore, all forces experienced in this roller coaster scenario solely arise from keeping the passenger on the track, and these forces always act perpendicular to the current tangent of the track.

**EXAMPLE 11** (Two curved shells with string inside). Consider two doubly-curved shells of the same shape (e.g., hyperbolic paraboloids or large Pringles chips) as shown in Fig. 3.4. For example, they could be of the shape of Fig. 3.3. The experiment neglects gravity and friction and is assumed to be static. The string is fixed on both sides and under tension. It is constrained between the two shells, which move toward each other. In the unconstrained area, the string follows a straight line, analogous to a geodesic line in three-dimensional space. However, in the constrained region, the string's course deviates from a straight line, since forces act on the string. Especially, only normal contact forces from the shells act on the string, leading it to undergo a tangential shift when the shells are pressed together, minimizing its length until the shells touch. Therefore, the string slides on the surface, due to the action of the forces coming from the prestress and the contact forces, to minimize its strain energy. In this state, the string behaves as a geodesic curve, with only normal forces acting on it. The direction to further shorten the string is hindered by the shells, resulting in the string following a geodesic line from the shells' perspective. This mechanical interpretation aligns with the definition of geodesic curves,

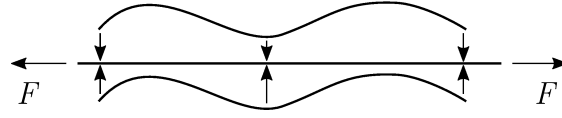


**Figure 3.4:** Prestressed string clamped between two shells.

which involve only normal accelerations. Thus, we obtain a mechanical understanding of geodesic lines.

### 3.4 Riemannian Exponential Map

The Riemannian exponential map can be derived from the notion of geodesics, but it has a different motivation. Eq. (3.17) gives a geodesic curve for a given tangent vector at an initial point. Thus, Eq. (3.17) defines a mapping

$$\gamma : \begin{cases} \mathbb{R} \rightarrow \mathcal{M}, \\ t \mapsto \gamma(t; \mathbf{x}, \boldsymbol{\xi}), \end{cases} \quad \boldsymbol{\xi} \in T_{\mathbf{x}}\mathcal{M}. \quad (3.18)$$

The Riemannian exponential map is the answer to the following question: If a tangent vector  $\mathbf{v}$  is given at position  $\mathbf{x}$ , where do we end up after walking  $\|\mathbf{v}\|$  along the induced geodesic? This is given by solving Eq. (3.17) for  $t = 1$  or evaluating Eq. (3.18) at  $t = 1$ . The Riemannian exponential map needs a point  $\mathbf{x} \in \mathcal{M}$  and a direction  $\boldsymbol{\xi} \in T\mathcal{M}$  and formally, it is a mapping

$$\text{Exp} : \begin{cases} T\mathcal{M} \rightarrow \mathcal{M}, \\ \boldsymbol{\xi} \mapsto \text{Exp}_{\mathbf{x}} \boldsymbol{\xi} = \gamma(1; \mathbf{x}, \boldsymbol{\xi}), \end{cases} \quad (3.19)$$

where also the identity  $\gamma(1; \mathbf{x}, \boldsymbol{\xi}) = \gamma(\|\boldsymbol{\xi}\|_{\mathbf{x}}; \mathbf{x}, \boldsymbol{\xi}/\|\boldsymbol{\xi}\|_{\mathbf{x}})$  holds, see do Carmo [dC92]. This kind of mapping sends tangent vectors at some point back onto the manifold, similar to retractions introduced in Section 2.6 on page 33. From Definition 14 on page 34 it can be seen that the exponential map is a retraction, since  $\gamma(0; \mathbf{x}, \boldsymbol{\xi}) = \mathbf{x}$  and  $\frac{\partial \gamma(t; \mathbf{x}, \boldsymbol{\xi})}{\partial t} \Big|_{t=0} = \boldsymbol{\xi}$ . The Riemannian exponential map is a canonical retraction, it allows a characterization of retractions, namely how similar a given retraction is to the exponential map.

A retraction  $\mathbf{R}_{\mathbf{x}}$  is called a *second-order retraction*, if it fulfills

$$\left. \frac{D}{dt^2} \mathbf{R}_{\mathbf{x}}(t\boldsymbol{\xi}) \right|_{t=0} = 0. \quad (3.20)$$



This simply means that the initial (covariant) acceleration is zero as in the case of a geodesic curve and equivalently for the Riemannian exponential map. Thus,  $\frac{D}{dt^2}(\gamma)$  indicates the second derivative in a covariant sense, i.e.,  $\frac{D}{dt^2}(\gamma) = \nabla_{\dot{\gamma}}\dot{\gamma}$ . A geodesic curve fulfills this for all  $t$  but a second-order retraction only at  $t = 0$ . If a retraction fails to fulfill Eq. (3.20) but satisfies Definition 14, it is simply called retraction or to emphasize the difference to a second-order retraction, it can be called a *first-order retraction*.

For the unit sphere  $\mathcal{S}^2$  the exponential map is given by

$$\exp_{\mathbf{x}}(\Delta\mathbf{x}) = \cos(\|\Delta\mathbf{x}\|)\mathbf{x} + \frac{\sin(\|\Delta\mathbf{x}\|)}{\|\Delta\mathbf{x}\|}\Delta\mathbf{x}. \quad (3.21)$$

The closest point projection always provides a second-order retraction, see Boumal [Bou23], i.e., the closest point projection on the unit sphere, namely the *radial return normalization* given by  $\mathbf{R}_{\mathbf{x}}(\boldsymbol{\eta}) = \frac{\mathbf{x}+\boldsymbol{\eta}}{\|\mathbf{x}+\boldsymbol{\eta}\|}$  in Eq. (2.57) on page 34, is a second-order retraction.

## 3.5 Riemannian Hessian

The notion of change of vector fields on manifolds was captured by the covariant derivative and parallel transport Section 3.2 or, more generally by an affine connection as defined in Section 3.1. Nevertheless, for optimization algorithms, i.e., Newton-type algorithms, it is of further interest to have a convenient notion of the second-order information of a cost function, which indicates first-order derivatives of the Riemannian gradient of Section 2.7.3.<sup>2</sup> This is done by the generalization of a Hessian of an Euclidean cost function, namely the Riemannian Hessian.

**Definition 20.** Let  $f : \mathcal{M} \rightarrow \mathbb{R}$  be a function defined on a manifold  $(\mathcal{M}, g)$  with its Riemannian connection  $\nabla$ . The *Riemannian Hessian* is the mapping  $\text{Hess } f(\mathbf{x}) : T_{\mathbf{x}}\mathcal{M} \rightarrow T_{\mathbf{x}}\mathcal{M}$  given by

$$\text{Hess } f(\mathbf{x})[\boldsymbol{\xi}_{\mathbf{x}}] = \nabla_{\boldsymbol{\xi}_{\mathbf{x}}} \text{grad } f(\mathbf{x}). \quad (3.22)$$

Due to its importance in later derivations, several representations of this Riemannian Hessian are shown. In contrast to the Riemannian gradient of Section 2.7.3 on page 38, the concept of the Riemannian Hessian is not a standard topic in differential geometry.

<sup>2</sup>The given derivation also applies, if a root of a tangent vector field is of interest and no cost function is given. Then, the Riemannian Hessian is simply the Riemannian Jacobian of a vector field but the following derivations are practically analogous.

There are some results in [Abs08; ONe83]. Often it is defined via iterated covariant differentiation

$$\nabla_{\xi} \nabla_{\eta} f(\mathbf{x}) = \nabla^2 f(\mathbf{x})[\xi, \eta] + \nabla_{\nabla_{\xi} \eta} f(\mathbf{x}), \quad (3.23)$$

where on the right-hand side the first term is identified as Riemannian Hessian. Here,  $[\xi, \eta]$  is not the Lie bracket but simply the two arguments of the function. This yields by rearranging the terms,

$$\langle \text{Hess } f(\mathbf{x})[\xi], \eta \rangle_{\mathbf{x}} = \nabla_{\xi} \nabla_{\eta} f - \nabla_{\nabla_{\xi} \eta} f. \quad (3.24)$$

For some vector fields  $\xi, \eta \in \mathfrak{X}(\mathcal{M})$ . The definition in Eq. (3.22) requires  $\xi$  only at a specific  $\mathbf{x}$ , namely  $\xi_{\mathbf{x}}$  as a tangent vector, i.e., an element of  $T_{\mathbf{x}}\mathcal{M}$  but Eq. (3.24) needs it as a vector field or as an element of the tangent bundle  $T\mathcal{M}$ . For reference, see also [ONe83, Definition 48; Abs08, Proposition 5.5.2].

For completeness, the Riemannian Hessian is defined in coordinates. Consider a parameterization  $\varphi : \mathbb{R}^n \rightarrow \mathcal{M}$  and the corresponding coordinate basis  $\{\mathbf{g}_i\}$  as given by Eq. (2.16) on page 22 with curvilinear coordinates  $\theta^i$ . Furthermore, consider the corresponding transformed function  $\hat{f} = f \circ \varphi$ . Then, the components of the Riemannian Hessian defined via Eq. (3.22), using the covariant derivative of Eq. (3.5) of the Riemannian gradient defined in Eq. (2.75) on page 39, reads

$$\begin{aligned} \widetilde{\text{Hess } f(\boldsymbol{\theta})}^k{}_i &= \left( \frac{\partial(\widetilde{\text{grad } f})^k}{\partial \theta^i} + (\widetilde{\text{grad } f})^j \Gamma_{ij}^k \right) \\ &= \left( \frac{\partial^2 \tilde{f}}{\partial \theta^i \partial \theta^m} g^{km} + g^{jn} \frac{\partial \tilde{f}}{\partial \theta^n} \Gamma_{ij}^k \right), \end{aligned} \quad (3.25)$$

where the Levi-Civita connection property, being invariant w.r.t. the metric was used, see Definition 18 on page 54. This means in this case  $\nabla_k g_{ij} = 0$ . This definition yields a (1,1)-tensor as Riemannian Hessian. For the reader who is familiar with differential geometry, this definition may seem unfamiliar.

In literature, often a (0,2)-tensor is defined as

$$\begin{aligned} \widetilde{\text{Hess } f(\boldsymbol{\theta})}_{li} &= \widetilde{\text{Hess } f(\boldsymbol{\theta})}^k{}_i g_{kl} = \left( \frac{\partial^2 \tilde{f}}{\partial \theta^i \partial \theta^m} g^{km} + g^{jn} \frac{\partial \tilde{f}}{\partial \theta^n} \Gamma_{ij}^k \right) g_{kl} \\ &= \left( \frac{\partial^2 \tilde{f}}{\partial \theta^i \partial \theta^l} - \Gamma_{li}^n \frac{\partial \tilde{f}}{\partial \theta^n} \right), \end{aligned} \quad (3.26)$$

where the transformation rule of the Christoffel symbols  $g^{jn} \Gamma_{ij}^k g_{kl} = -\Gamma_{li}^n$  was used, which is derived in Appendix A.1. The (0,2)-tensor has some drawbacks, as mentioned

in [Abs08, Sec. 5.7], i.e., the  $(0, 2)$ -tensor via a congruent transformation<sup>3</sup>, which does not preserve eigenvalues, making it dependent on the chosen chart. In contrast to this, the definition as a  $(1, 1)$ -tensor yields transforms via a similarity transformation<sup>4</sup>, which preserves eigenvalues. Thus, they do not depend on the chosen chart. Hence, the work at hand follows do Carmo [dC92] and Absil et al. [Abs08] by choosing the  $(1, 1)$ -tensor as the better definition of the Riemannian Hessian.

Furthermore, the symmetry property of the Riemannian Hessian is discussed here, since it will be needed to examine the correct tangent operator in Section 6.2. Here, the first part of Eq. (3.26) is the second partial derivative, which is automatically symmetric due to the Schwarz theorem. In contrast to this, the symmetry of the second part depends on the symmetry of the Christoffel symbols  $\Gamma^n_{li}$ . For an arbitrary affine connection, they are in general not symmetric. They are only symmetric for a *torsion-free* affine connection, where the coefficients are defined in a coordinate (holonomic) basis. This constraint is satisfied by the Levi-Civita connection. Thus, this symmetry yields a self-adjoint Riemannian Hessian, i.e.,

$$\begin{aligned} \text{Hess } f(\mathbf{x})[\boldsymbol{\xi}_x, \boldsymbol{\eta}_x] &= \langle \nabla_{\boldsymbol{\xi}_x} \text{grad } f(\mathbf{x}), \boldsymbol{\eta}_x \rangle_x = \langle \nabla_{\boldsymbol{\eta}_x} \text{grad } f(\mathbf{x}), \boldsymbol{\xi}_x \rangle_x \\ &= \text{Hess } f(\mathbf{x})[\boldsymbol{\eta}_x, \boldsymbol{\xi}_x]. \end{aligned} \quad (3.27)$$

For symmetry or self-adjointness of the Riemannian Hessian, the reader is referred to [Abs08; Mis73; Rom05; MS95; Sim92a; RA17; Ste15].

In Euclidean spaces, e.g.  $\mathbb{R}^n$ , with the usual metric, the Riemannian Hessian boils down to

$$\text{Hess } f(\mathbf{x}) = \begin{bmatrix} \frac{\partial^2 f}{\partial x^1 \partial x^1} & \cdots & \frac{\partial^2 f}{\partial x^n \partial x^1} \\ \vdots & \ddots & \vdots \\ \frac{\partial^2 f}{\partial x^1 \partial x^n} & \cdots & \frac{\partial^2 f}{\partial x^n \partial x^n} \end{bmatrix} \mathbf{E}^i \otimes \mathbf{E}^j, \quad (3.28)$$

where a distinction between  $(1, 1)$ -tensor and  $(0, 2)$ -tensor is trivial.

### Riemannian Submanifolds

If the manifold at hand is embedded, there is a convenient way to construct the Riemannian Hessian. In particular, even using the  $(1, 1)$ -tensor definition of the Riemannian Hessian in Eq. (3.26) does not provide a convenient way to construct the Hessian. It needs the introduction of local coordinates, and the explicit calculation of the Christoffel symbols of the connection, and it suffers from potential singularities of the parameterization. For example, in the case of the unit sphere  $\mathcal{S}^2$  a parameterization has necessarily singularities

<sup>3</sup>A congruent transformation of a matrix is  $\mathbf{A} \mapsto \mathbf{P}^T \mathbf{A} \mathbf{P}$ .

<sup>4</sup>A similarity transformation of a matrix is  $\mathbf{A} \mapsto \mathbf{P}^{-1} \mathbf{A} \mathbf{P}$ .

as discussed in Section 6.3. Therefore, as in the case of the Riemannian gradient in Eq. (2.83), there is also a convenient way to derive the Riemannian Hessian by using Euclidean derivatives and projection into the tangent space. This is elaborated in Absil et al. [Abs13] and Boumal [Bou23, Ch. 5.11]. Since the Hessian includes curvature information, it seems natural that the derivative of the projection is needed. The projection  $\mathbf{P}_x : \mathcal{E} \rightarrow T_x\mathcal{M}$  onto the tangent space from the embedding space is the same as given in Eq. (2.79). Consider the projection defined as  $\mathbf{P}(\mathbf{x}, \mathbf{v}) : \mathcal{M} \times \mathcal{E} \rightarrow T_x\mathcal{M}$ , such that  $\mathbf{P}(\mathbf{x}, \mathbf{v}) = \mathbf{P}_x(\mathbf{v})$ . Then the derivative w.r.t. the first slot encodes how the tangent space varies (bends) in its embedding space. This derivative is denoted by

$$\mathcal{P}_u^x : \begin{cases} \mathcal{E} \rightarrow \mathcal{E} \\ \mathbf{v} \mapsto \mathcal{P}_u^x(\mathbf{v}) = D_u\mathbf{P}(\mathbf{x}, \mathbf{v}). \end{cases} \quad (3.29)$$

Due to its definition of taking vectors in the embedding space  $\mathcal{E}$  as derivative directions, it also returns a vector living in the embedding space. If the directions are taken from the tangent space or the normal space, the following notation is common.

**Definition 21.** The *second fundamental form* of a manifold  $\mathcal{M}$  at a point  $\mathbf{x}$  is given by

$$\mathbb{I}^x : \begin{cases} T_x\mathcal{M} \times T_x\mathcal{M} \rightarrow N_x\mathcal{M}, \\ (\mathbf{u}, \mathbf{v}) \mapsto \mathbb{I}^x(\mathbf{u}, \mathbf{v}) = \mathcal{P}_u^x(\mathbf{v}). \end{cases} \quad (3.30)$$

Similarly, the *Weingarten map* of a manifold  $\mathcal{M}$  at point  $\mathbf{x}$  is given by

$$\mathcal{W}^x : \begin{cases} T_x\mathcal{M} \times N_x\mathcal{M} \rightarrow T_x\mathcal{M}, \\ (\mathbf{u}, \mathbf{n}) \mapsto \mathcal{W}^x(\mathbf{u}, \mathbf{n}) = \mathcal{P}_u^x(\mathbf{n}), \end{cases} \quad (3.31)$$

where  $\mathbf{n}$  is a normal vector to  $\mathcal{M}$  at  $\mathbf{x}$ . Thus, the Weingarten map is the directional derivative of the normal vector field. It is also sometimes called the *shape operator*.

Since a vector in the embedding space can always be decomposed into a normal and a tangent part, the object  $\mathcal{P}_u^x$  can also be decomposed as

$$\mathcal{P}_u^x(\mathbf{v}) = \mathbb{I}^x(\mathbf{u}, \mathbf{P}_x^\perp(\mathbf{v})) + \mathcal{W}^x(\mathbf{u}, \mathbf{P}_x(\mathbf{v})) \quad (3.32)$$

### Riemannian Connection on Riemannian Submanifolds

Let  $\mathcal{M}$  be an embedded submanifold of  $\overline{\mathcal{M}}$ . The Riemannian connection  $\nabla$  of  $\mathcal{M}$  can be defined using the connection  $\bar{\nabla}$  of  $\overline{\mathcal{M}}$  [Abs08, Ch. 5.3.3]. The relation is given by

$$\nabla_{\eta_x} \xi = \mathbf{P}_x \bar{\nabla}_{\bar{\eta}_x} \bar{\xi}, \quad (3.33)$$

with  $\boldsymbol{\xi} \in \mathfrak{X}(\mathcal{M})$  and  $\boldsymbol{\eta} \in T_{\mathbf{x}}\mathcal{M}$  and for the embedding space we have  $\bar{\boldsymbol{\xi}} \in \mathfrak{X}(\overline{\mathcal{M}})$  and  $\bar{\boldsymbol{\eta}} \in T_{\mathbf{x}}\overline{\mathcal{M}}$ . If the embedding space is a vector space, the connection boils down to the usual derivative, and this results in

$$\nabla_{\boldsymbol{\eta}_{\mathbf{x}}}\boldsymbol{\xi} = \mathbf{P}_{\mathbf{x}}D_{\bar{\boldsymbol{\eta}}_{\mathbf{x}}}\bar{\boldsymbol{\xi}}. \quad (3.34)$$

Plugging in the Riemannian Hessian from Definition 20 yields

$$\text{Hess } f(\mathbf{x})[\boldsymbol{\eta}_{\mathbf{x}}] = \nabla_{\boldsymbol{\eta}_{\mathbf{x}}}\overline{\text{grad } f(\mathbf{x})} = \mathbf{P}_{\mathbf{x}}D_{\bar{\boldsymbol{\eta}}_{\mathbf{x}}}\text{grad } f(\mathbf{x}) \quad (3.35)$$

The quantity  $\overline{\text{grad } f(\mathbf{x})}$  is the extension of the Riemannian gradient  $\text{grad } f(\mathbf{x})$  into the embedding space. Substituting the projection formula of the Riemannian gradient from Eq. (2.83) on page 40, in Eq. (3.35) can be stated as

$$\begin{aligned} \text{Hess } f(\mathbf{x})[\boldsymbol{\eta}_{\mathbf{x}}] &= \mathbf{P}_{\mathbf{x}}D_{\bar{\boldsymbol{\eta}}_{\mathbf{x}}}\overline{\text{grad } f(\mathbf{x})} \\ &= \mathbf{P}_{\mathbf{x}}D_{\bar{\boldsymbol{\eta}}_{\mathbf{x}}}(\mathbf{P}_{\mathbf{x}}\text{grad } \bar{f}(\mathbf{x})) \\ &= \mathbf{P}_{\mathbf{x}}D_{\bar{\boldsymbol{\eta}}_{\mathbf{x}}}\mathbf{P}_{\mathbf{x}}\text{grad } \bar{f}(\mathbf{x}) + \mathbf{P}_{\mathbf{x}}\mathbf{P}_{\mathbf{x}}(D_{\bar{\boldsymbol{\eta}}_{\mathbf{x}}}\text{grad } \bar{f}(\mathbf{x})) \\ &= \mathbf{P}_{\mathbf{x}}D_{\bar{\boldsymbol{\eta}}_{\mathbf{x}}}\mathbf{P}_{\mathbf{x}}\text{grad } \bar{f}(\mathbf{x}) + \mathbf{P}_{\mathbf{x}}(\text{Hess } \bar{f}(\mathbf{x})[\boldsymbol{\eta}_{\mathbf{x}}]). \end{aligned} \quad (3.36)$$

In the last equation, the property of projectors, namely  $\mathbf{P}_{\mathbf{x}}\mathbf{P}_{\mathbf{x}} = \mathbf{P}_{\mathbf{x}}$ , was used. Thus, similar to the Riemannian gradient, the Riemannian Hessian can be constructed from a simple derivative in a vector space and correct the result. So, the Riemannian Hessian can be written in terms of four quantities: (i) the projection  $\mathbf{P}_{\mathbf{x}}$  from the embedding space onto the tangent space of the submanifold, (ii) the directional derivative of  $\mathbf{P}_{\mathbf{x}}$ , (iii) the gradient  $\text{grad } \bar{f}$  and (iv) the Hessian  $\text{Hess } \bar{f}$  of the Euclidean extension of the functional, respectively.

In Absil et al. [Abs13] and Boumal [Bou23, Ch. 5.11] the quantity  $\mathbf{P}_{\mathbf{x}}D_{\bar{\boldsymbol{\eta}}_{\mathbf{x}}}\mathbf{P}_{\mathbf{x}}$  was derived as being related to the Weingarten map defined in Definition 21. Thus, the final (convenient) representation of the Riemannian Hessian seen from the embedding space is

$$\text{Hess } f(\mathbf{x})[\boldsymbol{\eta}_{\mathbf{x}}] = \mathcal{W}^{\mathbf{x}}(\boldsymbol{\eta}_{\mathbf{x}}, \mathbf{P}_{\mathbf{x}}^{\perp}(\text{grad } \bar{f}(\mathbf{x}))) + \mathbf{P}_{\mathbf{x}}(\text{Hess } \bar{f}(\mathbf{x})[\boldsymbol{\eta}_{\mathbf{x}}]). \quad (3.37)$$

Thus, the Riemannian Hessian can be constructed with the projected embedded Hessian and the change of the normal part of the embedded gradient which encodes the curvature information of the manifold  $\mathcal{M}$ .

**EXAMPLE 12** (Unit sphere  $\mathcal{S}^n$ ). For the  $n$ -dimensional unit sphere  $\mathcal{S}^n$  the Weingarten map can be calculated explicitly. The Weingarten map from Eq. (3.31) is then for the

embedded unit sphere

$$\mathcal{W}^{\mathbf{x}}(\mathbf{u}, \mathbf{n}) = -\mathbf{u}(\mathbf{x} \cdot \mathbf{n}), \quad (3.38)$$

where  $\mathbf{n}$  is an arbitrary normal vector field.

For the usage of the Riemannian Hessian in Eq. (3.37), this boils down to

$$\mathcal{W}(\boldsymbol{\eta}_{\mathbf{x}}, \mathbf{P}_{\mathbf{x}}^{\perp}(\text{grad } \bar{f}(\mathbf{x}))) = -\boldsymbol{\eta}_{\mathbf{x}}(\mathbf{x} \cdot \text{grad } \bar{f}(\mathbf{x})), \quad (3.39)$$

---

where applying  $\mathbf{P}_{\mathbf{x}}^{\perp}$  is redundant, since the dot product with  $\boldsymbol{\eta}_{\mathbf{x}}$  already projects onto the normal space.

Later, in the finite element solution scheme  $\mathcal{M}$  is the product manifold of nodal position vectors and nodal directors  $(\mathbb{R}^3 \times \mathcal{S}^2)^n$ . In Eq. (3.37), it is tempting to directly neglect the gradient part. This is a bad idea for the following reason: the normal part of the embedded gradient does not vanish at the optimum, since, by definition, only the norm of the Riemannian gradient vanishes, which is only the tangential part. This results in more iterations, e.g., in a method of Newton-type, see Müller and Bischoff [MB22] for details. Consequently, even at equilibrium, where the (tangential) Riemannian gradient vanishes, the eigenvalues depend on this term, making it crucial for stability analysis. Even where the relative contribution is small, for the example of the Reissner-Mindlin shell with  $(\mathbb{R}^3 \times \mathcal{S}^2)^n$ , the needed iterations differ substantially. The significance of this part is elaborated on in Müller and Bischoff [MB22, Sec. 10.2.2. and Appendix 8].

# 4

---

## Foundations of Finite Elasticity

This chapter deals with the fundamentals of finite elasticity for continua, which is the point of departure for the structural models discussed later. First, the kinematic equations are stated, then the notion of traction and stress is presented, and then balance principles are discussed. Constitutive theory and objectivity are also briefly introduced. Basic textbooks like Marsden and Hughes [MH94], Truesdell and Noll [TN04], Truesdell and Toupin [TT60], Ogden [Ogd97], Holzapfel [Hol02], and Misner et al. [Mis73] are used as the basis for this chapter. Thus, together with Chapters 2 and 3 several objects of continuum mechanics are stated in a precise geometric way.

### 4.1 Kinematics

In the sense of a phenomenological mathematical description, we define a body  $B$ , by a set of points  $P \in B$ . These points  $P$  are the *particles* of the body, which are in a one-to-one relation to a domain  $\mathcal{B} \subset \mathbb{R}^3$ .

#### 4.1.1 Configuration, Motion and Deformation

A *configuration* of a body  $B$  is given by the bijective mapping

$$\Phi : \begin{cases} B \rightarrow \mathcal{B} \subset \mathbb{R}^3, \\ P \mapsto \Phi(P), \end{cases} \quad (4.1)$$

which is an embedding of the body  $B$ . A configuration describes one particular state of the body. Since the body is allowed to move, we obtain a family of configurations, depending on the time  $t$ . A *motion* of a body  $B$  is given by the bijective mapping

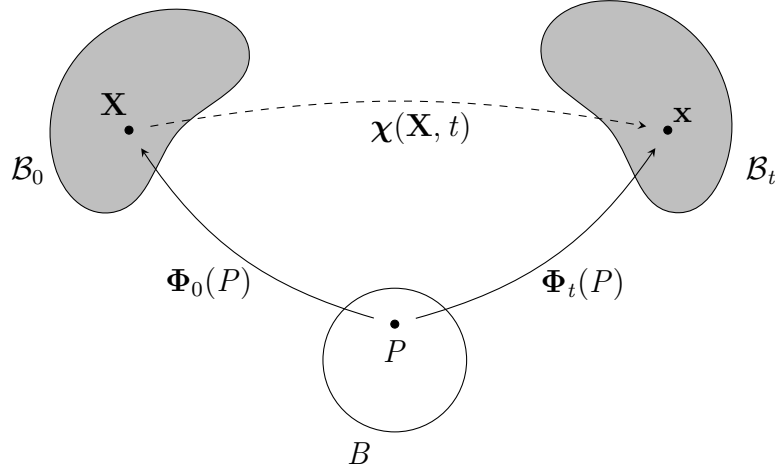


**Figure 4.1:** Motion, configuration and deformation of a body  $\mathcal{B}$ .

$$\Phi : \begin{cases} B \times T \rightarrow \mathcal{B}_t \subset \mathbb{R}^3, \\ (P, t) \mapsto \Phi(P, t) = \Phi_t(P). \end{cases} \quad (4.2)$$

This is also called the *material description* of the motion since the particle  $P$  is inserted and the placement w.r.t. time is returned. Often, a special configuration is picked, which is called *reference configuration*. This configuration has certain properties such as a known stress state or a homogeneous temperature. This configuration is described by the following mapping

$$\Phi_0 : \begin{cases} B \rightarrow \mathcal{B}_0 \subset \mathbb{R}^3, \\ P \mapsto \Phi(P, 0) = \Phi_0(P) = \mathbf{X}, \end{cases} \quad (4.3)$$

where  $\mathbf{X}$  is the reference position of the particle  $P$ . We assume that  $\Phi_0^{-1}(\mathbf{X})$  exists and is smooth. The relation between the reference configuration and the current configuration is given by the *deformation map*

$$\chi : \begin{cases} \mathcal{B} \times T \rightarrow \mathcal{B}_t \subset \mathbb{R}^3, \\ \mathbf{X} \mapsto \Phi_t \circ \Phi_0^{-1}(\mathbf{X}) = \chi(\mathbf{X}, t), \end{cases} \quad (4.4)$$

or simply *deformation*. These three mappings are illustrated in Fig. 4.1. This deformation is assumed to be a bijective mapping and sufficiently smooth. The notation  $\chi_{\mathbf{X}}$  refers to a path of the particle at  $\mathbf{X}$  and  $\chi_t$  refers to the configuration at a fixed time  $t$ .

With an abuse of notation, it is common to also use  $\mathbf{X}$  for the parameterization of  $\mathcal{B}_0$ . Similarly, the *current configuration* of the body is denoted by  $\Phi_t(B)$ , and the parameterization and current position of the particle  $P$  is denoted by  $\mathbf{x}$  of  $\mathcal{B}_t$ . Formally, the



parameterizations of the reference configuration and current configuration are given by

$$\mathbf{X} : \begin{cases} B \rightarrow \mathcal{B}_0 \subset \mathbb{R}^3, \\ \Theta \mapsto \Phi_0(P) = X^I(\Theta)\mathbf{E}_I, \end{cases} \quad \mathbf{x} : \begin{cases} B \rightarrow \mathcal{B}_t \subset \mathbb{R}^3, \\ \theta \mapsto \Phi_t(P) = x^i(\theta)\mathbf{e}_i, \end{cases} \quad (4.5)$$

where  $\Theta = \Theta^I \hat{\mathbf{E}}_I$  and  $\theta = \theta^i \hat{\mathbf{e}}_i$  are the curvilinear coordinates of the particle  $P$  in the reference and current configuration. The notion of (co-)tangent spaces and (co-)tangent bundles of Sections 2.4.3 and 2.4.4 on pages 23 and 25 is also employed here. Tensor fields that are defined on the tangent bundle  $T\mathcal{B}_t$  are called *Eulerian* or *spatial* tensors. Tensor fields defined on tangent bundle  $T\mathcal{B}_0$  are called *Lagrangian* or *material* tensors. The same holds for cotangent tensor fields living on  $T^*\mathcal{B}_0$  or  $T^*\mathcal{B}_t$ . For indices related to the reference configuration, capital Latin letters are employed, whereas small Latin letters are used for the current configuration. Similar to Eqs. (2.15) and (2.16) on page 22 these curvilinear coordinates induce a coordinate basis.

This basis consists of the following tangent vectors

$$\mathbf{G}_I = \frac{\partial X^J(\Theta)}{\partial \Theta^I} \mathbf{E}_J \quad \text{and} \quad \mathbf{g}_i = \frac{\partial x^j(\theta)}{\partial \theta^i} \mathbf{e}_j. \quad (4.6)$$

They can also be used to equip the manifolds  $\mathcal{B}_0$  and  $\mathcal{B}_t$  with a Riemannian metric, as defined in Section 2.7.1 on page 35. The metric tensors are

$$\begin{aligned} \mathbf{G} &= (\mathbf{G}_I \cdot \mathbf{G}_J) \mathbf{G}^I \otimes \mathbf{G}^J = G_{IJ} \mathbf{G}^I \otimes \mathbf{G}^J \\ \mathbf{g} &= (\mathbf{g}_i \cdot \mathbf{g}_j) \mathbf{g}^i \otimes \mathbf{g}^j = g_{ij} \mathbf{g}^i \otimes \mathbf{g}^j. \end{aligned} \quad (4.7)$$

Their inverses read

$$\mathbf{G}^{-1} = G^{IJ} \mathbf{G}_I \otimes \mathbf{G}_J \quad \text{and} \quad \mathbf{g}^{-1} = g^{ij} \mathbf{g}_i \otimes \mathbf{g}_j. \quad (4.8)$$

These are also identified by  $\mathbf{g} = \mathbf{g}^b$ ,  $\mathbf{g}^{-1} = \mathbf{g}^\sharp$ ,  $\mathbf{G} = \mathbf{G}^b$  and  $\mathbf{G}^{-1} = \mathbf{G}^\sharp$ . The contravariant bases are denoted by  $\{\mathbf{G}^I\}$  and  $\{\mathbf{g}^i\}$ , respectively. The following Jacobians are introduced, which contain the given base vectors

$$\begin{aligned} \mathbf{J} &: \begin{cases} T_\Theta \mathcal{A} \rightarrow T_{\mathbf{x}} \mathcal{B}_0, \\ \Theta \mapsto \frac{\partial X^J}{\partial \Theta^I} \mathbf{E}_J \otimes \mathbf{E}^I = [\mathbf{G}_1, \mathbf{G}_2, \mathbf{G}_3], \end{cases} & \mathbf{j} &: \begin{cases} T_\theta \mathcal{A} \rightarrow T_{\mathbf{x}} \mathcal{B}_t, \\ \theta \mapsto \frac{\partial x^j}{\partial \theta^i} \mathbf{e}_j \otimes \mathbf{e}^i = [\mathbf{g}_1, \mathbf{g}_2, \mathbf{g}_3], \end{cases} \\ \mathbf{J}^{-T} &: \begin{cases} T_\Theta^* \mathcal{A} \rightarrow T_{\mathbf{x}}^* \mathcal{B}_0, \\ \Theta \mapsto \frac{\partial \Theta^I}{\partial X^I} \mathbf{E}_J \otimes \mathbf{E}^I = [\mathbf{G}^1, \mathbf{G}^2, \mathbf{G}^3], \end{cases} & \mathbf{j}^{-T} &: \begin{cases} T_\theta^* \mathcal{A} \rightarrow T_{\mathbf{x}}^* \mathcal{B}_t, \\ \theta \mapsto \frac{\partial \theta^i}{\partial x^i} \mathbf{e}_j \otimes \mathbf{e}^i = [\mathbf{g}^1, \mathbf{g}^2, \mathbf{g}^3]. \end{cases} \end{aligned} \quad (4.9)$$

The Jacobians  $\mathbf{J}$  and  $\mathbf{j}$  can also be referred as  $\nabla_{\Theta}\mathbf{X}(\Theta)$  and  $\nabla_{\theta}\mathbf{x}(\theta)$ , respectively. The metric tensors can also be stated using these quantities  $\mathbf{G} = \mathbf{J}^T \cdot \mathbf{J}$  and  $\mathbf{g} = \mathbf{j}^T \cdot \mathbf{j}$ , and similar for their inverses.

**Velocity and Acceleration** If the mapping from Eq. (4.4) is a  $C^1$ -motion, or a  $C^1$ -diffeomorphism between  $\mathcal{B}_0$  and  $\mathcal{B}_t$ , the material velocity  $\mathbf{V} : \mathcal{B}_0 \times T \rightarrow T_{\mathbf{x}}\mathcal{B}_t$  can be defined by

$$\mathbf{V}(\mathbf{X},t) = \frac{\partial \boldsymbol{\chi}(\mathbf{X},t)}{\partial t} = V^a(\mathbf{X},t)\mathbf{g}_a, \quad (4.10)$$

where the components  $V^a(\mathbf{X},t)$  of  $\mathbf{V}$  are living at the spatial position  $\mathbf{x} = \boldsymbol{\chi}(\mathbf{X},t)$ . Thus, despite the notation of an uppercase  $\mathbf{V}$ , it lives in the current configuration and is an element of  $T_{\mathbf{x}}\mathcal{B}_t$ . The material acceleration  $\mathbf{A} : \mathcal{B}_0 \times T \rightarrow T_{\mathbf{x}}\mathcal{B}_t$  can be defined by

$$\mathbf{A}(\mathbf{X},t) = \dot{\mathbf{V}}(\mathbf{X},t) = \left( \frac{\partial V^a(\mathbf{X},t)}{\partial t} + \gamma_{bc}^a(\boldsymbol{\chi}(\mathbf{X},t)) V^b V^c \right) \mathbf{g}_a, \quad (4.11)$$

where  $\gamma_{bc}^a(\boldsymbol{\chi}(\mathbf{X},t))$  are the Christoffel symbols of the current configuration, see Eq. (3.11). The spatial counterparts, namely spatial velocity  $\mathbf{v} = \mathbf{V} \circ \Phi^{-1}$  and spatial acceleration  $\mathbf{a} = \mathbf{A} \circ \boldsymbol{\chi}^{-1}$ , read

$$\begin{aligned} \mathbf{v}(\mathbf{x}(t),t) &= \mathbf{V}(\boldsymbol{\chi}^{-1}(\mathbf{x}(t)),t) = V^a(\boldsymbol{\chi}^{-1}(\mathbf{x}(t)),t) \mathbf{g}_a = v^a(\mathbf{x}(t),t) \mathbf{g}_a, \\ \mathbf{a}(\mathbf{x}(t),t) &= \dot{\mathbf{v}}(\mathbf{x}(t),t) = a^a(\mathbf{x}(t),t) \mathbf{g}_a = \frac{\partial v^a}{\partial t} + v^a|_b v^b, \end{aligned} \quad (4.12)$$

where the identity  $\mathbf{A}(\boldsymbol{\chi}^{-1}(\mathbf{x}(t)),t) = \dot{\mathbf{V}}(\boldsymbol{\chi}^{-1}(\mathbf{x}(t)),t) = \dot{\mathbf{v}}(\mathbf{x}(t),t)$  was used in the latter equation. Additionally, the shortcut of the coordinate expression of the covariant derivative  $v^a|_b$  is used, see Eq. (3.7) on page 53. Thus, a covariant derivative was identified, which yields  $\mathbf{a} = \dot{\mathbf{v}} = \partial \mathbf{v} / \partial t + \nabla_{\mathbf{v}} \mathbf{v}$  in coordinate-free representation. The quantity  $\dot{\mathbf{v}}$  is called *material time derivative* of  $\mathbf{v}$ .

The velocity  $\mathbf{V}$  answers the question: “Which spatial velocity does the particle at material position  $\mathbf{X}$  have at time  $t$ ?” On the other hand, the velocity  $\mathbf{v}$  answers the question: “Which spatial velocity does the particle at spatial position  $\mathbf{x}$  have at time  $t$ ?” The corresponding quantities defined in the reference configuration can be obtained by pulling back these vector fields with  $\boldsymbol{\chi}$ . This can be done by the inverse operation of the push-forward of vector fields defined in Eq. (2.43) on page 29. This yields the *convected velocity*

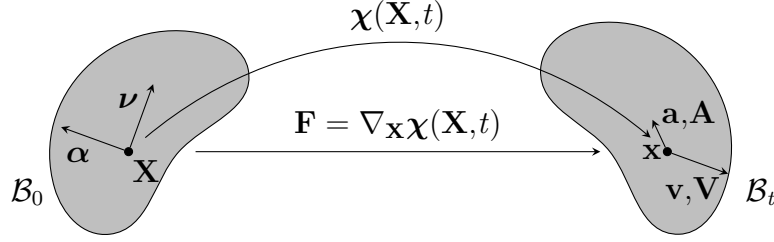


**Figure 4.2:** The spatial and material velocities and accelerations.

$\boldsymbol{\nu} = \boldsymbol{\chi}^*(\mathbf{v})$  and the *convected acceleration*  $\boldsymbol{\alpha} = \boldsymbol{\chi}^*(\mathbf{a})$  as

$$\begin{aligned}\boldsymbol{\nu}(\mathbf{X}, t) &= \left. \frac{\partial \chi^{-1}(\mathbf{x})^A}{\partial x^a} \right|_{\mathbf{x}=\boldsymbol{\chi}(\mathbf{X}, t)} v^a(\boldsymbol{\chi}(\mathbf{X}, t)) \mathbf{G}_A = \left. \frac{\partial \chi^{-1}(\mathbf{x})^A}{\partial x^a} \right|_{\mathbf{x}=\boldsymbol{\chi}(\mathbf{X}, t)} V^a(\mathbf{X}) \mathbf{G}_A = \mathbf{F}^{-1} \cdot \mathbf{V}, \\ \boldsymbol{\alpha}(\mathbf{X}, t) &= \mathbf{F}^{-1} \cdot \mathbf{A}.\end{aligned}\tag{4.13}$$

The tensor  $\mathbf{F}$  is the deformation gradient, which is defined next. For a visual interpretation of the given results, see Fig. 4.2. Therein, it becomes clear where which object lives. The convected velocity for example is a quantity living in the reference configuration and is, therefore, attached to the body on the left, where  $\mathbf{V}$  is attached to the current configuration, which is the body on the right-hand side.

### 4.1.2 Deformation Gradient

The deformation from Eq. (4.4) is a diffeomorphism between the reference and current configuration as in Definition 6 on page 17. It induces a push-forward operation between these two manifolds as in Section 2.5 on page 28. Since the body is embedded into  $\mathbb{R}^3$  this boils down to the simple statement

$$\boldsymbol{\chi}_*(\mathbf{G}_I) = \frac{d\Phi^i}{dX^J} \frac{\partial X^J}{\partial \Theta^I} \mathbf{e}_i = \frac{d\Phi^i}{dX^J} G_I^J \mathbf{e}_i,\tag{4.14}$$

where the notation is slightly abused, since here  $G_I^J$  denotes the  $J$ -th coordinates of the  $I$ -th base vector. This mapping also defines the Jacobian of the deformation  $\boldsymbol{\chi}$ , which is called the *deformation gradient*. It is defined as

$$\mathbf{F} = \frac{d\Phi^i}{dX^J} \mathbf{e}_i \otimes \mathbf{E}^J = F^i_j \mathbf{e}_i \otimes \mathbf{E}^j.\tag{4.15}$$

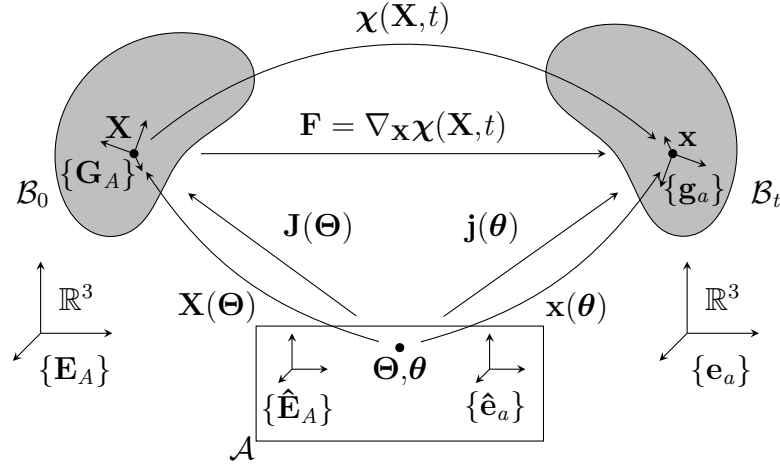


**Figure 4.3:** Motion, configuration and the coordinate frames for the parameter space  $\mathcal{A}$  as  $\{\hat{\mathbf{E}}_A\}, \{\hat{\mathbf{e}}_a\}$ , for the embedding space of  $\mathcal{B}_0$  as  $\mathbf{E}_A$ , for the embedding space of  $\mathcal{B}_t$  as  $\mathbf{e}_a$  and the coordinate bases for the point  $\mathbf{X} \in \mathcal{B}_0$  and  $\mathbf{x} \in \mathcal{B}_t$  as  $\{\mathbf{g}_a\}$  and  $\{\mathbf{G}_A\}$ , respectively. The linearized maps between the different coordinate systems are also shown.

The tensorial mapping is given by  $\mathbf{F} : T_{\mathbf{X}}\mathcal{B}_0 \rightarrow T_{\mathbf{x}}\mathcal{B}_t$ . By reviewing the definition of  $\chi$  in Eq. (4.4), a different view on the deformation gradient can be obtained. It reads

$$\mathbf{F} = \nabla_{\mathbf{x}}\chi = \frac{d\Phi^i}{dX^J} \mathbf{e}_i \otimes \mathbf{E}^J = \frac{\partial x^i}{\partial \theta^j} \frac{\partial \theta^j}{\partial \Theta^I} \frac{\partial \Theta^I}{\partial X^J} \mathbf{e}_i \otimes \mathbf{E}^J = \mathbf{j} \cdot \mathbf{T} \cdot \mathbf{J}^{-1}, \quad (4.16)$$

where  $\mathbf{T} = \frac{\partial \theta^j}{\partial \Theta^I} \hat{\mathbf{e}}_j \otimes \hat{\mathbf{E}}^I$  is the tensor responsible for the change of coordinates between  $\theta^i$  and  $\Theta^J$ . If the same coordinates are chosen, namely  $\theta^i = \Theta^i$  and  $\hat{\mathbf{e}}_i = \hat{\mathbf{E}}_i$ , then  $\mathbf{T}$  is the identify mapping. These relations are depicted in Fig. 4.3, where the interplay between reference configuration, current configuration, motion, and deformation is shown. Several bases are also shown, namely the two coordinate bases  $\{\mathbf{G}_A\}, \{\mathbf{g}_a\}$  for the embedding tangent space of  $T_{\mathbf{X}}\mathcal{B}_0$  and  $T_{\mathbf{x}}\mathcal{B}_t$ , respectively, the two bases  $\{\mathbf{E}_A\}, \{\mathbf{e}_a\}$  for the embedding space of  $\mathcal{B}_0$  and  $\mathcal{B}_t$ , and the two bases  $\{\hat{\mathbf{E}}_A\}, \{\hat{\mathbf{e}}_a\}$  for the parameter space  $\mathcal{A}$ . and the two bases  $\{\mathbf{E}_A\}, \{\mathbf{e}_a\}$  for the embedding space of  $\mathcal{B}_0$  and  $\mathcal{B}_t$ , respectively.

If both curvilinear coordinate systems coincide, it can be interpreted as a single coordinate system. This coordinate system is called *convective coordinate system*, since it follows the deformation. The deformation gradient then reads  $\mathbf{F} = \mathbf{j} \cdot \mathbf{J}^{-1}$ , which boils down to

$$\mathbf{F} = \delta^i_J \mathbf{g}_i \otimes \mathbf{G}^J. \quad (4.17)$$

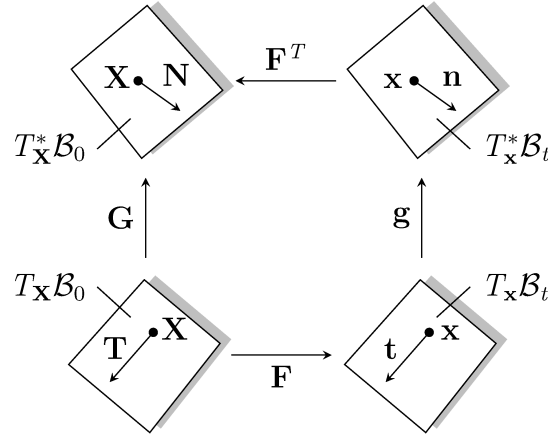


**Figure 4.4:** Commutative diagram between metric tensors and pull-back and push-forward of the deformation gradient.

This also simplifies the push-forward operation of Eq. (4.14), since we have now

$$\chi_*(\mathbf{G}_I) = \mathbf{F} \cdot \mathbf{G}_I = \delta^i_J \mathbf{g}_i(\mathbf{G}^J \cdot \mathbf{G}_I) = \delta^i_I \mathbf{g}_i. \quad (4.18)$$

In the convective coordinate system, a push-forward operation simply replaces the base vectors while leaving the components as is, except for changing their domain from  $\mathbf{X}$  to  $\mathbf{x} = \Phi(\mathbf{X}, t)$ . Similar results are obtained for the pull-back operation. This is not repeated here, since it is already covered in Section 2.5 on page 28. The metrics, push-forwards, and pull-backs via the deformation gradient are related in such a way that the diagram of Fig. 4.4 commutes as in Fig. 2.12 on page 37.

At the end of this section, mathematical nomenclature is introduced to characterize the deformation map in Eq. (4.4). Since the deformation map is assumed to be continuous and has a continuous inverse between the embedded reference and current configuration, it is a homeomorphism. Thus, no cracks are possible during the deformation. The deformation map is a homotopy<sup>1</sup>, since  $\chi$  maps continuously between  $\mathcal{B}_0$  and  $\mathcal{B}_t$ . Furthermore, since  $\mathcal{B}_0$  and  $\mathcal{B}_t$  are embeddings,  $\chi$  is an isotopy, which means that  $\mathcal{B}_0$  and  $\mathcal{B}_t$  can be connected through embeddings. This embedding requirement also precludes a local and global penetration of matter. In the numerical algorithms shown later, precluding the global penetration is not explicitly enforced, e.g., by some self-contact algorithms. Local penetration is usually precluded by an appropriate material law, which returns infinite

<sup>1</sup>A homotopy between two functions  $f, g$  is a continuous function  $h$  with  $t = [t_0, t_E]$ , such that  $h(t_0) = f$  and  $h(t_E) = g$ .

energy for such configurations. It can be stated via the requirement

$$\det \mathbf{F}(t) > 0, \quad (4.19)$$

which enforces invertibility.

### 4.1.3 Strain

The concept of strain can be introduced by the deformation gradient. It can be used to relate metrics of the current and reference configuration. As motivation, consider the Eulerian stretch of a Lagrangian vector. Let  $\mathbf{T} \in T_{\mathbf{x}}\mathcal{B}_0$  with  $\|\mathbf{T}\|_{\mathbf{G}} = 1$ . The pushed-forward quantity  $\boldsymbol{\lambda} \in T_{\mathbf{x}}\mathcal{B}_t$  is obtained via  $\boldsymbol{\lambda} = \boldsymbol{\chi}_*(\mathbf{T}) = \mathbf{F} \cdot \mathbf{T}$ . The deformed length can then be calculated as

$$\begin{aligned} \lambda &= \|\boldsymbol{\lambda}\|_{\mathbf{g}} = \sqrt{\langle \boldsymbol{\lambda}, \boldsymbol{\lambda} \rangle_{\mathbf{x}}} = \sqrt{\boldsymbol{\lambda} \cdot \mathbf{g} \cdot \boldsymbol{\lambda}} = \sqrt{(\mathbf{F} \cdot \mathbf{T}) \cdot \mathbf{g} \cdot (\mathbf{F} \cdot \mathbf{T})} \\ &= \sqrt{\mathbf{T} \cdot (\mathbf{F}^T \cdot \mathbf{g} \cdot \mathbf{F}) \cdot \mathbf{T}} = \sqrt{\mathbf{T} \cdot \mathbf{C} \cdot \mathbf{T}}. \end{aligned} \quad (4.20)$$

Based on this, the *right Cauchy-Green strain tensor*  $\mathbf{C}$  can be identified. It links the tangent space and cotangent space of the reference configuration in the sense, that it is the Eulerian metric  $\mathbf{g}$  in the reference configuration. This means it can also be used as a musical isomorphism to map vectors from tangent space to cotangent space and vice versa. Thus, it can also be defined by the pull-back of the Eulerian metric, which can be derived from generalizing Eq. (2.55) on page 33 as

$$\mathbf{C} = \boldsymbol{\chi}^*(\mathbf{g}) = \mathbf{F}^T \cdot \mathbf{g} \cdot \mathbf{F} \quad \text{or} \quad C_{AB} = \delta^a_A g_{ab} \delta^b_B, \quad (4.21)$$

where the right-hand side states the components in the convective coordinate basis  $\{\mathbf{G}_I\}$  and where the deformation gradient is taken from Eq. (4.17). The tensorial mapping is given by  $\mathbf{C} : T_{\mathbf{x}}\mathcal{B}_0 \rightarrow T_{\mathbf{x}}^*\mathcal{B}_0$ . In the reference basis  $\{\mathbf{E}_I\}$ , these components would read  $\tilde{C}_{AB} = F^a_A g_{ab} F^b_B$  with the deformation gradient defined as in Eq. (4.15).

Similar derivations can be performed for the *left Cauchy-Green strain tensor*, which can be obtained through the inverse pull-back operation. This operation differs from the push-forward operation, as it involves transporting covectors from the reference configuration to the current configuration. In this case, the inverse pull-back is needed. To maintain consistency, the inverse pull-back is denoted as  $\boldsymbol{\chi}_*$ , while the notation  $(\boldsymbol{\chi}^*)^{-1}$  is avoided to prevent confusion. Consequently, we define the left Cauchy-Green strain tensor as

$$\mathbf{c} = \boldsymbol{\chi}_*(\mathbf{G}) = \mathbf{F}^{-T} \cdot \mathbf{G} \cdot \mathbf{F}^{-1} \quad \text{or} \quad c_{ab} = \delta^A_a G_{AB} \delta^B_b, \quad (4.22)$$

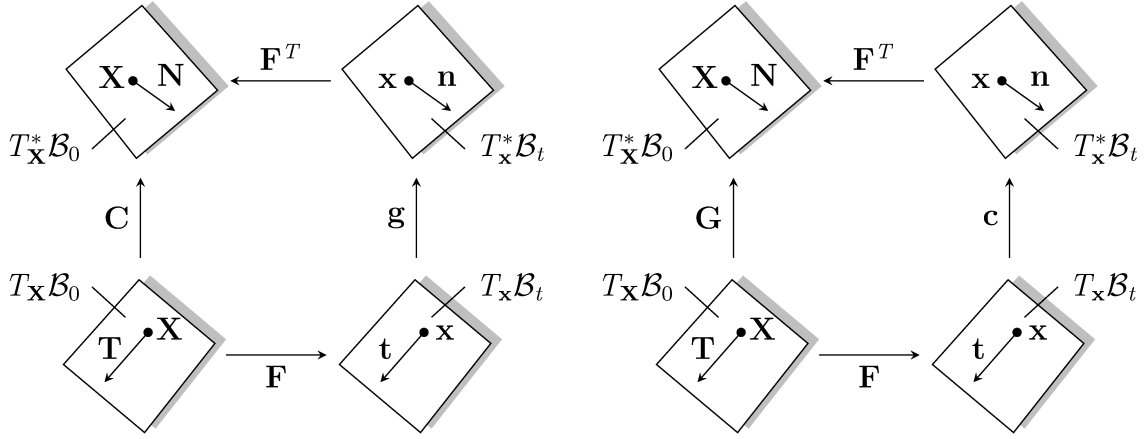


**Figure 4.5:** Commutative diagrams between metric tensors and pulled-back and pushed-forward metrics.

where the right-hand side states the components in the convective coordinate basis  $\{\mathbf{g}_I\}$ . The tensorial mapping is given by  $\mathbf{c} : T_x \mathcal{B}_t \rightarrow T_x^* \mathcal{B}_t$ . Again, in the spatial coordinate system  $\{\mathbf{e}_I\}$ , these components would read  $c_{ab} = (F^{-1})^A_a G_{AB} (F^{-1})^B_b$ . Thus, the left Cauchy-Green strain tensor is the Lagrangian metric viewed in the current configuration. Its inverse  $\mathbf{b} = \mathbf{c}^{-1}$  is often called the finger tensor after Finger [Fin94].<sup>2</sup>

Fig. 4.5 shows the mapping properties of the Cauchy-Green strain tensors. On the left-hand side, the right Cauchy-Green strain tensor is shown, which maps vectors from the tangent space of the reference configuration to the cotangent space of the reference configuration. Analogously, on the right-hand side, the left Cauchy-Green strain tensor is shown, which maps vectors from the tangent space of the current configuration to the cotangent space of the current configuration. The commutative diagrams show that the right Cauchy-Green strain tensor is the pull-back of the Eulerian metric, while the left Cauchy-Green strain tensor is the push-forward of the Lagrangian metric. The transformed metrics can not only be used to measure length but also to measure *change* of length and angles. This can be motivated by comparing the squared lengths of the tangent  $\mathbf{T} \in T_X \mathcal{B}_0$  and the pushed-forward  $\boldsymbol{\lambda} = \mathbf{F} \cdot \mathbf{T} \in T_x \mathcal{B}_t$  with  $\|\boldsymbol{\lambda}\|_{\mathbf{g}} = \lambda$ . Thus, the *Green* strain reads

$$\begin{aligned} \epsilon_{\text{Green}} &= \frac{1}{2}(\lambda^2 - 1) = \frac{1}{2}(\|\boldsymbol{\lambda}\|_{\mathbf{g}}^2 - 1) = \frac{1}{2}(\|\mathbf{T}\|_{\mathbf{C}}^2 - \|\mathbf{T}\|_{\mathbf{G}}^2) \\ &= \mathbf{T} \cdot \frac{1}{2}(\mathbf{C} - \mathbf{G}) \cdot \mathbf{T} = \mathbf{T} \cdot \mathbf{E} \cdot \mathbf{T}, \end{aligned} \quad (4.23)$$

<sup>2</sup>In fact,  $\mathbf{C}$  is introduced by Green [Gre48] with the components at the bottom of page 297,  $\mathbf{C}^{-1}$  was used by Cauchy [Cau27] with the components of equations 10 and 11 on page 62. Additionally, Piola [Pio33] also derived similar quantities, as stated in Freed [Fre14].

where the *Green-Lagrangian strain tensor* can be identified as

$$\mathbf{E} = \frac{1}{2}(\mathbf{C} - \mathbf{G}) \quad \text{or} \quad E_{AB} = \frac{1}{2}(C_{AB} - G_{AB}) = \frac{1}{2}(\delta^a_A g_{ab} \delta^b_B - G_{AB}). \quad (4.24)$$

The components are, as before, the ones of a convective coordinate system. The same comparison can be made in the tangent space in the current configuration with  $\mathbf{t} \in T_{\mathbf{x}}\mathcal{B}_t$  with the deformed length  $\|\mathbf{t}\|_{\mathbf{g}} = 1$  and the initial length  $\|\mathbf{t}\|_{\mathbf{c}} = \frac{1}{\lambda}$ . This yields the *Euler-Almansi strain*

$$\epsilon_{\text{Almansi}} = \frac{1}{2}\left(1 - \frac{1}{\lambda^2}\right) = \frac{1}{2}(\|\mathbf{t}\|_{\mathbf{g}}^2 - \|\mathbf{t}\|_{\mathbf{c}}^2) = \mathbf{t} \cdot \frac{1}{2}(\mathbf{g} - \mathbf{c}) \cdot \mathbf{t} = \mathbf{T} \cdot \mathbf{e} \cdot \mathbf{T}, \quad (4.25)$$

where the *Euler-Almansi strain tensor* can be identified as

$$\mathbf{e} = \frac{1}{2}(\mathbf{g} - \mathbf{c}) \quad \text{or} \quad e_{ab} = \frac{1}{2}(g_{ab} - c_{ab}) = \frac{1}{2}(g_{ab} - \delta^A_a G_{AB} \delta^B_b). \quad (4.26)$$

Therefore, in the convective coordinate system, the components of the Euler-Almansi strain tensor and the components of the Green-Lagrangian strain tensor are equivalent, but are linked to a different basis. For the sake of completeness, the tensors are  $\mathbf{e} = e_{ab} \mathbf{g}^a \otimes \mathbf{g}^b$  and  $\mathbf{E} = E_{AB} \mathbf{G}^A \otimes \mathbf{G}^B$ . These strain measures can be seen as specific cases of more general possible strain measures. This family of strain measures is called *Seth-Hill strain tensor family*, defined in the seminal works of Seth [Set64] and Hill [Hil68]. They can be defined as

$$\mathbf{E}_m(\mathbf{C}) = \begin{cases} \frac{1}{m}(\mathbf{C}^{m/2} - \mathbf{G}) & \text{for } m \neq 0 \\ \frac{1}{2} \ln \mathbf{C} & \text{for } m = 0, \end{cases} \quad \text{and} \quad \mathbf{e}_m(\mathbf{c}) = \begin{cases} \frac{1}{m}(\mathbf{g} - \mathbf{c}^{m/2}) & \text{for } m \neq 0 \\ \frac{1}{2} \ln \mathbf{c} & \text{for } m = 0, \end{cases} \quad (4.27)$$

for the Lagrangian and Eulerian settings, respectively. For the Lagrangian setting, the strain measures *Biot strain* ( $m = 1$ ) and *Hencky strain* ( $m = 0$ ) are also common [Hen28; Bio39].

All these strain measures share the same strain-free state, which is equivalent to  $\mathbf{E} = \mathbf{0}$  or  $\mathbf{G} = \boldsymbol{\chi}^*(\mathbf{g}) = \mathbf{C}$ . Such deformations are called *rigid body motions*, or in the mathematical mapping nomenclature, *isometric mapping* (modulo reflections), since they preserve the metric components at each point.



## 4.2 Traction and Stress

The *stress* in a physical body is a central concept for phenomenological continuum mechanics. The roots of the concept can be found in Navier [Nav21]. He asserts that two neighboring molecules  $P_i$  and  $P_j$  exert forces onto each other. In the undeformed state these forces cancel out,  $\Delta \mathbf{f}_{ij} = \mathbf{0} = \mathbf{f}_i - \mathbf{f}_j$ . If external forces act on the body, the equilibrium still needs to be fulfilled between neighboring molecules, and therefore,  $\Delta \mathbf{f}_{ij} \neq \mathbf{0}$ .

Influenced by Navier [Nav21], the concept of stress originated from the works of Cauchy [Cau27]. Stress is the response to externally applied loads. This response of the body can be represented by a second-order tensor field, which transmits the applied loads internally. Since Cauchy made this notion precise, the stress field inside the body bears his name: *Cauchy stress*, with the symbol  $\boldsymbol{\sigma}$ .

Cauchy established the relationship between the traction on the surface of a body and the stress field  $\boldsymbol{\sigma}$  in [Cau27, p. 48, eq. 20]. Euler's cut principle extends this relationship to an arbitrary cut through the body, as depicted in Fig. 4.6. The resulting free traction is denoted as  $\mathbf{t}$ . In addition, Cauchy asserted in [Cau27] that this traction exhibits a specific functional dependency. The traction depends on time  $t$  and on the position  $\mathbf{x}$ , where the cut is made. While the dependence on position and time is expected, Cauchy also asserted that the traction is independent of the curvature of the cut-out surface, relying solely on its orientation. Thus, we have

$$\mathbf{t} = \mathbf{t}(\mathbf{x}, t, \mathbf{n}), \quad (4.28)$$

where  $\mathbf{n}$  denotes the outward normal of the surface at position  $\mathbf{n}$ , in the sense of Section 2.8.3 on page 44. This dependence on the normal without dependence on the curvature is known as *Cauchy's postulate*.

Cauchy made this relation more explicit by stating that the dependence on the normal is even linear. Thus, *Cauchy's stress theorem* states that there exists a  $(0, 2)$ -second-order tensor field such that

$$\mathbf{t} = \boldsymbol{\sigma} \cdot \mathbf{n} \quad \text{or} \quad t^a = \sigma^{ab} n_b, \quad (4.29)$$

where  $\boldsymbol{\sigma}$  is called *Cauchy's stress tensor*.<sup>3</sup> The tensorial mapping is given by  $\boldsymbol{\sigma} : T_{\mathbf{x}}^* \mathcal{B}_t \rightarrow T_{\mathbf{x}} \mathcal{B}_t$ .

<sup>3</sup>Early teaching textbooks are Rankine [Ran51] or Lamé [Lam52], where in the latter, stresses and strains appear together under the concept of *elasticity*. Additionally, Lamé studied the transformation rules of these quantities. More historical details can be found in Reich [Rei13], Belhoste [Bel91], and Sokolnikoff [Sok56].

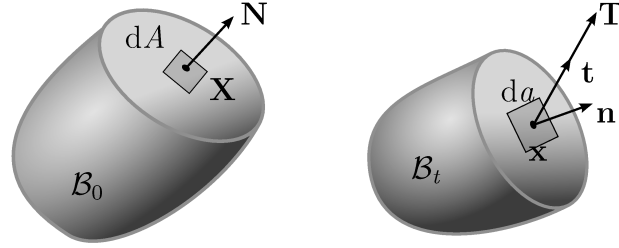


**Figure 4.6:** Traction vectors and normals of cut through the body of the reference and current configuration.

The traction vector  $\mathbf{t}$  is the notion of force per *deformed area*. To study these objects, it is also convenient to represent  $\mathbf{t}$  by a traction vector that relates the force to the undeformed area. This object can be defined by the functional relation  $\mathbf{T} = \mathbf{T}(\mathbf{X}, t, \mathbf{N})$  with the reference coordinate  $\mathbf{X}$  and the reference normal  $\mathbf{N}$  of the cut. The traction vector  $\mathbf{T}$  still lives in the tangent space  $T_{\mathbf{x}}\mathcal{B}_t$  but is simply a rescaled version of  $\mathbf{t}$ . The functional dependence can be stated as

$$\mathbf{T} = \mathbf{P} \cdot \mathbf{N} \quad \text{or} \quad T^a = P^{aB} N_B, \quad (4.30)$$

where  $\mathbf{P}$  is called the *first Piola-Kirchhoff stress tensor* [Pio33; Kir52]. The tensorial mapping is given by  $\mathbf{P} : T_{\mathbf{X}}^*\mathcal{B}_0 \rightarrow T_{\mathbf{x}}\mathcal{B}_t$ . It is the multidimensional equivalent of the one-dimensional *engineering stress*. Starting from the identity of an infinitesimal surface force

$$\mathbf{t} da = \boldsymbol{\sigma} \cdot \mathbf{n} da = \boldsymbol{\sigma} \cdot d\mathbf{a} = \mathbf{T} dA = \mathbf{P} \cdot \mathbf{N} da = \mathbf{P} \cdot d\mathbf{A}, \quad (4.31)$$

the relation between  $\boldsymbol{\sigma}$  and  $\mathbf{P}$  can be obtained via the Piola transform of the second leg of the Cauchy stress via Eq. (2.113) on page 48 as

$$\mathbf{P} = J\boldsymbol{\sigma} \cdot \mathbf{F}^{-T}. \quad (4.32)$$

If a material stress tensor is required, the first leg can also be pulled back. This yields the *second Piola-Kirchhoff stress tensor*  $\mathbf{S} : T_{\mathbf{X}}^*\mathcal{B}_0 \rightarrow T_{\mathbf{X}}\mathcal{B}_0$  as

$$\mathbf{S} = J\mathbf{F}^{-1} \cdot \boldsymbol{\sigma} \cdot \mathbf{F}^{-T} = \mathbf{F}^{-1} \cdot \mathbf{P}. \quad (4.33)$$

In the Cartesian bases  $\{\mathbf{E}_A\}$ ,  $\{\mathbf{e}_a\}$ , or in the bases of the convective coordinate system  $\{\mathbf{G}_A\}$ ,  $\{\mathbf{g}_a\}$  these stress tensors can be written as

$$\begin{aligned}\boldsymbol{\sigma} &= \sigma^{ab} \mathbf{e}_a \otimes \mathbf{e}_b = \tilde{\sigma}^{ab} \mathbf{g}_a \otimes \mathbf{g}_b, \\ \mathbf{P} &= P^{aA} \mathbf{e}_a \otimes \mathbf{E}_A = J \sigma^{ab} (F^{-1})^A_b \mathbf{e}_a \otimes \mathbf{E}_A = J \tilde{\sigma}^{ab} \delta^A_b \mathbf{g}_a \otimes \mathbf{G}_A, \\ \mathbf{S} &= S^{AB} \mathbf{E}_A \otimes \mathbf{E}_B = J \sigma^{ab} (F^{-1})^A_a (F^{-1})^B_b \mathbf{E}_A \otimes \mathbf{E}_B = J \tilde{\sigma}^{ab} \delta^A_a \delta^B_b \mathbf{G}_A \otimes \mathbf{G}_B,\end{aligned}\tag{4.34}$$

where  $\tilde{\sigma}^{dc} = \sigma^{ab} (\mathbf{e}_a \cdot \mathbf{g}^d) (\mathbf{e}_b \cdot \mathbf{g}^c)$  and  $J = \det \mathbf{F}$ .

The last equalities are particularly interesting as they allow a convenient stress description by exchanging the base vectors (and multiplying by  $J$ ), since the Kronecker-deltas are just leftovers of the notation. This is only numerically useful since in this non-Cartesian basis, the stresses are difficult to interpret. The reason for this is, that the direction and magnitude of the base vectors change. Thus, in a post-processing step, the stresses are usually defined in a global coordinate system for solid simulations, and for shell simulations, they are defined in a local Cartesian coordinate system constructed from  $\mathbf{g}_a$ .

The curvilinear convective coordinate system representation, frequently employed in shell analysis, is also utilized later in this study. Additionally, the base vectors  $\mathbf{E}_A$  and  $\mathbf{e}_a$  are usually the same. They are simply the three Cartesian base vectors of  $\mathbb{R}^3$ .

## 4.3 Balance Principles

In this section, the common balance principles of solid mechanics are stated, namely, conservation of mass, balance of momentum and balance of angular momentum in their spatial and material format. Again, special interest resides in stating these principles in a non-Cartesian coordinate system, since this is later needed for specializing them for shells.

### 4.3.1 Conservation of Mass

Although conservation of mass is an obvious requirement from a physical point of view, its mathematical description in curvilinear coordinate systems is not. The total mass of the reference configuration  $\mathcal{B}_0$  is given by  $M$ . It can be computed with the density  $\rho_0(\mathbf{X}, t)$  and the Riemannian volume form  $\mathbf{dV}$  from Section 2.8 on page 42, as

$$M = \text{Vol}(\mathcal{B}_0) = \int_{\mathcal{B}_0} \rho_0(\mathbf{X}, t) \mathbf{dV} = \int_{\mathcal{B}_0} \rho_0(\mathbf{X}, t) \sqrt{\det([G_{AB}])(\mathbf{X})} \, dV. \quad (4.35)$$

Conservation of mass means that the total mass remains constant w.r.t. time, i.e.,  $\dot{M} = 0$ . Using the localization theorem [MH94, Ch. 2, p. 122 ], Eq. (4.35) yields the result  $\dot{\rho}_0 = 0$  with  $\frac{d}{dt}(\rho) = \dot{\rho}$ . The same can be stated in the current configuration, here the total mass should be  $M$  again. This yields

$$M = \text{Vol}(\mathcal{B}_t) = \int_{\mathcal{B}_t} \rho(\mathbf{x}(t), t) \mathbf{d}\mathbf{v} = \int_{\mathcal{B}_t} \rho(\mathbf{x}(t), t) \sqrt{\det([g_{ab}])(\mathbf{x}, t)} \, dv. \quad (4.36)$$

Equating the total masses of the current and reference configuration, yields via the localization theorem, a relation between the densities given by

$$\rho_0 = \rho J. \quad (4.37)$$

Requiring  $\dot{M} = 0$  yields

$$\begin{aligned} \dot{M} &= \frac{d}{dt} \int_{\mathcal{B}_t} \rho(\mathbf{x}(t), t) \mathbf{d}\mathbf{v} \\ &= \frac{d}{dt} \int_{\mathcal{B}_0} \rho(\boldsymbol{\chi}(\mathbf{X}, t), t) J(\mathbf{X}, t) \mathbf{dV}, \end{aligned} \quad (4.38)$$

with the identity Eq. (2.105) on page 46.

Since the integration domain is now time-independent, differentiation and integration commute. This yields

$$\dot{M} = \int_{\mathcal{B}_0} \frac{d}{dt} \rho(\boldsymbol{\chi}(\mathbf{X}, t), t) J(\mathbf{X}, t) + \rho(\boldsymbol{\chi}(\mathbf{X}, t), t) \frac{d}{dt} J(\mathbf{X}, t) \, d\mathbf{V}. \quad (4.39)$$

Both derivatives can be computed separately with the chain rule as

$$\frac{d}{dt} \rho(\boldsymbol{\chi}(\mathbf{X}, t), t) = \frac{\partial}{\partial t} \rho(\boldsymbol{\chi}(\mathbf{X}, t), t) + \frac{\partial \rho}{\partial x^i} \frac{\partial \Phi^i}{\partial t} = \frac{\partial \rho}{\partial t} + D_{\mathbf{v}(\mathbf{x}, t)} \rho(\boldsymbol{\chi}(\mathbf{X}, t), t), \quad (4.40)$$

$$\frac{d}{dt} J(\mathbf{X}, t) = J(\mathbf{X}, t) \operatorname{div} \mathbf{v}(\boldsymbol{\chi}(\mathbf{X}, t), t), \quad (4.41)$$

where the first equation is often called *material time derivative* of the spatial scalar field  $\rho$ . In the second equation,  $J$  depends on  $\sqrt{\det([g_{ab}])(\mathbf{x}(t), t)}$  as seen in Eq. (2.105) on page 46. For a detailed derivation, we refer to [MH94, Ch. 1, p. 86, 5.4 Proposition]. The covariant divergence  $\operatorname{div} \mathbf{v} = v^a_{|a}$  is defined in Eqs. (3.7) and (A.2) on pages 53 and 201, respectively. Plugging both results into Eq. (4.39), we have

$$\begin{aligned} \dot{M} &= \int_{\mathcal{B}_0} \dot{\rho} J + \rho J \operatorname{div} \mathbf{v} \, d\mathbf{V}, \\ &= \int_{\mathcal{B}_t} \frac{\partial \rho}{\partial t} + D_{\mathbf{v}} \rho + \rho \operatorname{div} \mathbf{v} \, d\mathbf{v}, \\ &= \int_{\mathcal{B}_t} \frac{\partial \rho}{\partial t} + \operatorname{div}(\rho \mathbf{v}) \, d\mathbf{v} = 0, \end{aligned} \quad (4.42)$$

which yields with the localization theorem  $\dot{\rho} + \rho \operatorname{div}(\mathbf{v}) = 0$ .

Thus, the conservation of mass can be stated as

$$\dot{\rho}_0 = 0 \quad \text{or} \quad \dot{\rho} + \rho \operatorname{div}(\mathbf{v}) = 0, \quad (4.43)$$

$$\frac{\partial \rho_0}{\partial t} = 0 \quad \text{or} \quad \frac{\partial \rho}{\partial t} + \frac{\partial \rho}{\partial x^a} v^a + \rho v^a_{|a} = 0. \quad (4.44)$$

### 4.3.2 Balance of Linear and Angular Momentum

The balance of linear momentum states that the total linear momentum of a system stays constant unless external forces act on it. This is equivalent to Newton's second law of motion, which can be stated as  $\mathbf{F} = \partial(m\mathbf{v})/\partial t$ , where the change of momentum of a rigid body is equal to the forces acting on it. For continuum mechanics, this can be stated as follows: Using the mass density and the velocity, the *total linear momentum* can be defined via the vector-valued integration

$$\mathbf{L}(t) = \int_{\mathcal{B}_t} \rho(\mathbf{x}, t) \mathbf{v}(\mathbf{x}, t) \, d\mathbf{v} = \int_{\mathcal{B}_0} \rho_0(\mathbf{X}) \mathbf{V}(\mathbf{X}, t) \, d\mathbf{V}. \quad (4.45)$$

The *balance of linear momentum* then states, with  $\mathbf{b}(\mathbf{x}, t)$  as a body force per unit mass and  $\mathbf{t}$  as the traction vector defined in Eq. (4.29), as

$$\frac{d}{dt} \mathbf{L}(t) = \frac{d}{dt} \int_{\mathcal{B}_t} \rho(\mathbf{x}, t) \mathbf{v}(\mathbf{x}, t) \, d\mathbf{v} = \int_{\partial\mathcal{B}_t} \mathbf{t}(\mathbf{x}, t) \, d\mathbf{a} + \int_{\mathcal{B}_t} \mathbf{b}(\mathbf{x}, t) \, d\mathbf{v}. \quad (4.46)$$

Similarly, the *total angular momentum* reads

$$\mathbf{J}(t) = \int_{\mathcal{B}_t} \rho(\mathbf{x}, t) \mathbf{x} \times \mathbf{v}(\mathbf{x}, t) \, d\mathbf{v} = \int_{\mathcal{B}_0} \rho_0(\mathbf{X}) \mathbf{\Phi}(\mathbf{X}, t) \times \mathbf{V}(\mathbf{X}, t) \, d\mathbf{V}. \quad (4.47)$$

Then the *balance of angular momentum* reads

$$\frac{d}{dt} \mathbf{J}(t) = \int_{\mathcal{B}_t} \rho(\mathbf{x}, t) \mathbf{x} \times \mathbf{v}(\mathbf{x}, t) \, d\mathbf{v} = \int_{\partial\mathcal{B}_t} \mathbf{x} \times \mathbf{t}(\mathbf{x}, t) \, d\mathbf{a} + \int_{\mathcal{B}_t} \mathbf{x} \times \mathbf{b}(\mathbf{x}, t) \, d\mathbf{v}. \quad (4.48)$$

These equations, involving integrals of vector-valued functions, only make sense in a vector space, namely  $\mathbb{R}^3$ . Thus,  $\mathbf{L}$  and  $\mathbf{J}$  need to be defined in the Cartesian coordinate system  $\{\mathbf{E}_i\}$ . To circumvent the remedy of relying on the linear structure of space, as needed in the case of non-linear spacetime, Marsden and Hughes [MH94] show how to derive linear and angular momentum using a relativistic view on the balance of energy, see [MH94, p. 165, 4.13 Theorem]. Either way, the local balance of angular momentum boils down to symmetry conditions on the stress, namely

$$\boldsymbol{\sigma}^T = \boldsymbol{\sigma}, \quad \mathbf{S}^T = \mathbf{S} \quad \text{and} \quad \mathbf{P} \cdot \mathbf{F}^T = \mathbf{F} \cdot \mathbf{P}^T. \quad (4.49)$$

In contrast to this, the local form of balance of linear momentum can be derived from Eq. (4.46) as an Eulerian, two-point or material statement as

$$\rho \dot{\mathbf{v}} = \rho \mathbf{b} + \operatorname{div} \boldsymbol{\sigma} \quad \text{or} \quad \rho \left( \frac{\partial v^a}{\partial t} + v^b v^a|_b \right) = \rho b^a + \sigma^{ab}|_b, \quad (4.50)$$

$$\rho_0 \dot{\mathbf{V}} = \rho_0 \mathbf{B} + \operatorname{Div} \mathbf{P} \quad \text{or} \quad \rho_0 \left( \frac{\partial V^a}{\partial t} + V^b V^a|_b \right) = \rho_0 B^a + P^{aA}|_A, \quad (4.51)$$

$$\rho_0 \boldsymbol{\alpha} = \rho_0 \mathbf{F}^{-1} \mathbf{B} + \operatorname{Div}_{\mathbf{C}} \mathbf{S} \quad \text{or} \quad \rho_0 \alpha^A = \rho_0 (\mathbf{F}^{-1} \mathbf{B})^A + (\operatorname{Div}_{\mathbf{C}} \mathbf{S})^A, \quad (4.52)$$

where the first equation can be found in [Cau27, P. 111, Eq. 16] and is also named *Cauchy's equation of equilibrium*, if  $\dot{\mathbf{v}} = \mathbf{0}$ . The last version is barely stated in literature but can be found without derivation in [MH94, p. 136]. The divergence w.r.t. the right Cauchy-Green tensor  $\mathbf{C}$  is defined as  $(\operatorname{Div}_{\mathbf{C}} \mathbf{S})^A = \frac{1}{\sqrt{\det([C_{CD}]})} \frac{\partial}{\partial X^B} (\sqrt{\det([C_{CD}]}) S^{AB})$ .

## 4.4 Elastic Constitutive Theory

Although in Chapter 7 inelastic material response is studied, this section is dedicated solely to discussing elastic material response. In the following, the notion of elastic materials and their constitutive equations are discussed. Especially, the definition of path-independent material response will be stated, since this is needed to discuss erroneous interpolation schemes in Section 6.3. Multiple notions of elastic materials exist and will be mentioned later. This is needed since there are definitions of elastic material models, which are not path-independent. However, the focus lies on the case of *Green-elastic* materials.

Green-elastic material models postulate the existence of a *Helmholtz free-energy function*  $\psi$ . It is also known as *explicit elasticity* [Fre14, Ch. 5.1] or *hyperelasticity* [TN04, Ch. 42]. To derive the constitutive relation between the Helmholtz free-energy function  $\psi$  and the second Piola-Kirchhoff stress  $\mathbf{S}$ , the second law of thermodynamics is used. The second law of thermodynamics can be stated as the material version of the *Clausius-Planck inequality*. This yields

$$\mathcal{D} = \mathbf{S} : \dot{\mathbf{E}} - \dot{\psi} \geq 0, \quad (4.53)$$

where  $\mathcal{D}$  is the dissipation of the process, which should be greater or equal to zero, and  $\mathbf{E}$  is the Green-Lagrangian strain tensor. The term  $\mathbf{S} : \dot{\mathbf{E}}$  is called *stress power*. It can be interpreted as the rate at which work is done on the material point. Thus, yielding

$$\dot{W} = \mathbf{S} : \dot{\mathbf{E}}, \quad (4.54)$$

where  $W$  is the work. Nevertheless, since  $\psi$  in Eq. (4.53) is assumed to be a function of the strains, the chain rule can be applied and this yields

$$\mathcal{D} = \mathbf{S} : \dot{\mathbf{E}} - \frac{\partial \psi}{\partial \mathbf{E}} : \dot{\mathbf{E}} \geq 0. \quad (4.55)$$

The second law of thermodynamics should hold for arbitrary processes, therefore

$$\mathcal{D} \geq 0, \quad \forall \dot{\mathbf{E}}. \quad (4.56)$$

Consequently,

$$\mathcal{D} = \left( \mathbf{S} - \frac{\partial \psi}{\partial \mathbf{E}} \right) : \dot{\mathbf{E}} \geq 0, \quad \forall \dot{\mathbf{E}}. \quad (4.57)$$

This yields the constitutive equation

$$\mathbf{S} = \frac{\partial \psi}{\partial \mathbf{E}}. \quad (4.58)$$

This procedure is called *Coleman-Noll procedure* in literature, named after Coleman and Noll [CN63]. Therefore,  $\mathcal{D} \equiv 0$ , for Green-elastic material. Since the stresses can be derived from a potential, it also follows that the response of the material is *path-independent*. Let the work of a time interval  $t \in [t_1, t_2]$  be calculated via the stress power Eq. (4.54). This yields

$$W = \int_{t_1}^{t_2} \mathbf{S} : \dot{\mathbf{E}} \, dt = \int_{t_1}^{t_2} \frac{\partial \psi}{\partial \mathbf{E}} : \dot{\mathbf{E}} \, dt = \int_{t_1}^{t_2} \dot{\psi}(\mathbf{E}(t)) \, dt = \psi(\mathbf{E}_2) - \psi(\mathbf{E}_1), \quad (4.59)$$

where  $\mathbf{E}_2 = \mathbf{E}(t_2)$  and  $\mathbf{E}_1 = \mathbf{E}(t_1)$ . Thus, the work done on the particle does only depend on the initial and final state and not on the path taken, rendering it path-independent. For closed paths, where  $\mathbf{E}_2 = \mathbf{E}_1$ , the net work done is exactly zero.

REMARK 1. In literature, taking the derivatives in Eq. (4.58) is not always defined precisely. In the following, using the tools of Chapter 2 on page 13, these statements can be presented in a more precise way. The internal free energy

$$\psi : \begin{cases} \text{Sym}_3 \rightarrow \mathbb{R}, \\ \mathbf{E} \rightarrow \psi(\mathbf{E}) \end{cases} \quad (4.60)$$

is a function of symmetric matrices. This is only half of the truth since by definition the Green-Lagrangian strain reads  $\mathbf{E} = \frac{1}{2}(\mathbf{C} - \mathbf{I})$  in a Euclidean basis. Since  $\mathbf{C} \in \mathcal{S}_{++}^3$ , where  $\mathcal{S}_{++}^3$  denotes the space of symmetric positive definite matrices, it follows that  $\mathbf{E}$  is



not an arbitrary symmetric matrix, due to the dependence on  $\mathbf{C}$ . Thus, if we consider a different free energy function in terms of  $\mathbf{C}$ , we have

$$\hat{\psi} : \begin{cases} \mathcal{S}_{++}^3 \rightarrow \mathbb{R}, \\ \mathbf{C} \mapsto \hat{\psi}(\mathbf{C}). \end{cases} \quad (4.61)$$

Taking derivatives here is non-trivial. This problem can be tackled with the tools given in Section 2.7.4 on page 40. Thus, this boils down to simply taking the derivative in the embedding space and then projecting it onto the tangent space. The tangent bundle of  $\mathcal{S}_{++}^3$  is the space of symmetric matrices at each point, namely  $\text{Sym}_3 = T\mathcal{S}_{++}^3$ . Thus, the tangent space at  $\mathbf{C}$ ,  $T_{\mathbf{C}}\mathcal{S}_{++}^3$  is also  $\text{Sym}_3$ . Therefore, the correct procedure is creating a function living in the embedding space

$$\tilde{\psi} : \begin{cases} \mathbb{R}^{3 \times 3} \rightarrow \mathbb{R}, \\ \mathbf{C} \mapsto \hat{\psi}(\mathbf{C}), \end{cases} \quad (4.62)$$

and then projecting it into the tangent space. Thus, we have

$$\frac{\partial \hat{\psi}(\mathbf{E})}{\partial \mathbf{E}} = \text{sym} \left( \frac{\partial \tilde{\psi}(\mathbf{E})}{\partial \mathbf{E}} \right), \quad (4.63)$$

where  $\text{sym}(\mathbf{A}) = \frac{1}{2}(\mathbf{A} + \mathbf{A}^T)$  is the projection onto the tangent space  $T_{\mathbf{C}}\mathcal{S}_{++}^3$ , which is the projection into the space of symmetric matrices. Performing the derivative operation followed by symmetrization does *not* yield the same result as taking the derivative of energy with respect to a symmetric argument, for the example Eq. (4.58). This would yield a result, where the off-diagonal terms are scaled by a factor of two. Usually, switching to Voigt notation prohibits this error, see for some discussions Srinivasan and Panda [SP22] not related to mechanics. Nevertheless, in the context of continuum mechanics, Chapter 2, i.e., Eq. (2.83) on page 40 provides the tools to rigorously derive the correct result.

Furthermore, enhanced assumed strain (EAS) methods, such as the influential work by Simo and Armero [SA92], do usually not investigate the manifold nature of the enhanced Green-Lagrangian strains, denoted as  $\tilde{\mathbf{E}} = \mathbf{E} + \mathbf{E}_{\text{enhanced}}$ . Consequently, the new strain can implicitly violate the constraint  $\mathbf{C} \in \mathcal{S}_{++}^3$ , which does not represent an incompatibility between the elements, (which is common for EAS methods) but rather a localized penetration of matter at the material point, which is undesired. Although this issue is not discussed in the literature, to the knowledge of the author, it is reasonable to assume that it is not problematic in practice. However, future considerations should

take this into account. Similarly, a related issue concerning the constraint  $\mathbf{C} \in \mathcal{S}_{++}^3$  is discussed in Section 5.4 on page 124, albeit in a slightly different but related context.

---

In contrast to this, there is the weaker requirement of *Cauchy-elastic* materials, which only requires that the stress depends on the current state and not on the deformation history. Thus, again in terms of the second Piola-Kirchhoff stress

$$\mathbf{S} = \mathfrak{h}(\mathbf{E}), \quad (4.64)$$

where  $\mathfrak{h}$  is called *response function* and Eq. (4.64) is called *stress-strain relation*.

**Implicit Elasticity** The last class of elastic materials is the so-called hypo-elastic material class, see Truesdell and Noll [TN04]. Their constitutive equation in terms of the Cauchy stress is given by

$$\dot{\boldsymbol{\sigma}} = \mathfrak{g}(\boldsymbol{\sigma}, \mathbf{L}), \quad (4.65)$$

where  $\mathfrak{g}$  is the hypo-elastic response function and  $\mathbf{L} = \dot{\mathbf{F}} \cdot \mathbf{F}^{-1}$  is the velocity gradient in terms of the deformation gradient. This elastic material behavior is derived from a stress-rate/strain-rate relation and is therefore incremental. However, it can be proven that such material models do not dissipate energy but can model path dependency. Consequently, these models yield different results, if the path to the final state is different. The results of these models depend only on the path and not on the rate at which they traveled the path as stated in Noll [Nol55, p. 35].

## 4.5 Potential Energy and Weak Form

The weak form can be obtained via the method of weighted residuals derived by Galerkin [Gal15]. There are several methods to derive a fitting formulation, which can be programmed and solved approximately by a computer. In this work, only the finite element method is considered, which needs a potential formulation or a weak form. The former can be derived using e.g. the *minimum of potential energy* and the latter can be derived using the *principle of virtual work* (or *principle of virtual displacements*). The principle of virtual work uses the *strong form* as given, e.g., in Eq. (4.52). This strong form is then

multiplied by a test function field  $\delta \mathbf{u}$  and integrated over the domain, which yields

$$\begin{aligned} G(\mathbf{u}, \delta \mathbf{u}) &= \int_{\Omega} (\rho_0 \dot{\mathbf{V}} - \rho_0 \mathbf{B} + \text{Div } \mathbf{P}) \cdot \delta \mathbf{u} \, dv \\ &= \int_{\Omega} \rho_0 (\dot{\mathbf{V}} - \mathbf{B}) \cdot \delta \mathbf{u} + \mathbf{P} : \text{Grad } \delta \mathbf{u} \, dv - \int_{\partial \mathcal{B}_{0,N}} \mathbf{T} \cdot \delta \mathbf{u} \, da, \end{aligned} \quad (4.66)$$

where the second line stems from applying the divergence theorem to remove the derivative of  $\mathbf{P}$ . The traction  $\mathbf{T}$  is defined as in Eq. (4.30) and  $\partial \mathcal{B}_{0,N}$  denotes the part of the boundary of the reference body, where Neumann boundary conditions are applied.

Using the principle of minimum potential energy, Eq. (4.66) can be derived alternatively. From the potential energy

$$\Pi(\mathbf{u}) = \Pi_{\text{int}}(\mathbf{u}) - \Pi_{\text{ext}}(\mathbf{u}) = \int_{\Omega} \psi(\mathbf{F}(\mathbf{u})) - \mathbf{B} \cdot \mathbf{u} \, dV - \int_{\partial \mathcal{B}_{0,N}} \mathbf{T} \cdot \mathbf{u} \, dA, \quad (4.67)$$

the weak form can be derived with the Gâteaux derivative, as

$$\delta \Pi(\mathbf{u}, \delta \mathbf{u}) = D_{\delta \mathbf{u}} \Pi(\mathbf{u}) = G(\mathbf{u}, \delta \mathbf{u}) = \left. \frac{d\Pi(\mathbf{u} + \epsilon \delta \mathbf{u})}{d\epsilon} \right|_{\epsilon=0}, \quad (4.68)$$

which is called the first variation of the energy. The Gâteaux derivative is the directional derivative in the direction of the variation in this infinite-dimensional function space, e.g.  $H^1(\mathbb{R}^3)$ . Similarly, if the problem at hand is non-linear, the linearization of the weak form is needed. Thus, the linearization of Eq. (4.68) reads

$$\Delta \delta \Pi(\mathbf{u}, \delta \mathbf{u}) = D_{\Delta \mathbf{u}} D_{\delta \mathbf{u}} \Pi(\mathbf{u}) = D_{\Delta \mathbf{u}} G(\mathbf{u}, \delta \mathbf{u}). \quad (4.69)$$

This is called the second variation of the energy or linearization of the weak form, depending on the context. As mentioned abstractly in Section 1.1, this simple and seemingly innocent concept will come back to haunt us, as the used Gâteaux derivative does not generalize straightforwardly to non-linear spaces. For later convenience, the internal potential energy and its derivatives are restated in material form, as

$$\begin{aligned} \Pi_{\text{int}}(\mathbf{u}) &= \int_{\mathcal{B}_0} \hat{\psi}(\mathbf{E}(\mathbf{u})) \, dV, \\ \delta \Pi(\mathbf{u}, \delta \mathbf{u}) &= \int_{\mathcal{B}_0} \frac{\partial \hat{\psi}}{\partial \mathbf{E}} : \delta \mathbf{E} \, dV = \int_{\mathcal{B}_0} \mathbf{S} : \delta \mathbf{E} \, dV, \\ \Delta \delta \Pi(\mathbf{u}, \delta \mathbf{u}, \Delta \mathbf{u}) &= \int_{\mathcal{B}_0} \mathbf{S} : D_{\Delta \mathbf{u}} \delta \mathbf{E} + D_{\Delta \mathbf{u}} \mathbf{S} : \delta \mathbf{E} \, dV, \end{aligned} \quad (4.70)$$

in terms of the Green-Lagrangian strain  $\mathbf{E}$  and the second Piola-Kirchhoff stress  $\mathbf{S}$ . Historically, finding an approximate solution by minimizing an energy functional w.r.t. degrees of freedom was suggested by Ritz [Rit09]. The notion of potential energy can be dated back to Rankine [Ran53]. More details on the history of Galerkin's method can be found in Repin [Rep17].

## 4.6 Objectivity

In general, objectivity can be stated in several ways. It is the requirement that a physical quantity is independent of a *change of observer*. It is also often denoted by *material frame-indifference*, stating that the frame in which the process is recorded, does not influence the process. For details, refer to Truesdell and Noll [TN04] and Holzapfel [Hol02]. This change of an observer can be mathematically encoded in a *superimposed rigid-body motion*, which is not the same but leads to the same requirements for the theory. Later, several interpolations of the director field and their relation to objectivity are investigated, and therefore, the notion of *superimposed rigid-body motions* will be needed.

Consider a motion as given in Eq. (4.2) on page 68 as  $\chi$ , the deformation map from Eq. (4.4) reads  $\mathbf{x} = \chi(\mathbf{X}, t)$ . Consider another motion  $\chi^+$  and the corresponding deformation reads  $\mathbf{x}^+ = \chi^+(\mathbf{X}, t)$ .

The deformation  $\chi^+$  is assumed to be a superimposed rigid-body motion, then deformations are related as

$$\mathbf{x}^+ = \chi^+(\mathbf{X}, t) = \mathbf{c}(t) + \mathbf{Q}(t) \cdot \chi(\mathbf{X}, t), \quad (4.71)$$

where  $\mathbf{c} : I \rightarrow \mathbb{R}^3$  is a translation in space and  $\mathbf{Q} : I \rightarrow \mathcal{SO}(3)$  is a rotation. From this new deformation, the deformation gradient can be derived as

$$\begin{aligned} \mathbf{F}^+ &= \frac{d\chi^+}{d\mathbf{X}} = \mathbf{Q}(t) \cdot \frac{d\chi}{d\mathbf{X}} = \mathbf{Q} \cdot \mathbf{F}, \\ (F^+)^a{}_A &= Q^a{}_b F^b{}_A. \end{aligned} \quad (4.72)$$

From this gradient, several transformation laws for different objects can be derived. For notational convenience, the explicit dependence of  $\mathbf{Q}$  on the time  $t$  is neglected. For example, the right Cauchy-Green strain tensor from Eq. (4.21) for the new configuration reads

$$\mathbf{C}^+ = (\mathbf{F}^+)^T \cdot \mathbf{F}^+ = (\mathbf{Q} \cdot \mathbf{F})^T \cdot \mathbf{Q} \cdot \mathbf{F} = \mathbf{F}^T \cdot \mathbf{Q}^T \cdot \mathbf{Q} \cdot \mathbf{F} = \mathbf{F}^T \cdot \mathbf{F}, \quad (4.73)$$

which results in the same quantity. Here,  $\mathbf{Q}^T \cdot \mathbf{Q} = \mathbf{I}$  was exploited, since it is an orthogonal matrix. It yields the same quantity since  $\mathbf{C}$  is defined in the reference configuration  $\mathcal{B}_0$  and should be therefore unaffected by the rotation of the spatial object. Consequently, the transformation law for  $\mathbf{C}$  to be an objective quantity is trivial. Similarly, it holds  $\mathbf{E}^+ = \mathbf{E}$  for the Green-Lagrangian strain, which is a quantity derived from  $\mathbf{C}$ . This is different for Eulerian quantities, such as the Cauchy stress, as shown below. The transformations of vectors and covectors are given by

$$\begin{aligned} \mathbf{t}^+ &= \mathbf{Q} \cdot \mathbf{t}, \\ (t^+)^a &= Q^a_b t^b, \end{aligned} \tag{4.74}$$

and

$$\begin{aligned} \mathbf{n}^+ &= \mathbf{g} \cdot \mathbf{Q} \cdot \mathbf{g}^{-1} \cdot \mathbf{n} = \mathbf{Q}^T \cdot \mathbf{n}, \\ (n^+)_a &= g_{ab} Q^b_c g^{cd} n_d = (\mathbf{Q}^T)_a^d n_d, \end{aligned} \tag{4.75}$$

where  $(\mathbf{Q}^T)_a^d = g_{ab} Q^b_c g^{cd}$  is the metric transpose, as defined in Eq. (2.70) on page 37. Cauchy's stress theorem from Eq. (4.29) on page 77, yields for both tractions  $\mathbf{t} = \boldsymbol{\sigma} \cdot \mathbf{n}$  and  $\mathbf{t}^+ = \boldsymbol{\sigma}^+ \cdot \mathbf{n}^+$ . This yields

$$\begin{aligned} \mathbf{t}^+ &= \mathbf{Q} \cdot \mathbf{t}, \\ \boldsymbol{\sigma}^+ \cdot \mathbf{n}^+ &= \mathbf{Q} \cdot \boldsymbol{\sigma} \cdot \mathbf{n}, \\ \boldsymbol{\sigma}^+ \cdot \mathbf{Q}^T \cdot \mathbf{n} &= \mathbf{Q} \cdot \boldsymbol{\sigma} \cdot \mathbf{n}, \end{aligned} \tag{4.76}$$

which gives by comparison

$$\boldsymbol{\sigma}^+ = \mathbf{Q} \cdot \boldsymbol{\sigma} \cdot \mathbf{Q}^t. \tag{4.77}$$

Note, that  $\mathbf{Q}^t$  denotes the algebraic transpose of  $\mathbf{Q}$ , see for details Eq. (2.71) on page 38. Strain energy functions, as given in Section 4.4, can also be investigated concerning their objectivity properties. These strain energy functions should yield the same energy, independent of superimposed rigid-body motions. This simply boils down to the requirement for different strain energy functions

$$\begin{aligned} \tilde{\psi}(\mathbf{F}) &= \tilde{\psi}(\mathbf{F}^+) = \tilde{\psi}(\mathbf{QF}), \\ \hat{\psi}(\mathbf{E}) &= \hat{\psi}(\mathbf{E}^+) = \hat{\psi}(\mathbf{E}), \\ \bar{\psi}(\mathbf{C}) &= \bar{\psi}(\mathbf{C}^+) = \bar{\psi}(\mathbf{C}). \end{aligned} \tag{4.78}$$



# 5

---

## The Non-linear Reissner-Mindlin Shell Model

This chapter focuses on the theoretical and computational derivation of the non-linear Reissner-Mindlin shell. First, geometric quantities, namely the kinematics of the shell, are stated. Then, the stress resultants from the three-dimensional stress state are derived in Section 5.2, followed by the balance laws for the shell's stress resultants in Section 5.3. Later, the corresponding correct variation and linearization using projection-based interpolation are derived in Section 5.5. In contrast to Müller and Bischoff [MB22], where everything is derived in terms of stress resultants, the derivations here assume a stress-based implementation. Furthermore, in Section 5.3.4 the Reissner-Mindlin assumptions are discussed.

By formulating everything in a stress-based manner, a more general formulation that accommodates non-trivial material laws is possible. However, this formulation requires addressing the vanishing transverse normal stress constraint, which is discussed in detail in Section 5.4. For an alternative perspective, readers are referred to textbooks such as Bařar and Krätzig [BK13], Green and Zerna [GZ63], Zerna [Zer67], and Green et al. [Gre71], as well as Simo and Fox [SF89] and subsequent papers [SF89; Sim90a; Sim90b; SK92; Sim92b]

## 5.1 Geometry and Kinematics

### 5.1.1 Motion, Configuration and Deformation

The set of all geometric descriptions of the shell structure can be stated as

$$\mathcal{M} = \{(\bar{\boldsymbol{\varphi}}, \bar{\mathbf{t}}) : \Omega \rightarrow \mathbb{R}^3 \times \mathcal{S}^2\}, \quad (5.1)$$

where  $\mathcal{B}_t^C$  is the deformed midsurface and  $\mathcal{S}^2$  is the two-dimensional unit sphere. This benign kinematic description is the source of the idiosyncrasies of non-linear Reissner-Mindlin shell formulations discussed in Chapter 6 on page 149. Therefore,  $\mathcal{M}$  represents the set of functions mapping from  $\Omega$  onto  $M = \mathbb{R}^3 \times \mathcal{S}^2$ . The set  $\Omega \subset \mathbb{R}^2$  is the two-dimensional parameter space. The points of the three-dimensional parameter space  $\mathcal{A} = \Omega \times [h^-, h^+]$  are defined as

$$\boldsymbol{\xi} = \xi^i \tilde{\mathbf{E}}_i \quad (5.2)$$

where  $\tilde{\mathbf{E}}_\alpha$  denote Cartesian base vectors. Furthermore,

$$\bar{\boldsymbol{\xi}} = \xi^\alpha \tilde{\mathbf{E}}_\alpha, \quad (5.3)$$

denotes the points on  $\Omega$  with  $\alpha \in [1, 2]$ . Here,  $h^-$  and  $h^+$  denote top and bottom surface coordinates of the shell and  $h = (h^+ - h^-)$  is the shell thickness. Furthermore, the parameterization of the shell's midsurface is given by

$$\boldsymbol{\varphi} : \Omega \rightarrow \mathcal{B}_t^C, \quad (5.4)$$

which induces a convective coordinate system, i.e., we have  $\boldsymbol{\xi} = \boldsymbol{\Theta} = \boldsymbol{\theta}$  in comparison to Section 4.1.1 on page 67. The director field is defined as

$$\mathbf{t} : \Omega \rightarrow \mathcal{S}^2, \quad (5.5)$$

which defines a field of unit vectors that are initially normal to the midsurface. The independent representation of  $\bar{\boldsymbol{\varphi}}$  and  $\bar{\mathbf{t}}$  allows the kinematic description of transverse shear deformation and thus realizes a Reissner-Mindlin type model. If two specific functions  $\boldsymbol{\varphi}_0$  and  $\mathbf{t}_0$  are chosen, the shell's reference geometry is defined. Using these quantities, the stress-free reference configuration reads

$$\mathcal{B}_0 = \{\mathbf{X} \in \mathbb{R}^3 \mid \mathbf{X} = \boldsymbol{\varphi}_0 + \xi^3 \mathbf{t}_0 \text{ with } (\boldsymbol{\varphi}_0, \mathbf{t}_0) \in \mathcal{M} \text{ and } \xi^3 \in [h^-, h^+] \subset \mathbb{R}\}. \quad (5.6)$$



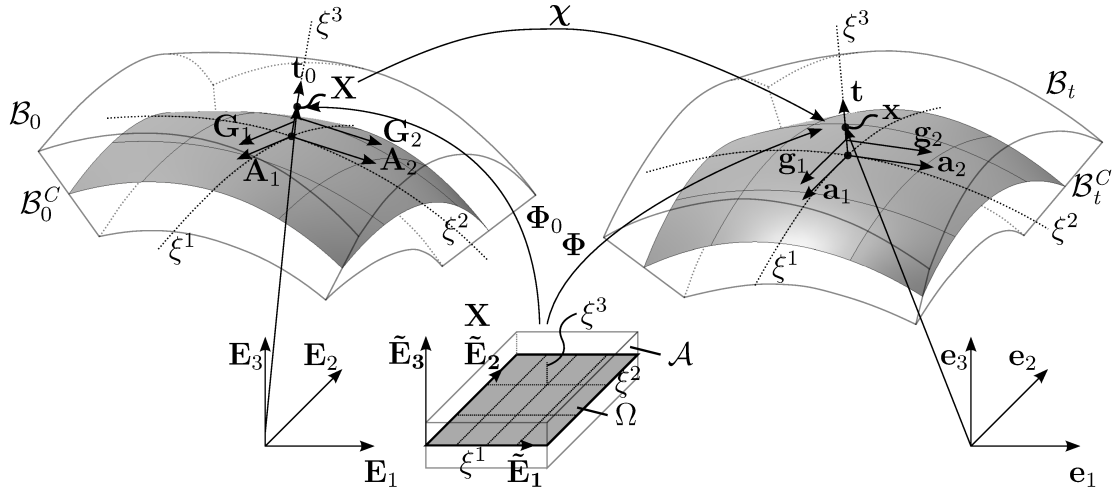


**Figure 5.1:** Kinematics of the shell. Reference and current configuration.

Similarly, a configuration at time  $t$  is given by

$$\mathcal{B}_t = \{\mathbf{x} \in \mathbb{R}^3 \mid \mathbf{x} = \boldsymbol{\varphi} + \xi^3 \mathbf{t} \text{ with } (\boldsymbol{\varphi}, \mathbf{t}) \in \mathcal{M} \text{ and } \xi^3 \in [h^-, h^+] \subset \mathbb{R}\}. \quad (5.7)$$

The reference and current positions of a point in the shell body are given by the parameterizations

$$\begin{aligned} \mathbf{X} &= \boldsymbol{\Phi}_0(\boldsymbol{\xi}) = \boldsymbol{\varphi}_0(\xi^1, \xi^2) + \xi^3 \mathbf{t}_0(\xi^1, \xi^2), \\ \mathbf{x} &= \boldsymbol{\Phi}(\boldsymbol{\xi}) = \boldsymbol{\varphi}(\xi^1, \xi^2) + \xi^3 \mathbf{t}(\xi^1, \xi^2), \end{aligned} \quad (5.8)$$

where the maps  $\boldsymbol{\Phi} : \mathcal{A} \rightarrow \mathcal{B}_t$  and  $\boldsymbol{\Phi}_0 : \mathcal{A} \rightarrow \mathcal{B}_0$ , respectively, are defined. These maps define a curvilinear coordinate system  $\boldsymbol{\xi}$  in the reference and current configuration, as depicted in Fig. 5.1. In this figure, the reference configuration is shown on the left-hand side, and the current configuration is on the right-hand side. Therein, the midsurfaces are shown and the shell's bodies are indicated. The mappings from the parameter space  $\Omega$  to the shell's bodies are also indicated and thereby the parameterization  $\boldsymbol{\Phi}_0$  and  $\boldsymbol{\Phi}$  are visualized. The corresponding tangent vectors are indicated by arrows. The deformation is then defined as a mapping  $\chi_t : \mathcal{B}_0 \rightarrow \mathcal{B}_t$  with

$$\chi_t = \boldsymbol{\Phi} \circ \boldsymbol{\Phi}_0^{-1}. \quad (5.9)$$

The spatial velocity and spatial acceleration read

$$\begin{aligned} \mathbf{v} &= \dot{\boldsymbol{\Phi}}(\boldsymbol{\xi}) = \dot{\boldsymbol{\varphi}}(\xi^1, \xi^2) + \xi^3 \dot{\mathbf{t}}(\xi^1, \xi^2), \\ \mathbf{a} &= \ddot{\boldsymbol{\Phi}}(\boldsymbol{\xi}) = \ddot{\boldsymbol{\varphi}}(\xi^1, \xi^2) + \xi^3 \ddot{\mathbf{t}}(\xi^1, \xi^2). \end{aligned} \quad (5.10)$$

This definition exploits the parameterization as a shortcut to define the spatial velocity. More formally and following Eqs. (4.10) and (4.12) on page 70,

$$\mathbf{v}(\boldsymbol{\xi}, t) = \frac{d\boldsymbol{\chi}(\boldsymbol{\chi}^{-1}(\boldsymbol{\Phi}(\boldsymbol{\xi}), t), t)}{dt} = \frac{d\boldsymbol{\Phi}(\boldsymbol{\xi})}{dt}, \quad (5.11)$$

and equivalently for the spatial acceleration

$$\mathbf{a}(\boldsymbol{\xi}, t) = \frac{d^2\boldsymbol{\Phi}(\boldsymbol{\xi})}{dt^2}. \quad (5.12)$$

Furthermore, the objects  $\dot{\mathbf{t}}$  and  $\ddot{\mathbf{t}}$  are elements of the tangent bundle of the unit sphere  $T\mathcal{S}^2$ . Therefore, special care has to be taken in the following derivation to reflect this peculiarity. This fact is often accompanied by the definition of angular velocity, which is defined as

$$\dot{\mathbf{t}} = \mathbf{w} \times \mathbf{t}, \quad (5.13)$$

where  $\mathbf{w} \in T\mathcal{S}^2$ , but now the fact that  $\dot{\mathbf{t}}$  is an element of the tangent bundle  $T\mathcal{S}^2$  is made explicit.

REMARK 2. The configuration space  $\mathcal{M}$  can be interpreted as a fiber bundle. The base space is the midsurface  $\mathcal{B}_t^C$  and the directors living on the unit sphere  $\mathcal{S}^2$  are the fibers. This is in high contrast to the three-dimensional case from Chapter 4 on page 67, where the configuration space is no fiber bundle, except for Cosserat-type theories, where the base space would be  $\mathbb{R}^3$  and the fibers  $\mathcal{SO}(3)$ . Furthermore, it is worth noting that in this work only trivial fiber bundles are considered. Thus, in a more engineering voice, shells with kinks are not considered, since at the kinks two directors need to be defined, which makes the fiber bundle non-trivial.

### 5.1.2 Tangent Space Mappings

From the three-dimensional setting, the Jacobian of the shell's body can be directly used. Thus, from Eq. (4.9) on page 69, the Jacobians  $\mathbf{J}, \mathbf{j}$  are not repeated here. The metrics of the shell's reference and current configuration read

$$\mathbf{g} = \mathbf{j}^T \cdot \mathbf{j} = \mathbf{g}_i \cdot \mathbf{g}_j = g_{ij} \quad \text{and} \quad \mathbf{G} = \mathbf{J}^T \cdot \mathbf{J} = \mathbf{G}_i \cdot \mathbf{G}_j = G_{ij}. \quad (5.14)$$

Furthermore, the deformation gradient as given in Section 4.1.2 on page 71, now referring to the shell's body, is given as

$$\mathbf{F} = \mathbf{j} \cdot \mathbf{J}^{-1}. \quad (5.15)$$

Additionally, all these maps, Eqs. (5.7) and (5.9) can be restricted to the midsurface  $\xi^3 = 0$ . This yields

$$\bar{\boldsymbol{\chi}} = \boldsymbol{\chi}\Big|_{\xi^3=0}, \quad \hat{\mathbf{J}} = \mathbf{J}\Big|_{\xi^3=0}, \quad \hat{\mathbf{j}} = \mathbf{j}\Big|_{\xi^3=0} \quad \text{and} \quad \hat{\mathbf{F}} = \nabla \bar{\boldsymbol{\chi}} = \mathbf{F}\Big|_{\xi^3=0}. \quad (5.16)$$

Furthermore, the Jacobians of the two-dimensional midsurface mapping  $\boldsymbol{\varphi}$  are

$$\bar{\mathbf{J}} = \nabla \boldsymbol{\varphi}_0, \quad \bar{\mathbf{j}} = \nabla \boldsymbol{\varphi} \quad \text{and} \quad \bar{\mathbf{F}} = \boldsymbol{\varphi} \circ \boldsymbol{\varphi}_0^{-1}. \quad (5.17)$$

The parameterization in Eq. (5.8) defines a coordinate basis for both the reference and the current configuration as given in Eq. (2.16). These two bases  $\{\mathbf{g}_i\}_{i=1..3}$  and  $\{\mathbf{G}_I\}_{I=1..3}$  are given by

$$\begin{aligned} \frac{\partial \mathbf{x}}{\partial \xi^\alpha} &= \mathbf{g}_\alpha = \boldsymbol{\varphi}_{,\alpha} + \xi^3 \mathbf{t}_{,\alpha} = \mathbf{a}_\alpha + \xi^3 \mathbf{t}_{,\alpha}, \\ \frac{\partial \mathbf{x}}{\partial \xi^3} &= \mathbf{g}_3 = \mathbf{a}_3 = \mathbf{t}, \\ \frac{\partial \mathbf{X}}{\partial \xi^\alpha} &= \mathbf{G}_\alpha = \boldsymbol{\varphi}_{0,\alpha} + \xi^3 \mathbf{t}_{0,\alpha} = \mathbf{A}_\alpha + \xi^3 \mathbf{t}_{0,\alpha}, \\ \frac{\partial \mathbf{X}}{\partial \xi^3} &= \mathbf{G}_3 = \mathbf{A}_3 = \mathbf{t}_0, \end{aligned} \quad (5.18)$$

which are also depicted in Fig. 5.1. Additionally, the midsurface parameterization given by Eq. (5.4) also induces a coordinate basis for the reference and current midsurfaces, respectively. These are denoted by  $\mathbf{a}_\alpha = \boldsymbol{\varphi}_{,\alpha}$  and  $\mathbf{A}_\alpha = \boldsymbol{\varphi}_{0,\alpha}$ . As indicated,  $\{\mathbf{G}_I\}$  and  $\{\mathbf{g}_i\}$  define two bases on the tangent space on the reference  $T_{\mathbf{x}}\mathcal{B}_0$  and the tangent space on the current configuration  $T_{\mathbf{x}}\mathcal{B}_t$ , respectively. Similarly,  $\{\mathbf{A}_I\}$  and  $\{\mathbf{a}_i\}$  also define a basis, but on the shell's midsurface on the reference configuration  $T_{\boldsymbol{\varphi}_0}\mathcal{B}_0^C$  and on the current configuration  $T_{\boldsymbol{\varphi}}\mathcal{B}_t^C$ . Thus, this yields the midsurface mapping of Eq. (5.16)

$$\begin{aligned} \hat{\mathbf{j}} &: \begin{cases} T_{\boldsymbol{\xi}}\mathcal{A} \rightarrow T_{\boldsymbol{\varphi}_0}\mathcal{B}_0^C, \\ \boldsymbol{\xi} \mapsto \nabla_{\boldsymbol{\xi}} \mathbf{X}|_{\xi^3=0} = [\mathbf{A}_1, \mathbf{A}_2, \mathbf{t}_0], \end{cases} & \hat{\mathbf{j}} &: \begin{cases} T_{\boldsymbol{\theta}}\mathcal{A} \rightarrow T_{\boldsymbol{\varphi}}\mathcal{B}_t^C, \\ \boldsymbol{\xi} \mapsto \nabla_{\boldsymbol{\xi}} \mathbf{x}|_{\xi^3=0} = [\mathbf{a}_1, \mathbf{a}_2, \mathbf{t}], \end{cases} \\ \hat{\mathbf{j}}^{-T} &: \begin{cases} T_{\boldsymbol{\xi}}^*\mathcal{A} \rightarrow T_{\boldsymbol{\varphi}_0}^*\mathcal{B}_0^C, \\ \boldsymbol{\xi} \mapsto (\nabla_{\boldsymbol{\xi}} \mathbf{X}|_{\xi^3=0})^{-T} = [\mathbf{A}^1, \mathbf{A}^2, \mathbf{A}^3], \end{cases} & \hat{\mathbf{j}}^{-T} &: \begin{cases} T_{\boldsymbol{\xi}}^*\mathcal{A} \rightarrow T_{\boldsymbol{\varphi}}^*\mathcal{B}_t^C, \\ \boldsymbol{\xi} \mapsto (\nabla_{\boldsymbol{\xi}} \mathbf{x}|_{\xi^3=0})^{-T} = [\mathbf{a}^1, \mathbf{a}^2, \mathbf{a}^3], \end{cases} \end{aligned} \quad (5.19)$$

and for Eq. (5.17)

$$\begin{aligned}
 \bar{\mathbf{J}} &: \begin{cases} T_{\bar{\xi}} \mathcal{A} \rightarrow T_{\varphi_0} \mathcal{B}_0^C, \\ \bar{\xi} \mapsto \nabla_{\bar{\xi}} \varphi_0 = [\mathbf{A}_1, \mathbf{A}_2], \end{cases} & \bar{\mathbf{j}} &: \begin{cases} T_{\theta} \mathcal{A} \rightarrow T_{\varphi} \mathcal{B}_t^C, \\ \bar{\xi} \mapsto \nabla_{\bar{\xi}} \varphi = [\mathbf{a}_1, \mathbf{a}_2], \end{cases} \\
 \bar{\mathbf{J}}^{-T} &: \begin{cases} T_{\bar{\xi}}^* \mathcal{A} \rightarrow T_{\varphi_0}^* \mathcal{B}_0^C, \\ \bar{\xi} \mapsto (\nabla_{\bar{\xi}} \varphi_0)^{-T} = [\mathbf{A}^1, \mathbf{A}^2], \end{cases} & \bar{\mathbf{j}}^{-T} &: \begin{cases} T_{\bar{\xi}}^* \mathcal{A} \rightarrow T_{\varphi}^* \mathcal{B}_t^C, \\ \bar{\xi} \mapsto (\nabla_{\bar{\xi}} \varphi)^{-T} = [\mathbf{a}^1, \mathbf{a}^2], \end{cases}
 \end{aligned} \tag{5.20}$$

where  $\bar{\xi}$  was defined in Eq. (5.3).

### 5.1.3 Shell Shifter and Transformation of Integrals

At this point, the given tensors are defined in the base  $\{\mathbf{G}_i\}$  and  $\{\mathbf{g}_i\}$ . Occasionally, it is convenient or necessary to represent these tensors on the shell midsurface tangent basis  $\{\mathbf{A}_i\}$  and  $\{\mathbf{a}_i\}$ . This is simply done by a coordinate transformation. For the representation of the tensors in the midsurface base system, a tensor that maps between the shell's midsurface base vectors and the shell's body base vectors is needed, i.e.  $\mathbf{g}_a = \mathbf{z} \cdot \mathbf{a}_b$ . This tensor is called *shifter tensor* or *shell shifter*.

Similar to the mapping of the deformation gradient  $\mathbf{g}_a = \mathbf{F} \cdot \mathbf{G}_A$  the shifter tensors  $\mathbf{Z}$  and  $\mathbf{z}$  for the reference configuration and current configuration can be defined as

$$\begin{aligned}
 \mathbf{z} &= (\delta^\mu_\alpha + \xi^3 b^\mu_\alpha) \mathbf{a}_\mu \otimes \mathbf{a}^\alpha - \xi^3 b^\mu_\alpha \gamma_\mu \mathbf{t} \otimes \mathbf{a}^\alpha + \mathbf{t} \otimes \mathbf{a}^3, \\
 \mathbf{Z} &= (\delta^\mu_\alpha + \xi^3 B^\mu_\alpha) \mathbf{A}_\mu \otimes \mathbf{A}^\alpha + \mathbf{t}_0 \otimes \mathbf{A}^3,
 \end{aligned} \tag{5.21}$$

with  $b_{\beta\alpha} = \mathbf{t}_{,\beta} \cdot \mathbf{a}_\alpha$  and  $b^\mu_\alpha = a^{\mu\beta} b_{\beta\alpha}$  and equivalently for the reference configuration. Here,  $a^{\mu\beta}$  denotes the coefficients of the metric inverse of the midsurface, such that  $a_{\mu\beta} = \mathbf{a}_\alpha \cdot \mathbf{a}_\beta$ . For a derivation, see Appendix A.6. All these mappings are visually summarized in Fig. 5.2. Therein, the interplay between the mappings of tangent spaces and co-tangent spaces is indicated and also their commutative relations are made graphically clear.

From the definition of the determinant for mixed tensors Eq. (2.101), it results that the determinant of the shifter tensor  $\det \mathbf{z}$  is merely the determinant of its component matrix  $\det([z^\mu_\alpha])$ . It can be shown that this determinant is given by

$$\det \mathbf{z} = \det([z^\mu_\alpha]) = 1 - 2\xi^3 H + (\xi^3)^2 K, \tag{5.22}$$

where the shortcuts  $K = \det([b^\mu_\alpha])$  and  $H = -(b^1_1 + b^2_2)/2$  were used. The scalars  $K$  and  $H$ , for the case where  $\mathbf{t}$  is the midsurface unit normal, exactly boil down to the usual surface definitions of *Gaussian curvature* and *mean curvature*. The same statement can be derived for the reference configuration. For details, see Appendix A.7 on page 205.

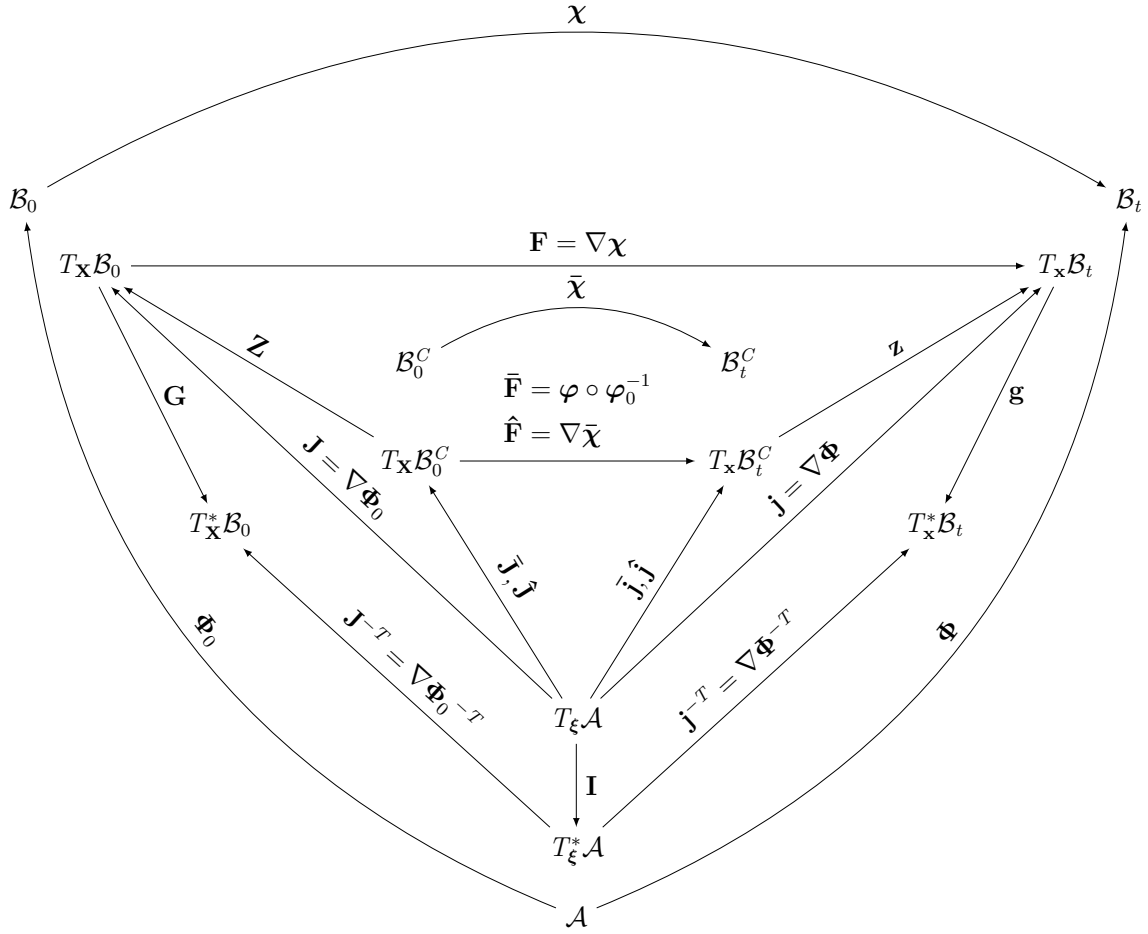


**Figure 5.2:** Linear and non-linear commutative mapping diagram of the shell's body and the shell midsurface.

Additionally, for a convenient reference, all the relevant mappings are summarized in Table 5.1.

**Through-the-thickness Integration** In the following, several quantities are interpreted as integrated quantities on the reference midsurface or current midsurface. This relation is often attributed to the determinant of the shifter tensor but, as it is shown in the following, this is not always the correct quantity.

In the end, the three-dimensional integration element  $\mathbf{dv}$  should be expressed as an object of the through-the-thickness integration element  $\mathbf{dl}$  and the midsurface integration element  $\mathbf{da}$ . In particular, this means splitting the Riemannian volume form up into a surface form and a line form. This generically yields

$$\mathbf{dv} = \mathbf{dl} \cdot \mathbf{da} = z \, d\xi^3 \, \mathbf{da}. \quad (5.23)$$

**Table 5.1:** Summary of different tensorial mappings in the shell body and on the shell's midsurface. All the quantity expressions are given in the convective coordinate basis  $\{\mathbf{G}_i\}$ ,  $\{\mathbf{g}_i\}$ ,  $\{\mathbf{A}_i\}$ ,  $\{\mathbf{a}_i\}$  and their contravariant counterparts.

Mapping	Component-free	Index notation	Determinant	Expression
$\mathbf{J}$ $T_\xi \mathcal{A} \rightarrow T_{\mathbf{X}} \mathcal{B}_0$	$\nabla \Phi_0$	$[\mathbf{G}_1, \mathbf{G}_2, \mathbf{G}_3]^{ij}$	$J$	$\mathbf{G}_3 \cdot (\mathbf{G}_1 \times \mathbf{G}_2)$
$\mathbf{j}$ $T_\xi \mathcal{A} \rightarrow T_{\mathbf{x}} \mathcal{B}_t$	$\nabla \Phi$	$[\mathbf{g}_1, \mathbf{g}_2, \mathbf{g}_3]^{ij}$	$j$	$\mathbf{g}_3 \cdot (\mathbf{g}_1 \times \mathbf{g}_2)$
$\mathbf{G}$ $T_{\mathbf{X}} \mathcal{B}_0 \rightarrow T_{\mathbf{X}}^* \mathcal{B}_0$	$\mathbf{J}^T \cdot \mathbf{J}$	$\mathbf{G}_I \cdot \mathbf{G}_J$	$G$	$\det([G_A{}^B]) = 1$
$\mathbf{g}$ $T_{\mathbf{x}} \mathcal{B}_t \rightarrow T_{\mathbf{x}}^* \mathcal{B}_t$	$\mathbf{j}^T \cdot \mathbf{j}$	$\mathbf{g}_i \cdot \mathbf{g}_j$	$g$	$\det([g_a{}^b]) = 1$
$\mathbf{F}$ $T_{\mathbf{X}} \mathcal{B}_0 \rightarrow T_{\mathbf{x}} \mathcal{B}_t$	$\mathbf{j} \cdot \mathbf{J}^{-1}$	$\delta^i{}_J \mathbf{g}_i \otimes \mathbf{G}^J$	$\det \mathbf{F} = j/J$	$\frac{\sqrt{\det([g_{ab}]})}{\sqrt{\det([G_{AB}]})}$
$\bar{\mathbf{J}}$ $T_\xi \Omega \rightarrow T_{\varphi_0} \mathcal{B}_0^C$	$\nabla \varphi_0$	$[\mathbf{A}_1, \mathbf{A}_2]^{I\alpha}$	$\bar{J}$	$\sqrt{\det([A_{\alpha\beta}]})$
$\hat{\mathbf{J}}$ $T_\xi \Omega \rightarrow T_{\varphi_0} \mathcal{B}_0^C$	$\nabla \Phi_0 _{\xi^3=0}$	$[\mathbf{A}_1, \mathbf{A}_2, \mathbf{t}_0]^{IJ}$	$\hat{J}$	$\mathbf{A}_3 \cdot (\mathbf{A}_1 \times \mathbf{A}_2)$
$\bar{\mathbf{j}}$ $T_\xi \Omega \rightarrow T_\varphi \mathcal{B}_t^C$	$\nabla \varphi$	$[\mathbf{a}_1, \mathbf{a}_2]^{i\alpha}$	$\bar{j}$	$\sqrt{\det([a_{\alpha\beta}]})$
$\hat{\mathbf{j}}$ $T_\xi \Omega \rightarrow T_\varphi \mathcal{B}_t^C$	$\nabla \Phi _{\xi^3=0}$	$[\mathbf{a}_1, \mathbf{a}_2, \mathbf{t}]^{ij}$	$\hat{j}$	$\mathbf{a}_3 \cdot (\mathbf{a}_1 \times \mathbf{a}_2)$
$\mathbf{A}$ $T_{\varphi_0} \mathcal{B}_0^C \rightarrow T_{\varphi_0}^* \mathcal{B}_0^C$	$\bar{\mathbf{J}}^T \cdot \bar{\mathbf{J}}$	$\mathbf{A}_\alpha \cdot \mathbf{A}_\beta$	$A$	$\det([A_\alpha{}^\beta]) = 1$
$\mathbf{a}$ $T_\varphi \mathcal{B}_t^C \rightarrow T_\varphi^* \mathcal{B}_t^C$	$\bar{\mathbf{j}}^T \cdot \bar{\mathbf{j}}$	$\mathbf{a}_\alpha \cdot \mathbf{a}_\beta$	$a$	$\det([a_\alpha{}^\beta]) = 1$
$\mathbf{Z}$ $T_{\varphi_0} \mathcal{B}_0^C \rightarrow T_{\mathbf{X}} \mathcal{B}_0$	$\mathbf{J} \cdot \hat{\mathbf{J}}^{-1}$	$\delta^I{}_J \mathbf{G}_I \otimes \mathbf{A}^J$	$\det \mathbf{Z} = J/\hat{J}$	$1 - 2\xi^3 H_0 + (\xi^3)^2 K_0$
$\mathbf{z}$ $T_\varphi \mathcal{B}_t^C \rightarrow T_{\mathbf{x}} \mathcal{B}_t$	$\mathbf{j} \cdot \hat{\mathbf{j}}^{-1}$	$\delta^i{}_j \mathbf{g}_i \otimes \mathbf{a}^j$	$\det \mathbf{z} = j/\hat{j}$	$1 - 2\xi^3 H + (\xi^3)^2 K$
$\bar{\mathbf{F}}$ $T_{\mathbf{X}} \mathcal{B}_0^C \rightarrow T_{\mathbf{x}} \mathcal{B}_t^C$	$\bar{\mathbf{j}} \cdot \bar{\mathbf{J}}^{-1}$	$\delta^\alpha{}_\alpha \mathbf{a}_i \otimes \mathbf{A}^J$	$\det \bar{\mathbf{F}} = \bar{j}/\bar{J}$	$\frac{\sqrt{\det([a_{\alpha\beta}]})}{\sqrt{\det([A_{\alpha\beta}]})}$
$\mathbf{B}$ $T_{\varphi_0}^* \mathcal{B}_0^C \rightarrow T_{\varphi_0} \mathcal{B}_0^C$	$[\mathbf{t}_{0,1}, \mathbf{t}_{0,2}]^T \cdot \bar{\mathbf{J}}$	$\mathbf{t}_{0,\beta} \cdot \mathbf{A}_\alpha \mathbf{A}^\beta \otimes \mathbf{A}^\alpha$	$\det \mathbf{B}$	$\frac{\det([B_{\alpha\beta}])}{\det([A_{\alpha\beta}])} = K_0$
$\mathbf{b}$ $T_\varphi^* \mathcal{B}_t^C \rightarrow T_\varphi \mathcal{B}_t^C$	$[\mathbf{t}_{,1}, \mathbf{t}_{,2}]^T \cdot \bar{\mathbf{j}}$	$\mathbf{t}_{,\beta} \cdot \mathbf{a}_\alpha \mathbf{a}^\beta \otimes \mathbf{a}^\alpha$	$\det \mathbf{b}$	$\frac{\det([b_{\alpha\beta}])}{\det([a_{\alpha\beta}])} = K$
			$z = j/\bar{j}$	$\frac{\sqrt{\det([g_{ij}]})}{\sqrt{\det([a_{\alpha\beta}]})}$
			$Z = J/\bar{J}$	$\frac{\sqrt{\det([G_{IJ}]})}{\sqrt{\det([A_{\alpha\beta}]})}$

Therefore, following Sections 2.8.2 and 2.8.4 and Eq. (2.103) on pages 43, 45 and 46, the midsurface integration element reads  $\mathbf{d}\mathbf{a} = \sqrt{\det([a_{ab}])} d\xi^1 d\xi^2 = \|\mathbf{a}_1 \times \mathbf{a}_2\| d\xi^1 d\xi^2$  and the volume integration element reads

$$\begin{aligned}
 d\mathbf{v} &= \sqrt{\det([g_{ab}])} dv = \mathbf{g}_1 \cdot (\mathbf{g}_2 \times \mathbf{g}_3) d\xi^1 d\xi^2 d\xi^3 = \frac{\mathbf{g}_1 \cdot (\mathbf{g}_2 \times \mathbf{g}_3)}{\sqrt{\det([a_{ab}])}} \sqrt{\det([a_{ab}])} d\xi^1 d\xi^2 d\xi^3 \\
 &= \frac{\mathbf{g}_3 \cdot (\mathbf{g}_1 \times \mathbf{g}_2)}{\|\mathbf{a}_1 \times \mathbf{a}_2\|} \|\mathbf{a}_1 \times \mathbf{a}_2\| d\xi^1 d\xi^2 d\xi^3 = \frac{\mathbf{g}_3 \cdot (\mathbf{g}_1 \times \mathbf{g}_2)}{\|\mathbf{a}_1 \times \mathbf{a}_2\|} d\xi^3 \mathbf{d}\mathbf{a}.
 \end{aligned} \tag{5.24}$$

Comparing the last equality to Eq. (5.23), we get for the current configuration the scalar quantity

$$z = \frac{\mathbf{g}_3 \cdot (\mathbf{g}_1 \times \mathbf{g}_2)}{\|\mathbf{a}_1 \times \mathbf{a}_2\|}, \quad (5.25)$$

and for the reference configuration

$$Z = \frac{\mathbf{G}_3 \cdot (\mathbf{G}_1 \times \mathbf{G}_2)}{\|\mathbf{A}_1 \times \mathbf{A}_2\|}. \quad (5.26)$$

REMARK 3. The Eq. (5.25) does *not* correspond to the determinant of the shell shifter as given in Eq. (5.22). Nevertheless, they are the same, if the director  $\mathbf{t}$  is the shell's unit normal, e.g. in the context of a Kirchhoff-Love-type deformation. The quantity given in Eq. (5.22) can be restated as

$$\det \mathbf{z} = \frac{\mathbf{g}_3 \cdot (\mathbf{g}_1 \times \mathbf{g}_2)}{\mathbf{t} \cdot (\mathbf{a}_1 \times \mathbf{a}_2)}, \quad (5.27)$$

which differs from  $z$  in the denominator. Alternatively, if the shell shifter's defining statement  $\mathbf{g}_a = \mathbf{z} \cdot \mathbf{a}_b$  would be restated with  $\mathbf{a}_3 = \mathbf{a}_1 \times \mathbf{a}_2$  instead of  $\mathbf{a}_3 = \mathbf{t}$ , they would directly coincide, see also for similar remarks Büchter [Büc92]. Nevertheless, they are sometimes, in the author's humble opinion, wrongly used to transform integrals and push-forward or pull-back quantities, see, e.g., Simo et al. [Sim90a, Eq. 2.13] and subsequent derivations. Usually the deviation of  $\mathbf{t}$  from the shell normal is small and therefore these errors are usually not very pronounced.

### 5.1.4 Strain

The definition of the Green-Lagrangian strain tensor can directly be taken from Eq. (4.23). It is given by

$$\mathbf{E} = E_{ij} \mathbf{G}^i \otimes \mathbf{G}^j, \quad (5.28)$$

with the components

$$\begin{aligned}
 E_{\alpha\beta} &= \frac{1}{2}(g_{\alpha\beta} - G_{\alpha\beta}) = \frac{1}{2}(\mathbf{g}_\alpha \cdot \mathbf{g}_\beta - \mathbf{G}_\alpha \cdot \mathbf{G}_\beta) \\
 &= \varepsilon_{\alpha\beta} + 2\xi^3 \kappa_{\alpha\beta} + (\xi^3)^2 \rho_{\alpha\beta}, \\
 2E_{\alpha 3} &= 2E_{3\alpha} = \mathbf{g}_\alpha \cdot \mathbf{g}_3 - \mathbf{G}_\alpha \cdot \mathbf{G}_3 = \gamma_\alpha, \\
 2E_{33} &= \mathbf{g}_3 \cdot \mathbf{g}_3 - \mathbf{G}_3 \cdot \mathbf{G}_3 = 0.
 \end{aligned} \tag{5.29}$$

Since in the following a stress-based implementation is derived, it is enough to derive this in the  $\mathbf{G}^i \otimes \mathbf{G}^j$ -basis. Here, the usual Reissner-Mindlin kinematic assumptions  $\mathbf{t}_{,\alpha} \cdot \mathbf{t} = 0$  and  $\mathbf{t} \cdot \mathbf{t} = \mathbf{t}_0 \cdot \mathbf{t}_0 = 1$  apply via the unit director definition of  $\mathbf{t}$ . The quadratic part  $\rho_{\alpha\beta}$  of  $E_{\alpha\beta}$  in  $\xi^3$  is usually neglected but is kept here for the sake of completeness. For the implications of neglecting it, see Büchter [Büc92, Chapter 3.7, Annahme A4, Chapter 9.1.3, Equation 9.34]. The different components in Eq. (5.29) can be interpreted as membrane strain  $\varepsilon_{\alpha\beta}$ , curvature  $\kappa_{\alpha\beta}$ , second-order curvature  $\rho_{\alpha\beta}$ , and transverse shear strain  $\gamma_\alpha$ . They read

$$\begin{aligned}
 \varepsilon_{\alpha\beta} &= \frac{1}{2}(\mathbf{a}_\alpha \cdot \mathbf{a}_\beta - \mathbf{A}_\alpha \cdot \mathbf{A}_\beta), \\
 \kappa_{\alpha\beta} &= \frac{1}{2}(\mathbf{a}_\alpha \cdot \mathbf{t}_{,\beta} + \mathbf{t}_{,\alpha} \cdot \mathbf{a}_\beta - \mathbf{A}_\alpha \cdot \mathbf{t}_{0,\beta} - \mathbf{t}_{0,\alpha} \cdot \mathbf{A}_\beta), \\
 \rho_{\alpha\beta} &= \frac{1}{2}(\mathbf{t}_{,\alpha} \cdot \mathbf{t}_{,\beta} - \mathbf{t}_{0,\alpha} \cdot \mathbf{t}_{0,\beta}), \\
 \gamma_\alpha &= \mathbf{a}_{,\alpha} \cdot \mathbf{t} - \mathbf{A}_{,\alpha} \cdot \mathbf{t}_0.
 \end{aligned} \tag{5.30}$$

The definitions Eq. (5.30) provide a straightforward method for phenomenologically interpreting the three-dimensional strains as shell quantities. Vanishing membrane strain, for instance, indicates a shell deformation in which the midsurface is only bent and not stretched. Therefore, for such deformation the corresponding midsurface deformation is isometric.

Furthermore, according to a Voigt-like notation the strain matrix components can be vectorized as

$$\mathbf{E}_V = \begin{bmatrix} E_{11} \\ E_{22} \\ 2E_{12} \\ 2E_{13} \\ 2E_{23} \end{bmatrix} \tag{5.31}$$



## 5.2 Stress Resultants

This section deals with the definition of stress resultants. First, the physical stress resultants from the Cauchy stress are derived in Section 5.2.1 as component-free vectorial quantities. For more physical insight, the correct components of these vectorial quantities are investigated in Section 5.2.2. The following derivations can be partially found in [Sim89] and for the case of the Kirchhoff-Love shell with other simplifications in [BK13]. For completeness, the definitions of these stress resultants are given here including derivation, since they, in the author's humble opinion, cannot be found in the literature in this detailed form.

### 5.2.1 Cauchy Stress Resultants

In the following, to derive resultants of the Cauchy stress w.r.t. to the coordinates  $\xi^i$ , consider a cut with  $\xi^1 = \text{const.}$  denoted by

$$\mathcal{C}_2 = \{\mathbf{x} \in \mathbb{R}^3 \mid \mathbf{x} = \Phi|_{\xi^2=\text{const.}}\}, \quad (5.32)$$

and the corresponding midsurface line by

$$\mathcal{C}_2^C = \{\mathbf{x} \in \mathbb{R}^3 \mid \mathbf{x} = \Phi|_{\xi^2=\text{const.}, \xi^3=0}\}. \quad (5.33)$$

In the following, the reader can track the derivations with Fig. 5.3. In the cuboid-shaped parameter space, the one-form field normal to the surface of this cut can be defined as  $\tilde{\mathbf{N}} d\xi^2 d\xi^3 = \tilde{\mathbf{E}}^2 d\xi^1 d\xi^3$ . Since the Cauchy stress lives in the current configuration, this normal has to be pushed forward to get the normal of the deformed surface with  $\xi^1 = \text{const.}$ . This map transforms the normal from the parameter space to the current configuration, which is denoted by  $\Phi_*$  in Fig. 5.3.

This is done using the Piola transform from Section 2.8.5 on page 47, which defines the push-forward of normals. This yields

$$\Phi_*(\tilde{\mathbf{E}}^2 d\xi^1 d\xi^3) = j\mathbf{j}^{-T} \cdot \tilde{\mathbf{E}}^2 d\xi^1 d\xi^3 = j\mathbf{g}^2 d\xi^1 d\xi^3 \quad (5.34)$$

as the push-forward from the parameter space to the current configuration.

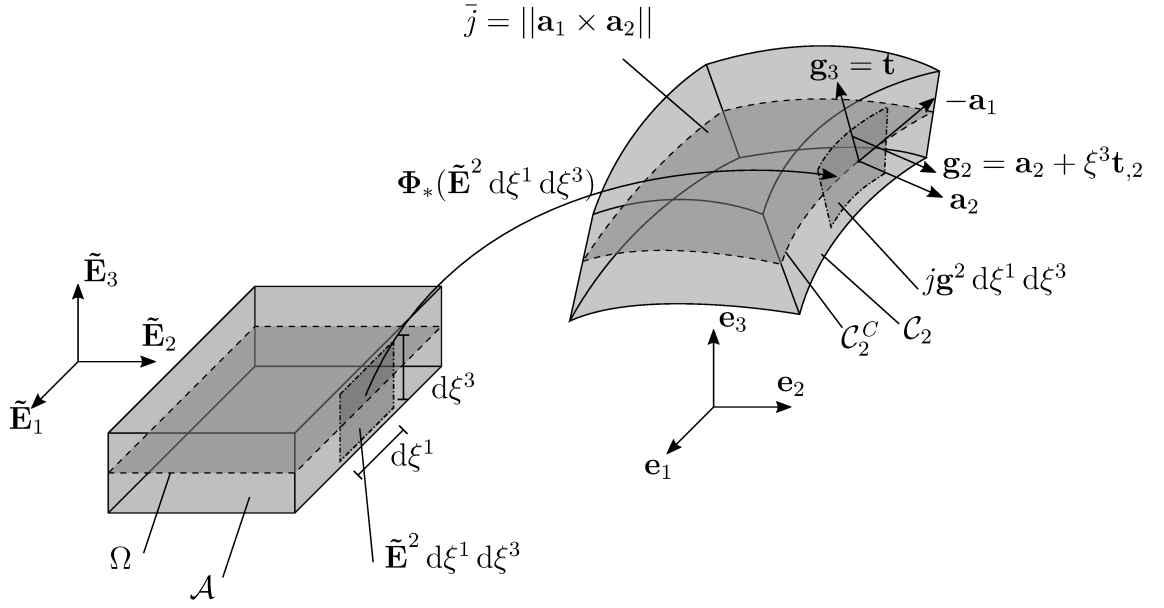


**Figure 5.3:** Push-forward operation of the normal of the cut in the parameter space to the current configuration.

Now, the integration over the thickness coordinate of the traction defined via this surface normal and the Cauchy stresses using Cauchy theorem from Eq. (4.29), reads

$$\mathbf{T}^2 = \int_{h^-}^{h^+} j \boldsymbol{\sigma} \cdot \mathbf{g}^2 d\xi^3. \quad (5.35)$$

Integrating  $\mathbf{T}^2$  over the rest of the domain, i.e. over  $\xi^1$  and  $\xi^2$ , reads

$$\hat{\mathbf{T}}^2 = \int \int \int_{h^-}^{h^+} j \boldsymbol{\sigma} \cdot \mathbf{g}^2 d\xi^3 d\xi^2 d\xi^1. \quad (5.36)$$

As elaborated already in Section 4.3.2 on page 82 the vectorial integrals over the two-dimensional domain only make sense, if a Cartesian basis is used. Since, these integrations are not carried out but are used only to define the stress resultants, no specific choice is needed. Similarly, the to-be-determined *stress resultant*  $\mathbf{n}^2$  is integrated over the midsurface. This reads

$$\hat{\mathbf{T}}^2 = \int \int \mathbf{n}^2 d\mathbf{a} = \int \int \mathbf{n}^2 \bar{j} da = \int \int \mathbf{n}^2 \bar{j} d\xi^1 d\xi^2. \quad (5.37)$$

Equating Eqs. (5.36) and (5.37) yields

$$\int \int \mathbf{n}^2 \bar{j} \, d\xi^1 \, d\xi^2 = \int \int \int_{h^-}^{h^+} j \boldsymbol{\sigma} \cdot \mathbf{g}^2 \, d\xi^3 \, d\xi^2 \, d\xi^1. \quad (5.38)$$

By comparing coefficients in Eq. (5.38) the stress resultant can be identified. Additionally, since the derivations are equivalent for the other direction, the 2 is replaced by  $\alpha$ , and now the stress resultant  $\mathbf{n}^\alpha$  is defined as

$$\mathbf{n}^\alpha = \frac{1}{\bar{j}} \int_{h^-}^{h^+} j \boldsymbol{\sigma} \cdot \mathbf{g}^\alpha \, d\xi^3 = \int_{h^-}^{h^+} z \boldsymbol{\sigma} \cdot \mathbf{g}^\alpha \, d\xi^3, \quad (5.39)$$

which is the stress resultant acting on the midsurface line  $\mathcal{C}_\alpha^C$  per unit  $d\xi^{3-\alpha}$ . The same procedure can be done for the *stress couple*  $\mathbf{m}^\alpha$ , where the moment of the traction about the midsurface, namely  $(\mathbf{x} - \boldsymbol{\varphi}) \times \boldsymbol{\sigma} \cdot \mathbf{g}^\alpha j$  is computed. This yields

$$\mathbf{m}^\alpha = \frac{1}{\bar{j}} \int_{h^-}^{h^+} (\mathbf{x} - \boldsymbol{\varphi}) \times \boldsymbol{\sigma} \cdot \mathbf{g}^\alpha j \, d\xi^3 = \mathbf{t} \times \int_{h^-}^{h^+} z \xi^3 \boldsymbol{\sigma} \cdot \mathbf{g}^\alpha \, d\xi^3, \quad (5.40)$$

where  $\mathbf{x} - \boldsymbol{\varphi} = \xi^3 \mathbf{t}$  was used. Note, that the moment vector  $\mathbf{m}^\alpha$  lies in the tangent bundle of the unit sphere  $T\mathcal{S}^2$ , due to  $\mathbf{t} \times (\dots)$  in Eq. (5.40). At some points, the alternative definition will also be used, which is implicitly given as

$$\hat{\mathbf{m}}^\alpha = \int_{h^-}^{h^+} z \xi^3 \boldsymbol{\sigma} \cdot \mathbf{g}^\alpha \, d\xi^3, \quad \mathbf{m}^\alpha = \mathbf{t} \times \hat{\mathbf{m}}^\alpha. \quad (5.41)$$

Finally, the last stress resultant stemming from the integration in the direction of the normal  $\mathbf{g}^3$  is missing, it is defined as the *across-the-thickness stress resultant*  $\mathbf{l}$ . It reads,

$$\mathbf{l} = \int_{h^-}^{h^+} z \boldsymbol{\sigma} \cdot \mathbf{g}^3 \, d\xi^3. \quad (5.42)$$

All these stress resultants can be stated using the first Piola-Kirchhoff stress tensor  $\mathbf{P}$  instead of using the Cauchy stress. This can be done using the alternative push-forward between the parameter space and the reference configuration similar to Eq. (5.34) as

$$\boldsymbol{\Phi}_{0,*}(\hat{\mathbf{E}}^1 \, d\xi^2 \, d\xi^3) = J \mathbf{J}^{-T} \cdot \hat{\mathbf{E}}^1 \, d\xi^2 \, d\xi^3 = J \mathbf{G}^1 \, d\xi^2 \, d\xi^3. \quad (5.43)$$

Using the defining equation of  $\mathbf{PN} = \boldsymbol{\sigma}\mathbf{n}$  from Eq. (4.31) on page 78, we have

$$j\boldsymbol{\sigma} \cdot \mathbf{g}^i = J\mathbf{P} \cdot \mathbf{G}^I. \quad (5.44)$$

This yields the alternative representation

$$\begin{aligned} \mathbf{n}^\alpha &= \frac{1}{j} \int_{h^-}^{h^+} J\mathbf{P} \cdot \mathbf{G}^\alpha \, d\xi^3, \\ \mathbf{m}^\alpha &= \mathbf{t} \times \frac{1}{j} \int_{h^-}^{h^+} \xi^3 J\mathbf{P} \cdot \mathbf{G}^\alpha \, d\xi^3, \\ \mathbf{l} &= \frac{1}{j} \int_{h^-}^{h^+} J\mathbf{P} \cdot \mathbf{G}^3 \, d\xi^3. \end{aligned} \quad (5.45)$$

### 5.2.2 Stress Resultant Components

The components of  $\mathbf{n}^\alpha$  from Eq. (5.39) can be written as

$$\mathbf{n}^\alpha = n^{\beta\alpha} \mathbf{a}_\beta + q^\alpha \mathbf{t}, \quad \text{with} \quad \mathbf{n} = n^{\alpha\beta} \mathbf{a}_\alpha \otimes \mathbf{a}_\beta, \quad \mathbf{q} = q^\alpha \mathbf{a}_\alpha. \quad (5.46)$$

These components are the *normal forces*  $n^{\alpha\beta}$  and the *shear forces*  $q^\alpha$ . The decomposition indicated in Eq. (5.46) is visualized in Fig. 5.4, where a cut along the shell's thickness direction is shown. Therein, the traction  $j\boldsymbol{\sigma} \cdot \mathbf{g}^\alpha$  and the normal  $j\mathbf{g}^\alpha$ , are shown, which are needed quantities for the through-the-thickness integration of  $\mathbf{n}^\alpha$ . The dashed line indicates the shell's midsurface and the components of  $\mathbf{n}^\alpha$  in this cut are shown. Plugging this into the definition of Eq. (5.39), using the results from Appendix A.5 on page 203 and noting that  $\boldsymbol{\sigma} \cdot \mathbf{g}^\alpha = \sigma^{\beta\alpha} \mathbf{g}_\beta + \sigma^{3\alpha} \mathbf{t}$ , yields

$$\begin{aligned} \mathbf{n}^\alpha &= \int_{h^-}^{h^+} z [\sigma^{\beta\alpha} (\mathbf{a}_\beta + \xi^3 b^\lambda_\beta (\mathbf{a}_\lambda - \gamma_\lambda \mathbf{t})) + \sigma^{3\alpha} \mathbf{t}] \, d\xi^3, \\ &= \int_{h^-}^{h^+} z [(\sigma^{\beta\alpha} + \xi^3 \sigma^{\lambda\alpha} b^\beta_\lambda) \mathbf{a}_\beta + (\sigma^{3\alpha} - \xi^3 \sigma^{\beta\alpha} b^\lambda_\beta \gamma_\lambda) \mathbf{t}] \, d\xi^3, \\ &= \int_{h^-}^{h^+} z [\sigma^{\beta\alpha} + \xi^3 \sigma^{\lambda\alpha} b^\beta_\lambda] \, d\xi^3 \mathbf{a}_\beta + \int_{h^-}^{h^+} z [\sigma^{3\alpha} - \xi^3 \sigma^{\beta\alpha} b^\lambda_\beta \gamma_\lambda] \, d\xi^3 \mathbf{t}, \end{aligned} \quad (5.47)$$

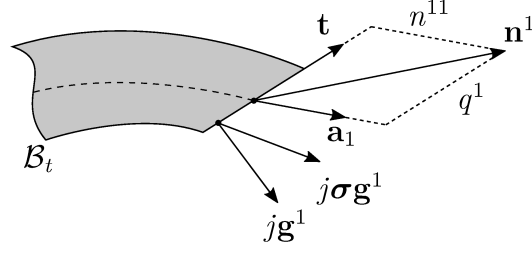


**Figure 5.4:** Decomposition of the stress resultant  $\mathbf{n}^1$ .

where the Cauchy membrane forces per length and the transversal shear forces per length can be identified by comparing coefficients with Eq. (5.46), such that

$$\begin{aligned} n^{\beta\alpha} &= \int_{h^-}^{h^+} z[\sigma^{\beta\alpha} + \xi^3 \sigma^{\lambda\alpha} b^\beta{}_\lambda] d\xi^3, \\ q^\alpha &= \int_{h^-}^{h^+} z[\sigma^{3\alpha} - \xi^3 \sigma^{\beta\alpha} b^\lambda{}_\beta \gamma_\lambda] d\xi^3. \end{aligned} \quad (5.48)$$

Similar to before, the bending moments Eq. (5.40), read

$$\begin{aligned} \mathbf{m}^\alpha &= \int_{h^-}^{h^+} z(\mathbf{x} - \boldsymbol{\varphi}) \times \boldsymbol{\sigma} \cdot \mathbf{g}^\alpha d\xi^3 = \mathbf{t} \times \int_{h^-}^{h^+} z\xi^3(\sigma^{\beta\alpha} \mathbf{g}_\beta + \sigma^{3\alpha} \mathbf{t}) d\xi^3 \\ &= \mathbf{t} \times \int_{h^-}^{h^+} z\xi^3[\sigma^{\beta\alpha} + \xi^3 \sigma^{\lambda\alpha} b^\beta{}_\lambda] d\xi^3 \mathbf{a}_\beta + \mathbf{t} \times \int_{h^-}^{h^+} z\xi^3[\sigma^{3\alpha} - \xi^3 \sigma^{\beta\alpha} b^\lambda{}_\beta \gamma_\lambda] d\xi^3 \mathbf{t} \\ &= \mathbf{t} \times \int_{h^-}^{h^+} z\xi^3[\sigma^{\beta\alpha} + \xi^3 \sigma^{\lambda\alpha} b^\beta{}_\lambda] d\xi^3 \mathbf{a}_\beta, \end{aligned} \quad (5.49)$$

If the alternative definition Eq. (5.41) of the moment couple is used, the corresponding decomposition reads

$$\hat{\mathbf{m}}^\alpha = \hat{m}^{\beta\alpha} \mathbf{a}_\beta + \hat{m}^{\alpha 3} \mathbf{t}, \quad \text{with} \quad \hat{\mathbf{m}} = \hat{m}^{\alpha\beta} \mathbf{a}_\alpha \otimes \mathbf{a}_\beta + \hat{m}^{\alpha 3} (\mathbf{a}_\alpha \otimes \mathbf{t} + \mathbf{t} \otimes \mathbf{a}_\alpha). \quad (5.50)$$

The components then read

$$\begin{aligned} \hat{m}^{\beta\alpha} &= \int_{h^-}^{h^+} z\xi^3[\sigma^{\beta\alpha} + \xi^3 \sigma^{\lambda\alpha} b^\beta{}_\lambda] d\xi^3, \\ \hat{m}^{\alpha 3} &= \int_{h^-}^{h^+} z\xi^3[\sigma^{3\alpha} - \xi^3 \sigma^{\beta\alpha} b^\lambda{}_\beta \gamma_\lambda] d\xi^3. \end{aligned} \quad (5.51)$$

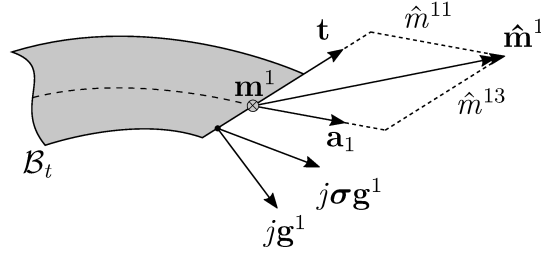


**Figure 5.5:** Decomposition of the stress resultant  $\mathbf{m}^1$  and  $\hat{\mathbf{m}}^1$ .

Observe, that the moments  $\hat{m}^{\alpha 3}$  do not explicitly enter  $\mathbf{m}^\alpha$  but only  $\hat{\mathbf{m}}^\alpha$ . Again the components are visualized in Fig. 5.5. Again the normal is shown and the orthogonality of  $\mathbf{m}^1$  and  $\hat{\mathbf{m}}^1$  is made obvious.

If Eqs. (5.48) and (5.49) are compared, the so-called *effective stress resultants* can be derived as

$$\begin{aligned}\tilde{n}^{\beta\alpha} &= n^{\beta\alpha} - b^\beta_\lambda \hat{m}^{\alpha\lambda} = \int_{h^-}^{h^+} z [\sigma^{\beta\alpha} - (\xi^3)^2 b^\beta_\lambda \sigma^{\mu\lambda} b^\alpha_\mu] d\xi^3 \\ \tilde{q}^\alpha &= q^\alpha + b^\gamma_\lambda \gamma_\gamma \hat{m}^{\alpha\lambda} = \int_{h^-}^{h^+} z [\sigma^{3\alpha} + (\xi^3)^2 \gamma_\gamma b^\gamma_\lambda \sigma^{\mu\lambda} b^\alpha_\mu] d\xi^3\end{aligned}\tag{5.52}$$

where  $\tilde{n}^{\alpha\beta}$  is apparently a symmetric tensor, since  $\sigma^{ij}$  is symmetric and the parts linear in  $\xi^3$  cancel. These effective stress resultants and their importance are discussed at the end of this chapter.

The last missing derivation is for the through-the-thickness resultant Eq. (5.42). Realizing that the identity  $\boldsymbol{\sigma} \mathbf{g}^3 = \sigma^{\alpha 3} \mathbf{g}_\alpha + \sigma^{33} \mathbf{t} = \sigma^{\alpha 3} (\mathbf{a}_\alpha + \xi^3 \mathbf{t}_{,\alpha}) + \sigma^{33} \mathbf{t}$  holds and again using the result from Appendix A.5 on page 203 for the directors derivatives  $\mathbf{t}_{,\alpha}$ , yields

$$\mathbf{l} = \int_{h^-}^{h^+} z [\sigma^{\alpha 3} (\mathbf{a}_\alpha + \xi^3 (b^\mu_\alpha (\mathbf{a}_\mu - \gamma_\mu \mathbf{t}))) + \sigma^{33} \mathbf{t}] d\xi^3.\tag{5.53}$$

Using  $\boldsymbol{\sigma} \cdot \mathbf{g}^3 = \sigma^{\alpha 3} \mathbf{g}_\alpha + \sigma^{33} \mathbf{t} = \sigma^{\alpha 3} (\mathbf{a}_\alpha + \xi^3 \mathbf{t}_{,\alpha}) + \sigma^{33} \mathbf{t}$  and the results from Appendix A.5 yields

$$\begin{aligned}\mathbf{l} &= \int_{h^-}^{h^+} z [\sigma^{\alpha 3} (\mathbf{a}_\alpha + \xi^3 b^\mu_\alpha \mathbf{a}_\mu) + (\sigma^{33} - \xi^3 \sigma^{\alpha 3} b^\mu_\alpha \gamma_\mu) \mathbf{t}] d\xi^3, \\ &= \int_{h^-}^{h^+} z [(\sigma^{\alpha 3} + \xi^3 \sigma^{\lambda 3} b^\alpha_\lambda) \mathbf{a}_\alpha + (\sigma^{33} - \xi^3 \sigma^{\alpha 3} b^\mu_\alpha \gamma_\mu) \mathbf{t}] d\xi^3.\end{aligned}\tag{5.54}$$

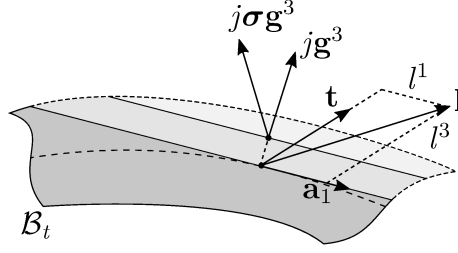


**Figure 5.6:** Decomposition of the stress resultant  $\mathbf{l}$ .

which can be decomposed again with  $\mathbf{l} = l^\alpha \mathbf{a}_\alpha + l^3 \mathbf{t}$ . Again, these components are visualized in Fig. 5.6. Since the integration is done via a cut tangentially to the midsurface, the cut depicted in Fig. 5.6 seems a bit unconventional. It is indicated by several cuts with different grey levels. The normal for integration is now  $j\mathbf{g}^3$  and the corresponding traction is  $j\boldsymbol{\sigma}\mathbf{g}^3$ . Later it is assumed that the normal stress  $\sigma^{33} = 0$  can be neglected, but for a better interpretation, this assumption is not yet inserted at this point. Again, the corresponding effective stress resultant components  $\tilde{l}^i$  can be derived as

$$\begin{aligned}
 \tilde{l}^\alpha &= l^\alpha - b^\alpha_\lambda \hat{m}^{3\lambda} = l^\alpha - \int_{h^-}^{h^+} z \xi^3 [b^\alpha_\lambda \sigma^{3\lambda} - \xi^3 b^\alpha_\lambda \sigma^{\beta\lambda} b^\gamma_\beta \gamma_\gamma] d\xi^3 \\
 &= \int_{h^-}^{h^+} z [\sigma^{\alpha 3} + (\xi^3)^2 b^\alpha_\lambda \sigma^{\beta\lambda} b^\gamma_\beta \gamma_\gamma] d\xi^3 \\
 \tilde{l}^3 &= l^3 + \gamma_\gamma b^\gamma_\lambda \hat{m}^{3\lambda} = l^3 + \int_{h^-}^{h^+} z \xi^3 [\gamma_\gamma b^\gamma_\lambda \sigma^{3\lambda} - \xi^3 \gamma_\gamma b^\gamma_\lambda \sigma^{\beta\lambda} b^\alpha_\beta \gamma_\alpha] d\xi^3 \\
 &= \int_{h^-}^{h^+} z [\sigma^{33} - (\xi^3)^2 \gamma_\gamma b^\gamma_\lambda \sigma^{\beta\lambda} b^\alpha_\beta \gamma_\alpha] d\xi^3
 \end{aligned} \tag{5.55}$$

For slender shells, all the definitions of effective stress resultants from Eqs. (5.51), (5.52) and (5.55) boil down to the trivial relations

$$\begin{aligned}
 \tilde{n}^{\beta\alpha} &\approx \int_{h^-}^{h^+} \sigma^{\beta\alpha} d\xi^3, & \tilde{q}^\alpha &\approx \int_{h^-}^{h^+} \sigma^{3\alpha} d\xi^3, & \hat{m}^{\beta\alpha} &\approx \int_{h^-}^{h^+} \xi^3 \sigma^{\beta\alpha} d\xi^3, \\
 \hat{m}^{3\alpha} &\approx \int_{h^-}^{h^+} \xi^3 \sigma^{3\alpha} d\xi^3, & \tilde{l}^\alpha &\approx \int_{h^-}^{h^+} \sigma^{\alpha 3} d\xi^3, & \tilde{l}^3 &\approx \int_{h^-}^{h^+} \sigma^{33} d\xi^3,
 \end{aligned} \tag{5.56}$$

where  $z \approx 1$  and neglecting quadratic parts in  $\xi^3$ , such that the error is  $\mathcal{O}((\xi^3)^2)$ . In contrast to this, the physical stress resultants are more involved even for slender shells,

namely

$$\begin{aligned}
 n^{\beta\alpha} &\approx \int_{h^-}^{h^+} \sigma^{\beta\alpha} + \xi^3 \sigma^{\lambda\alpha} b^\beta{}_\lambda \, d\xi^3, & q^\alpha &\approx \int_{h^-}^{h^+} \sigma^{3\alpha} - \xi^3 \sigma^{\beta\alpha} b^\lambda{}_\beta \gamma_\lambda \, d\xi^3, & \hat{m}^{\beta\alpha} &\approx \int_{h^-}^{h^+} \xi^3 \sigma^{\beta\alpha} \, d\xi^3, \\
 \hat{m}^{3\alpha} &\approx \int_{h^-}^{h^+} \xi^3 \sigma^{3\alpha} \, d\xi^3, & l^\alpha &\approx \int_{h^-}^{h^+} \sigma^{\alpha 3} + \xi^3 \sigma^{\lambda 3} b^\alpha{}_\lambda \, d\xi^3, \\
 l^3 &\approx \int_{h^-}^{h^+} \sigma^{33} - \xi^3 \sigma^{\alpha 3} b^\mu{}_\alpha \gamma_\mu \, d\xi^3,
 \end{aligned} \tag{5.57}$$

Thus, even for slender shells, these relations are crucial to obtain correct stress resultants.

For reference, there is also a summary of the stress resultant quantities in Table 5.2 and for the effective stress resultants in Table 5.3.

**REMARK 4.** The effective stress resultants will appear naturally in the balance laws in the next chapter. Nevertheless, they can be already interpreted, if the moments are assumed to be symmetric. This yields a trivial relation between the effective stress resultants and the physical stress, since in Table 5.3, all the term quadratic in  $\xi^3$  vanish. Consequently, the effective membrane stress resultants and moments then read

$$\tilde{n}^{\beta\alpha} = \int_{h^-}^{h^+} z \sigma^{\beta\alpha} \, d\xi^3 \quad \text{and} \quad \hat{m}^{\beta\alpha} = \int_{h^-}^{h^+} z \xi^3 \sigma^{\beta\alpha} \, d\xi^3, \tag{5.58}$$

The same quantities can be also derived, if the three-dimensional stress and three-dimensional strain are transformed using the shell shifter  $\mathbf{z}$ . For example, the Cauchy stress can be transformed as  $\hat{\boldsymbol{\sigma}} = \mathbf{z}^{-t} \cdot \boldsymbol{\sigma} \cdot \mathbf{z}^{-1}$ , where  $\hat{\boldsymbol{\sigma}}$  is the stress in the midsurface basis. For more properties of these mappings refer to [Bis17]. These transformed stresses and strains then yield the same energy contribution as the physical stress and strain. From this, using a standard Coleman-Noll procedure and through-the-thickness integration, effective stress resultants are automatically obtained. These effective stress resultants are unphysical but provide, with the corresponding midsurface strain components, also the same energy as the physical stress and strain. Therefore, in a stress-resultant-based formulation, effective stress resultants can be used to obtain the correct energy. This is convenient since everything can be carried out, purely in the two-dimensional midsurface setting.

---



**Table 5.2:** Summary of important stress resultant formulas

	Vectorial	$\mathbf{a}_\alpha$ components $\int_{h^-}^{h^+} z(\bullet) d\xi^3$	$\mathbf{t}$ components $\int_{h^-}^{h^+} z(\bullet) d\xi^3$
$\mathbf{n}^\alpha$	$\int_{h^-}^{h^+} z \boldsymbol{\sigma} \mathbf{g}^\alpha d\xi^3$	$n^{\beta\alpha}, \sigma^{\beta\alpha} + \xi^3 \sigma^{\lambda\alpha} b^\beta_\lambda$	$q^\alpha, \sigma^{3\alpha} - \xi^3 \sigma^{\beta\alpha} b^\lambda_\beta \gamma_\lambda$
$\hat{\mathbf{m}}^\alpha$	$\int_{h^-}^{h^+} z \xi^3 \boldsymbol{\sigma} \mathbf{g}^\alpha d\xi^3$	$\hat{m}^{\beta\alpha}, \xi^3 [\sigma^{\beta\alpha} + \xi^3 \sigma^{\lambda\alpha} b^\beta_\lambda]$	$\hat{m}^{3\alpha}, \xi^3 [\sigma^{3\alpha} - \xi^3 \sigma^{\beta\alpha} b^\lambda_\beta \gamma_\lambda]$
$\mathbf{l}$	$\int_{h^-}^{h^+} z \boldsymbol{\sigma} \mathbf{g}^3 d\xi^3$	$l^\alpha, \sigma^{\alpha 3} + \xi^3 \sigma^{\lambda 3} b^\alpha_\lambda$	$l^3, \sigma^{33} - \xi^3 \sigma^{\alpha 3} b^\mu_\alpha \gamma_\mu$

**Table 5.3:** Effective stress resultant components

Eff. res.	in terms of resultants	in terms of stresses $\int_{h^-}^{h^+} z(\bullet) d\xi^3$
$\tilde{n}^{\beta\alpha}$	$n^{\beta\alpha} - b^\beta_\lambda m^{\alpha\lambda}$	$\sigma^{\beta\alpha} - (\xi^3)^2 b^\beta_\lambda \sigma^{\mu\lambda} b^\alpha_\mu$
$\tilde{q}^\alpha$	$q^\alpha + b^\gamma_\lambda \gamma_\gamma m^{\alpha\lambda}$	$\sigma^{3\alpha} + (\xi^3)^2 \gamma_\gamma b^\gamma_\lambda \sigma^{\mu\lambda} b^\alpha_\mu$
$\tilde{m}^{\beta\alpha}$	$\hat{m}^{\beta\alpha}$	$\xi^3 \sigma^{\beta\alpha} + (\xi^3)^2 \sigma^{\lambda\alpha} b^\beta_\lambda$
$\hat{m}^{3\alpha}$	$\hat{m}^{3\alpha}$	$\xi^3 \sigma^{3\alpha} - (\xi^3)^2 \sigma^{\beta\alpha} b^\lambda_\beta \gamma_\lambda$
$\tilde{l}^\alpha$	$l^\alpha - b^\alpha_\lambda \hat{m}^{3\lambda}$	$\sigma^{\alpha 3} + (\xi^3)^2 b^\alpha_\lambda \sigma^{\beta\lambda} b^\gamma_\beta \gamma_\gamma$
$\tilde{l}^3$	$l^3 + \gamma_\gamma b^\gamma_\lambda \hat{m}^{3\lambda}$	$\sigma^{33} - (\xi^3)^2 \gamma_\gamma b^\gamma_\lambda \sigma^{\beta\lambda} b^\alpha_\beta \gamma_\alpha$

REMARK 5. From Eq. (5.57) it is clear that the true membrane forces are *intrinsically unsymmetric* even for slender shells, only the moments recover their symmetry in the thin limit. The membrane forces only become symmetric, if the linear part  $\xi^3$  in Eq. (5.57) is also neglected. In contrast to this, the effective stress resultants Eq. (5.56) are always symmetric, independent of the thickness, which will be derived as a requirement of equilibrium in Section 5.3.

REMARK 6. Frequently, the quantities  $q^\alpha$  and  $m^{\alpha 3}$  are subject to so-called *shear correction factors*. For the stress resultants  $q^\alpha, m^{\alpha 3}$  and their work-conjugate strains  $\mathbf{a}_\alpha \cdot \mathbf{t}, \mathbf{t}_{,\alpha} \cdot \mathbf{t}$ , respectively, it is derived that the underlying stress contribution is constant for  $q^\alpha$  and linear for  $m^{\alpha 3}$ . But physically, it would be more appropriate to use a quadratic ansatz for the former and a cubic ansatz for the latter. Consequently, the energy contribution is modified to mimic the energy if the stresses have the desired through-thickness distribution (quadratic or cubic, respectively). Therefore, the shear correction factor for  $q^\alpha$  is  $\alpha = 5/6$  and for  $m^{\alpha 3}$  it is  $\beta = 7/10$ , whereas the latter was derived in Pietraszkiewicz [Pie79a] as elaborated in Pietraszkiewicz [Pie79b, p. 78]. Also in Bischoff [Bis99] the same factor is derived. The former, ( $\alpha = 5/6$ ), was classically derived implicitly in Reissner [Rei45], see equation 8 therein.

### 5.2.3 Pulled-back Quantities

The derived resultants are forces and bending moments acting per deformed area. They can be recast to resultants acting per reference area, via a simple pull-back using  $\det \bar{\mathbf{F}} = \bar{j}/\bar{J}$ . Since the aforementioned quantities are defined in the convective coordinate system  $\mathbf{a}^\alpha$  and  $\mathbf{A}^\alpha$ , these pull-back operations are trivial. We have the midsurface deformation gradient as  $\bar{\mathbf{F}} = \delta^i_I \mathbf{a}_i \otimes \mathbf{A}^I$ . This is similar to the reasoning behind why the stress components differ only by  $\det \mathbf{F} = j/J$  and by exchanging the corresponding base vectors in Eq. (4.34). The derived resultants are true forces and true moments acting per deformed area. This yields

$$\begin{aligned} \mathbf{N}^\alpha &= \det \bar{\mathbf{F}} \mathbf{n}^\alpha, \\ \hat{\mathbf{M}}^\alpha &= \det \bar{\mathbf{F}} \hat{\mathbf{m}}^\alpha, \\ \mathbf{L} &= \det \bar{\mathbf{F}} \mathbf{l}, \end{aligned} \tag{5.59}$$

The stress components only differ by  $J$  and by replacing the corresponding base vectors, see also Eq. (4.34) on page 79.

### 5.2.4 Calculations in a Local Cartesian Frame

To derive the above-mentioned Cauchy stress resultants, several transformations are involved from the curvilinear second Piola-Kirchhoff stress tensor to the local Cartesian Cauchy stress tensor. For simplicity, this section employs matrix notation. This local Cartesian basis is constructed from the reference basis vectors  $\mathbf{G}_i$ , which are the columns of  $\mathbf{J}$ , by Gram-Schmidt orthonormalization [Llo97]. For the used mappings, refer to Section 5.1.2 on page 94. The Gram-Schmidt orthonormalization reads

$$\check{\mathbf{J}} = \text{GramSchmidt}(\mathbf{J}) = [\check{\mathbf{E}}_1, \check{\mathbf{E}}_2, \check{\mathbf{E}}_3] \tag{5.60}$$

For the definition of the mappings refer to Table 5.1 on page 98. Thus, the components of the Green-Lagrangian strain can be transformed by the identity  $\mathbf{E}_{IJ} \mathbf{G}^I \otimes \mathbf{G}^J = \check{E}_{KL} \check{\mathbf{E}}^K \otimes \check{\mathbf{E}}^L$ , such that

$$\check{E}_{KL} = E_{IJ} (\mathbf{G}^I \cdot \check{\mathbf{E}}_K) (\mathbf{G}^J \cdot \check{\mathbf{E}}_L). \tag{5.61}$$

In matrix notation for the components, this yields

$$\check{\mathbf{E}} = (\check{\mathbf{J}}\mathbf{J}^{-1})^T \mathbf{E} (\check{\mathbf{J}}\mathbf{J}^{-1}), \tag{5.62}$$

which can then be used to compute the second Piola-Kirchhoff stresses in the local Cartesian frame in the reference configuration.

As stated in Eq. (5.15) on page 94, the deformation gradient is given by  $\mathbf{F} = \mathbf{j}\mathbf{J}^{-1}$ . Then, to obtain the Cauchy stress from it, the push-forward transformation defined in Eq. (4.33) on page 78 is used, such that, again in matrix notation,  $\check{\boldsymbol{\sigma}} = \frac{1}{\det \mathbf{F}} \mathbf{F} \mathbf{S} \mathbf{F}^T$ . Consequently, the components  $\check{\boldsymbol{\sigma}}$  live in the coordinate system given by  $\check{\mathbf{E}}_i$ . These stress components  $\check{\boldsymbol{\sigma}}$  can be transformed into a local Cartesian frame on the deformed configuration, which can also be defined as  $\check{\mathbf{j}} = \text{GramSchmidt}(\mathbf{j}) = [\check{\mathbf{e}}_1, \check{\mathbf{e}}_2, \check{\mathbf{e}}_3]$ . This transformation can also be defined using the identity  $\check{\sigma}^{IJ} \check{\mathbf{E}}_I \otimes \check{\mathbf{E}}_J = \check{\sigma}^{kl} \check{\mathbf{e}}_k \otimes \check{\mathbf{e}}_l$ , which yields

$$\check{\sigma}^{kl} = \check{\sigma}^{IJ} (\check{\mathbf{E}}_I \cdot \check{\mathbf{e}}^k) (\check{\mathbf{E}}_J \cdot \check{\mathbf{e}}^l), \quad (5.63)$$

or in matrix notation

$$\check{\boldsymbol{\sigma}} = (\check{\mathbf{J}} \check{\mathbf{j}}^T)^T \check{\boldsymbol{\sigma}} (\check{\mathbf{J}} \check{\mathbf{j}}^T), \quad (5.64)$$

where it was exploited that  $\check{\mathbf{j}}^T = \check{\mathbf{j}}^{-1}$ , since it is an orthonormal matrix.

These components  $\check{\sigma}^{ij}$  can now be shown on the deformed three-dimensional object or can be used to integrate the Cauchy stress resultant components in the  $\check{\mathbf{e}}_i$ -basis, which will be done in Chapter 7 on page 175. In contrast to the involved representation from Table 5.2, the integration in a local Cartesian coordinate system is straightforward. The components of the Cauchy stress resultants are then given by

$$\begin{aligned} \check{n}^{\alpha\beta} &= \int_{h^-}^{h^+} \check{\sigma}^{\beta\alpha} d\xi^3, \\ \check{m}^{\alpha\beta} &= \int_{h^-}^{h^+} \xi^3 \check{\sigma}^{\beta\alpha} d\xi^3, \\ \check{q}^\alpha &= \int_{h^-}^{h^+} \check{\sigma}^{\alpha 3} d\xi^3, \end{aligned} \quad (5.65)$$

where all the nonlinearity is hidden now in the components  $\check{\sigma}^{ij}$ . These are also unsymmetric since also the curvature information of the shell is contained in them.

## 5.3 Balance Principles

The following derivation of the balance law can be found in several ways with or without simplifications in literature but not with the provided differential geometric reasoning. For example, in Bařar and Krätzig [BK13], Green and Zerna [GZ63], and Green et al. [Gre71], the quantities are derived with the kinematic Kirchhoff-Love assumptions. Further references are Zerna [Zer67] and Pietraszkiewicz [Pie79b] and Simo et al. [Sim89]. Nevertheless, the author hopes that the following section clarifies several inaccuracies found in the given literature.

### 5.3.1 Conservation of Mass

The local balance of mass is given by Eq. (4.37) on page 80 as

$$\rho_0 = \det \mathbf{F} \rho = \frac{j}{J} \rho. \quad (5.66)$$

Integrating the spatial mass density  $\rho$  using Eq. (5.25) on page 99 and  $z = j/\bar{j}$  yields the following relations

$$\begin{aligned} \bar{\rho} &= \frac{1}{\bar{j}} \int_{h^-}^{h^+} j \rho \, d\xi^3 \approx \int_{h^-}^{h^+} \rho \, d\xi^3 = h \rho, \\ \frac{1}{\bar{j}} \int_{h^-}^{h^+} j \rho \xi^3 \, d\xi^3 &\approx \int_{h^-}^{h^+} \rho \xi^3 \, d\xi^3 = 0, \\ \bar{I} &= \frac{1}{\bar{j}} \int_{h^-}^{h^+} j \rho (\xi^3)^2 \, d\xi^3 \approx \int_{h^-}^{h^+} \rho (\xi^3)^2 \, d\xi^3 = \frac{h^3}{12} \rho, \end{aligned} \quad (5.67)$$

where  $\bar{\rho}$  and  $\bar{I}$  are called surface density and surface inertia, respectively. The following identities are obtained

$$\bar{\rho}_0 = \det \bar{\mathbf{F}} \bar{\rho} = \frac{\bar{j}}{\bar{J}} \bar{\rho}, \quad \bar{I}_0 = \det \bar{\mathbf{F}} \bar{I} = \frac{\bar{j}}{\bar{J}} \bar{I}, \quad (5.68)$$

where  $\det \bar{\mathbf{F}} = \bar{j}/\bar{J} = \|\mathbf{a}_1 \times \mathbf{a}_2\|/\|\mathbf{A}_1 \times \mathbf{A}_2\|$  is the midsurface deformation gradient determinant. These identities are derived using the balance of mass of the three-dimensional theory and with the following simplification

$$Z = \frac{(\mathbf{G}_1 \times \mathbf{G}_2) \cdot \mathbf{t}_0}{\|\mathbf{A}_1 \times \mathbf{A}_2\|} = \frac{j_0}{\bar{j}_0} \approx 1 \quad (5.69)$$

which relates the infinitesimal surface area element to the infinitesimal volume element of the reference configuration, such that

$$dV = Z dA\xi^3. \tag{5.70}$$

### 5.3.2 Balance of Linear Momentum

The total linear momentum of the three-dimensional theory was given in Eq. (4.45) on page 82, if the velocity definition of the shell Eq. (5.10) on page 93 is plugged in, it reads

$$\begin{aligned}
 \mathbf{L} &= \int_{\mathcal{B}_t} \rho \mathbf{v} \, d\mathbf{v} = \int_{\mathcal{B}_t^C} \frac{1}{j} \int_{h^-}^{h^+} j \rho \mathbf{v} \, d\xi^3 \, d\mathbf{a} = \int_{\mathcal{B}_t^C} \frac{1}{j} \int_{h^-}^{h^+} j \rho (\dot{\boldsymbol{\varphi}} + \xi^3 \dot{\mathbf{t}}) \, d\xi^3 \, d\mathbf{a}, \\
 &= \int_{\mathcal{B}_t^C} \frac{1}{j} \int_{h^-}^{h^+} j \rho \, d\xi^3 \dot{\boldsymbol{\varphi}} \, d\mathbf{a} + \underbrace{\int_{\mathcal{B}_t^C} \frac{1}{j} \int_{h^-}^{h^+} j \rho \xi^3 \, d\xi^3}_{\approx 0} \dot{\mathbf{t}} \, d\mathbf{a}, \\
 &= \int_{\mathcal{B}_t^C} \bar{\rho} \dot{\boldsymbol{\varphi}} \, d\mathbf{a},
 \end{aligned} \tag{5.71}$$

where  $z = j/\bar{j}$  was used, see for reference Table 5.1 on page 98, and the density results of Eq. (5.67). The following volume-to-midsurface integral transformation will be frequently used:

$$\begin{aligned}
 \int_{\mathcal{B}_t} (\bullet) \, d\mathbf{v} &= \int_{\mathcal{B}_t^C} \int_{h^-}^{h^+} (\bullet) z \, d\xi^3 \, d\mathbf{a} = \int_{\mathcal{B}_t^C} \frac{1}{j} \int_{h^-}^{h^+} (\bullet) j \, d\xi^3 \, d\mathbf{a} = \int_{\mathcal{B}_t^C} \frac{1}{j} \int_{h^-}^{h^+} (\bullet) j \bar{j} \, d\xi^3 \, d\mathbf{a} \\
 &= \int_{\mathcal{B}_t^C} \int_{h^-}^{h^+} (\bullet) j \, d\xi^3 \, d\mathbf{a}.
 \end{aligned} \tag{5.72}$$

The three-dimensional balance of linear momentum as given in Section 4.3.2 on page 82 reads

$$\frac{d}{dt} \mathbf{L} = \int_{\mathcal{B}_t} \rho \hat{\mathbf{b}} \, d\mathbf{v} + \int_{\partial \mathcal{B}_t} \hat{\mathbf{t}} \, d\mathbf{a}. \tag{5.73}$$

Using the Cauchy theorem from Eq. (4.29) on page 77, yields

$$\frac{d}{dt} \int_{\mathcal{B}_t} \bar{\rho} \mathbf{v} \, d\mathbf{a} = \int_{\mathcal{B}_t} \rho \hat{\mathbf{b}} \, d\mathbf{v} + \int_{\partial \mathcal{B}_t} \boldsymbol{\sigma} \mathbf{n} \, d\mathbf{a} \tag{5.74}$$

and using Eq. (5.71) for the left-hand side gives

$$\frac{d}{dt} \int_{\mathcal{B}_t^C} \bar{\rho} \dot{\boldsymbol{\varphi}} \, d\mathbf{a} = \int_{\mathcal{B}_t} \rho \hat{\mathbf{b}} \, d\mathbf{v} + \int_{\partial \mathcal{B}_t} \boldsymbol{\sigma} \mathbf{n} \, d\mathbf{a}. \tag{5.75}$$

Similar to before, the push-forward of the current normal  $\mathbf{n}$  can be stated as

$$\mathbf{n} da = j \nabla \Phi^{-T} \hat{\mathbf{N}} d\Omega, \quad (5.76)$$

where the last equation is a Nanson-type mapping or the Piola transform from the parameter space to the current configuration, see Section 2.8.5 on page 47. This is the same procedure as visualized already in Section 5.2 in Fig. 5.3 on page 102. Inserting the definition Eq. (5.23) in Eq. (5.75) yields

$$\frac{d}{dt} \int_{\mathcal{B}_t^C} \bar{\rho} \dot{\boldsymbol{\varphi}} d\mathbf{a} = \int_{\mathcal{B}_t^C} \int_{h^-}^{h^+} j \rho \hat{\mathbf{b}} d\xi^3 da + \int_{\partial \mathcal{B}_t^C} j \boldsymbol{\sigma} \nabla \Phi^{-T} \hat{\mathbf{N}} da, \quad (5.77)$$

where  $da$  in the last term has to be understood as the infinitesimal top, bottom, and lateral surface element of the body, respectively. Now, this term is explicitly decomposed into the surface integral over the top and bottom and over the lateral surfaces (of the parameter space). Their corresponding normals are  $\hat{\mathbf{N}} = \nu_\alpha \tilde{\mathbf{E}}^\alpha$  and  $\hat{\mathbf{N}} = \pm \tilde{\mathbf{E}}^3$ , respectively. This results in

$$\begin{aligned} \frac{d}{dt} \int_{\mathcal{B}_t^C} \bar{\rho} \dot{\boldsymbol{\varphi}} d\mathbf{a} &= \int_{\mathcal{B}_t^C} \int_{h^-}^{h^+} j \rho \hat{\mathbf{b}} d\xi^3 da + \underbrace{\int_{\partial \mathcal{B}_t^C} \int_{h^-}^{h^+} j \boldsymbol{\sigma} \nabla \Phi^{-T} \nu_\alpha \tilde{\mathbf{E}}^\alpha d\xi^3 d\Gamma}_{\text{lateral surfaces}} \\ &+ \underbrace{\int_{\mathcal{B}_t^C} [j \boldsymbol{\sigma} \nabla \Phi^{-T} \tilde{\mathbf{E}}^3] \Big|_{\xi^3=h^-}^{\xi^3=h^+} da}_{\text{top and bottom surface}}, \end{aligned} \quad (5.78)$$

where  $d\Gamma$  is the line integration element of the midsurface line at the lateral surface boundary  $\partial \mathcal{B}_t^C$ , which is defined by the relation  $d\Gamma = \nu_\alpha \tilde{\mathbf{E}}^\alpha d\Gamma$ .

With the mapping property  $\mathbf{g}^\alpha = \nabla \Phi^{-T} \tilde{\mathbf{E}}^\alpha$  and  $\mathbf{g}^3 = \nabla \Phi^{-T} \tilde{\mathbf{E}}^3$  Eq. (5.78) reads

$$\frac{d}{dt} \int_{\mathcal{B}_t^C} \bar{\rho} \dot{\boldsymbol{\varphi}} d\mathbf{a} = \int_{\mathcal{B}_t^C} \int_{h^-}^{h^+} j \rho \hat{\mathbf{b}} d\xi^3 + \int_{\partial \mathcal{B}_t^C} \int_{h^-}^{h^+} j \boldsymbol{\sigma} \mathbf{g}^\alpha \nu_\alpha d\xi^3 d\Gamma + \int_{\mathcal{B}_t^C} [j \boldsymbol{\sigma} \mathbf{g}^3] \Big|_{\xi^3=h^-}^{\xi^3=h^+} da. \quad (5.79)$$

If the definition of the stress resultants Eq. (5.39) on page 103 is inserted, the second part of the right-hand side of Eq. (5.79) can be written as

$$\int_{\partial \mathcal{B}_t^C} \int_{h^-}^{h^+} j \boldsymbol{\sigma} \mathbf{g}^\alpha \nu_\alpha d\xi^3 d\Gamma = \int_{\partial \mathcal{B}_t^C} \bar{\mathbf{j}} \mathbf{n}^\alpha \nu_\alpha da \quad (5.80)$$

and with the divergence theorem for surfaces, we have

$$\int_{\partial \mathcal{B}_t^C} \bar{j} \mathbf{n}^\alpha \nu_\alpha \, da = \int_{\mathcal{B}_t^C} (\bar{j} \mathbf{n}^\alpha)_{,\alpha} \, da. \quad (5.81)$$

Furthermore, the loading integrals can be grouped as

$$\int_{\mathcal{B}_t^C} \left( [j \boldsymbol{\sigma} \mathbf{g}^3] \Big|_{\xi^3=h^-}^{\xi^3=h^+} + \int_{h^-}^{h^+} j \rho \mathbf{b} d\xi^3 \right) da \quad (5.82)$$

and the integrant can be derived as the loading term

$$\bar{\mathbf{n}} = \frac{1}{\bar{j}} \left[ [j \boldsymbol{\sigma} \mathbf{g}^3] \Big|_{\xi^3=h^-}^{\xi^3=h^+} + \int_{h^-}^{h^+} j \rho \mathbf{b} d\xi^3 \right], \quad (5.83)$$

which was normalized over the midsurface area.

If Eqs. (5.80) and (5.83) are inserted into Eq. (5.79), it can be written as

$$\frac{d}{dt} \int_{\mathcal{B}_t^C} \bar{\rho} \dot{\boldsymbol{\varphi}} \, da = \int_{\mathcal{B}_t^C} (\bar{j} \mathbf{n}^\alpha)_{,\alpha} \, da + \int_{\mathcal{B}_t^C} \bar{j} \bar{\mathbf{n}} \, da. \quad (5.84)$$

Then, exploiting the balance of mass for the surface Eq. (5.68) yields

$$\int_{\mathcal{B}_0^C} \bar{\rho}_0 \dot{\boldsymbol{\varphi}} \, dA = \int_{\mathcal{B}_t^C} (\bar{j} \mathbf{n}^\alpha)_{,\alpha} \, da + \int_{\mathcal{B}_t^C} \bar{j} \bar{\mathbf{n}} \, da. \quad (5.85)$$

Using again the volume transport, the balance of mass, and factoring  $\bar{j}$  out from the right-hand side yields

$$\int_{\mathcal{B}_t^C} \bar{\rho} \dot{\boldsymbol{\varphi}} \, \mathbf{d}\mathbf{a} = \int_{\mathcal{B}_t^C} \left( \frac{1}{\bar{j}} (\bar{j} \mathbf{n}^\alpha)_{,\alpha} + \bar{\mathbf{n}} \right) \bar{j} \, da. \quad (5.86)$$

With the identity  $\mathbf{d}\mathbf{a} = \bar{j} \, da$  this simplifies to

$$\int_{\mathcal{B}_t^C} \bar{\rho} \dot{\boldsymbol{\varphi}} \, \mathbf{d}\mathbf{a} = \int_{\mathcal{B}_t^C} \left( \frac{1}{\bar{j}} (\bar{j} \mathbf{n}^\alpha)_{,\alpha} + \bar{\mathbf{n}} \right) \mathbf{d}\mathbf{a}, \quad (5.87)$$



and finally using the usual localization theorem [MH94, Ch. 2, p. 122 ], the local balance of linear momentum reads

$$\bar{\rho}\dot{\boldsymbol{\varphi}} = \frac{1}{j}(\bar{j}\mathbf{n}^\alpha)_{,\alpha} + \bar{\mathbf{n}}, \quad (5.88)$$

which can be found similarly in Green and Zerna [GZ63, Eq. 10.4.12, 10.4.15], Libai and Simmonds [LS83, Eq. 3.32f]. and Simo and Fox [SF89, Eq. 4.12] but without or less detailed derivation. These references did not recast the equation in the following form. If the surface divergence identity is plugged in, see Appendix A.2, then Eq. (5.88) reduces to

$$\bar{\rho}\dot{\boldsymbol{\varphi}} = \overline{\text{div}} \mathbf{n} + \bar{\mathbf{n}}, \quad (5.89)$$

where a bar is added to the Riemannian divergence operator to separate it from the Euclidean three-dimensional divergence. This recast form provides a striking resemblance to the three-dimensional theory, see Eq. (4.52) on page 83.

### 5.3.3 Balance of Angular Momentum

From the three-dimensional equations Eq. (4.47), we have

$$\mathbf{J}(t) = \int_{\mathcal{B}_t} \rho \mathbf{x} \times \mathbf{v} \, d\mathbf{v} = \int_{\mathcal{B}_t^C} \int_{h^-}^{h^+} j\rho (\boldsymbol{\varphi} + \xi^3 \mathbf{t}) \times (\dot{\boldsymbol{\varphi}} + \xi^3 \dot{\mathbf{t}}) \, d\xi^3 \, d\mathbf{a}, \quad (5.90)$$

where  $z = j/\bar{j}$  was used, see for reference Table 5.1. This results in

$$\mathbf{J}(t) = \int_{\mathcal{B}_t^C} \int_{h^-}^{h^+} j\rho \boldsymbol{\varphi} \times \dot{\boldsymbol{\varphi}} + j\rho \xi^3 (\mathbf{t} \times \dot{\boldsymbol{\varphi}} + \dot{\boldsymbol{\varphi}} \times \mathbf{t}) + j\rho (\xi^3)^2 \mathbf{t} \times \dot{\mathbf{t}} \, d\xi^3 \, d\mathbf{a}. \quad (5.91)$$

Using the simplifications from Eq. (5.67) on page 112, volume transport and the balance of mass and simultaneously taking the temporal derivative yields

$$\frac{\partial}{\partial t} \mathbf{J}(t) = \int_{\mathcal{B}_t^C} \bar{\rho} \boldsymbol{\varphi} \times \dot{\boldsymbol{\varphi}} \, d\mathbf{a} + \int_{\mathcal{B}_t^C} \bar{I} \dot{\boldsymbol{\omega}} \, d\mathbf{a}, \quad (5.92)$$

where the definition  $\dot{\boldsymbol{\omega}} = \mathbf{t} \times \ddot{\mathbf{t}}$  was used. Thus, using Eq. (5.92) the balance of angular momentum from Eq. (4.48) on page 82 reads

$$\int_{\mathcal{B}_t^C} \bar{\rho} \boldsymbol{\varphi} \times \ddot{\boldsymbol{\varphi}} \, d\mathbf{a} + \int_{\mathcal{B}_t^C} \bar{I} \dot{\boldsymbol{\omega}} \, d\mathbf{a} = \int_{\partial \mathcal{B}_t} \mathbf{x} \times \hat{\mathbf{t}} \, d\mathbf{a} + \int_{\mathcal{B}_t} \mathbf{x} \times \hat{\mathbf{b}} \, d\mathbf{v}. \quad (5.93)$$

The first term of the right-hand side of Eq. (5.93) can be transformed using the definition of the normal from Eq. (5.76) and Cauchy's theorem to

$$\int_{\partial \mathcal{B}_t} (\boldsymbol{\varphi} + \xi^3 \mathbf{t}) \times j \boldsymbol{\sigma} \nabla \Phi^{-T} \hat{\mathbf{N}} \, da. \quad (5.94)$$

It can be decomposed into the surface integral over the top and bottom and over the lateral surfaces (of the parameter space). The normals reads  $\hat{\mathbf{N}} = \nu_\alpha \tilde{\mathbf{E}}^\alpha$  or  $\hat{\mathbf{N}} = \pm \tilde{\mathbf{E}}^3$  and  $\mathbf{g}^\alpha = \nabla \Phi^{-T} \tilde{\mathbf{E}}^\alpha$  and  $\mathbf{g}^3 = \nabla \Phi^{-T} \tilde{\mathbf{E}}^3$ , respectively. This yields,

$$\int_{\partial \mathcal{B}_t} \int_{h^-}^{h^+} (\boldsymbol{\varphi} + \xi^3 \mathbf{t}) \times j \boldsymbol{\sigma} \mathbf{g}^\alpha \nu_\alpha \, d\xi^3 \, d\Gamma + \int_{\mathcal{B}_t^C} [(\boldsymbol{\varphi} + \xi^3 \mathbf{t}) \times j \boldsymbol{\sigma} \cdot \mathbf{g}^3] \Big|_{\xi^3=h^-}^{\xi^3=h^+} \, da. \quad (5.95)$$

The loading term or the second term of the right-hand side of Eq. (5.93) reads, with the shell's kinematics,

$$\int_{\mathcal{B}_t} \mathbf{x} \times \hat{\mathbf{b}} \, d\mathbf{v} = \int_{\mathcal{B}_t^C} \int_{h^-}^{h^+} j (\boldsymbol{\varphi} + \xi^3 \mathbf{t}) \times \hat{\mathbf{b}} \, d\xi^3 \, da. \quad (5.96)$$

The loading of the top and bottom surface at the right-hand side of Eq. (5.95) can be grouped with Eq. (5.96) such that

$$\begin{aligned} & \int_{\mathcal{B}_t^C} \int_{h^-}^{h^+} j (\boldsymbol{\varphi} + \xi^3 \mathbf{t}) \times \hat{\mathbf{b}} \, d\xi^3 \, da + \int_{\mathcal{B}_t^C} [(\boldsymbol{\varphi} + \xi^3 \mathbf{t}) \times j \boldsymbol{\sigma} \cdot \mathbf{g}^3] \Big|_{\xi^3=h^-}^{\xi^3=h^+} \, da, \\ &= \int_{\mathcal{B}_t^C} \int_{h^-}^{h^+} j \boldsymbol{\varphi} \times \hat{\mathbf{b}} \, d\xi^3 + [\boldsymbol{\varphi} \times j \boldsymbol{\sigma} \cdot \mathbf{g}^3] \Big|_{\xi^3=h^-}^{\xi^3=h^+} \, da, \\ &+ \int_{\mathcal{B}_t^C} \int_{h^-}^{h^+} j \xi^3 \mathbf{t} \times \hat{\mathbf{b}} \, d\xi^3 + [\xi^3 \mathbf{t} \times j \boldsymbol{\sigma} \cdot \mathbf{g}^3] \Big|_{\xi^3=h^-}^{\xi^3=h^+} \, da, \\ &= \int_{\mathcal{B}_t^C} \boldsymbol{\varphi} \times \bar{\mathbf{n}} \bar{j} + \bar{\mathbf{m}} \bar{j} \, da, \end{aligned} \quad (5.97)$$

where the applied forces from Eq. (5.83) were identified. Furthermore, the applied moments were also identified as

$$\bar{\mathbf{m}} = \frac{1}{\bar{j}} \mathbf{t} \times \left[ [j\xi^3 \boldsymbol{\sigma} \mathbf{g}^3] \Big|_{\xi^3=h^-}^{\xi^3=h^+} + \int_{h^-}^{h^+} \xi^3 j \rho \hat{\mathbf{b}} d\xi^3 \right], \quad (5.98)$$

which are living obviously in the tangent bundle  $T\mathcal{S}^2$ . The first term with  $\mathbf{t} \times (\bullet)$  denotes the moments from integrated tractions on the top and bottom surfaces and the latter term denotes the moments from integrated tractions on the lateral surfaces. The first part in Eq. (5.95) can be derived similarly as before for the membrane forces. This reads

$$\int_{\partial \mathcal{B}_t} \int_{h^-}^{h^+} (\boldsymbol{\varphi} + \xi^3 \mathbf{t}) \times j \boldsymbol{\sigma} \cdot \mathbf{g}^\alpha \nu_\alpha d\xi^3 d\Gamma. \quad (5.99)$$

Inserting the definition of the stress resultants Eqs. (5.39) and (5.40) on page 103, and the divergence theorem for surfaces into Eq. (5.99) yields

$$\int_{\partial \mathcal{B}_t} \int_{h^-}^{h^+} (\boldsymbol{\varphi} + \xi^3 \mathbf{t}) \times j \boldsymbol{\sigma} \cdot \mathbf{g}^\alpha \nu_\alpha d\xi^3 d\Gamma = \int_{\mathcal{B}_t^C} \boldsymbol{\varphi} \times (\bar{j} \mathbf{n}^\alpha)_{,\alpha} + \mathbf{a}_\alpha \times (\bar{j} \mathbf{n}^\alpha) + (\bar{j} \mathbf{m}^\alpha)_{,\alpha} da. \quad (5.100)$$

Thus collecting everything and factoring with the identity  $\mathbf{d}\mathbf{a} = \bar{j} da$ , and with Eqs. (5.92), (5.97), (5.98) and (5.100), Eq. (5.93) reads

$$\int_{\mathcal{B}_t^C} \bar{\rho} \boldsymbol{\varphi} \times \ddot{\boldsymbol{\varphi}} + \bar{I} \dot{\boldsymbol{\omega}} \mathbf{d}\mathbf{a} = \int_{\mathcal{B}_t^C} \bar{j} \left( \bar{\mathbf{m}} + \boldsymbol{\varphi} \times \bar{\mathbf{n}} + \frac{1}{\bar{j}} \boldsymbol{\varphi} \times (\bar{j} \mathbf{n}^\alpha)_{,\alpha} + \frac{1}{\bar{j}} (\bar{j} \mathbf{m}^\alpha)_{,\alpha} + \mathbf{a}_\alpha \times \mathbf{n}^\alpha \right) da. \quad (5.101)$$

The linear momentum from Eq. (5.88) can be identified by grouping all terms with signature  $\boldsymbol{\varphi} \times (\bullet)$ . This yields for the remainder

$$\begin{aligned} \int_{\mathcal{B}_t^C} \bar{I} \dot{\boldsymbol{\omega}} \mathbf{d}\mathbf{a} &= \int_{\mathcal{B}_t^C} \bar{j} \left( \bar{\mathbf{m}} + \frac{1}{\bar{j}} (\bar{j} \mathbf{m}^\alpha)_{,\alpha} + \mathbf{a}_\alpha \times \mathbf{n}^\alpha \right) da \\ &= \int_{\mathcal{B}_t^C} \bar{\mathbf{m}} + \frac{1}{\bar{j}} (\bar{j} \mathbf{m}^\alpha)_{,\alpha} + \mathbf{a}_\alpha \times \mathbf{n}^\alpha \mathbf{d}\mathbf{a}, \end{aligned} \quad (5.102)$$

and finally using the usual localization arguments, the local balance of angular momentum reads

$$\bar{I} \dot{\boldsymbol{\omega}} = \bar{\mathbf{m}} + \frac{1}{\bar{j}} (\bar{j} \mathbf{m}^\alpha)_{,\alpha} + \mathbf{a}_\alpha \times \mathbf{n}^\alpha, \quad (5.103)$$

where, as before, the Riemannian divergence term can be identified

$$\bar{I} \dot{\boldsymbol{\omega}} = \bar{\mathbf{m}} + \overline{\operatorname{div}} \mathbf{m} + \mathbf{a}_\alpha \times \mathbf{n}^\alpha. \quad (5.104)$$

The three-dimensional angular momentum  $\boldsymbol{\sigma}^T = \boldsymbol{\sigma}$  can also be investigated to derive an alternative version of the angular momentum for the shell. This reads

$$\mathbf{n}^\alpha \times \mathbf{a}_\alpha + \hat{\mathbf{m}} \times \mathbf{t}_{,\alpha} + \mathbf{l} \times \mathbf{t} = \mathbf{0}, \quad (5.105)$$

refer to Appendix A.8 on page 206 for a derivation. Eq. (5.103) is defined in the direction of  $\dot{\boldsymbol{\omega}}$  in the tangent bundle  $T\mathcal{S}^2$ . If Eq. (5.105) and the identity Eq. (5.41) with the product rule  $\overline{\operatorname{div}} \mathbf{m} = \mathbf{t}_{,\alpha} \times \hat{\mathbf{m}}^\alpha + \mathbf{t} \times \overline{\operatorname{div}} \hat{\mathbf{m}}$  are used, Eq. (5.103) reads

$$\mathbf{t} \times (\overline{\operatorname{div}} \hat{\mathbf{m}} + \hat{\mathbf{m}} - \mathbf{l} - \bar{I} \ddot{\mathbf{t}}) = \mathbf{0}, \quad (5.106)$$

with  $\dot{\boldsymbol{\omega}} = \mathbf{t} \times \ddot{\mathbf{t}}$  and  $\bar{\mathbf{m}} = \mathbf{t} \times \hat{\mathbf{m}}$ , which is the right-hand side of Eq. (5.98). Eq. (5.106) can be stated in a more manifold-esque way, such that

$$\overline{\operatorname{div}} \hat{\mathbf{m}} + \hat{\mathbf{m}} - \mathbf{l} - \bar{I} \ddot{\mathbf{t}} = \mathbf{0} \quad \text{in } T\mathcal{S}^2. \quad (5.107)$$

The last two equations clean up the arguable polluted version of the angular momentum balance from Eq. (5.104) since it removes the dependence on the membrane forces. Thus, it is again a PDE with unknowns  $\hat{\mathbf{m}}, \mathbf{l}$  and  $\ddot{\mathbf{t}}$  defined in the tangent bundle of  $T\mathcal{S}^2$ .

Furthermore, investigating the components of Eq. (5.105) and identifying the effective stress resultants from Eqs. (5.52) and (5.55) on pages 106 and 107 yields

$$\tilde{n}^{\beta\alpha} \mathbf{a}_\alpha \times \mathbf{a}_\beta + \mathbf{t} \times \mathbf{a}_\alpha (\tilde{l}^\alpha - \tilde{q}^\alpha) + l^3 \mathbf{t} \times \mathbf{t} = \mathbf{0}. \quad (5.108)$$

The derivation can be found at Appendix A.8 on page 206. Since the vectors  $\mathbf{a}_\alpha$  and  $\mathbf{t}$  are linearly independent, this results in the local angular momentum balance

$$\tilde{n}^{\beta\alpha} \varepsilon_{\alpha\beta} = 0 \quad \tilde{l}^\alpha - \tilde{q}^\alpha = 0, \quad (5.109)$$

which can be, to the author's best knowledge, only found in this form in Simo et al. [Sim90b, Eq. 2.11]. It states the symmetry of the effective membrane stress resultants and relates the effective transverse shear stress resultants  $\tilde{q}^\alpha$  to the effective stress resultants

$\tilde{l}^\alpha$ . It should be mentioned that using the definitions of the effective stress resultants from Table 5.3 on page 109 the result can be written in a more compact format. This can be accomplished by introducing the curvature tensor  $\boldsymbol{\beta} = \beta_j^i \mathbf{a}_i \otimes \mathbf{a}^j$ , the stress resultant tensor  $\mathbf{n} = b^{ij} \mathbf{a}_i \otimes \mathbf{a}_j$  and the stress resultant *moment* tensor  $\tilde{\mathbf{m}} = \hat{m}^{ij} \mathbf{a}_i \otimes \mathbf{a}_j$ , such that

$$\beta_j^i = \begin{bmatrix} b_1^1 & b_2^1 & 0 \\ b_1^2 & b_2^2 & 0 \\ -\gamma_\gamma b_1^\gamma & -\gamma_\gamma b_2^\gamma & 1 \end{bmatrix}, \tilde{m}^{ij} = \begin{bmatrix} \hat{m}^{11} & \hat{m}^{12} & \hat{m}^{31} \\ \hat{m}^{21} & \hat{m}^{22} & \hat{m}^{32} \\ 0 & 0 & 0 \end{bmatrix}, n^{ij} = \begin{bmatrix} n^{11} & n^{12} & l^1 \\ n^{21} & n^{22} & l^2 \\ q^1 & q^3 & l^3 \end{bmatrix}. \quad (5.110)$$

Then, the *effective* stress resultant tensor  $\tilde{\mathbf{n}} = \tilde{n}^{ij} \mathbf{a}_i \otimes \mathbf{a}_j$  can be simply written as

$$\tilde{\mathbf{n}} = \mathbf{n} - \boldsymbol{\beta} \tilde{\mathbf{m}}. \quad (5.111)$$

Now the angular momentum balance from Eq. (5.109) reads simply

$$\tilde{\mathbf{n}} = \tilde{\mathbf{n}}^t. \quad (5.112)$$

The quantity  $\boldsymbol{\beta}$  has a remarkable resemblance with the shifter tensor components from Eq. (5.21) on page 96. The relation

$$\beta_j^i = \delta_j^i - z_j^i \Big|_{\xi^3=1} \quad (5.113)$$

holds.

### 5.3.4 The Reissner-Mindlin Assumptions

This section deals with the intrinsic Reissner-Mindlin assumptions, which separate the shell model from a three-dimensional solid model. First, the usual assumptions that are incorporated in the Reissner-Mindlin shell model are stated. For this, first, the assumptions of a Kirchhoff-Love shell model are stated. These assumptions are:

1. Straight material fibers perpendicular to the midsurface, referred to as transverse normals, remain straight during deformation.
2. Transverse normals rotate during deformation such that they remain perpendicular to the midsurface during deformation.
3. The normal stress in the direction of the transverse normals can be neglected.

The Reissner-Mindlin shell model relaxes the second assumption, allowing the reference normals to rotate freely. These assumptions are now investigated by using the derived stress resultants and balance laws.

The component of the through-the-thickness stress resultants  $l^3$  and the *shear moment*  $\hat{m}^{\alpha 3}$  do not appear in Eq. (5.89) or Eq. (5.112). Therefore, equilibrium does not tell anything about these components, consequently, they are undetermined from the stress-resultant equilibria.

Consider the strains from Eq. (5.29) enhanced with an *extensible* director. This yields as thickness stretch  $\chi = \frac{1}{2}(\mathbf{t} \cdot \mathbf{t} - \mathbf{t}_0 \cdot \mathbf{t}_0)$  and the *shear curvature*  $\chi_{,\alpha} = \mathbf{t} \cdot \mathbf{t}_{,\alpha} - \mathbf{t}_0 \cdot \mathbf{t}_{0,\alpha}$ . Using a Saint Venant-Kirchhoff material law  $\mathbf{S} = \lambda \operatorname{tr}(\mathbf{E} : \mathbf{G}^{-1}) + 2\mu \mathbf{E}^\sharp$ , the stress resultants can be written as follows

$$\tilde{n}^{\alpha\beta} = \frac{D}{\det \bar{\mathbf{F}}} \left( \frac{2\nu}{1-2\nu} A^{\alpha\beta} \chi + \left[ \frac{2\nu}{1-2\nu} A^{\alpha\beta} A^{\gamma\delta} + (1-2\nu)(A^{\alpha\gamma} A^{\beta\delta} + A^{\alpha\delta} A^{\beta\gamma}) \right] \varepsilon_{\gamma\delta} \right) \quad (5.114)$$

$$\tilde{q}^\alpha = \frac{Gh}{\det \bar{\mathbf{F}}} A^{\alpha\beta} \gamma_{\beta} \quad (5.115)$$

$$\tilde{m}^{\alpha\beta} = \frac{B}{\det \bar{\mathbf{F}}} \left( \nu A^{\alpha\beta} A^{\gamma\delta} + \frac{1-2\nu}{2} A^{\alpha\gamma} A^{\beta\delta} + A^{\alpha\delta} A^{\beta\gamma} \right) \quad (5.116)$$

$$\tilde{m}^{3\alpha} = \frac{B}{\det \bar{\mathbf{F}}} A^{\alpha\beta} \chi_{,\beta} \quad (5.117)$$

$$\tilde{l}^3 = \frac{D}{\det \bar{\mathbf{F}}} (A^{\alpha\beta} \varepsilon_{\alpha\beta} \nu - (1-\nu)\chi) \frac{1-\nu}{2\nu-1}, \quad (5.118)$$

with  $D = Eh/(2(1+\nu))$  and  $B = Eh^3/(12(1-\nu^2))$ . Lamé's first parameter  $\lambda$  and Lamé's second parameter  $\mu$  are related to Young's modulus  $E$  and Poisson's ratio  $\nu$  via  $\lambda = \frac{E\nu}{(1+\nu)(1-2\nu)}$  and  $\mu = \frac{E}{2(1+\nu)}$ . The determinant  $\det \bar{\mathbf{F}}$  in the denominator is the push-forward of the reference quantities to the current configuration. This derivation uses the midsurface reference metric tensor and incorporates the simplifications  $z \approx 1$  and  $G^{\alpha\beta} \approx A^{\alpha\beta}$ . Furthermore, it assumes that the moments  $\tilde{m}^{\alpha\beta}$  are symmetric. Thus, from Eq. (5.56) it is clear that  $\tilde{l}^3$  is  $\int_{h^-}^{h^+} \sigma^{33} d\xi^3$ . Therefore, the Reissner-Mindlin assumption of negligible transversal stresses yields  $\tilde{l}^3 = 0$ . Consequently, using this in Eq. (5.118),  $\chi$  can be derived directly from the in-plane stretch. This yields the common result

$$\chi = \frac{\nu(\varepsilon_{11} + \varepsilon_{22})}{\nu - 1}. \quad (5.119)$$

Thus, Eq. (5.119) can be inserted in Eq. (5.114), which yields a relation of plane stress type between the membrane stress resultants and the membrane strains. This yields

$$\tilde{n}^{\alpha\beta} = \frac{D}{\det \bar{\mathbf{F}}} \left( A^{\alpha\beta} A^{\gamma\delta} \frac{2\nu}{1-\nu} + (A^{\alpha\gamma} A^{\beta\delta} + A^{\alpha\delta} A^{\beta\gamma}) \right) \varepsilon_{\gamma\delta}, \quad (5.120)$$

which boils down to

$$\tilde{n}^{\alpha\beta} = \frac{2D}{\det \bar{\mathbf{F}}(\nu - 1)}(\nu \varepsilon_{22} + \varepsilon_{11}), \quad (5.121)$$

in a local Cartesian coordinate system. This is the well-known formula from a plane stress assumption in solids. The shell itself is not in an in-plane stress state, since the transverse shear forces are not zero. Additionally, since the spatial change of  $\chi$  is also known,  $\tilde{m}^{3\alpha}$  is also directly derivable from the membrane strains. The spatial change of  $\chi$  reads, as the partial derivative of Eq. (5.119),

$$\chi_{,\alpha} = \frac{\nu(\varepsilon_{11,\alpha} + \varepsilon_{22,\alpha})}{\nu - 1}, \quad (5.122)$$

and consequently

$$\tilde{m}^{3\alpha} = \frac{\nu B}{\det \bar{\mathbf{F}}(\nu - 1)} A^{\alpha\beta}(\varepsilon_{11,\beta} + \varepsilon_{22,\beta}). \quad (5.123)$$

In the author's humble opinion, the literature does not address the consequences of Eq. (5.123) on a material law. There are some results, e.g., in Green et al. [Gre65], but it only states, that the transverse shear moment  $\tilde{m}^{3\alpha}$  will remain indeterminate from an equilibrium point of view, which was also derived here above. In the context of plane stress, the apparent inconsistency arising from assuming negligible transversal strain ( $\chi$ ) in the kinematic description, even when it exists in reality, is effectively addressed by postulating negligible transversal stress ( $\sigma^{33}$ ). Then, the transversal strain can be computed from the membrane strains via an appropriate post-process. This pivotal insight was originally formulated by Mindlin [Min51]. In the specific scenario of  $\tilde{m}^{3\alpha}$ , the literature, to the best of the author's knowledge, does not provide a resolution for the omission of the corresponding strain  $\chi_{,\alpha}$ . Nevertheless, it is conceivable that analogous reasoning to the plane stress case may be applicable in this context. This issue is briefly explored and discussed here.

The transverse shear moment in Eq. (5.123),  $\tilde{m}^{3\alpha}$ , is directly derivable from the membrane strains. In particular, it is a function of the spatial derivatives of the membrane strains. Thus, often in common applications for a Reissner-Mindlin shell formulation, it seems reasonable to assume that  $\tilde{m}^{3\alpha} \approx 0$ , since often no abrupt changes in the membrane strains occur. Similar to the vanishing normal stress assumption  $\sigma^{33} = 0$ ,  $\tilde{m}^{3\alpha} \approx 0$  seems to be violated, where the abrupt changing load is applied due to the induced local transverse normal stress from equilibria. For  $\sigma^{33} \approx 0$ , this violation rapidly decays for slender shells in the vicinity of the load application and this seems also to be reasonable for  $\tilde{m}^{3\alpha} \approx 0$  since it can be seen as a derived quantity influenced by thickness change

induced from transverse normal stress. If the simulated problem does not adhere to this assumption, then the Reissner-Mindlin shell formulation is not appropriate.

Consequently, the same reasoning can be applied in this case as for the plane stress assumption and this yields  $\tilde{m}^{3\alpha} \approx 0$  and  $\chi_{,\alpha}$  can be computed from Eq. (5.122) by a post-process. Thus, a Reissner-Mindlin shell formulation simply assumes  $\mathbf{t} \in \mathcal{S}^2$ , which yields  $\chi = 0$  and  $\chi_{,\alpha} = 0$  from the point of view of an implementation. The corresponding real strain can then be computed from the membrane strains via an appropriate post-process.

The previous paragraph can be summarized as follows:

1. The Reissner-Mindlin shell model assumes that the through-the-thickness stress resultant component  $\tilde{l}^3$  is negligible.
2. It is reasonable to assume that the shear moment resultant  $\tilde{m}^{3\alpha} \approx 0$  is negligible for common Reissner-Mindlin applications.
3. The thickness change and the shear curvature are directly derivable from the in-plane strains through the material model.
4. Since thickness change is not a degree of freedom, Reissner-Mindlin shell formulations pretend that the corresponding strain component is zero.
5. This is achieved by incorporating an inextensible director field.

The assumption that the transverse stress  $\sigma^{33}$  is negligible, follows, for slender shells, directly from the vanishing of through-the-thickness stress resultant component  $\tilde{l}^3$ . The stress-based shell formulation has to enforce this constraint on the stress via condensation, as done by inserting Eq. (5.118) into Eq. (5.114). This can be done analytically only for simple material models, but not for general ones. The numerical satisfaction of this constraint is the topic of the next section.

### 5.4 Stress Normal Constraint for Non-trivial Material Laws

The following section describes how the vanishing transverse normal stress condition of the Reissner-Mindlin shell model, can be tackled algorithmically. First, the straightforward general approach found in the literature and discuss its shortcomings are discussed. After this, a cure for this problem is presented by interpreting it from the perspective of differential geometry. This leads to a new algorithm, which can solve the problem of the vanishing transverse normal stress condition with fewer iterations and without premature



termination. Thus, yielding a more robust algorithm. Klinkel and Govindjee [KG02] proposed a solution to the problem of the vanishing transverse normal stress condition. It is done via iteratively solving for the stretch in the direction of the normal of the shell from the assumption of vanishing transverse normal stress  $\sigma^{33}$ . It is widely used because it is implemented, for instance, in the open-source material library MUESLI [Por17] and for some material laws in the commercial software LS-DYNA [Liv19]. The approach at hand is quite basic but quite general and can be used for any material model. It also boils down to a similar algorithm if stress rates and strain rates are used. The approach of Klinkel and Govindjee [KG02] was used often earlier in industry and academia as discussed in Schoenfeld and Benson [SB93]. Furthermore, there are other approaches, such as Schoenfeld and Benson [SB93], Jetteur [Jet86], Simo and Taylor [ST86], and Simo and Govindjee [SG88], which are restricted to special material laws.

### 5.4.1 Existing Algorithm

The basic iterative algorithm can be described as follows. To fulfill the vanishing normal stress condition, Klinkel and Govindjee [KG02] use a standard Newton iteration to solve

$$S^{33}(C_{33}) = 0. \quad (5.124)$$

All the equations are written in the total Lagrangian setting using the second Piola-Kirchhoff stresses and the right Cauchy-Green strain tensor. This is without a loss of generality since the arguments apply similarly to the other settings.

Considering the dependence of the second Piola-Kirchhoff stress tensor on the right Cauchy-Green tensor  $\mathbf{S}(\mathbf{C})$ , with particular emphasis on the transverse stress  $S^{33}(\mathbf{C})$ . Furthermore, given that only  $C_{33}$  is unknown, the functional relation  $S^{33}(C_{33})$  is the sole point of interest. Using a Newton scheme to solve this yields

$$S_{i+1}^{33} = S_i^{33} + \left. \frac{\partial S^{33}(C_{33})}{\partial C_{33}} \right|_i \Delta C_{33} = S_i^{33} + 2C_i^{33} \Delta C_{33} \stackrel{!}{=} 0 \quad (5.125)$$

and this equation can be solved for the update

$$\Delta C_{33} = -\frac{S_i^{33}}{2C_i^{33}}, \quad (5.126)$$

which can then be used to update the stretch, such that,

$$C_{33}^{i+1} = C_{33}^i + \Delta C_{33}, \quad (5.127)$$

until  $|S^{33}| < \epsilon$ , where  $\epsilon$  is a scalar, which denotes a user defined convergence tolerance. As one can see if  $\Delta C_{33}$  has a certain relation to  $C_{33}^i$  the update in Eq. (5.127) can lead to a  $C_{33}^{i+1}$  that propagates to a violation of the positive definiteness of  $\mathbf{C}^{i+1}$ . This corresponds to a penetration of matter or mathematically speaking the deformation gradient  $\mathbf{F}$  is not positive definite anymore. Thus, the deformation mapping is not a homeomorphism anymore. This unphysical drawback is not academic and is not only a problem for post-processing. This can be seen directly, if the algorithm of [KG02] is used in combination with material laws that need to extract the stretches  $\lambda_I$  of the deformation gradient  $\mathbf{F}$  and these appear in  $\mathbf{C}$  as the squared stretches  $\lambda_I^2$ . Therefore, if negative eigenvalues of  $\mathbf{C}$  occur during the iteration referenced in Eq. (5.127) on the preceding page, the iteration stops. This is because the stretches must be obtained by taking the square root to derive  $\lambda_I$ , and passing complex numbers to the material routine is not possible. One can consider workarounds by setting the negative squared stretches to zero or one and hoping for good enough convergence. This is still an unsatisfactory situation.

### 5.4.2 Proposed Algorithm

The algorithm of Section 5.4.1 neglects the geometric structure of the problem. This is incorporated in the solution in the proposed algorithm. It cannot be found in the literature for the problem of vanishing transverse normal stress, but the objects of differential geometry to develop the algorithm can be found in the mathematical literature. This is indicated at the appropriate places.

The right Cauchy-Green tensor  $\mathbf{C}$  is an element of the space of *symmetric positive definite matrices*, i.e. we have  $\mathbf{C} \in \mathcal{S}_{++}^3$ . This space of symmetric positive definite matrices reads

$$\mathcal{S}_{++}^n = \{\mathbf{X} \in \mathbb{R}^{n \times n} \mid \mathbf{X}^T = \mathbf{X} \wedge \mathbf{X} \succ 0\}. \quad (5.128)$$

Consequently, the following approach uses update routines that satisfy the geometric constraint on  $\mathbf{C}$  exactly to stay in the positive definite (physical) regime. To interpret everything in terms of differential geometry, it can be shown that  $\mathcal{S}_{++}^3$  is a Riemannian manifold, as defined in Definition 15. To satisfy the geometric constraint exactly, the algorithm uses retractions, as defined in Section 2.6. To be precise, a retraction in this case is a function that maps an object from the tangent space  $T_{\mathbf{x}}\mathcal{S}_{++}^3$  at the position  $\mathbf{x} \in \mathcal{S}_{++}^3$  back onto the manifold. A general retraction is in this case a mapping

$$R : T_{\mathbf{C}}\mathcal{S}_{++}^3 \rightarrow \mathcal{S}_{++}^3. \quad (5.129)$$

As discussed before, the update from Eq. (5.127) violates this constraint, since it does not always map onto  $\mathcal{S}_{++}^3$ . The corresponding tangent space is given by

$$T_{\mathbf{C}}\mathcal{S}_{++}^n = \{\boldsymbol{\eta} \in \mathbb{R}^{n \times n} \mid \boldsymbol{\eta}^T = \boldsymbol{\eta}\}, \quad (5.130)$$

which is the space of symmetric matrices.

This is naturally resolved by using a retraction. Two possible retractions are stated, namely the exponential map of  $\mathcal{S}_{++}^3$  and a second-order retraction. To have the notion of an exponential map, first, a Riemannian metric has to be chosen for  $T\mathcal{S}_{++}^3$ . If the induced metric  $g(\boldsymbol{\xi}, \boldsymbol{\eta}) = \langle \boldsymbol{\xi}, \boldsymbol{\eta} \rangle = \text{tr}(\boldsymbol{\xi}\boldsymbol{\eta})$ , given by an embedding space  $\mathbb{R}^{3 \times 3}$ , is used, the exponential map boils down to the standard update given by Eq. (5.127). But usually for  $\mathcal{S}_{++}^3$ , or in fact for  $\mathcal{S}_{++}^n$ , another Riemannian metric is used, namely

$$g_{\mathbf{C}}(\boldsymbol{\xi}, \boldsymbol{\eta}) = \langle \boldsymbol{\xi}, \boldsymbol{\eta} \rangle_{\mathbf{C}} = \text{tr}(\mathbf{C}^{-1}\boldsymbol{\xi}\mathbf{C}^{-1}\boldsymbol{\eta}), \quad \boldsymbol{\xi}, \boldsymbol{\eta} \in T_{\mathbf{C}}\mathcal{S}_{++}^n, \mathbf{C} \in \mathcal{S}_{++}^n. \quad (5.131)$$

Here, for simpler notation, everything is written in matrix notation. Thus,  $\mathbf{A}\mathbf{B}$  is the usual matrix product. This metric provides better results (faster convergence) for optimization on  $\mathcal{S}_{++}^n$  than the induced metric, which is elaborated in e.g. Sra and Hosseini [SH15] and Jeuris et al. [Jeu12]. Additionally, it circumvents the so-called *swelling effect* of averaging symmetric positive definite matrices, see [Yua20, Fig. 3]. Thus, this metric admits the following property. Consider two matrices  $\mathbf{A}, \mathbf{B}$  of  $\mathcal{S}_{++}^n$  with the same determinant  $d$ . The geodesic curve  $\boldsymbol{\gamma}(t) \in \mathcal{S}_{++}^n$  connecting  $\mathbf{A}$  and  $\mathbf{B}$  derived from this metric satisfies  $\det \boldsymbol{\gamma}(t) = d$ . Thus, the geodesic connecting two matrices is a path with matrices with the same determinant. This, would not be the case for the induced metric, since then the geodesic would merely be a straight line in the embedding space  $\mathbb{R}^{n \times n}$ , namely  $\boldsymbol{\gamma}(t) = \mathbf{A} + t(\mathbf{B} - \mathbf{A})$ . For reference, the notion of geodesic curves is defined in Section 3.3 on page 57. The general exponential map is defined in Section 3.4 on page 60 and retractions are defined in Section 2.6 on page 33. Nonetheless, the exponential map of  $\mathcal{S}_{++}^n$  equipped with the metric from Eq. (5.131) yields the exponential map

$$\mathbf{C}_{\text{exp}}^{i+1} = \mathbf{C}^i \exp((\mathbf{C}^i)^{-1} \Delta \mathbf{C}), \quad (5.132)$$

as derived in [Vis18].

As discussed before, the exponential map is not the only way to define retractions, it may also be handy to have another retraction. For a second-order retraction, it is possible to define

$$\mathbf{C}_{\text{2nd}}^{i+1} = \mathbf{C}^i + \Delta \mathbf{C} + \frac{1}{2} \Delta \mathbf{C} (\mathbf{C}^i)^{-1} \Delta \mathbf{C}. \quad (5.133)$$

Both retractions fulfill the constraint that  $\mathbf{C}_{i+1} \in \mathcal{S}_{++}^n \forall \Delta \mathbf{C}$ . The nomenclature of second-order retraction is defined in Section 3.4 on page 60. The given second-order retraction can be found in [Jeu12; Hua17] in the context of optimization on manifolds, not related to the mechanical context given here.

Similar to [KG02], we want to use a Newton method, namely a Riemannian Newton method. Since retractions are already discussed, we only need the Riemannian gradient. Similar to the derivations of Section 2.7.4 on page 39,  $\mathcal{S}_{++}^3$  can be embedded into  $\text{Sym}(n)$ . Thus, interpreting it as a Riemannian submanifold, we derive this object by projecting a gradient defined in the vector space  $\text{Sym}(n)$ . Consider a scalar-valued function  $f : \text{Sym}(n) \rightarrow \mathbb{R}$  and the restriction  $f : \mathcal{S}_{++}^n \rightarrow \mathbb{R}$ , where  $\text{Sym}(n)$  is the space of symmetric matrices. The Riemannian gradient is then given by

$$\text{grad}^{\text{spd}} f = \mathbf{C} \text{grad}^{\text{sym}} \bar{f}(\mathbf{X}) \mathbf{C}, \quad (5.134)$$

where  $(\bullet)^{\text{sym}}$  denotes the derivatives in the space of symmetric matrices  $\text{Sym}(n)$ . This means taking the symmetric part of a derivative defined in  $\mathbb{R}^{n \times n}$ . It can be derived via the fact that the (Riemannian) gradient of a function times a tangent vector should be equal to a directional derivative in the direction of the tangent vector in the embedding space, see Definition 16 on page 38. This yields

$$\begin{aligned} g(\text{grad}^{\text{spd}} f, \boldsymbol{\xi})_{\mathbf{C}} &= D_{\boldsymbol{\xi}} \bar{f}(\mathbf{C}) \\ \text{tr}(\mathbf{C}^{-1} \text{grad}^{\text{spd}} f \mathbf{C}^{-1} \boldsymbol{\xi}) &= \text{tr}(\text{grad}^{\text{sym}} \bar{f} \boldsymbol{\xi}), \end{aligned} \quad (5.135)$$

which yields Eq. (5.134) via comparing both sides. This formula of Eq. (5.134) is also given in [Jeu12] without derivation.

Since now all ingredients are given, they can be applied to the problem of finding a root of Eq. (5.124). Since  $\mathbf{C}$  is considered fixed, except for the entry  $C_{33}$ , the increment  $\Delta \mathbf{C}$  is nearly empty and has also only one non-zero component in the (3,3)-slot. Therefore, all values stay the same, except the (3,3)-slot. We get for the different retractions

$$C_{33, \text{exp}}^{i+1} = C_{33}^i + \frac{\det \mathbf{C}^i (\exp \frac{\Delta C_{33} m_{12}}{\det \mathbf{C}^i} - 1)}{m_{12}}, \quad (5.136)$$

$$C_{33, \text{2nd}}^{i+1} = C_{33}^i + \Delta C_{33} + \frac{(\Delta C_{33})^2 m_{12}}{2 \det \mathbf{C}^i}, \quad (5.137)$$

with  $m_{12} = C_{11}^i C_{22}^i - (C_{12}^i)^2$ , which is the minor of the (3,3)-block of  $\mathbf{C}$ . The update  $\Delta C_{33}$  for this case is also given by Eq. (5.126), since it can be shown, that the right Cauchy-Green tensors in Eq. (5.134) cancel in the metric definition Eq. (5.131), if the

update is derived via

$$\mathbf{S}^{i+1} = \mathbf{S}^i + \langle (\text{grad}^{\text{spd}} f)^i, \Delta \mathbf{C} \rangle_{\mathbf{C}}. \quad (5.138)$$

### 5.4.3 Model Problem

Consider for the following example that the tensors are all defined in an appropriate Euclidean basis. Consider a Neo-Hookean energy as given by

$$W(\mathbf{C}) = \frac{\mu}{2} (\text{tr } \mathbf{C} - 3 - 2 \ln J) + \frac{\lambda}{2} (\ln J)^2, \quad (5.139)$$

where a common choice of the volumetric contribution was used, see [JW08, Eq. 6.27].  $J = \det \mathbf{F}$  or here as function of  $\mathbf{C}$ , it is given via  $J = \sqrt{\det \mathbf{C}}$ , since  $\mathbf{C} = \mathbf{F}^T \mathbf{F}$ . The derivatives, i.e., the stresses and tangent moduli can be derived as

$$\mathbf{S}(\mathbf{C}) = \mu(\mathbf{I} - \mathbf{C}^{-1}) + \lambda \ln J \mathbf{C}^{-1}. \quad (5.140)$$

The corresponding tangent reads

$$\mathbb{C}(\mathbf{C}) = \lambda \mathbf{C}^{-1} \otimes \mathbf{C}^{-1} + 2(\mu - \lambda \ln J) \mathcal{I}, \quad (5.141)$$

with  $\mathcal{I} = \mathcal{I}^{IJKL} \mathbf{E}_I \otimes \mathbf{E}_J \otimes \mathbf{E}_K \otimes \mathbf{E}_L$  with the components

$$\mathcal{I}^{IJKL} = \frac{1}{2} ((\mathbf{C}^{-1})^{IK} (\mathbf{C}^{-1})^{JL} + (\mathbf{C}^{-1})^{IL} (\mathbf{C}^{-1})^{JK}). \quad (5.142)$$

Consider an arbitrarily chosen deformation state of an integration point of the Reissner-Mindlin shell with the following right Cauchy-Green tensor

$$\mathbf{C} = \begin{bmatrix} 1.1 & 0.1 & 0.5 \\ 0.1 & 1.2 & 0.2 \\ 0.5 & 0.2 & C_{33} \end{bmatrix} \mathbf{E}^I \otimes \mathbf{E}^J. \quad (5.143)$$

Starting from this state, the algorithm from Eq. (5.126) is used to calculate the Newton step. If this is then updated using the retraction from literature Eq. (5.127) or with one of the two proposed retractions Eqs. (5.136) and (5.137) different iteration histories are obtained for the convergence to  $S^{33} \approx 0$ . This is depicted in Fig. 5.7. It considers the iteration as converged if  $|S^{33}| < 1e-10$ . The  $x$ -axis corresponds to the initial value of  $C_{33,0}$  and the  $y$ -axis shows the needed number of iterations to reach convergence. Additionally, the border, where  $\mathbf{C}$  is not positive definite anymore, for a given  $C_{33,0}$  is also depicted in

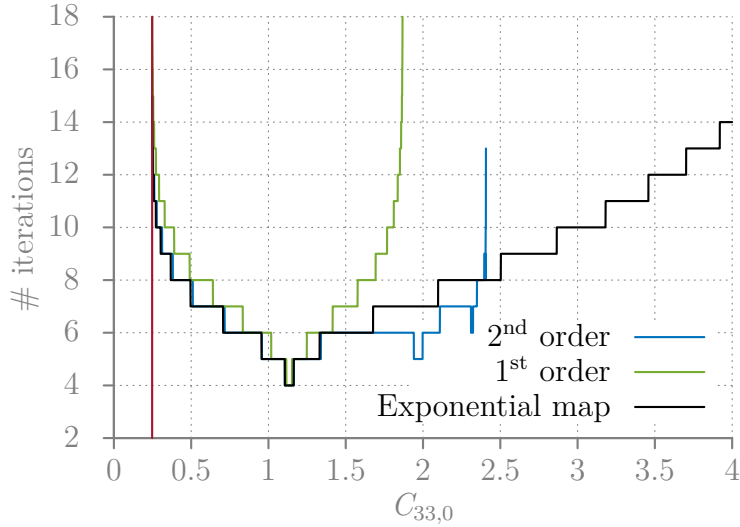


**Figure 5.7:** Number of iterations needed to reach  $|S^{33}| < 1e-10$  as function of the initial value  $C_{33,0}$ . The three different retractions from Eqs. (5.127), (5.136) and (5.137) are shown. The standard approach from Eq. (5.127) is denoted by “1<sup>st</sup> order”. The red vertical line indicates, where the tensor of Eq. (5.143) loses positive definiteness.

red. This border is for Eq. (5.143) approximately at  $C_{33} \leq 0.247$ . If the initial value is chosen smaller, complex values for  $S_{33}$  are obtained and the algorithm is considered as failed. For larger values, the exponential map Eq. (5.136) and the second-order retraction Eq. (5.137) behave superior to the retraction Eq. (5.127) proposed in [KG02]. They yield fewer iterations and have a wider domain of convergence. For  $C_{33,0} > 2.4$ , the second-order retraction does not converge, despite being faster for some smaller initial values, in comparison to the exponential map. In contrast to the other retraction methods, the exponential map does always converge. Hence, in this example, the exponential map and the second-order retraction are not only more stable but also converge with fewer iterations in comparison to the existing algorithm. Thus, the higher computational effort of Eq. (5.136) can be considered to be a good investment.

The failure of the linear retraction from Eq. (5.127) can be simply explained with Fig. 5.8. It shows the function  $S^{33}(C_{33})$  and its linearization at  $C_{33,0} = 1.9$  (the red square) in dashed black. This is then solved using Eq. (5.126) and then updated via Eq. (5.127), which yields the value for  $C_{33}$  indicated by the red circle. This yields an indefinite tensor  $\mathbf{C}$  and the solution procedure fails since the new point yields a point left of the vertical black line, which indicates where Eq. (5.143) loses positive definiteness. That’s why in Fig. 5.7 the linear retraction from Eq. (5.127) fails for initial values  $C_{33,0}$  larger than approximately 1.9. The red triangle indicates the value of  $C_{33}$  after the first update with

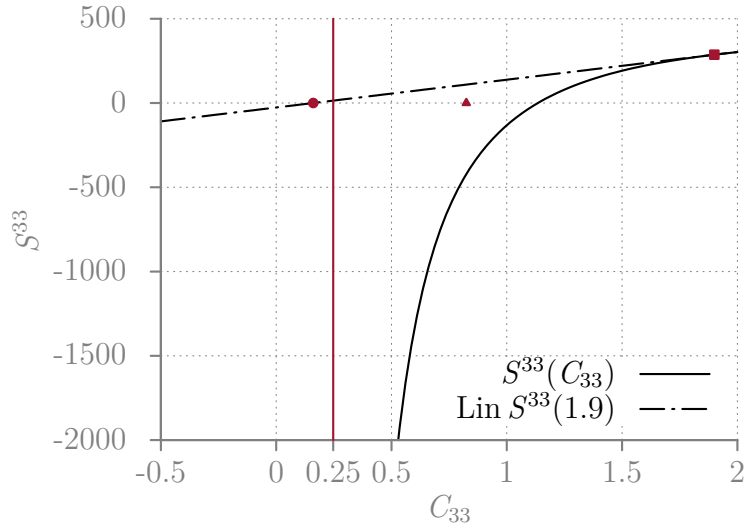


**Figure 5.8:** The function  $S^{33}(C_{33})$  in black and its linearization in dash-dotted black. The point of linearization  $C_{33,0} = 1.9$  is indicated with the red square. The first iterate of Eq. (5.126) using Eq. (5.127) yields the value for  $C_{33}$  at the red circle. The red vertical line indicates, where Eq. (5.143) loses positive definiteness. The red triangle indicates the value of  $C_{33}$  after the first iterate updated with the exponential map from Eq. (5.136).

the exponential map from Eq. (5.136), which is closer to the solution and does not violate positive definiteness.

#### 5.4.4 Conclusion

The proposed algorithm solves the problem of fulfilling zero stress constraints found in structural models. It circumvents the failure and yields fewer iterations in comparison to the standard approach found in the literature. It can still be chosen between the exponential and the second-order retraction. A similar conclusion can be drawn for material models that directly involve the deformation gradient  $\mathbf{F}$ , which is an element of the set of positive definite matrices  $\mathcal{PD}(3)$ . Here, the violation of this constraint can also lead to termination if the material routine dictates the evaluation of terms like  $\det \mathbf{F}^{-2/3}$  or  $\ln \det \mathbf{F}$ . In this case, the problem can be transformed to the positive definite matrices  $\mathcal{SO}(3)$  by  $\mathbf{C} = \mathbf{F}^T \mathbf{F}$ . Furthermore, a similar procedure can be used for incompressible materials with  $\det \mathbf{F} = 1$  or  $\det \mathbf{C} = 1$  with different tangent spaces and different retractions definitions. Beam models, where two zero stress constraints are present, can be treated similarly. The author assumes that this leads to similar improvements.

## 5.5 Variation, Linearization and Discretization

The following section is devoted to the derivation of the algebraic quantities, namely the *Riemannian algebraic stiffness matrix* and the *Riemannian algebraic residual vector*. On this path, the *Euclidean algebraic stiffness matrix* and the *Euclidean algebraic residual vector* are derived as intermediate quantities. But before this, a template for the derivation of the algebraic quantities is given. This is constructed from deriving the Euclidean weak form and its linearization. The discretization of the latter quantities is then done by using the projection-based interpolation scheme. This provides quantities living in a six-dimensional space per node, which are then projected onto the five-dimensional manifold  $\mathbb{R}^3 \times \mathcal{S}^2$ . This yields the *Riemannian algebraic stiffness matrix* and the *Riemannian algebraic residual vector*

### 5.5.1 Euclidean Variation and Linearization of the Continuous Energy

The total potential energy functional depends on the function of the midsurface position  $\varphi \in \mathfrak{X}(\mathbb{R}^3)$  and the function of the director field  $\mathbf{t} \in \mathfrak{X}(\mathcal{S}^2)$ , as in Eq. (5.8) on page 93. Therefore, the functional  $\hat{\Pi}$  takes values from the *non-linear manifold*  $\mathcal{M}$ . The total potential energy  $\hat{\Pi} : \mathcal{M} \rightarrow \mathbb{R}$  reads

$$\hat{\Pi}(\hat{\Phi}) = \int_{\hat{\mathcal{B}}_0} \bar{\psi}(\mathbf{E}(\boldsymbol{\xi}, \boldsymbol{\xi}^3)) \, dV - \hat{\Pi}^{\text{ext}}(\hat{\Phi}). \quad (5.144)$$

Here,  $\hat{\Phi} \in \mathcal{M} = \mathfrak{X}(M)$  is an element of the continuous non-linear configuration space. Furthermore,  $\bar{\psi}$  denotes a generic strain energy *volume* density functional.  $\hat{\Pi}^{\text{ext}}$  indicates an arbitrary but linear external load functional.

As elaborated below in Section 6.1.3 and in [MB22], it is sufficient to derive all the quantities in the continuous Euclidean embedding space first and then obtain the correct variation and linearization by proper discretization and projection afterward. Consequently, the embedded version of  $\hat{\Phi} = [\hat{\varphi} \ \hat{\mathbf{t}}]^T$  is introduced as

$$\Phi = \begin{bmatrix} \varphi \\ \mathbf{t} \end{bmatrix}. \quad (5.145)$$

We have  $\Phi \in \mathcal{M}_E = \mathfrak{X}(M_E)$ , where  $M_E = \mathbb{R}^3 \times \mathbb{R}^3$ , i.e. a function living in a vector space. Furthermore, we have the function  $\Pi : \mathcal{M}_E \rightarrow \mathbb{R}$ , which takes the corresponding arguments from the embedding space. Formally, this is done using an inclusion map, as defined in Eq. (2.6) on page 18, but this notion is not dragged along here.



The constitutive relations from the strain energy density  $\bar{\psi}$  resulting from a standard Coleman-Noll procedure [CN63] read in terms of the Green-Lagrangian strain and second Piola-Kirchhoff stress

$$\mathbf{S} = \frac{\partial \bar{\psi}(\mathbf{E})}{\partial \mathbf{E}}. \quad (5.146)$$

The first Euclidean variation of the potential energy reads

$$\begin{aligned} \delta \Pi(\Phi) &= \left. \frac{\partial \Pi(\Phi + \epsilon \delta \Phi)}{\partial \epsilon} \right|_{\epsilon=0} = G(\Phi; \delta \Phi) = \int_{\mathcal{B}_0^C} \frac{\partial \hat{\psi}}{\partial E_{AB}} \delta E_{AB} \, d\mathbf{V} = \int_{\mathcal{B}_0^C} S^{AB} \delta E_{AB} \, d\mathbf{V}, \\ \forall \delta \Phi &\in \mathbb{W}_{k,p}^{l,q}(\Omega, M_E). \end{aligned} \quad (5.147)$$

Here,  $\mathbb{W}_{k,p}^{l,q}(\Omega, M_E)$  denotes a template Sobolev space, depends on the exact definition of the strain energy density  $\bar{\psi}$ , ensuring that the integration in Eq. (5.144) is well-defined. The subscripts and superscripts  $k, p$  and  $l, q$  are the order of the derivatives and the order of the integrability of the functions of the midsurface position and the director field, respectively.

For the derivation of the weak form above, the Gâteaux derivative of the potential energy functional was used. In the current notation, the energy  $\Pi(\Phi)$ , has to be understood as a continuous functional, taking functions as arguments. The term *Euclidean* is supposed to indicate that the function takes arguments from the embedding space  $\mathcal{M}_E$ . Thus, everything takes place in the function space that is also a vector space,  $\mathbb{W}_{k,p}^{l,q}(\Omega, M_E)$ . This allows the usage of the vector space definition of the Gâteaux derivative, without introducing some generalization to non-linear spaces.

The Green-Lagrangian strains in the convective coordinate system are defined in Section 5.1.4 on page 99, thus the first variation reads, with these kinematics

$$G(\Phi; \delta \Phi) = \int_{\mathcal{B}_0} S^{AB} \delta E_{AB} \, d\mathbf{V} = \int_{\mathcal{B}_0} S^{\alpha\beta} \left( \delta \varepsilon_{\alpha\beta} + 2\xi^3 \delta \kappa_{\alpha\beta} + (\xi^3)^2 \delta \rho_{\alpha\beta} \right) + S^{\alpha 3} \delta \gamma_\alpha \, d\mathbf{V}. \quad (5.148)$$

The variations of the different strain components read

$$\begin{aligned}
 \delta\varepsilon_{\alpha\beta} &= \frac{1}{2}(\delta\mathbf{a}_\alpha \cdot \mathbf{a}_\beta + \mathbf{a}_\alpha \cdot \delta\mathbf{a}_\beta), \\
 \delta\kappa_{\alpha\beta} &= \frac{1}{2}(\delta\mathbf{a}_\alpha \cdot \mathbf{t}_{,\beta} + \delta\mathbf{t}_{,\alpha} \cdot \mathbf{a}_\beta + \mathbf{a}_\alpha \cdot \delta\mathbf{t}_{,\beta} + \mathbf{t}_{,\alpha} \cdot \delta\mathbf{a}_\beta), \\
 \delta\rho_{\alpha\beta} &= \frac{1}{2}(\delta\mathbf{t}_{,\alpha} \cdot \mathbf{t}_{,\beta} + \mathbf{t}_{,\alpha} \cdot \delta\mathbf{t}_{,\beta}), \\
 \gamma_\alpha &= \delta\mathbf{a}_{,\alpha} \cdot \mathbf{t} + \mathbf{a}_{,\alpha} \cdot \delta\mathbf{t}.
 \end{aligned} \tag{5.149}$$

These quantities can be rearranged according to Voigt notation given for the strains in Eq. (5.31) on page 100 as

$$\begin{aligned}
 \delta\varepsilon_V &= \begin{bmatrix} \delta\varepsilon_{11} \\ \delta\varepsilon_{22} \\ 2\varepsilon_{12} \end{bmatrix}, \quad \delta\kappa_V = \begin{bmatrix} \delta\kappa_{11} \\ \delta\kappa_{22} \\ 2\delta\kappa_{12} \end{bmatrix}, \quad \delta\rho_V = \begin{bmatrix} \delta\rho_{11} \\ \delta\rho_{22} \\ 2\delta\rho_{12} \end{bmatrix}, \quad \delta\gamma_V = \begin{bmatrix} \delta\gamma_1 \\ \delta\gamma_2 \end{bmatrix}, \\
 \delta\mathbf{E}_V &= \begin{bmatrix} \delta\varepsilon_V + 2\xi^3\delta\kappa_V + (\xi^3)^2\delta\rho_V \\ \delta\gamma_V \end{bmatrix}.
 \end{aligned} \tag{5.150}$$

Introducing the quantities

$$\mathcal{B}^{\text{mm}} = \begin{bmatrix} \mathbf{a}_1^T \frac{\partial}{\partial\xi^1} \\ \mathbf{a}_2^T \frac{\partial}{\partial\xi^2} \\ \mathbf{a}_1^T \frac{\partial}{\partial\xi^2} + \mathbf{a}_2^T \frac{\partial}{\partial\xi^1} \end{bmatrix}_{3 \times 3}, \quad \mathcal{B}^{\text{bm}} = \begin{bmatrix} \mathbf{t}_{,1}^T \frac{\partial}{\partial\xi^1} \\ \mathbf{t}_{,2}^T \frac{\partial}{\partial\xi^2} \\ \mathbf{t}_{,1}^T \frac{\partial}{\partial\xi^2} + \mathbf{t}_{,2}^T \frac{\partial}{\partial\xi^1} \end{bmatrix}_{3 \times 3}, \tag{5.151}$$

$$\mathcal{B}^{\text{sm}} = \begin{bmatrix} \mathbf{t}^T \frac{\partial}{\partial\xi^1} \\ \mathbf{t}^T \frac{\partial}{\partial\xi^2} \end{bmatrix}_{2 \times 3}, \quad \mathcal{B}^{\text{sd}} = \begin{bmatrix} \mathbf{a}_1^T \\ \mathbf{a}_2^T \end{bmatrix}_{2 \times 3}, \tag{5.152}$$

the *continuous* strain-displacement differential operator of the Euclidean problem is obtained as

$$\mathcal{B} = \begin{bmatrix} \mathcal{B}^{\text{mm}} + \xi^3\mathcal{B}^{\text{bm}} & \xi^3(\mathcal{B}^{\text{mm}} + \xi^3\mathcal{B}^{\text{bm}}) \\ \mathcal{B}^{\text{sm}} & \mathcal{B}^{\text{sd}} \end{bmatrix}_{5 \times 6}, \tag{5.153}$$

or using the base vectors  $\mathbf{g}_i$  of the shell's body, yields

$$\mathcal{B}^{\text{gm}} = \mathcal{B}^{\text{gb}} = \begin{bmatrix} \mathbf{g}_{,1}^T \frac{\partial}{\partial\xi^1} \\ \mathbf{g}_{,2}^T \frac{\partial}{\partial\xi^2} \\ \mathbf{g}_{,1}^T \frac{\partial}{\partial\xi^2} + \mathbf{g}_{,2}^T \frac{\partial}{\partial\xi^1} \end{bmatrix}_{3 \times 3}. \tag{5.154}$$

The strain-displacement differential operator of the Euclidean problem can be rewritten as

$$\mathcal{B} = \begin{bmatrix} \mathcal{B}^{\text{gm}} & \xi^3 \mathcal{B}^{\text{gb}} \\ \mathcal{B}^{\text{sm}} & \mathcal{B}^{\text{sd}} \end{bmatrix}_{5 \times 6}. \quad (5.155)$$

The first superscript denotes the corresponding strain: “m” for membrane, “b” for bending, “s” for shear, and “g”, where a mix of membrane and bending strain is at play. The second superscript denotes the variables for which the variation takes place: “m” for midsurface displacement and “d” for the director. The vector of strain variations is  $\delta \mathbf{E}_V = \mathcal{B} \delta \Phi$ . In line with this notation, the following notation for the stress is introduced,

$$\mathbf{S}_V = [S^{11} \ S^{22} \ S^{12} \ S^{13} \ S^{23}]^T, \quad (5.156)$$

according to the strain variation definition Eq. (5.150). The Euclidean weak form can be written, by inserting  $\mathcal{B}$  and  $\mathbf{S}_V$  into Eq. (5.147), as

$$G(\Phi, \delta \Phi) = \int_{\mathcal{B}_0} [\mathcal{B}(\Phi) \delta \Phi] \cdot \mathbf{S}_V \, dV \int_{\mathcal{B}_0} \delta \mathbf{E}_V(\Phi) \cdot \mathbf{S}_V \, dV. \quad (5.157)$$

### Linearization of the Continuous Euclidean Weak Form

Linearization of a weak form living in a vector space is a standard exercise in finite element analysis. With the Gâteaux derivative, we obtain the following expression for the Euclidean linearization of the weak form

$$\begin{aligned} D_{\Delta \Phi} G(\Phi, \delta \Phi) &= \int_{\mathcal{B}_0} \underbrace{[D_{\Delta \Phi} \mathcal{B} \delta \Phi]}_{\text{geometric part}} \cdot \mathbf{S}_V \\ &+ \underbrace{\mathcal{B} \delta \Phi \cdot [D_{\Delta \Phi} \mathbf{S}_V]}_{\text{material part}} \, dV, \quad \Delta \Phi \in \mathbb{W}_{k,p}^{l,q}(\Omega, M_E). \end{aligned} \quad (5.158)$$

The two individual contributions resulting from the application of the product rule of differentiation represent the classical separation of the tangent stiffness into a geometric and a material part. In the following derivations, these contributions are treated separately.

### Material Part

The material part can be straightforwardly computed as

$$[\mathcal{B}(\Phi)\delta\Phi] \cdot D_{\Delta\Phi}\mathbf{S}_V(\mathbf{E}_V(\Phi)) = [\mathcal{B}(\Phi)\delta\Phi] \cdot \left. \frac{\partial\mathbf{S}_V(\mathbf{E}_V(\Phi + \epsilon\Delta\Phi))}{\partial\epsilon} \right|_{\epsilon=0} = \delta\Phi_{1 \times 6}^T \mathcal{B}_{6 \times 5}^T \mathbb{C}_{5 \times 5} \mathcal{B}_{5 \times 6} \Delta\Phi_{6 \times 1}. \quad (5.159)$$

The material tangent moduli are defined as

$$\mathbb{C}_{5 \times 5} = \frac{\partial\mathbf{S}_V}{\partial\mathbf{E}_V}. \quad (5.160)$$

### Geometric Part

By computing the Gâteaux derivative, the geometric part is obtained as

$$\{D_{\Delta\Phi}\mathcal{B}\delta\Phi\} \cdot \tilde{\mathbf{S}} = \left\{ \left. \frac{\partial\mathcal{B}(\Phi + \epsilon\Delta\Phi)}{\partial\epsilon} \right|_{\epsilon=0} \delta\Phi \right\} \cdot \tilde{\mathbf{S}}. \quad (5.161)$$

which, in turn, can be rewritten as

$$\begin{aligned} \{D_{\Delta\Phi}\mathcal{B}\delta\Phi\} \cdot \tilde{\mathbf{S}} &= \delta\Phi^T [\mathbf{k}^g] \Delta\Phi \\ &= \begin{bmatrix} \Delta\delta\varepsilon + 2\xi^3 \Delta\delta\kappa + (\xi^3)^2 \Delta\delta\rho \\ \Delta\delta\gamma \end{bmatrix} \cdot \mathbf{S}_V, \end{aligned} \quad (5.162)$$

to implicitly define  $\mathbf{k}^g$ , which is the integrant of the quantity that will lead to the geometric stiffness matrix. Furthermore, the linearization of the strain variations are given by

$$\begin{aligned} \Delta\delta\varepsilon_{\alpha\beta} &= \frac{1}{2}(\delta\mathbf{a}_\alpha \cdot \Delta\mathbf{a}_\beta + \Delta\mathbf{a}_\alpha \cdot \delta\mathbf{a}_\beta), \\ \Delta\delta\kappa_{\alpha\beta} &= \frac{1}{2}(\delta\mathbf{a}_\alpha \cdot \Delta\mathbf{t}_{,\beta} + \delta\mathbf{a}_\beta \cdot \Delta\mathbf{t}_{,\alpha} + \Delta\mathbf{a}_\alpha \cdot \delta\mathbf{t}_{,\beta} \\ &\quad + \Delta\mathbf{a}_\beta \cdot \delta\mathbf{t}_{,\alpha} + \mathbf{a}_\alpha \cdot \Delta\delta\mathbf{t}_{,\beta} + \mathbf{a}_\beta \cdot \Delta\delta\mathbf{t}_{,\alpha}), \\ \Delta\delta\rho_{\alpha\beta} &= \frac{1}{2}(\Delta\delta\mathbf{t}_{,\alpha} \cdot \mathbf{t}_{,\beta} + \Delta\mathbf{t}_{,\alpha} \cdot \delta\mathbf{t}_{,\beta} + \delta\mathbf{t}_{,\alpha} \cdot \Delta\mathbf{t}_{,\beta} + \mathbf{t}_{,\alpha} \cdot \Delta\delta\mathbf{t}_{,\beta}), \\ \Delta\delta\gamma_\alpha &= \delta\mathbf{a}_\alpha \cdot \Delta\mathbf{t} + \Delta\mathbf{a}_\alpha \cdot \delta\mathbf{t} + \mathbf{a}_\alpha \cdot \Delta\delta\mathbf{t}. \end{aligned} \quad (5.163)$$

Then, this yields as linearization of the weak form

$$D_{\Delta\Phi} G(\Phi, \delta\Phi) = \int_{\mathcal{B}_0^C} \begin{bmatrix} \delta\varphi \\ \delta\mathbf{t} \end{bmatrix}^T \left( \underbrace{\mathcal{B}^T \mathbb{C} \mathcal{B}}_{\text{material}} + \underbrace{\mathbf{k}^g}_{\text{geometric}} \right) \begin{bmatrix} \Delta\varphi \\ \Delta\mathbf{t} \end{bmatrix} dV. \quad (5.164)$$

By discretization, this quantity would yield the *Euclidean algebraic stiffness matrix* of an extensible director formulation living in  $\mathbb{R}^3$ . This would result in a six-parameter formulation but without any stiffness associated with the thickness stretch, due to the missing corresponding strain in Eq. (5.29) on page 100. The reduction to a five-parameter model is done as follows: First, Eqs. (5.157) and (5.164) are discretized and the *Euclidean algebraic Hessian* and the *Euclidean algebraic residual* are extracted. These are then projected by exploiting the fact that the unit sphere of the nodal directors can be embedded into  $\mathbb{R}^3$ . This yields at the end of the next section the *Riemannian algebraic stiffness matrix* and *Riemannian algebraic residual*, which can be implemented in a finite element code.

## 5.5.2 Discretization

In the previous section, the weak form and its linearization were shown for the continuous Euclidean energy from Eq. (5.144). In this section, a specific discretization for the non-linear director field is introduced, and simultaneously, the canonical discretization for the midsurface interpolation is presented.

### Interpolation, Variation, and Linearization of the Midsurface Position

At first, we present the quantities of the midsurface interpolation. These can be trivially obtained by the standard interpolation procedure

$$\begin{aligned} \varphi_0^h &= \sum_{I=1}^n N^I \varphi_{I,0}, & \varphi_{0,\alpha}^h &= \mathbf{A}_\alpha^h = \sum_{I=1}^n N_{,\alpha}^I \varphi_{I,0}, \\ \varphi^h &= \sum_{I=1}^n N^I \varphi_I, & \varphi_{,\alpha}^h &= \mathbf{a}_\alpha^h = \sum_{I=1}^n N_{,\alpha}^I \varphi_I, \\ \delta\varphi^h &= \sum_{I=1}^n N^I \delta\varphi_I, & \delta\varphi_{,\alpha}^h &= \delta\mathbf{a}_\alpha^h = \sum_{I=1}^n N_{,\alpha}^I \delta\varphi_I, \\ \Delta\delta\varphi^h &= 0 & \Delta\delta\varphi_{,\alpha}^h &= \Delta\delta\mathbf{a}_\alpha^h = 0, \end{aligned} \quad (5.165)$$

where the superscript h denotes discrete quantities, i.e., discrete functions. Here,  $N^I$  is the basis function of node  $I$ . The linearization of the variation  $\Delta\delta\varphi^h$  of the field  $\varphi^h$

vanishes since the variation does not depend on the nodal values  $\varphi_I$ . This is different for the director field  $\mathbf{t}$ , which will be treated next.

### Interpolation, Variation, and Linearization of the Director Field

In contrast to the interpolation of the midsurface position, for the director field, a non-linear interpolation scheme to ensure unit length is needed. Here, only the projection-based version is defined, other choices are introduced in Section 6.3 on page 167. The projection-based interpolation again exploits, in general, an embedding space, since it interpolates linearly in the embedding space and then projects back onto the unit sphere. Nevertheless, first, the ad hoc definition of the *nodal reference directors*  $\mathbf{t}_{0,I}$  is introduced. This initialization step is done according to the algorithm proposed in [Dor13]. Then, the interpolated reference director field is defined as

$$\begin{aligned} \mathbf{t}_0^h &= \mathcal{P}_0(\mathbf{w}_0^h) = \frac{\mathbf{w}_0^h}{\|\mathbf{w}_0^h\|}, \quad \mathbf{w}_0^h = \sum_{I=1}^n N^I \mathbf{t}_{0,I}, \\ \mathbf{t}_{0,\alpha}^h &= \frac{\partial \mathcal{P}_0(\mathbf{w}_0^h)}{\partial \mathbf{w}_0^h} \frac{\partial \mathbf{w}_0^h}{\partial \xi^\alpha} = \frac{\mathbf{I} - \mathbf{t}_0^h \otimes \mathbf{t}_0^h}{\|\mathbf{w}_0^h\|} \sum_{I=1}^n N_{,\alpha}^I \mathbf{t}_{0,I} = \mathcal{P}'_0 \sum_{I=1}^n N_{,\alpha}^I \mathbf{t}_{0,I}, \end{aligned} \quad (5.166)$$

where  $\mathcal{P}_0(\mathbf{w}_0^h)$  denotes the closest point projection onto the unit sphere, which simply yields the normalized vector  $\mathbf{w}_0^h / \|\mathbf{w}_0^h\|$ . The derivative of the closest point projection w.r.t. to its argument reads

$$\frac{\partial \mathcal{P}_0(\mathbf{w}_0^h)}{\partial \mathbf{w}_0^h} = \frac{\partial \frac{\mathbf{w}_0^h}{(\mathbf{w}_0^h \cdot \mathbf{w}_0^h)^{1/2}}}{\partial \mathbf{w}_0^h} = \frac{\mathbf{I}}{\|\mathbf{w}_0^h\|} - \frac{\mathbf{w}_0^h \otimes \mathbf{w}_0^h}{\|\mathbf{w}_0^h\|^3} = \frac{\mathbf{I}}{\|\mathbf{w}_0^h\|} - \frac{\mathbf{t}_0^h \otimes \mathbf{t}_0^h}{\|\mathbf{w}_0^h\|}. \quad (5.167)$$

Thus, the only remaining potential error for the reference interpolation of the director is its angle deviation from the surface normal. At this point, it is worth noting, that for non-interpolatory “interpolations” the nodal directors do in general *not* have unit length — this is only true for the interpolated director. Projection-based interpolation for the director is applied. Thus, we introduce the projection-based interpolation for the current director field as

$$\begin{aligned} \mathbf{w}^h &= \sum_{I=1}^n N^I \mathbf{t}_I, \quad \mathbf{t}^h = \mathcal{P}(\mathbf{w}^h) = \frac{\mathbf{w}^h}{\|\mathbf{w}^h\|}, \\ \mathbf{t}_{,\alpha}^h &= \frac{\mathbf{I} - \mathbf{t}^h \otimes \mathbf{t}^h}{\|\mathbf{w}^h\|} \sum_{I=1}^n N_{,\alpha}^I \mathbf{t}_I = \mathcal{P}' \sum_{I=1}^n N_{,\alpha}^I \mathbf{t}_I. \end{aligned} \quad (5.168)$$

In the following, for a more compact notation, the superscript h, which denotes discretized quantities, is omitted.

The following operators are introduced:

$$\begin{aligned}
 \mathcal{P}' &= \frac{\mathbf{I} - \mathbf{t} \otimes \mathbf{t}}{\|\mathbf{w}\|}, & \mathcal{P}'_0 &= \frac{\mathbf{I} - \mathbf{t}_0 \otimes \mathbf{t}_0}{\|\mathbf{w}_0\|}, \\
 \mathcal{Q}_\alpha &= \frac{1}{\|\mathbf{w}\|^2} \left[ (\mathbf{t} \cdot \mathbf{w}_{,\alpha}) (3\mathbf{t} \otimes \mathbf{t} - \mathbf{I}) - 2 \operatorname{sym}(\mathbf{w}_{,\alpha} \otimes \mathbf{t}) \right], \\
 \mathcal{S}(\mathbf{v}) &= \frac{1}{\|\mathbf{w}\|^2} \left[ (\mathbf{t} \cdot \mathbf{v}) (3\mathbf{t} \otimes \mathbf{t} - \mathbf{I}) - 2 \operatorname{sym}(\mathbf{v} \otimes \mathbf{t}) \right], \\
 \mathcal{W}_\alpha^I &= \mathcal{Q}_\alpha N^I + \mathcal{P}' N_{,\alpha}^I, \\
 \mathcal{X}_\alpha(\mathbf{v}) &= \frac{2 \operatorname{sym}}{\|\mathbf{w}\|^3} \left[ 3(\mathbf{t} \cdot \mathbf{w}_{,\alpha}) [\mathbf{v} \otimes \mathbf{t} + \frac{1}{2}(\mathbf{v} \cdot \mathbf{t})(\mathbf{I} - 5\mathbf{t} \otimes \mathbf{t})] + 3\left[\frac{1}{2}(\mathbf{v} \cdot \mathbf{w}_{,\alpha})(\mathbf{t} \otimes \mathbf{t} - \frac{1}{3}\mathbf{I}) \right. \right. \\
 &\quad \left. \left. + (\mathbf{v} \cdot \mathbf{t})\mathbf{w}_{,\alpha} \otimes \mathbf{t} - \mathbf{v} \otimes \mathbf{w}_{,\alpha} \right], \right.
 \end{aligned} \tag{5.169}$$

which are shortcuts to conveniently write the following director derivatives. Consequently, the variation and linearization of the director quantities can be derived as

$$\begin{aligned}
 \delta \mathbf{t} &= \sum_{I=1}^n \frac{\partial \mathbf{t}}{\partial \mathbf{t}_I} \delta \mathbf{t}_I = \mathcal{P}' \sum_{I=1}^n N^I \delta \mathbf{t}_I, \\
 \delta \mathbf{t}_{,\alpha} &= \sum_{I=1}^n \frac{\partial \mathbf{t}_{,\alpha}}{\partial \mathbf{t}_I} \delta \mathbf{t}_I = \sum_{I=1}^n \mathcal{W}_\alpha^I \delta \mathbf{t}_I, \\
 \Delta \mathbf{t} &= \sum_{I=1}^n \frac{\partial \mathbf{t}}{\partial \mathbf{t}_I} \Delta \mathbf{t}_I = \mathcal{P}' \sum_{I=1}^n N^I \Delta \mathbf{t}_I, \\
 \Delta \mathbf{t}_{,\alpha} &= \sum_{I=1}^n \frac{\partial \mathbf{t}_{,\alpha}}{\partial \mathbf{t}_I} \Delta \mathbf{t}_I = \sum_{I=1}^n \mathcal{W}_\alpha^I \Delta \mathbf{t}_I
 \end{aligned} \tag{5.170}$$

and the linearization of the variation reads

$$\begin{aligned}
 \Delta \delta \mathbf{t} &= \sum_{I=1}^n \sum_{J=1}^n \Delta \mathbf{t}_J \frac{\partial^2 \mathbf{t}}{\partial \mathbf{t}_J \partial \mathbf{t}_I} \delta \mathbf{t}_I = \Delta \delta t^k \mathbf{e}_k \\
 &= \sum_{J=1}^n \sum_{I=1}^n \delta t_J^l (\mathcal{P}'')_{lj}^k N^J N^I \Delta t_I^j \mathbf{e}_k, \\
 \Delta \delta \mathbf{t}_{,\alpha} &= \sum_{I=1}^n \sum_{J=1}^n \Delta \mathbf{t}_J \frac{\partial^2 \mathbf{t}_{,\alpha}}{\partial \mathbf{t}_J \partial \mathbf{t}_I} \delta \mathbf{t}_I = (\Delta \delta t_{,\alpha})^k \mathbf{e}_k \\
 &= \sum_{I=1}^n \sum_{J=1}^n \delta t_J^l [N^I N^J (\mathcal{P}''')_{lmj}^k w_{,\alpha}^m + (\mathcal{P}'')_{lj}^k (N_{,\alpha}^I N^J + N^I N_{,\alpha}^J)] \Delta t_I^j \mathbf{e}_k.
 \end{aligned} \tag{5.171}$$

The partial derivatives of the projector onto the unit sphere  $\mathcal{P}$  are summarized in Appendix A.3 on page 202. Furthermore, in the first derivative  $\mathcal{P}'$  only the numerator is a projection matrix, since  $(\mathcal{P}')^n = \frac{1}{\|\mathbf{w}\|^n} \mathcal{P}'$  instead of  $(\mathcal{P}')^n = \mathcal{P}'$ .

Additionally, the quantities of Eq. (5.171) always occur in a scalar product with  $\mathbf{a}_\alpha$  or  $\mathbf{t}_{,\alpha}$ . They can be rewritten using the dummy vector  $\mathbf{v}$ , that represents  $\mathbf{a}_\alpha$  or  $\mathbf{t}_{,\alpha}$ , which yields

$$\begin{aligned} \mathbf{v} \cdot \Delta \delta \mathbf{t} &= \sum_{J=1}^n \sum_{I=1}^n \delta \mathbf{t}_J \mathcal{S}(\mathbf{v}) N^J N^I \Delta \mathbf{t}_I, \\ \mathbf{v} \cdot \Delta \delta \mathbf{t}_{,\alpha} &= \sum_{I=1}^n \sum_{J=1}^n \delta \mathbf{t}_J [N^J N^I \mathcal{X}_\alpha(\mathbf{v}) + \mathcal{S}(\mathbf{v}) (N_{,\alpha}^I N^J + N^I N_{,\alpha}^J)] \Delta \mathbf{t}_I. \end{aligned} \tag{5.172}$$

## 5.6 Element Vectors and Matrices

Now, with the interpolations of the midsurface field and the unit director field at hand, the Euclidean continuous weak form and the Euclidean continuous tangent operator from Eqs. (5.157) and (5.164) can be discretized. This yields the Euclidean *algebraic* residual and Euclidean *algebraic* stiffness matrix, which could be implemented directly. Since the stiffness matrix still has a non-trivial kernel, due to a missing stiffness in the thickness direction, these Euclidean quantities are transformed and expressed through a tangent space basis to obtain the Riemannian Hessian and Riemannian gradient with the correct dimensionality<sup>1</sup>. More details on this procedure are discussed in Section 6.1. Thus, first, the Euclidean algebraic quantities are presented, and afterward, the base change and the projections to obtain the Riemannian quantities are applied.

### 5.6.1 Internal Forces and Material Stiffness Matrix

Using the aforementioned definitions for the interpolation, the Euclidean algebraic strain-displacement operator—resulting from the continuous one from Eq. (5.153)—for a

---

<sup>1</sup>The Riemannian gradient or Hessian can be used as notational surrogates, even in scenarios where no energy is present. In such cases, the weak form simplifies to a tangent vector field, and the stiffness matrix is equivalently described as the Riemannian Jacobian.



generic node  $I$  can be given as

$$\mathbf{B}_I = \left[ \begin{array}{c} \left[ \begin{array}{c} \mathbf{g}_1^T N_{,1}^I \\ \mathbf{g}_2^T N_{,2}^I \\ \mathbf{g}_1^T N_{,2}^I + \mathbf{g}_2^T N_{,1}^I \end{array} \right] \\ \left[ \begin{array}{c} \mathbf{t}^T N_{,1}^I \\ \mathbf{t}^T N_{,2}^I \end{array} \right] \end{array} \right] \xi^3 \left[ \begin{array}{c} \left[ \begin{array}{c} \mathbf{g}_1^T \mathbf{W}_1^I \\ \mathbf{g}_2^T \mathbf{W}_2^I \\ \mathbf{g}_1^T \mathbf{W}_2^I + \mathbf{g}_2^T \mathbf{W}_1^I \end{array} \right] \\ \left[ \begin{array}{c} \mathbf{a}_1^T N^I \\ \mathbf{a}_2^T N^I \end{array} \right] \mathcal{P}' \end{array} \right]_{5 \times 6}. \quad (5.173)$$

Then with the fundamental lemma of variational calculus, the Euclidean algebraic internal forces read

$$\mathbf{F}_{\text{int},I}^{\text{euk}} = \int_{\mathcal{B}_0} \mathbf{B}_I^T \mathbf{S}_V \, dV \quad (5.174)$$

and the material part of the Euclidean stiffness matrix is

$$\mathbf{K}_{\text{mat},JI}^{\text{euk}} = \int_{\mathcal{B}_0} \mathbf{B}_J^T \mathbf{C} \mathbf{B}_I \, dV. \quad (5.175)$$

## 5.6.2 Geometric Stiffness Matrix

The Euclidean, continuous geometric stiffness matrix defined in Eq. (5.162) depends on the linearization of the variation of the continuous strain. These are given in Eq. (5.163). They are discretized by plugging in the midsurface and director discretization from Section 5.5.2, respectively.

### Contribution from Membrane Strain

For the membrane strain, this yields

$$\begin{aligned} \Delta \delta \varepsilon_V : [S^{11} \ S^{22} \ S^{12}]^T &= \frac{1}{2} (\delta \mathbf{a}_\alpha \cdot \Delta \mathbf{a}_\beta + \Delta \mathbf{a}_\alpha \cdot \delta \mathbf{a}_\beta) S^{\alpha\beta} \\ &= \sum_{J=1}^n \sum_{I=1}^n \delta \varphi_J [S^{11} N_{,1}^J N_{,1}^I + S^{22} N_{,2}^J N_{,2}^I \\ &\quad + S^{12} (N_{,1}^J N_{,2}^I + N_{,2}^J N_{,1}^I)] \mathbf{I}_{3 \times 3} \Delta \varphi_I \\ &= \sum_{J=1}^n \sum_{I=1}^n \delta \varphi_J \hat{\mathbf{N}}^{JI} \Delta \varphi_I, \end{aligned} \quad (5.176)$$

using the abbreviation

$$\hat{\mathbf{N}}^{JI} = [S^{11} N_{,1}^J N_{,1}^I + S^{22} N_{,2}^J N_{,2}^I + S^{12} (N_{,1}^J N_{,2}^I + N_{,2}^J N_{,1}^I)] \mathbf{I}_{3 \times 3}. \quad (5.177)$$

The membrane contribution to the geometric stiffness matrix is then given by

$$\Delta \delta \boldsymbol{\varepsilon} : [S^{11} \ S^{22} \ S^{12}]^T = \sum_{J=1}^n \sum_{I=1}^n \begin{bmatrix} \delta \boldsymbol{\varphi}_J \\ \delta \mathbf{t}_J \end{bmatrix}^T \begin{bmatrix} \hat{\mathbf{N}}^{JI} & \mathbf{0}_{3 \times 3} \\ \mathbf{0}_{3 \times 3} & \mathbf{0}_{3 \times 3} \end{bmatrix} \begin{bmatrix} \Delta \boldsymbol{\varphi}_I \\ \Delta \mathbf{t}_I \end{bmatrix}. \quad (5.178)$$

### Contribution from Curvature

The linearization of the variation of the curvature reads

$$\begin{aligned} \Delta \delta \boldsymbol{\kappa} : [S^{11} \ S^{22} \ S^{12}]^T &= \frac{1}{2} (\delta \mathbf{a}_\alpha \cdot \Delta \mathbf{t}_{,\beta} + \delta \mathbf{a}_\beta \cdot \Delta \mathbf{t}_{,\alpha} + \Delta \mathbf{a}_\alpha \cdot \delta \mathbf{t}_{,\beta} \\ &+ \Delta \mathbf{a}_\beta \cdot \delta \mathbf{t}_{,\alpha} + \mathbf{a}_\alpha \cdot \Delta \delta \mathbf{t}_{,\beta} + \mathbf{a}_\beta \cdot \Delta \delta \mathbf{t}_{,\alpha}) S^{\alpha\beta} \\ &= \frac{1}{2} \sum_{J=1}^n \sum_{I=1}^n [N_{,\alpha}^J \delta \boldsymbol{\varphi}_J \cdot \boldsymbol{\mathcal{W}}_\beta^I \Delta \mathbf{t}_I + N_{,\beta}^J \delta \boldsymbol{\varphi}_J \cdot \boldsymbol{\mathcal{W}}_\alpha^I \Delta \mathbf{t}_I \\ &+ N_{,\alpha}^J \Delta \boldsymbol{\varphi}_J \cdot \boldsymbol{\mathcal{W}}_\beta^I \delta \mathbf{t}_I + N_{,\beta}^J \Delta \boldsymbol{\varphi}_J \cdot \boldsymbol{\mathcal{W}}_\alpha^I \delta \mathbf{t}_I \\ &+ \delta \mathbf{t}_J [N^J N^I (\boldsymbol{\chi}_{\alpha\beta} + \boldsymbol{\chi}_{\beta\alpha}) \\ &+ \boldsymbol{\mathcal{S}}_\alpha (N_{,\beta}^I N^J + N^I N_{,\beta}^J) \\ &+ \boldsymbol{\mathcal{S}}_\beta (N_{,\alpha}^I N^J + N^I N_{,\alpha}^J)] \Delta \mathbf{t}_I] S^{\alpha\beta}. \end{aligned} \quad (5.179)$$

Using the abbreviations

$$\begin{aligned} \mathcal{N}_1^{IJ} &= N_{,1}^I N^J + N_{,1}^J N^I, \\ \mathcal{N}_2^{IJ} &= N_{,2}^I N^J + N_{,2}^J N^I, \\ \hat{\mathbf{M}}^{JI} &= N_{,1}^J \boldsymbol{\mathcal{W}}_1^I \tilde{M}^{11} + N_{,2}^J \boldsymbol{\mathcal{W}}_2^I S^{22} + (N_{,1}^J \boldsymbol{\mathcal{W}}_2^I + N_{,2}^J \boldsymbol{\mathcal{W}}_1^I) S^{12}, \\ \hat{\mathbf{M}}^{IJ} &= \boldsymbol{\mathcal{W}}_1^J N_{,1}^I S^{11} + \boldsymbol{\mathcal{W}}_2^J N_{,2}^I S^{22} + (\boldsymbol{\mathcal{W}}_2^J N_{,1}^I + \boldsymbol{\mathcal{W}}_1^J N_{,2}^I) S^{12}, \\ \hat{\mathbf{M}}_{\boldsymbol{\chi}}^{JI} &= N^J N^I (S^{11} \boldsymbol{\chi}_1(\mathbf{a}_1) + S^{22} \boldsymbol{\chi}_2(\mathbf{a}_2) + (\boldsymbol{\chi}_2(\mathbf{a}_1) + \boldsymbol{\chi}_1(\mathbf{a}_2)) S^{12}), \\ \hat{\mathbf{M}}_{\boldsymbol{\mathcal{S}}}^{JI} &= \boldsymbol{\mathcal{S}}(\mathbf{a}_1) \mathcal{N}_1^{IJ} S^{11} + \boldsymbol{\mathcal{S}}(\mathbf{a}_2) \mathcal{N}_2^{IJ} S^{22} + [\boldsymbol{\mathcal{S}}(\mathbf{a}_1) \mathcal{N}_2^{IJ} + \boldsymbol{\mathcal{S}}(\mathbf{a}_2) \mathcal{N}_1^{IJ}] S^{12}, \end{aligned} \quad (5.180)$$

the bending moment contribution to the geometric stiffness matrix reads

$$\begin{aligned} \Delta\delta\boldsymbol{\kappa} : [S^{11} \ S^{22} \ S^{12}]^T = \\ \sum_{J=1}^n \sum_{I=1}^n \begin{bmatrix} \delta\boldsymbol{\varphi}_J \\ \delta\mathbf{t}_J \end{bmatrix}^T \begin{bmatrix} \mathbf{0}_{3 \times 3} & \hat{\mathbf{M}}^{JJ} \\ \hat{\mathbf{M}}^{IJ} & \hat{\mathbf{M}}_{\boldsymbol{\chi}}^{JJ} + \hat{\mathbf{M}}_{\boldsymbol{S}}^{JJ} \end{bmatrix} \begin{bmatrix} \Delta\boldsymbol{\varphi}_I \\ \Delta\mathbf{t}_I \end{bmatrix}. \end{aligned} \quad (5.181)$$

### Contribution from Second-Order Curvature

The linearization of the variation of the second-order curvature, reads

$$\begin{aligned} \Delta\delta\rho : [S^{11} \ S^{22} \ S^{12}]^T = & \frac{1}{2}(\Delta\delta\mathbf{t}_{,\alpha} \cdot \mathbf{t}_{,\beta} + \Delta\mathbf{t}_{,\alpha} \cdot \delta\mathbf{t}_{,\beta} + \delta\mathbf{t}_{,\alpha} \cdot \Delta\mathbf{t}_{,\beta} + \mathbf{t}_{,\alpha} \cdot \Delta\delta\mathbf{t}_{,\beta})S^{\alpha\beta} \\ = & \frac{1}{2}\left(\sum_{I=1}^n \sum_{J=1}^n \delta\mathbf{t}_J [N^J N^I \boldsymbol{\chi}_\alpha(\mathbf{t}_{,\beta}) + \boldsymbol{S}(\mathbf{t}_{,\beta})(N_{,\alpha}^I N^J + N^I N_{,\alpha}^J)] \Delta\mathbf{t}_I \right. \\ & + \sum_{I=1}^n \boldsymbol{\mathcal{W}}_\alpha^I \Delta\mathbf{t}_I \cdot \sum_{J=1}^n \boldsymbol{\mathcal{W}}_\beta^J \delta\mathbf{t}_J + \sum_{J=1}^n \boldsymbol{\mathcal{W}}_\alpha^J \delta\mathbf{t}_J \cdot \sum_{I=1}^n \boldsymbol{\mathcal{W}}_\beta^I \Delta\mathbf{t}_I \\ & \left. + \sum_{I=1}^n \sum_{J=1}^n \delta\mathbf{t}_J [N^J N^I \boldsymbol{\chi}_\beta(\mathbf{t}_{,\alpha}) + \boldsymbol{S}(\mathbf{t}_{,\alpha})(N_{,\beta}^I N^J + N^I N_{,\beta}^J)] \Delta\mathbf{t}_I\right) S^{\alpha\beta}, \end{aligned} \quad (5.182)$$

$$\begin{aligned} \Delta\delta\rho : [S^{11} \ S^{22} \ S^{12}]^T = & \frac{1}{2}(\Delta\delta\mathbf{t}_{,\alpha} \cdot \mathbf{t}_{,\beta} + \Delta\mathbf{t}_{,\alpha} \cdot \delta\mathbf{t}_{,\beta} + \delta\mathbf{t}_{,\alpha} \cdot \Delta\mathbf{t}_{,\beta} + \mathbf{t}_{,\alpha} \cdot \Delta\delta\mathbf{t}_{,\beta})S^{\alpha\beta} \\ = & \frac{1}{2}\left(\sum_{I=1}^n \sum_{J=1}^n \delta\mathbf{t}_J [N^J N^I \boldsymbol{\chi}_\alpha(\mathbf{t}_{,\beta}) + \boldsymbol{S}(\mathbf{t}_{,\beta})(N_{,\alpha}^I N^J + N^I N_{,\alpha}^J) + (\boldsymbol{\mathcal{W}}_\beta^J)^T \boldsymbol{\mathcal{W}}_\alpha^I + (\boldsymbol{\mathcal{W}}_\alpha^J)^T \boldsymbol{\mathcal{W}}_\beta^I \right. \\ & \left. + [N^J N^I \boldsymbol{\chi}_\beta(\mathbf{t}_{,\alpha}) + \boldsymbol{S}(\mathbf{t}_{,\alpha})(N_{,\beta}^I N^J + N^I N_{,\beta}^J)] \Delta\mathbf{t}_I\right) S^{\alpha\beta}. \end{aligned} \quad (5.183)$$

Using the abbreviations

$$\begin{aligned} \hat{\mathbf{M}}_{\boldsymbol{\chi}}^{JJ} &= N^J N^I (\boldsymbol{\chi}_1(\mathbf{t}_{,1}) S^{11} + \boldsymbol{\chi}_2(\mathbf{t}_{,2}) S^{22} + (\boldsymbol{\chi}_1(\mathbf{t}_{,2}) + \boldsymbol{\chi}_2(\mathbf{t}_{,1})) S^{21}), \\ \hat{\mathbf{M}}_{\boldsymbol{\mathcal{W}}}^{JJ} &= (\boldsymbol{\mathcal{W}}_1^J)^T \boldsymbol{\mathcal{W}}_1^I S^{11} + (\boldsymbol{\mathcal{W}}_2^J)^T \boldsymbol{\mathcal{W}}_2^I S^{22} + ((\boldsymbol{\mathcal{W}}_1^J)^T \boldsymbol{\mathcal{W}}_2^I + (\boldsymbol{\mathcal{W}}_2^J)^T \boldsymbol{\mathcal{W}}_1^I) S^{12}, \\ \hat{\mathbf{M}}_{\boldsymbol{S}}^{JJ} &= \boldsymbol{S}(\mathbf{t}_{,1}) \mathcal{N}_1^{IJ} S^{11} + \boldsymbol{S}(\mathbf{t}_{,2}) \mathcal{N}_2^{IJ} S^{22} + (\boldsymbol{S}(\mathbf{t}_{,2}) \mathcal{N}_1^{IJ} + \boldsymbol{S}(\mathbf{t}_{,1}) \mathcal{N}_2^{IJ}) S^{12}, \end{aligned} \quad (5.184)$$

the second-order bending contribution to the geometric stiffness matrix reads

$$\begin{aligned} \Delta\delta\rho : [S^{11} \ S^{22} \ S^{12}]^T = \\ \sum_{J=1}^n \sum_{I=1}^n \begin{bmatrix} \delta\varphi_J \\ \delta\mathbf{t}_J \end{bmatrix}^T \begin{bmatrix} \mathbf{0}_{3 \times 3} & \mathbf{0}_{3 \times 3} \\ \mathbf{0}_{3 \times 3} & \hat{\mathbf{M}}_{\mathcal{X}_\rho}^{JI} + \hat{\mathbf{M}}_{\mathcal{W}}^{JI} + \hat{\mathbf{M}}_{\mathcal{S}_\rho}^{JI} \end{bmatrix} \begin{bmatrix} \Delta\varphi_I \\ \Delta\mathbf{t}_I \end{bmatrix}. \end{aligned} \quad (5.185)$$

### Contribution from Transverse Shear

Similarly, the contribution from transverse shear reads

$$\begin{aligned} \Delta\delta\rho :: [S^{13} \ S^{23}]^T = [\delta\mathbf{a}_\alpha \cdot \Delta\mathbf{t} + \Delta\mathbf{a}_\alpha \cdot \delta\mathbf{t} + \mathbf{a}_\alpha \cdot \Delta\delta\mathbf{t}]S^{\alpha 3} \\ = \sum_{J=1}^n \sum_{I=1}^n [N_{,\alpha}^J \delta\varphi_J \cdot \mathcal{P}' N^I \Delta\mathbf{t}_I + N_{,\alpha}^I \Delta\varphi_I \cdot \mathcal{P}' N^J \delta\mathbf{t}_J + \delta\mathbf{t}_J (\mathcal{S}_\alpha) \Delta\mathbf{t}_I] S^{\alpha 3}, \\ = \sum_{J=1}^n \sum_{I=1}^n \delta\varphi_J \cdot \mathcal{P}' (N_{,1}^J N^I S^{13} + N_{,2}^J N^I S^{23}) \Delta\mathbf{t}_I + \Delta\varphi_I \cdot \mathcal{P}' (N_{,1}^I N^J S^{13} + N_{,2}^I N^J S^{23}) \delta\mathbf{t}_J, \\ + \delta\mathbf{t}_J N^J (\mathcal{S}(\mathbf{a}_1) S^{13} + \mathcal{S}(\mathbf{a}_2) S^{23}) N^I \Delta\mathbf{t}_I. \end{aligned} \quad (5.186)$$

This can be rearranged using the following shortcuts

$$\begin{aligned} \hat{\mathbf{Q}}^{JI} &= \mathcal{P}' N^I (N_{,1}^J S^{13} + N_{,2}^J S^{23}), \\ \hat{\mathbf{Q}}^{IJ} &= \mathcal{P}' N^J (N_{,1}^I S^{13} + N_{,2}^I S^{23}), \\ \hat{\mathbf{Q}}_{\mathcal{S}}^{JI} &= N^J N^I (\mathcal{S}_1 S^{13} + \mathcal{S}_2 S^{23}). \end{aligned} \quad (5.187)$$

The corresponding contribution to the geometric stiffness matrix is

$$\Delta\delta\rho : \mathbf{Q} = \sum_{J=1}^n \sum_{I=1}^n \begin{bmatrix} \delta\varphi_J \\ \delta\mathbf{t}_J \end{bmatrix}^T \begin{bmatrix} \mathbf{0}_{3 \times 3} & \hat{\mathbf{Q}}^{JI} \\ \hat{\mathbf{Q}}^{IJ} & \hat{\mathbf{Q}}_{\mathcal{S}}^{JI} \end{bmatrix} \begin{bmatrix} \Delta\varphi_I \\ \Delta\mathbf{t}_I \end{bmatrix}. \quad (5.188)$$

Finally, the Euclidean geometric stiffness contribution for a pair of nodes  $I$  and  $J$  is given by

$$\begin{aligned} \mathbf{K}_{\text{geo},JI}^{\text{euk}} = \\ \int_{\mathcal{B}_0^C} \begin{bmatrix} \hat{\mathbf{N}}^{JI} & \hat{\mathbf{Q}}^{JI} + \xi^3 \hat{\mathbf{M}}^{JI} \\ \hat{\mathbf{Q}}^{IJ} + \xi^3 \hat{\mathbf{M}}^{IJ} & \hat{\mathbf{Q}}_{\mathcal{S}}^{JI} + \xi^3 (\hat{\mathbf{M}}_{\mathcal{X}}^{JI} + \hat{\mathbf{M}}_{\mathcal{S}}^{JI}) + (\xi^3)^2 (\hat{\mathbf{M}}_{\mathcal{X}_\rho}^{JI} + \hat{\mathbf{M}}_{\mathcal{W}}^{JI} + \hat{\mathbf{M}}_{\mathcal{S}_\rho}^{JI}) \end{bmatrix} dV. \end{aligned} \quad (5.189)$$

This results in the total Euclidean algebraic stiffness matrix, which is the sum of the material stiffness matrix from Eq. (5.175) and the geometric stiffness matrix from Eq. (5.189) as

$$\mathbf{K}_{JI}^{\text{euk}} = \mathbf{K}_{\text{mat},JI}^{\text{euk}} + \mathbf{K}_{\text{geo},JI}^{\text{euk}}. \quad (5.190)$$

### Projecting the Euclidean Residual and Hessian

As stated at the beginning of this section, the Euclidean residual force vector and the Euclidean stiffness matrix are not the final results, since they still need to be projected onto the tangent space of the manifold of the configuration space. More formal reasoning for this procedure is given in Section 6.1.3 on page 153. For the internal forces, which are in this case the Riemann gradient, Eq. (2.83) on page 40, is applied with a subsequent tangent basis transformation, which cancels the projection matrix from Eq. (2.83) on page 40. The procedure for the correct stiffness matrix is similar, which is the Riemannian Hessian, where the results of Example 12 on page 66 can be applied to the node pair  $I$  and  $J$ . The residual force vector does depend on the internal forces from Eq. (5.174) and the external forces  $\mathbf{F}_{\text{ext}}$ . Nevertheless, assuming the external load as  $\mathbf{F}_{\text{ext}}^{\text{euk}}$ , and inserting the Euclidean internal forces from Eq. (5.174), the residual vector is obtained as

$$\mathbf{R}_I^{\text{euk}} = \text{grad}_I \bar{\Pi}(\Phi) = \begin{bmatrix} \mathbf{F}_{\text{int}}^{\text{euk},\varphi_I} \\ \mathbf{F}_{\text{int}}^{\text{euk},\mathbf{t}_I} \end{bmatrix} - \begin{bmatrix} \mathbf{F}_{\text{ext}}^{\text{euk},\varphi_I} \\ \mathbf{F}_{\text{ext}}^{\text{euk},\mathbf{t}_I} \end{bmatrix}. \quad (5.191)$$

Since the external moment load vector lies in the tangent space of  $\mathbf{t}_J$  (for conservative loading), this results in

$$\mathbf{t}_J^T \frac{\partial \bar{\Pi}}{\partial \mathbf{t}_J} = \mathbf{t}_J^T (\mathbf{F}_{\text{int}}^{\text{euk},\mathbf{t}_J} - \mathbf{F}_{\text{ext}}^{\text{euk},\mathbf{t}_J}) = \mathbf{t}_J^T \mathbf{F}_{\text{int}}^{\text{euk},\mathbf{t}_J}, \quad (5.192)$$

since  $\mathbf{t}_J^T \mathbf{F}_{\text{ext}}^{\mathbf{t}_J} = 0$ . The stiffness matrix thus further simplifies, because it is now independent of the external loads.

The following tangent space base matrix,

$$\Lambda_{\Phi^I} = \begin{bmatrix} \mathbf{I}_{3 \times 3} & \mathbf{0}_{3 \times 2} \\ \mathbf{0}_{3 \times 3} & \Lambda_I \end{bmatrix}_{6 \times 5}. \quad (5.193)$$

is introduced, which consists of the tangent base of  $\mathbb{R}^3$ , which is the identity, and the tangent base of  $\mathcal{S}^2$  at node  $I$ , which is  $\Lambda_I$ . With Eqs. (5.175), (5.189) and (5.191) to (5.193)

the reduced Riemannian stiffness matrix, can finally be written as

$$\begin{aligned}
 \mathbf{K}_{5 \times 5}^{JI, \text{riem}} &= \underbrace{(\boldsymbol{\Lambda}_{\Phi^J}^T)_{5 \times 6} \int_{\mathcal{B}_0} [\mathbf{B}^T \mathbf{C} \mathbf{B}]_{6 \times 6} \, dV \boldsymbol{\Lambda}_{\Phi^I}^I}_{\mathbf{K}^{JI, \text{eu, riem}}} \\
 &+ \underbrace{(\boldsymbol{\Lambda}_{\Phi^J}^T)_{5 \times 6} \int_{\mathcal{B}_0} \begin{bmatrix} \hat{\mathbf{N}}^{JI} & \hat{\mathbf{Q}}^{JI} + \xi^3 \hat{\mathbf{M}}^{JI} \\ \hat{\mathbf{Q}}^{IJ} + \xi^3 \hat{\mathbf{M}}^{IJ} & \hat{\mathbf{Q}}_{\mathcal{S}}^{JI} + \xi^3 \hat{\mathbf{M}}_{1, \text{tt}}^{JI} + (\xi^3)^2 \hat{\mathbf{M}}_{2, \text{tt}}^{JI} \end{bmatrix}}_{\mathbf{K}^{JI, \text{g, riem}}} \, dV \boldsymbol{\Lambda}_{\Phi^I}^I \quad (5.194) \\
 &- \underbrace{\begin{bmatrix} \mathbf{0}_{3 \times 3} & \mathbf{0}_{3 \times 2} \\ \mathbf{0}_{2 \times 3} & \mathbf{t}_J^T \mathbf{F}_{\text{int}}^{\text{euk}, \text{t}_J} \mathbf{I}_{2 \times 2} \delta_{IJ} \end{bmatrix}}_{\mathbf{K}^{JI, \text{g}2, \text{riem}}},
 \end{aligned}$$

where the following shortcuts were used:

$$\hat{\mathbf{M}}_{1, \text{tt}}^{JI} = \hat{\mathbf{M}}_{\mathcal{X}}^{JI} + \hat{\mathbf{M}}_{\mathcal{S}}^{JI}, \quad \text{and} \quad \hat{\mathbf{M}}_{2, \text{tt}}^{JI} = \hat{\mathbf{M}}_{\mathcal{X}_\rho}^{JI} + \hat{\mathbf{M}}_{\mathcal{W}}^{JI} + \hat{\mathbf{M}}_{\mathcal{S}_\rho}^{JI}. \quad (5.195)$$

With the reduced discrete Riemannian strain-displacement operator of node I

$$\begin{aligned}
 \mathbf{B}_I^{\text{riem}} &= \mathbf{B}_I \boldsymbol{\Lambda}_{\Phi^I} \\
 &= \begin{bmatrix} \begin{bmatrix} \mathbf{g}_1^T N_{,1}^I \\ \mathbf{g}_2^T N_{,2}^I \\ \mathbf{g}_1^T N_{,2}^I + \mathbf{a}_2^T N_{,1}^I \\ \mathbf{t}^T N_{,1}^I \\ \mathbf{t}^T N_{,2}^I \end{bmatrix} \xi^3 \begin{bmatrix} \mathbf{g}_1^T \boldsymbol{\mathcal{W}}_1^I \\ \mathbf{g}_2^T \boldsymbol{\mathcal{W}}_2^I \\ \mathbf{g}_1^T \boldsymbol{\mathcal{W}}_2^I + \mathbf{g}_2^T \boldsymbol{\mathcal{W}}_1^I \\ \mathbf{a}_1^T N^I \\ \mathbf{a}_2^T N^I \end{bmatrix} \boldsymbol{\Lambda}_I \\ \mathcal{P}' \boldsymbol{\Lambda}_I \end{bmatrix}_{5 \times 5} \quad (5.196)
 \end{aligned}$$

the stiffness matrix reads

$$\begin{aligned}
 \mathbf{K}_{5 \times 5}^{JI, \text{riem}} &= \int_{\mathcal{B}_0} \mathbf{B}_J^{\text{riem}, T} \mathbf{C} \mathbf{B}_I^{\text{riem}} \\
 &+ \begin{bmatrix} \hat{\mathbf{N}}^{JI} & (\hat{\mathbf{M}}^{JI} + \hat{\mathbf{Q}}^{JI}) \boldsymbol{\Lambda}_I \\ \boldsymbol{\Lambda}_J^T (\hat{\mathbf{M}}^{IJ} + \hat{\mathbf{Q}}^{IJ}) & \boldsymbol{\Lambda}_J^T (\hat{\mathbf{Q}}_{\mathcal{S}}^{JI} + \xi^3 \hat{\mathbf{M}}_{1, \text{tt}}^{JI} + (\xi^3)^2 \hat{\mathbf{M}}_{2, \text{tt}}^{JI}) \boldsymbol{\Lambda}_I - \mathbf{t}_J^T \mathbf{F}_{\text{int}}^{\text{euk}, \text{t}_J} \mathbf{I}_{2 \times 2} \delta_{IJ} \end{bmatrix} \, dV. \quad (5.197)
 \end{aligned}$$

The contribution  $\mathbf{t}_J^T \mathbf{F}_{\text{int}}^{\text{euk}, \text{t}_J} \mathbf{I}_{2 \times 2} \delta_{IJ}$  is not included in similar formulations found in the literature, except for [Sim90a], where it can be found as the final term in Equation (B.5) and Chapter C.2.4 (v) Geometric-diagonal. It is important to emphasize that this contribution *does not vanish at equilibrium*, as only the tangential part of the residual

disappears. Consequently, neglecting this term would lead to incorrect results when performing eigenvalue analysis to study stability issues. For reference, it stems from the Weingarten contribution of the Riemannian Hessian, see Eq. (3.39) on page 66. Furthermore, it remains non-zero even with mesh refinement. It is given by

$$\mathbf{K}_{5n \times 5n}^{\text{g}2, \text{riem}} = -\text{diag}[(\bar{M}^1 + \bar{Q}^1)\mathbf{H}_{5 \times 5}, \dots, (\bar{M}^n + \bar{Q}^n)\mathbf{H}_{5 \times 5}], \quad (5.198)$$

with

$$\begin{aligned} \bar{M}^I &= \mathbf{t}_I \cdot \int_{\mathcal{B}_0} \xi^3 [\mathcal{W}_1^I \mathbf{g}_1 S^{11} + \mathcal{W}_2^I \mathbf{g}_2 S^{22} \\ &\quad + (\mathcal{W}_2^I \mathbf{g}_1 + \mathcal{W}_1^I \mathbf{g}_2) S^{12}] \, \mathbf{dV}, \\ \bar{Q}^I &= \mathbf{t}_I \cdot \int_{\mathcal{B}_0} \mathcal{P}'(\mathbf{a}_1 S^{13} + \mathbf{a}_2 S^{23}) N^I \, \mathbf{dV}, \\ \mathbf{H}_{5 \times 5} &= \begin{bmatrix} \mathbf{0}_{3 \times 3} & \mathbf{0}_{3 \times 2} \\ \mathbf{0}_{2 \times 3} & \mathbf{I}_{2 \times 2} \end{bmatrix}. \end{aligned} \quad (5.199)$$

The interested reader is referred to [MB22] for a geometric and physical interpretation of  $\mathbf{K}^{\text{g}2, \text{riem}}$ .

Furthermore, with Eqs. (5.191) and (5.193) the final Riemannian gradient or residual in the tangent space representation reads

$$\begin{aligned} \mathbf{R}_{J, 5 \times 1}^{\text{riem}} &= \text{grad}_J \Pi(\Phi) = \Lambda_{\Phi_J}^T P_{\Phi_J} \text{grad}_J \bar{\Pi}(\Phi) \\ &= \begin{bmatrix} \frac{\partial \bar{\Pi}}{\partial \varphi_J} \\ \Lambda_{\mathbf{t}_J}^T \frac{\partial \bar{\Pi}}{\partial \mathbf{t}_J} \end{bmatrix} = \begin{bmatrix} \mathbf{F}_{\text{int}}^{\text{euk}, \varphi_J} \\ \Lambda_{\mathbf{t}_J}^T \mathbf{F}_{\text{int}}^{\text{euk}, \mathbf{t}_J} \end{bmatrix} - \begin{bmatrix} \mathbf{F}_{\text{ext}}^{\text{euk}, \varphi_J} \\ \Lambda_{\mathbf{t}_J}^T \mathbf{F}_{\text{ext}}^{\text{euk}, \mathbf{t}_J} \end{bmatrix}, \end{aligned} \quad (5.200)$$

where  $\Lambda_{\Phi_J}^T P_{\Phi_J} = \Lambda_{\Phi_J}^T$  has been used.

Now, with Eqs. (5.197) and (5.200) the algebraic problem is defined and can be solved for the unknowns  $\Delta \Phi$ . The solution algorithm needs to be still aware of the manifold structure of the problem since retractions need to be used to properly update the nodal directors in each step.





# 6

---

## Idiosyncrasies of Finite Elements for Non-linear Fields

This chapter deals with several uncommon problems that arise in the context of developing finite element formulation for non-linear configuration spaces, which naturally come into play, when large rotations are involved. Thus, the results of this chapter do not only apply to Reissner-Mindlin shell formulations but also to beam formulations, solid formulations of Cosserat-type and shell formulations, which include drilling rotations and other manifold-valued configuration spaces.

In particular, this chapter investigates the following problems: The first section discusses the general solution process from the continuous problem to the discrete problem to the algebraic problem, solved with Newton's method on a computer. Therein, also the correct linearization procedure is discussed, which includes the correct definition of the tangent operator.

In the second section, this very same tangent operator and its symmetry are discussed for the case of large rotations.

The third section deals with the discretization and interpolation of the functions mapping onto a manifold, e.g., onto the unit sphere.

### 6.1 From Functional Analysis to System Matrices

This section deals with several complications of functional analysis on manifolds up to the definition of the system vectors and system matrices. This section deals with this scenario from an engineering perspective. First, the historical context is given. Then, the linear case is revisited and after that, the peculiarities of the non-linear case are investigated.

### 6.1.1 Historical Overview and Remarks

Variation and linearization of a functional depending on quantities living in *continuous vector spaces* is a well-understood topic in the context of solving PDEs in such spaces. In the case of quantities living in non-linear spaces, the situation becomes more difficult. The engineering literature for finite element formulations including large rotations, often doesn't bother about the implications, when using values from non-linear manifolds in terms of proper definitions of infinite dimensional spaces, where the PDE or weak form is defined. Thus, this leads to several ambiguities and errors in derivations therein.

Nevertheless, finite element methods for the discretization of PDEs on manifolds have been studied in the literature for a long time. This is especially true for the physical fields, where the underlying manifold is of importance for a consistent underlying theory. In the context of the geometrically non-linear Reissner Mindlin shell, a proposed formulation dates back at least to Ramm [Ram76]. The historical context of the Reissner-Mindlin shell will be discussed in more detail in Section 6.3.1 and is not treated here. The theoretical derivations before usually deal with the geometrically linear case or even only plates, such as Mindlin [Min51]. Thus, therein no non-linear manifold is present. Another prominent example, where the manifold nature does date back earlier is in the context of micromagnetics, where the seminal work of Landau and Lifshitz [LL35], which dates back to the 1930s, is of importance. These are then followed by the work of Brown [Bro66], who laid the basis of the theory of *micromagnetics* using variational principles in the 1960s. In this context, the quantity living on a manifold is the magnetization vector field, which is a vector field on the unit sphere. These works from physics yield a large bouquet of methods treating the *large rotations* of the problem.

Unrelated to physics and unrelated to finite elements, in the context of algebraic optimization, the works of Luenberger [Lue72; Lue73] are early contributions. The authors state, that the optimization on geodesic curves (on manifolds), would be appropriate but is not reasonable from a computational point of view, which is to some extent not true anymore. This is especially due to the book from Absil et al. [Abs08], where the foundations of algebraic optimization on manifolds were collected from mathematical literature. This seems to be the go-to book for the topic of optimization on manifolds. It cleans up the situation and provides a good overview of the topic and consequently, yields a nice way how to deal with Riemannian quantities. This is especially true for the case of the *Riemannian gradient* and the *Riemannian Hessian*, which are the main ingredients for the optimization on manifolds. These can simply be obtained by exploiting the embedding space of a Riemannian submanifold as discussed in detail in Chapters 2 and 3. Furthermore, the notation of retractions was also a key discovery to replace the exponential map, which is not always available or expensive. This notion of retractions goes back to Adler et al. [Adl02].

In the context of finite elements for manifolds, thus dealing with functions and not with discrete points on a manifold, luckily, the works of Sander [San10] and subsequent papers [San12; San15; San16a; Gro15; Gro11; Gro19] cleaned up the situation for PDEs and weak forms living in non-linear spaces. For a theoretical treatment of these discrete and continuous non-linear function spaces, we refer to [Har18; HS20; Har15; Gro15]. At the time of writing, the mathematical investigations in this area are not yet finished in contrast to the linear theory. These works additionally deal, e.g., with the correct development of interpolation schemes, which are not trivial in the non-linear case since a naïve application of results from the linear theory does not always yield correct results.

This section states the basic results, hopefully, digestible for the reader unfamiliar with functional analysis on manifolds.

### 6.1.2 The Linear Case

Creating approximate solutions of PDEs in *linear* vector spaces using finite elements is nowadays a well-understood topic. For more details concerning boundary conditions and detailed definitions, the reader is referred to Braess [Bra07] and Brenner and Scott [BS07]. As a prototype of a PDE, Poisson's equation is considered. It is defined on a linear *continuous* vector space, i.e. in the function space  $\mathcal{D}(\Omega, \mathbb{R})$ , where  $\mathcal{D}(\Omega, \mathbb{R})$  denotes the space of functions defined on  $\Omega$  that map onto  $\mathbb{R}$ . Consequently, as prototype PDE, Poisson's equation is given as

$$-\Delta u = f \text{ on } \Omega, \quad (6.1)$$

where  $f \in L^2(\Omega)$  and  $L^2$  denotes the square-integrable functions on  $\Omega$ .  $\Delta$  is the Laplace operator, which is the divergence of the gradient. These PDEs are called strong forms in the context of finite element schemes. Their solution returns the unknown function  $u$ , which lives in a subset of  $\mathcal{D}(\Omega, \mathbb{R})$ , namely  $C^2(\Omega, \mathbb{R})$ , the space of twice differentiable functions. By using, e.g., Galerkin's method of weighted residuals [Gal15], the smoothness requirements of these continuous solutions can be relaxed, since derivatives can be shifted to the functions  $\delta u$  and the PDE only needs to be fulfilled in an integral sense. This is done by multiplying the PDE with a test function  $\delta u \in \mathcal{D}(\Omega, \mathbb{R})$  and integrating over the domain  $\Omega$ . Then integration by parts shifts the derivatives from  $u$  to  $\delta u$ . The arising boundary term is neglected to simplifying the subsequent statements. The weak form of Eq. (6.1), reads

$$G(u, \delta u) = \int_{\Omega} \nabla u \nabla \delta u \, dx = \int_{\Omega} f \delta u \, dx \quad \forall \delta u \in H^1(\Omega). \quad (6.2)$$

The function  $u$  and the test function  $\delta u$  both stem from the same function space  $H^1(\Omega)$ , where  $H^1(\Omega)$  is the space of scalar  $L^2$  functions with first-order weak derivative also in  $L^2(\Omega)$ .

The problem can also be formulated as a minimization problem, where the minimizers are the solutions of Eq. (6.2). This reads

$$\hat{\Pi} : H^1(\Omega) \rightarrow \mathbb{R}, \quad \Pi(u) = \int_{\Omega} \frac{1}{2} \nabla u \nabla u - fu \, dx. \quad (6.3)$$

Here, the first order optimality condition — the weak form — is recovered, by using a *Gâteaux directional derivative* defined in the infinite-dimensional function space. The result is the first variation of  $\hat{\Pi}$ . This results in

$$\delta \hat{\Pi} = G(u, \delta u) = \left. \frac{\partial \Pi(u + \epsilon \delta u)}{\partial \epsilon} \right|_{\epsilon=0} = \int_{\Omega} \nabla u \nabla \delta u - f \delta u \, dx = 0 \quad \forall \delta u \in H^1(\Omega). \quad (6.4)$$

Thus,  $\delta u$  can be interpreted as a perturbation vector based at  $u$  and as the direction of the directional derivative. From this infinite dimensional vector space  $H^1(\Omega)$ , where the solution lives, the finite element method introduces discrete finite element function spaces, such that  $V_h(\Omega) \subset H^1(\Omega)$ . For the definition of a single finite element, we follow Ciarlet [Cia02]. Consequently, a finite element is defined by its domain, a finite set of functions  $N^i$ , and a coefficient vector of nodal variables  $\mathbf{d}_i \in \mathbb{R}^d$ . The functions are usually called *ansatz functions*<sup>1</sup>, and the nodal variables are called *degrees of freedom*. These finite elements are used to construct a global function, that is constructed piecewise by the local finite element functions. This space is finite-dimensional since  $V_h(\Omega)$  is assumed to have a finite number of basis functions, the union of all element ansatz functions. Then, the discrete solution and discrete test function  $u_h, \delta u_h \in V_h(\Omega)$  can be constructed by

$$u_h = \sum_{i=1}^k N^i \mathbf{d}_i \quad \text{and} \quad \delta u_h = \sum_{i=1}^k N^i \delta \mathbf{d}_i. \quad (6.5)$$

If this is inserted into Eq. (6.4), the weak form in the discrete function space reads

$$\int_{\Omega} \nabla u_h \nabla \delta u_h - f \delta u_h \, dx = 0 \quad \forall \delta u_h \in V_h(\Omega), \quad (6.6)$$

---

<sup>1</sup>No consistent naming can be derived from literature here, often they are called *ansatz functions* or simply *basis functions* depending on the context or author. Nevertheless, these functions form a basis of the ansatz space  $V_h(\Omega)$

and the corresponding algebraic problem reads

$$\int_{\Omega} \sum_{i=1}^k \sum_{j=1}^k \nabla N^i \mathbf{d}_i \nabla N^j \delta \mathbf{d}_j - f \sum_{i=1}^k N^i \delta \mathbf{d}_i dx = 0 \quad \forall \delta \mathbf{d} \in (\mathbb{R}^d)^n, \quad (6.7)$$

which is the representation that can be solved using a computer, where  $\mathbf{d}$  is the collection of all nodal vectors  $\mathbf{d}_i$ . This is done using the *fundamental lemma of calculus of variations*. The final equation can be obtained as

$$\mathbf{R}(\mathbf{d}) = \mathbf{K}\mathbf{d} - \mathbf{f}_{\text{ext}} = \mathbf{0}, \quad (6.8)$$

with the stiffness matrix  $\mathbf{K}$  and the load vector  $\mathbf{f}_{\text{ext}}$ , where the subscript underlines the external nature of this quantity since it is applied from the outside as a load. The quantities  $\mathbf{K}$  and  $\mathbf{f}_{\text{ext}}$  are defined by

$$K_{ij} = \int_{\Omega} \nabla N^i \nabla N^j dx, \quad f_i = \int_{\Omega} f N^i dx, \quad (6.9)$$

where the integrals are evaluated using numerical quadrature rules and where a notion of assembly operations is neglected for simplicity. If the problem at hand is non-linear in  $u$  or  $\mathbf{d}$ , respectively, the solution for  $\mathbf{d}$  can be obtained using a Newton-Raphson method. This method can be expressed as

$$\left. \frac{\partial \mathbf{R}(\mathbf{d})}{\partial \mathbf{d}} \right|_{\mathbf{d}=\mathbf{d}_i} \Delta \mathbf{d} = -\mathbf{R}(\mathbf{d}_i), \quad \mathbf{d}_{i+1} = \mathbf{d}_i + \Delta \mathbf{d}. \quad (6.10)$$

For a given set of finite elements, there is a one-to-one correspondence between the set of coefficients  $\mathbf{d}_i$  and the constructed function  $u_h$ . Therefore, the finite element method can be used to translate a PDE into a problem of finding the correct vector in  $(\mathbb{R}^d)^n$ , where  $n$  denotes the number of nodes on the grid of finite elements. Thus, the solution procedure now lives in an algebraic space and is a function of the coefficient vector of nodal values. For the understanding of different developments, it is crucial to differentiate between methods that apply to the algebraic space  $(\mathbb{R}^d)^n$ , or the discrete function space  $V_h(\Omega)$  or the continuous function space  $H^1(\Omega)$ .

### 6.1.3 The Non-linear Case

For the non-linear case, we describe the problem by following Fig. 6.1. Understanding the distinction between continuous, discrete, and algebraic representations of potentials and weak forms is crucial when dealing with non-linear cases. For simplicity, assume again Poisson's equation but now on a manifold  $M$ . Thus, the equations from the linear

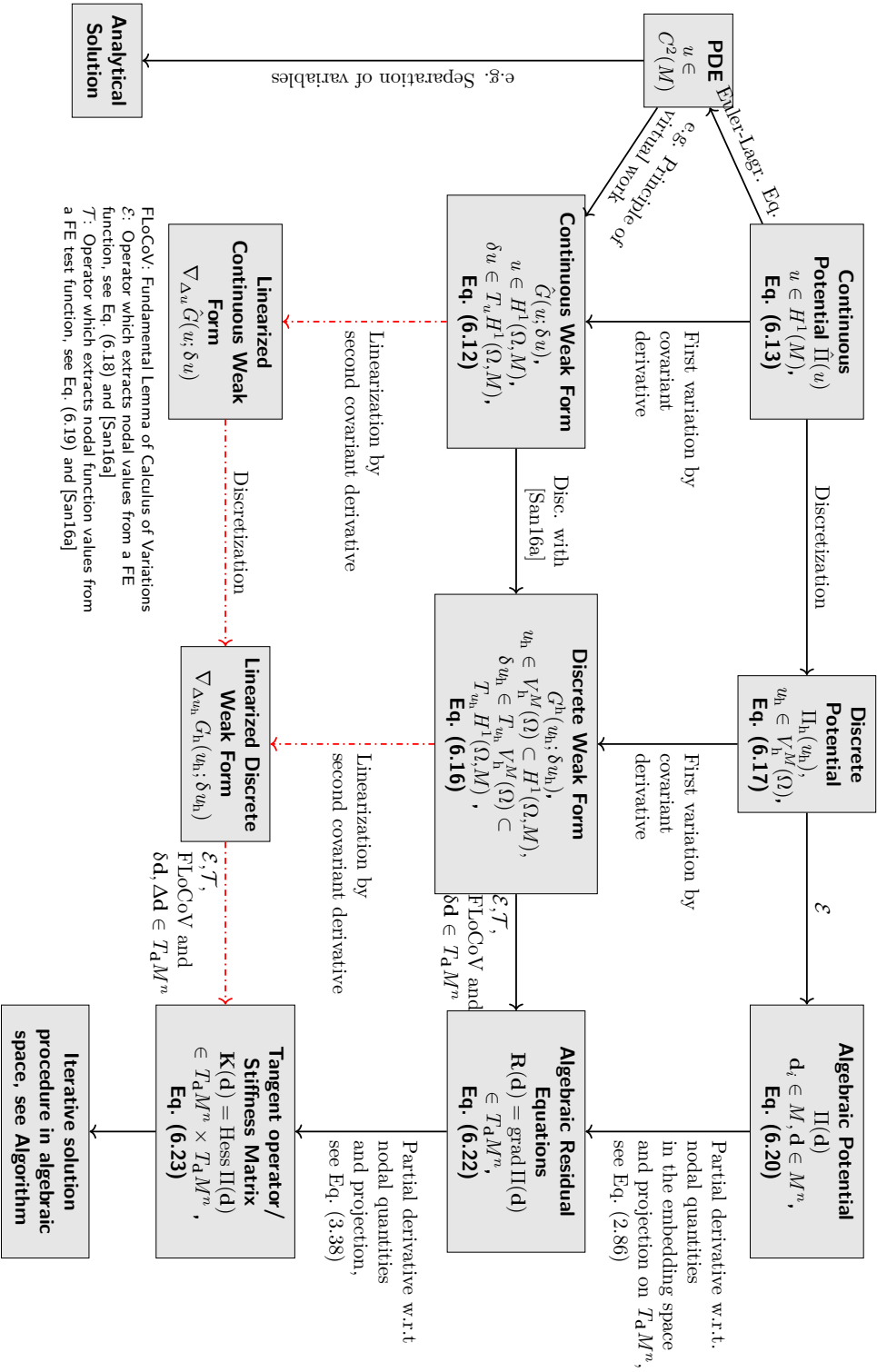


**Figure 6.1:** General solution process of the manifold-valued PDE or potential functionals. In red dash-dotted unfeasible paths to derive a consistent formulation.

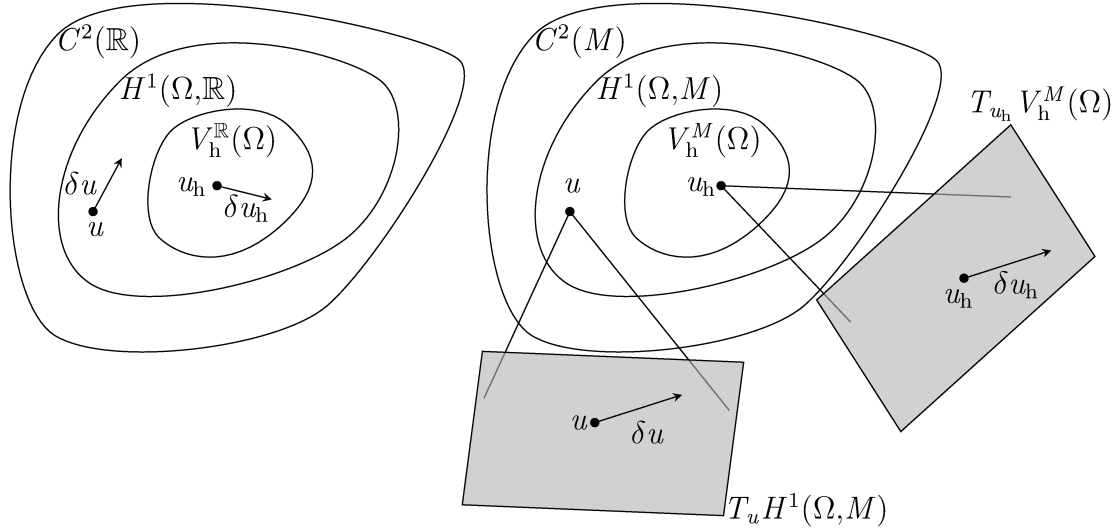


**Figure 6.2:** Spatial relation of different function spaces in a vector space (left) and for manifolds (right). This assumes that the corresponding finite element space  $V_h$  is conforming in  $H^1$ , i.e.  $V_h \subset H^1$ .

case can be restated for the manifold  $M$  as

$$-\Delta u = f \text{ on } \Omega, \quad (6.11)$$

where now  $u \in H^1(\Omega, M)$  and  $f \in L^2(\Omega, \mathbb{R}^3)$ . Furthermore,  $\Delta$  is the *Laplace–Beltrami operator* instead of the Laplace operator of Eq. (6.1) and in the following  $\nabla u$  denotes the covariant derivative of the field  $u$ . On manifolds, it can be also defined in local coordinates but for the understanding of this section, the definition is not needed explicitly. The weak form now reads

$$\hat{G}(u, \delta u) = \int_{\Omega} \langle \nabla u, \nabla \delta u \rangle dx - \int_{\Omega} \langle f, \delta u \rangle dx \quad \forall \delta u \in T_u H^1(\Omega, M), \quad (6.12)$$

where  $\langle \cdot, \cdot \rangle$  denotes some inner product of the manifold  $M$ . Especially, the test function now does not live in  $H^1(\Omega, M)$  but in the tangent space located at  $u$ , namely  $T_u H^1(\Omega, M)$ . This is in big contrast to the linear theory, where these two spaces can be canonically identified.

This is also depicted in Fig. 6.2, where on the left-hand side the test function spaces and ansatz function spaces coincide and the test functions live in the same space, but in the manifold case, on the right-hand side, this is not the case anymore. Here, the test functions live in the tangent space of the ansatz function space, which locally resembles the ansatz function space, which is indicated in the figure by “zooming in”. In Fig. 6.1 on

page 154, this situation corresponds to going from the left PDE box to the continuous weak form  $\hat{G}$ , which is done, e.g., using Galerkin's method of weighted residuals. Similar to the case before, the same problem can also be stated as a minimization problem, with the potential

$$\hat{\Pi} : H^1(\Omega, M) \rightarrow \mathbb{R}, \quad \Pi(u) = \int_{\Omega} \frac{1}{2} \langle \nabla u, \nabla u \rangle - \langle f, u \rangle dx. \quad (6.13)$$

The first variation of this continuous potential then yields the weak form Eq. (6.12), which corresponds to going downward in the left column in Fig. 6.1. The continuous weak form also needs to be linearized and therefore a connection on  $\mathcal{M}$  has to be introduced to arrive at the linearized continuous weak form, which means going another step downward in Fig. 6.1. The discretization of the linearized continuous weak form may or may not result in a consistent formulation if one moves from there to the right by discretization, since discretization is a more delicate issue on manifolds in contrast to the linear case, which is discussed now. How this variation and subsequent linearization should be performed was also a controversial topic in the literature. Especially, the Gâteaux directional derivative used in Eq. (6.4) is not well-defined in the manifold context. This special case will be revisited in Section 6.2. At least it is error-prone and can lead, in the best case, to missing terms in the resulting tangent operator. Due to similar reasons, but a bit more involved, the missing terms in the tangent operator of Ramm [Ram76; Ram77] can be explained.

To obtain a problem in the discrete function space  $V_h^M(\Omega) \subset H^1(\Omega, M)$ ,  $u$  and the test function  $\delta u$  have to be discretized to move from a continuous potential or a continuous weak form to the right in Fig. 6.1. This can be done using geodesic interpolation or projection-based interpolation, which will be described in Section 6.3 and which was also investigated numerically for the Reissner-Mindlin shell in [MB22]. Nevertheless, a generic interpolation function for a single finite element can be stated as  $\Upsilon : M^k \times \Omega_e \rightarrow M$ , where  $\Omega_e$  is the finite element's domain as a subset of  $\Omega$  and  $k$  is the number of nodes of the given element.  $M^k$  denotes the product space of all nodal algebraic quantities. Thus, we have a generic interpolation

$$u_h(x) = \Upsilon(\mathbf{d}_1, \dots, \mathbf{d}_k; x), \quad (6.14)$$

where it is apparent that in the case of finite element interpolation functions, the function  $u_h$  is possibly a non-linear function of the nodal coefficient vectors  $\mathbf{d}_i$ , which is in strong contrast to the linear interpolation formulas of the linear case given in Eq. (6.5). Similar, but a bit more involved, is the consistent construction of the test functions from the



given interpolation as

$$\delta u_h(x) = \sum_{i=1}^k D_{\delta \mathbf{d}_i} \Upsilon(\mathbf{d}_1, \dots, \mathbf{d}_k; x), \quad (6.15)$$

where the nodal algebraic test vectors are  $\delta \mathbf{d}_i \in T_{\mathbf{d}_i} M$ . This derivative also has to be understood as a covariant derivative on a manifold, since  $\mathbf{d}_i \in M$ . This construction is given in Sander [San16a].

REMARK 7. The underlying method can still be considered as a *Bubnov-Galerkin method*, even, if the ansatzes for the solution field and the test field do not coincide. For the Bubnov-Galerkin method, it is often sloppily stated, that for the linear case the ansatz function for the test field and the solution field are the same in contrast to *Petrov-Galerkin methods*, where this is not necessarily the case. Nevertheless, for the manifold case, where only the Bubnov-Galerkin method is considered here, the test functions can be constructed from the solution fields, see Eq. (6.15). Thus, they are still entangled and not separately chosen as in a Petrov-Galerkin method.

---

Then,  $\delta u_h$  is an element of  $T_u V_h^M(\Omega)$ . Therefore, the test function depends on the solution  $u$  itself due to the dependence of  $\mathbf{d}_i$  in the interpolation scheme, in contrast to the linear case in Eq. (6.5). The weak form represented in the discrete function space reads

$$G_h(u_h, \delta u_h) = \int_{\Omega} \langle \nabla u_h, \nabla \delta u_h \rangle - \langle f, \delta u_h \rangle dx = 0 \quad \forall \delta u_h \in T_{u_h} V_h^M(\Omega), \quad (6.16)$$

with  $u \in V_h^M(\Omega)$  and similarly the discrete potential reads

$$\Pi_h : V_h^M(\Omega) \rightarrow \mathbb{R}, \quad \Pi_h(u_h) = \int_{\Omega} \frac{1}{2} \langle \nabla u_h, \nabla u_h \rangle - \langle f, u_h \rangle dx, \quad (6.17)$$

which finalized the move from the left column's potential or weak form to the center column's potential and weak form.

The algebraic equivalent is also more involved in the linear case. To construct it, first, we need the nodal extractor operator

$$\mathcal{E} : V_h^M(\Omega) \rightarrow M^k, \quad (6.18)$$

which extracts from a given finite element function  $u_h$  the nodal quantities  $u_i$  living on the manifold  $M$ . Additionally, from the test functions  $\delta u^h \in T_{u_h} V_h^M$  a similar function is

needed to extract the algebraic nodal test function vectors. This function can be defined for a single element as

$$\mathcal{T} : T_{u_h} V_h^M(\Omega) \rightarrow (T_{\mathbf{d}_1} M, \dots, T_{\mathbf{d}_k} M). \quad (6.19)$$

These operators now allow the formal statement of the weak form and the potential in the algebraic setting. Namely, we have for the algebraic potential.

$$\Pi : M^n \rightarrow \mathbb{R}, \quad \Pi(\mathbf{d}) = \hat{\Pi}(\mathcal{E}^{-1}(\mathbf{d})), \quad (6.20)$$

and for the algebraic weak form  $G : M^n \times (T_{\mathbf{d}_1} M, \dots, T_{\mathbf{d}_n} M) \rightarrow \mathbb{R}$ , we have

$$G(\mathbf{d}, \delta \mathbf{d}) = \hat{G}(\mathcal{E}^{-1}(\mathbf{d}), \mathcal{T}^{-1}(\delta \mathbf{d})) = 0, \quad \forall \delta \mathbf{d} \in (T_{\mathbf{d}_1} M, \dots, T_{\mathbf{d}_n} M). \quad (6.21)$$

Thus, for the potential, we can move in Fig. 6.1 from the discrete potential  $\Pi_h$  to the algebraic potential  $\Pi$ . The last step to move from the weak form to the algebraic residual equation namely *the fundamental lemma of calculus of variations* is missing. It allows us to get rid of the algebraic tangent vector at each node due to their arbitrariness (within the tangent space) in Eq. (6.21). The rest of the equation has to vanish within the tangent space. Then, the algebraic residual equation reads

$$\mathbf{R} : \begin{cases} M^n \rightarrow (T_{\mathbf{d}_1} M, \dots, T_{\mathbf{d}_n} M), \\ \mathbf{R}(\mathbf{d}) = \text{grad } \Pi(\mathbf{d}) = \mathbf{0}, \end{cases} \quad (6.22)$$

which is intrinsically non-linear in the coefficients  $\mathbf{d}_i$ , since the interpolation given by Eq. (6.14) and the test functions in Eq. (6.15) is intrinsically non-linear w.r.t. the coefficients  $\mathbf{d}_i$ , even if the PDE seems to be linear in  $u$ . If a potential is at hand, the residual can be conveniently obtained using Eq. (2.83) on page 40 as the Riemannian gradient of Eq. (6.20). Namely, as stated before by computing the Euclidean derivative in the embedding space with a subsequent projection onto the tangent space. Thus, the nonlinearity is encoded in the space, where the PDE should be solved, Namely, in the tangent bundle  $TH^1(\Omega, M)$ . Nevertheless, we now ended up at the algebraic residual equations on the right column in Fig. 6.1. From there, Eq. (6.22) can be solved, e.g., with a manifold-aware Newton method as described in Algorithm 1. For this, another derivative information is needed. Thus, we need to take the first-order derivative of Eq. (6.22). If a potential is at hand, this would be equivalently the second derivative, i.e., the Riemannian Hessian. Thus, the tangent operator or stiffness matrix reads

$$\mathbf{K} : \begin{cases} M^n \rightarrow (T_{\mathbf{d}_1} M, \dots, T_{\mathbf{d}_n} M) \times (T_{\mathbf{d}_1} M, \dots, T_{\mathbf{d}_n} M), \\ \mathbf{K}(\mathbf{d}) = \text{Hess } \Pi(\mathbf{d}). \end{cases} \quad (6.23)$$

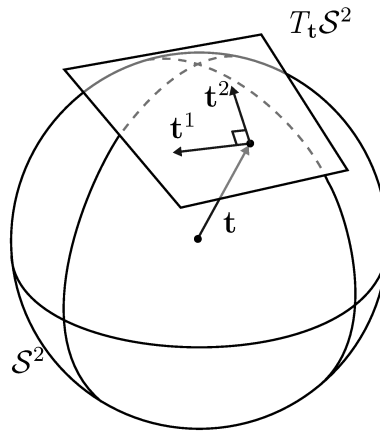


**Figure 6.3:** The unit sphere  $\mathcal{S}^2$  with a unit vector  $\mathbf{t}$  and the corresponding tangent space  $\Lambda = [\mathbf{t}^1 \ \mathbf{t}^2]$ .

This Hessian can then be also obtained, as done in Sander et al. [San16b] and Müller and Bischoff [MB22], with the formula given in Eq. (3.37) on page 65 by exploiting the embedding space to take derivatives therein and project afterward. Now, with Eqs. (6.22) and (6.23) at hand we can solve the non-linear minimization problem iteratively, ending up at the bottom right of Fig. 6.1.

Unfortunately, there is still a caveat. Since, the quantities from Eqs. (6.22) and (6.23) are living in the tangent space of the manifold but represented in the embedding space, they lack the correct dimensions. For example, in the context of the Reissner-Mindlin shell, the optimization of the directors is carried out on the unit sphere  $\mathcal{S}^2$ . The Riemannian Hessian  $\mathbf{K}$  therefore has a non-trivial kernel in the direction of the director, i.e., we have  $\mathbf{K}_{ij}\mathbf{d}_j = 0$ , where  $\mathbf{K}_{ij}$  is the  $i, j$ -th block of the stiffness matrix related to the  $i$ -th and  $j$ -th node. In more physical terms, there is no stiffness related to the length change of the director, and therefore in a naïve implementation, the director could arbitrarily change its length, which would yield to a termination of a direct solver, for example. This remedy is solved by applying a basis change, i.e., by defining a basis of the corresponding tangent space, which is called the *tangent basis*  $\Lambda$ . For the unit sphere  $\mathcal{S}^2$ , this tangent basis is indicated in Fig. 6.3, where the two vectors  $\mathbf{t}^i$  form the matrix  $\Lambda_{3 \times 2} = [\mathbf{t}^1 \ \mathbf{t}^2]$ . Thus, since  $\dim(M) = \dim(T_{\mathbf{d}_i}M)$ , this yields the correct dimensionality of the problem. This, is done by transforming the matrix block  $\mathbf{K}_{ij}$  from a  $3 \times 3$ -matrix to a  $2 \times 2$ -matrix as

$$\mathbf{K}_{\text{red},ij} = \Lambda_i^T \mathbf{K}_{ij} \Lambda_j. \quad (6.24)$$

This then yields the correct dimensions and the correct kernel of the system matrix  $\mathbf{K}$ , which is denoted by  $\mathbf{K}_{\text{red}}$  to denote the reduced system matrix by application of the basis change. Equivalently, the same can be done for the residual  $\mathbf{R}$  from Eq. (6.22) on

---

**Algorithm 1:** Riemannian Newton-Raphson using tangent base representation
 

---

**Goal** : Find stationary point of  $\Pi(\mathbf{d})$ , i.e. find  $\mathbf{d}$  such that  $\mathbf{R}_{\text{red}}(\mathbf{d}) = \mathbf{0}$ .

**input** : Initial iterate  $\mathbf{d}_0$ 
**output** : Converged solution:  $\mathbf{d}^*$ 
**while**  $\|\mathbf{R}_{\text{red}}(\mathbf{d}_k)\| > \text{tol}$  **do**
 $\mathbf{K}_{\text{red}}(\mathbf{d}^k)\Delta\mathbf{d}^k = -\mathbf{R}_{\text{red}}(\mathbf{d}^k)$  /\* Solve system in tangent space basis \*/

 $\Delta\mathbf{d}_E^k = \Lambda_{\mathbf{d}^k}\Delta\mathbf{d}^k$  /\* Reconstruct representation in embed. space  $\Delta\mathbf{d}_E^k$  \*/

 $\mathbf{d}_E^{k+1} = R_{\mathbf{d}_E^k}(\Delta\mathbf{d}_E^k)$  /\* Update using retraction, Section 2.6 \*/

 $\Lambda_I^{k+1}$  /\* Update/Construct new tangent basis, see [MB22] \*/

 $k \leftarrow k + 1$ 
**end**


---

page 158, such that

$$\mathbf{R}_{\text{red},i} = \Lambda_i^T \mathbf{R}_i. \quad (6.25)$$

These quantities can now be used to solve the non-linear system Eq. (6.22) without any singularities and without parameterizing the underlying manifold, which could otherwise lead to singularities. Furthermore, the tangent basis change allows us to write the optimization problem with the correct dimensions, i.e., the correct number of degrees of freedom. In literature, this is not the case since often Lagrange multipliers are used to enforce a constant length of the director, which would yield for the case of  $\mathcal{S}^2$  four degrees of freedom (three for the director in the embedding space and one for the Lagrange multiplier). Similarly, methods using a penalty approach to penalize length change also suffer from the same problem since these need to use three degrees of freedom (for the director in the embedding space). In the method indicated here the director change is defined in the two-dimensional tangent space basis, which yields an optimization problem with two degrees of freedom (for the director change in the tangent space basis). The overall algebraic Newton-Raphson method is given in Algorithm 1, where the system is solved in the tangent space basis, and the solution is transformed back to the embedding space, which is then forwarded to a retraction to correctly update the quantity on the manifold. Thus, we can solve the non-linear minimization problem iteratively, ending up at the bottom right of Fig. 6.1.

## 6.2 Symmetry of the Tangent Operator

### 6.2.1 Historical Overview and Remarks

The symmetry of the tangent operator is subject to a controversial discussion in the context of non-linear finite element formulations. Especially, in the context of three-dimensional beam formulations, after the contribution by Simo and Vu-Quoc [SV86] a discussion started if the tangent operator should be symmetric in general or only at equilibrium. Therein, the authors claim that the geometric stiffness is non-symmetric away from equilibrium and similarly Argyris [Arg82] derived this lack of symmetry as correct and inherited from the manifold structure. These faulty claims came from the wrong extension of the Gâteaux derivative to the non-linear manifold case, which is only valid for vector spaces. This missing symmetry was then fixed using an ad hoc procedure, which is simply the *symmetrization of the tangent operator*. Simo recovered from these ad hoc claims with the work in Simo [Sim92a], where he made the distinction between the second variation (using the Gateaux derivative) and the Riemannian Hessian precise. Therein, he concludes that under the assumption of a manifold, which is a compact Lie group, the symmetric part of the second variation is equal to the Riemannian Hessian, which is symmetric by definition for a torsion-free connection, as discussed in Chapter 3 on page 51. This result is not useful for the unit sphere, since it is indeed compact but not a Lie group. For an overview of Simo's results, the reader is referred to Makowski and Stumpf [MS95]. Nevertheless, from these results, several misconceptions and confusion about the correct tangent operator persist today. For reference in literature, the problems can be seen for shells with drilling rotations [Sue03; SW03], the Reissner-Mindlin shell [Dor16] and the three-dimensional beam literature [Mei19; Bau16; CG88; Arg78; Cri90]. These misconceptions often lead to very involved and arguably inefficient formulations with a symmetric or unsymmetric tangent operator. For more details on the historical contributions in the context of Reissner-Mindlin shells, we refer to Müller and Bischoff [MB22].

At equilibrium, the tangent operator should be symmetric, due to physical reasons, namely the *Maxwell-Betti reciprocal work theorem*. This theorem asserts that in an elastic structure, the work done by a force at point A, causing displacements at point B due to a force at point B, is equal to the work done by the force at point B, causing displacements at point A.

The tangent operator or more specifically the stiffness matrix is not only a tool to solve non-linear equations but also has an importance in physical insight into the problem at hand. Vanishing eigenvalues and other properties of linear algebra can be translated to enable the interpretation of the behavior of the structure. Thus, it is not only crucial to

have the correct operator in terms of the numerical efficiency of some solution procedure but also to gain insight into the underlying problem. Consequently, this chapter guides the derivation of the correct tangent operator, and especially its symmetry, not only for the case of the Reissner-Mindlin shell, but also for a more general energy (or weak form) defined for a non-linear configuration space.

The following chapter explores the result of Simo [Sim92a] for compact Lie groups and derives the correct tangent operator for the case of the unit sphere.

## 6.2.2 Point of Departure

For the subsequent derivations, we assume the existence of a potential  $\Pi : \mathcal{M} \rightarrow \mathbb{R}$ . This is without a loss of generality, but merely for notation convenience and identification purposes.  $\mathcal{M}$  can be thought of as, e.g., a product manifold  $M^n$ , where  $n$  are the number of Lagrangian nodes of a Lagrangian basis defined on some grid and  $M$  is a single discrete manifold. Indeed  $M$  will be here usually  $\mathcal{S}^2$ , the two-dimensional unit sphere or the special orthogonal manifold  $\mathcal{SO}(3)$ . Thus, the given quantities are *not* functionals but merely functions, i.e. they only depend on discrete nodal quantities and not on some (continuous) function. From the potential  $\Pi$ , a discrete weak form  $G : \mathcal{M} \times T_{\mathbf{x}}\mathcal{M} \rightarrow \mathbb{R}$  can be derived as

$$G(\mathbf{x}, \boldsymbol{\eta}_{\mathbf{x}}) = \langle \text{grad } \Pi(\mathbf{x}), \boldsymbol{\eta}_{\mathbf{x}} \rangle, \quad (6.26)$$

where  $\langle \cdot, \cdot \rangle$  is the inner product as given in the Riemannian metric definition, Definition 15 on page 35. The tangent vector  $\boldsymbol{\eta}_{\mathbf{x}}$  is the *variation* of the quantity  $\mathbf{x}$ . Recall that the notation  $\boldsymbol{\eta}_{\mathbf{x}}$  indicates a vector at  $\mathbf{x}$  and  $\boldsymbol{\eta}$  is a tangent vector field. For notational convenience,  $\boldsymbol{\eta}_{\mathbf{x}}$  indicates the direction of variation  $\delta\mathbf{x}$ . In several places in literature, the tangent operator is defined via an iterated directional derivative as linearization of the weak form. This introduced confusion in the non-linear manifold case, since in Eq. (6.26) not only the gradient is a function of  $\mathbf{x}$  but also the variation  $\boldsymbol{\eta}_{\mathbf{x}}$  depends on  $\mathbf{x}$ .

In the following, the iterated directional derivative will be called *second variation*. The second variation of  $\Pi$  is

$$\underbrace{\nabla_{\xi_{\mathbf{x}}} \langle \text{grad } \Pi(\mathbf{x}), \boldsymbol{\eta}_{\mathbf{x}} \rangle}_{\text{second variation}} = \underbrace{\langle \nabla_{\xi_{\mathbf{x}}} \text{grad } \Pi(\mathbf{x}), \boldsymbol{\eta}_{\mathbf{x}} \rangle}_{\text{Hessian}} + \langle \text{grad } \Pi(\mathbf{x}), \nabla_{\xi_{\mathbf{x}}} \boldsymbol{\eta}_{\mathbf{x}} \rangle, \quad (6.27)$$

where the Riemannian Hessian in this expression can be identified by comparing with Eqs. (3.22) and (3.23) on pages 61 and 62. Note, that this expression assumes that the given connection  $\nabla$  is invariant w.r.t. the metric as defined in Definition 18 on page 54. The confusion starts by investigating the second part. By the product rule, there is also

the covariant derivative of the variation in the direction of linearization. Since we are in the fully discrete algebraic setting, this does not make much sense, since the discrete nodal vector is not a function but only a vector defined at a specific position, but it still depends on the position since the very definition of tangent space is position-dependent. For now, we simply assume *some* functional dependence of the variation on the position. This will be discussed in more detail later. But this arbitrariness is the reason why the second variation is not uniquely defined. Therefore, e.g., Dornisch et al. [Dor16] and Simo and Vu-Quoc [SV86] simply create some ad hoc dependency by defining the variation through the manifold extension of their Gâteaux derivative. This expression can be found in [SV86, Ch. 3.1] and in [SV86, Ch. 3.2] the corresponding linearization. The authors in [SV86] do this derivation for the continuous case, where the quantities are not algebraic nodal quantities. Thus, the variation is a function of the space, i.e. the curvilinear coordinate of the centroid of the beam formulation in the given reference. This is similar to extending the Gâteaux derivative to function spaces on manifolds, which is not straightforwardly correctly possible. Nevertheless, they use the exponential map by an ad hoc procedure, which is their generalization of the Gâteaux derivative. The notation  $\mathcal{D}(\bullet)$  in the following denotes the space of function fields on the given manifold and  $(\bullet)$  is the space of vector fields on the given manifold. They used for a rotation matrix function  $\mathbf{R} \in \mathcal{D}(\mathcal{SO}(3))$  and its tangent vector field increment  $\Theta \in T_{\mathbf{R}}(\mathcal{SO}(3))$  the following definition, for a function  $f : \mathcal{D}(\mathcal{SO}(3)) \rightarrow \mathbb{R}$ ,

$$\left. \frac{\partial}{\partial \epsilon} f(\mathbf{R} \exp(\epsilon \Theta)) \right|_{\epsilon=0} = \langle \text{grad } f, \Theta \rangle_{\mathbf{R}}. \quad (6.28)$$

It resembles the usual definition of the Gâteaux derivative, which is for a function  $f : \mathcal{D}(\mathbb{R}^n) \rightarrow \mathbb{R}$  and a tangent vector field  $\mathbf{v} \in (\mathbb{R})$

$$\left. \frac{\partial}{\partial \epsilon} f(\mathbf{x} + \epsilon \mathbf{v}) \right|_{\epsilon=0} = \text{grad } f \cdot \mathbf{v}. \quad (6.29)$$

They extended this algebraic definition to functionals on non-linear spaces, which is at least to the author's knowledge not well-defined. Hence, the utilization of derivatives under specific assumptions within particular spaces remains highly ambiguous and error-prone, leading to discrepancies among various authors' approaches.

Ad hoc procedures are not introduced here, as the focus remains on the algebraic setting and the correct operators from differential geometry. Within this algebraic space, the utilization of the exponential map or more general retractions adheres to well-defined procedures.

### 6.2.3 Compact Lie Groups

In [Sim92a] it is shown that the symmetrization of the second variation yields the Riemannian Hessian if the manifold allows a bi-invariant metric. This result is studied in the following with a detailed derivation. The following will only be valid for compact Lie groups, e.g.  $\mathcal{SO}(n)$ ,  $\mathcal{S}^3$ ,  $\mathcal{O}(n)$  and not  $\mathcal{SL}(n)$ ,  $\mathcal{GL}(n)$ . Let  $\mathbf{x} \in M$  be a compact Lie group and  $\boldsymbol{\xi}_x, \boldsymbol{\eta}_x \in T_x M$ . We have as symmetric part of Eq. (6.27) on page 162

$$\begin{aligned} \text{sym}[\nabla_{\boldsymbol{\xi}_x} \langle \text{grad } \Pi(\mathbf{x}), \boldsymbol{\eta}_x \rangle] &= \frac{1}{2} (\nabla_{\boldsymbol{\xi}_x} \langle \text{grad } \Pi(\mathbf{x}), \boldsymbol{\eta}_x \rangle + \nabla_{\boldsymbol{\eta}_x} \langle \text{grad } \Pi(\mathbf{x}), \boldsymbol{\xi}_x \rangle) \\ &= \frac{1}{2} (\langle \nabla_{\boldsymbol{\xi}_x} \text{grad } \Pi(\mathbf{x}), \boldsymbol{\eta}_x \rangle + \langle \text{grad } \Pi(\mathbf{x}), \nabla_{\boldsymbol{\xi}_x} \boldsymbol{\eta}_x \rangle) \\ &\quad + \langle \nabla_{\boldsymbol{\eta}_x} \text{grad } \Pi(\mathbf{x}), \boldsymbol{\xi}_x \rangle + \langle \text{grad } \Pi(\mathbf{x}), \nabla_{\boldsymbol{\eta}_x} \boldsymbol{\xi}_x \rangle \end{aligned} \quad (6.30)$$

Inserting the definition of the Lie Bracket of the Levi-Civita connection, see Section 3.1 on page 53, we, have with  $\nabla_{\boldsymbol{\eta}_x} \boldsymbol{\xi}_x = -[\boldsymbol{\xi}_x, \boldsymbol{\eta}_x] + \nabla_{\boldsymbol{\xi}_x} \boldsymbol{\eta}_x$ ,

$$\begin{aligned} \text{sym}[\nabla_{\boldsymbol{\xi}_x} \langle \text{grad } \Pi(\mathbf{x}), \boldsymbol{\eta}_x \rangle] &= \frac{1}{2} (\langle \nabla_{\boldsymbol{\xi}_x} \text{grad } \Pi(\mathbf{x}), \boldsymbol{\eta}_x \rangle + \langle \text{grad } \Pi(\mathbf{x}), \nabla_{\boldsymbol{\xi}_x} \boldsymbol{\eta}_x \rangle) \\ &\quad + \langle \nabla_{\boldsymbol{\eta}_x} \text{grad } \Pi(\mathbf{x}), \boldsymbol{\xi}_x \rangle + \langle \text{grad } \Pi(\mathbf{x}), -[\boldsymbol{\xi}_x, \boldsymbol{\eta}_x] + \nabla_{\boldsymbol{\xi}_x} \boldsymbol{\eta}_x \rangle) \\ &= \langle \nabla_{\boldsymbol{\xi}_x} \text{grad } \Pi(\mathbf{x}), \boldsymbol{\eta}_x \rangle + \langle \text{grad } \Pi(\mathbf{x}), \nabla_{\boldsymbol{\xi}_x} \boldsymbol{\eta}_x \rangle \\ &\quad + \frac{1}{2} \langle \text{grad } \Pi(\mathbf{x}), -[\boldsymbol{\xi}_x, \boldsymbol{\eta}_x] \rangle \end{aligned} \quad (6.31)$$

Since  $\mathcal{M} = \mathcal{G}$  is an arbitrary compact Lie group, we can also identify the tangent vectors  $\boldsymbol{\xi}_x, \boldsymbol{\eta}_x$  as elements of  $\mathfrak{g} = T\mathcal{G}$ , i.e.,  $\boldsymbol{\xi}_x, \boldsymbol{\eta}_x \in \mathfrak{g}$ , where  $\mathfrak{g}$  denotes the corresponding Lie Algebra of the Lie group  $\mathcal{G}$ . The guarantee of the existence of a bi-invariant metric is coupled to the properties of compactness of a Lie group, and therefore we only consider this case [Gal90, Sec. 2.9, 2.47]. For this special case, the covariant derivative can be stated as

$$\nabla_{\boldsymbol{\xi}_x} \boldsymbol{\eta}_x = \frac{1}{2} [\boldsymbol{\xi}_x, \boldsymbol{\eta}_x], \quad (6.32)$$

where the formula for the covariant derivative for two left-invariant fields  $\boldsymbol{\xi}_x, \boldsymbol{\eta}_x$  can be written purely in terms of the Lie Bracket. This result can also be found in [Gal90, Ch. 2]. For a derivation refer to Appendix A.4 on page 202. With this result, Eq. (6.31) can be revisited, and we have

$$\begin{aligned} \text{sym}[\nabla_{\boldsymbol{\xi}_x} \langle \text{grad } \Pi(\mathbf{x}), \boldsymbol{\eta}_x \rangle] &= \langle \nabla_{\boldsymbol{\xi}_x} \text{grad } \Pi(\mathbf{x}), \boldsymbol{\eta}_x \rangle + \langle \text{grad } \Pi(\mathbf{x}), \nabla_{\boldsymbol{\xi}_x} \boldsymbol{\eta}_x \rangle \\ &\quad + \frac{1}{2} \langle \text{grad } \Pi(\mathbf{x}), -[\boldsymbol{\xi}_x, \boldsymbol{\eta}_x] \rangle, \end{aligned} \quad (6.33)$$



which results with Eq. (6.32) in

$$\text{sym}[\nabla_{\xi_{\mathbf{x}}} \langle \text{grad } \Pi(\mathbf{x}), \boldsymbol{\eta}_{\mathbf{x}} \rangle] = \langle \nabla_{\xi_{\mathbf{x}}} \text{grad } \Pi(\mathbf{x}), \boldsymbol{\eta}_{\mathbf{x}} \rangle, \quad (6.34)$$

which resembles the result of Simo [Sim92a]. The constructions found in the literature on three-dimensional beams [Mei19; CG88; Cri90; RA02] differ in one way or another from those in [Sim85], but they still adopted Simo's ad hoc construction with the Gâteaux derivative. However, it is important to note that this choice is not unique, therefore the second variation can be error-prone since it depends on an artificial selection of the functional dependency for obtaining its linearization. As a result, the skew-symmetric part of the second variation can be arbitrarily influenced by the choice of functional dependency for the variation. This sometimes even requires fewer iterations, as investigated in Ibrahimbegović et al. [Ibr95]. Nevertheless, the authors therein attributed this result to non-conservative loading. Due to the lack of a well-defined second variation, it is recommended to derive the Riemannian Hessian directly, which is directly well-defined and also a simpler procedure. Refer to the steps outlined in Section 3.5 on page 64 to achieve this.

### 6.2.4 The Unit Sphere

In the following, a similar connection between the Riemannian Hessian and the second variation of a potential  $\Pi$ , which takes values from the manifold  $\mathcal{S}^2$ , is explored. The unit sphere  $\mathcal{S}^2$  is compact but not a Lie group therefore the stated derivation does not hold in this case. Let  $\mathbf{x} \in \mathcal{S}^2$  and  $\xi_{\mathbf{x}}, \boldsymbol{\eta}_{\mathbf{x}} \in T_{\mathbf{x}}\mathcal{S}^2$ .

$$\underbrace{\langle \nabla_{\xi_{\mathbf{x}}} \text{grad } \Pi(\mathbf{x}), \boldsymbol{\eta}_{\mathbf{x}} \rangle}_{\text{Hessian}} = \underbrace{\nabla_{\xi_{\mathbf{x}}} \langle \text{grad } \Pi(\mathbf{x}), \boldsymbol{\eta}_{\mathbf{x}} \rangle}_{\text{second variation}} - \langle \text{grad } \Pi(\mathbf{x}), \nabla_{\xi_{\mathbf{x}}} \boldsymbol{\eta}_{\mathbf{x}} \rangle \quad (6.35)$$

Here the focus lies again at the last part  $\langle \text{grad } \Pi(\mathbf{x}), \nabla_{\xi_{\mathbf{x}}} \boldsymbol{\eta}_{\mathbf{x}} \rangle$ , i.e.,  $\nabla_{\xi_{\mathbf{x}}} \boldsymbol{\eta}_{\mathbf{x}}$ , which is the directional derivative of the variation in the direction of the linearization.

The variation  $\boldsymbol{\eta}_{\mathbf{x}}$  is a tangent vector of a geodesic curve  $\gamma$  at position  $\mathbf{x}$ , i.e.,  $\boldsymbol{\eta}_{\mathbf{x}} = \gamma'(0)$ . Therefore, to investigate a functional dependency of  $\nabla_{\xi_{\mathbf{x}}} \boldsymbol{\eta}_{\mathbf{x}}$ , we need to construct a vector field from  $\boldsymbol{\eta}_{\mathbf{x}}$  that can be derived in the direction  $\xi_{\mathbf{x}}$ . A canonical choice would be to simply create this functional dependency by parallel transporting  $\boldsymbol{\eta}_{\mathbf{x}}$  along the geodesic  $\gamma$  in the direction of  $\xi_{\mathbf{x}}$ . This is done by introducing parallel transported quantity  $\boldsymbol{\eta}_{\mathbf{x}}(t)$  in the direction of  $\xi_{\mathbf{x}}$  by

$$\boldsymbol{\eta}_{\mathbf{x}}(t) = \left. \frac{\partial}{\partial t} \exp_{\mathbf{x}}(s\boldsymbol{\eta}_{\mathbf{x}}(0) + t\xi_{\mathbf{x}}) \right|_{s=0}. \quad (6.36)$$

Now  $\boldsymbol{\eta}_{\mathbf{x}}(t)$  is a vector field along some geodesic curve realized by the exponential map. Therefore,  $\boldsymbol{\eta}_{\mathbf{x}}(t)$  is constructed explicitly in that way that it is parallel transported along the geodesic  $\boldsymbol{\gamma}$  in the direction of  $\boldsymbol{\xi}_{\mathbf{x}}$ .<sup>2</sup> By construction, the tangential part of  $\nabla_{\boldsymbol{\xi}_{\mathbf{x}}}\boldsymbol{\eta}_{\mathbf{x}}$  is zero and Eq. (6.35) simplifies to

$$\underbrace{\langle \nabla_{\boldsymbol{\xi}_{\mathbf{x}}}\text{grad}\Pi(\mathbf{x}), \boldsymbol{\eta}_{\mathbf{x}} \rangle}_{\text{Hessian}} = \underbrace{\nabla_{\boldsymbol{\xi}_{\mathbf{x}}}\langle \text{grad}\Pi(\mathbf{x}), \boldsymbol{\eta}_{\mathbf{x}} \rangle}_{\text{second variation}}. \quad (6.37)$$

This implies that the second variation directly yields the Riemannian Hessian as a tangent operator. But again the chosen functional dependency of the variation direction  $\boldsymbol{\eta}_{\mathbf{x}}$  and linearization direction  $\boldsymbol{\xi}_{\mathbf{x}}$  is arbitrary and for different choices, different results are obtained.

This further emphasizes the impracticality of utilizing the second variation as a tangent operator. Given its lack of a well-defined nature, it does not serve as a valuable candidate for an iterative solution scheme or as a quantity to assess stability through its eigenvalues.

### 6.2.5 Conclusion

In conclusion, the study reveals, that the functional dependency of the variation  $\boldsymbol{\eta}_{\mathbf{x}}$  on  $\mathbf{x}$  is crucial to obtain a symmetric or unsymmetric result. Simo introduced in [Sim85] a functional dependency by using the exponential map  $\boldsymbol{\eta}_{\mathbf{x}}$  and constructing a generalized Gâteaux derivative, which yields an unsymmetric tangent operator. This ad hoc construction led to the subsequent derivation of the Riemannian Hessian by symmetrizing the second variation in Simo [Sim92a]. However, the ad hoc construction of the functional dependency of the variation  $\boldsymbol{\eta}_{\mathbf{x}}$  on  $\mathbf{x}$ , is arbitrary and leads to different results for different choices of this functional dependency of the variation. Especially, the skew-symmetric part of the second variation is not well-defined and depends on the choice of the functional dependency of the variation direction  $\boldsymbol{\eta}_{\mathbf{x}}$ . This makes the second variation error-prone due to the artificial selection of functional dependency for its linearization. It was also shown that a special choice for functional dependency of the variation  $\boldsymbol{\eta}_{\mathbf{x}}$  for the case of the unit sphere, directly yields the equivalence of the second variation and the Riemannian Hessian.

Consequently, relying on the second variation as a tangent operator is impractical. Its lack of well-defined nature renders it unsuitable for iterative solution schemes or for stability assessment through eigenvalues. In light of these limitations, it seems reasonable

---

<sup>2</sup>If the evaluation at  $s = 0$  would be neglected, the resulting quantity  $\boldsymbol{\eta}^{\parallel}(s, t)$  would be a Jacobi field along the geodesic  $\boldsymbol{\gamma}$  in the direction of  $\boldsymbol{\xi}_{\mathbf{x}}$ . Jacobi fields are the displacement field of two infinitesimally close geodesics, see [Gal90, Ch. 3].

to directly use the Riemannian Hessian. This approach can be easily derived by following the procedure outlined in Section 3.5 on page 64. Utilizing the Riemannian Hessian directly proves to be more effective, and computationally feasible, and avoids the need to derive the second variation and subsequently make corrections.

## 6.3 Discretization and Interpolation

In the following, several choices for the interpolation of the director field for the Reissner-Mindlin shell formulation are discussed. Options from the literature are presented and discussed and after that suitable interpolations used in this work are presented.

### 6.3.1 Historical Overview and Remarks

This chapter discusses interpolation schemes for the director field in the context of the non-linear Reissner-Mindlin shell model. Nevertheless, the references and conclusions are also applicable to other models, such as Cosserat shells or beams, which need the interpolation in  $\mathcal{SO}(3)$  or on the unit quaternions  $\mathbb{H}_1$ . Numerous methods exist in the literature for interpolating the director in the non-linear Reissner-Mindlin model. Each has its distinct advantages and disadvantages. The most straightforward choice is to directly obtain a parametrization of the unit sphere. To obtain such a parameterization of quantities residing on the unit sphere, it is tempting to merely define the angle pair  $\alpha, \beta$ . According to the “hairy ball theorem”, this inevitably leads to singularities in the derivatives. These drawbacks can be found in the works [Ram76; Mün07; OO84; WG93; Gru89]. It appears straightforward to identify these angles as degrees of freedom and apply standard interpolation, such that  $\alpha = \sum_{I=1}^n N^I \alpha_I, \beta = \sum_{I=1}^n N^I \beta_I$ , see [WG93, Eq. 54] and [Gru89, Eq 5.1]. Then, the director can be constructed using the formula

$$\mathbf{t} = \mathbf{R}(\alpha, \beta) \mathbf{t}_0. \quad (6.38)$$

Unfortunately, using an *additive* update, such that  $\alpha_I^{k+1} = \alpha_I^k + \Delta \alpha_I$ , results in a non-objective formulation because rigid body rotations do not cancel in strain measurements. Furthermore, the parameterization contains singularities, which are not only a theoretical problem but also a practical one, since in the vicinity of the singularities, the stiffness matrix becomes ill-conditioned. Similar disadvantages can be found in the works Gruttmann et al. [Gru00] and Sansour and Wagner [SW03], where an incremental rotation vector  $\Delta \boldsymbol{\theta}$  is interpolated. All of these incremental quantities, however, reside in a linear space, for which standard interpolation techniques are applicable. In this case, the disadvantage is more severe than the advantage of a simple interpolation, as the construction

is non-objective because it contradicts the inherently non-linear nature of the problem. The drawbacks of these formulations are also discussed shortly in Sander [San10]. The article by Crisfield and Jelenić [CJ99] also points out the artificial path-dependence and non-objectivity of these approaches. Instead of employing rotation increments as degrees of freedom, one can construct nodal directors as  $\mathbf{t}_I = \mathbf{R}_I \mathbf{t}_0^I$ , and directly interpolate them,  $\mathbf{t} = \sum_{I=1}^n N^I \mathbf{R}_I \mathbf{t}_0$ , instead of the interpolating (rotational) degrees of freedom. The nodal rotation matrix  $\mathbf{R}$  can also be updated *multiplicatively* as  $\mathbf{R}_I^{k+1} = \Delta \mathbf{R}(\Delta \alpha_I, \Delta \beta_I) \mathbf{R}_I^k$ . This formulation uses incremental degrees of freedom  $\Delta \alpha_I, \Delta \beta_I$ , see [EM00]. Consequently, the relationship between the director at the interpolation point and the nodal degrees of freedom is

$$\mathbf{t} = \sum_{I=1}^n N^I \Delta \mathbf{R}(\Delta \alpha_I, \Delta \beta_I) \mathbf{R}_I \mathbf{t}_0. \quad (6.39)$$

Thus, Eq. (6.39) illustrates the complicated dependency of the interpolation scheme on the degrees of freedom  $\Delta \alpha_I, \Delta \beta_I$ .

The formulation is objective, and the singularity caused by parameterizing the unit sphere is generally insignificant because iterative changes in the angles  $\Delta \alpha_I, \Delta \beta_I$  are typically small.

However, the procedure results in a non-compact formulation and requires costly trigonometric function evaluations. Moreover, the interpolation does not preserve the director's length. This is not an important problem for low-order finite elements and fine meshes, but for higher-order elements, which are typically larger, the effect is not only more pronounced but also results in a degeneration of the convergence order. This dramatic consequence, which is rarely discussed in the literature, is examined in depth in Müller and Bischoff [MB22, Sec. 10.2] and will also be discussed in Chapter 7. The director  $\mathbf{t}$  can be normalized to eliminate this issue. However, as a result, expressions become even more complex. Rather than preserving the director length within the domain, several formulations introduce the director  $\mathbf{t}_{GP}$  as a history field at each Gauss point, see [Sim90a; Dor16; Bet96]. Subsequently, in these formulations, only the increment  $\Delta \mathbf{t}$  is interpolated from the nodes  $\Delta \mathbf{t}_{GP} = \sum_{I=1}^n N^I(\xi^1, \xi^2) \Delta \mathbf{t}_I$ . The Riemannian exponential map of the unit sphere, see Section 3.4 on page 60, is then used to update the directors at each Gauss point. This yields,

$$\begin{aligned} \mathbf{t}_{GP}^{k+1} &= \exp_{\mathbf{t}_{GP}^k}(\Delta \mathbf{t}_{GP}) \\ &= \cos(\|\Delta \mathbf{t}_{GP}\|) \mathbf{t}_{GP}^k + \frac{\sin \|\Delta \mathbf{t}_{GP}\|}{\|\Delta \mathbf{t}_{GP}\|} \Delta \mathbf{t}_{GP} \end{aligned} \quad (6.40)$$

or

$$\mathbf{t}_{GP}^{k+1} = \Delta \mathbf{R} \left( \sum_{I=1}^n N^I \Delta \boldsymbol{\theta}_I \right) \mathbf{R}_{GP}^k \mathbf{e}_3. \quad (6.41)$$

with  $\Delta \boldsymbol{\theta}_I = \Delta \mathbf{t}_I \times \mathbf{t}_I$  and  $\mathbf{e}_3 = [0,0,1]^T$ , where the latter can be chosen arbitrarily. The resulting scheme exhibits a non-objective and path-dependent nature, as formally demonstrated by Crisfield and Jelenić in their work on the objectivity of strain [CJ99]. Additionally, it should be noted that the interpolated increment  $\Delta \mathbf{t}_{GP}$  is not automatically in the tangent space of  $\mathbf{t}_{GP}$ , which can also lead to undesired consequences. The entire procedure seems to be error-prone in terms of singularities, non-objectivity, and path dependence. Moreover, the evaluation and linearization can be expensive due to the involved interpolation schemes.

To overcome these limitations, a seemingly appealing approach is to *eliminate* the need for parameterizing the unit sphere and the need to introduce rotation matrices altogether. This can be achieved by exploiting the relationships between submanifolds and their embeddings, as proposed in [Abs08] and described in Section 2.7.4 at an abstract level, independent of finite elements. In the book by Absil et al. [Abs08] mainly the optimization algorithms on manifolds are presented. Nonetheless, exploiting this embedding space is also beneficial for developing a path-independent and objective interpolation.

Fortunately, the research conducted by Sander [San10] and subsequent papers [San12; San15; San16a; Gro15; Gro11; Gro19] has greatly improved the situation regarding interpolation for finite elements in non-linear spaces. However, it is important to note that this field of research is still ongoing, and there are multiple viable choices to consider.

While some interpolation options can be found in the literature on the Reissner-Mindlin shell model or three-dimensional beam models, the works of Sander [San10] and subsequent publications stand out for their thorough exploration of the design space for proper interpolation schemes. These schemes fulfill crucial requirements, such as objectivity, path independence, and invariance to node numbering. In the subsequent section, we will describe several interpolation options specifically designed for the unit sphere/Reissner-Mindlin shell scenario.

### 6.3.2 Interpolation on Manifolds

In the subsequent discussion, we examine three different versions that utilize the director vectors as objects existing in the embedding space, specifically  $\mathbb{R}^3$ . Importantly, all of these approaches satisfy the conditions of being path-independent and objective.

**Nodal Finite Elements (NFE):** The first option is the nodal approach (NFE), where the directors have unit length at the nodes only, thus, violating the constraint in the domain.

$$\mathbf{t}_N = \sum_{I=1}^n N^I \mathbf{t}_I. \quad (6.42)$$

This interpolation scheme corresponds to the approaches used in several works, including those by Hughes and Liu [HL81], Belytschko et al. [Bel92], Simo et al. [Sim92b], Ramm [Ram76], and Benson et al. [Ben10]. The interpolation schemes used in the given references differ in their definitions of degrees of freedom and stiffness matrices. Therefore, it may not be possible to make a direct comparison between the NFE approach described here and the references cited. The NFE residual and stiffness matrix can be constructed from the PBE (projection-based finite element) approach, described in Section 5.6 on page 140 by omitting the normalization of the director and by replacing  $\mathcal{P}' = \mathbf{I}$ ,  $\mathcal{Q}_\alpha = \mathcal{X}_\alpha = \mathcal{S} = \mathbf{0}$  in all relevant quantities. This results in a simpler formulation compared to the PBE approach.

In the following, two approaches are discussed, that satisfy the unit length condition in the domain. They are deduced from general constructions found in the mathematical literature but the second one (PBE) can also be found in the engineering literature.

**Geodesic Finite Elements (GFE):** The first approach is based on the works of Sander [San10; San15] and Grohs [Gro11] to generalize the concept of interpolation from vector spaces to manifolds. If such an interpolation is used, the resulting finite elements are called *geodesic finite elements* (GFE). The interpolation scheme reads

$$\begin{aligned} \mathbf{t}_{\text{GFE}} &= \arg \min_{\mathbf{t} \in \mathcal{S}^2} \sum_{I=1}^n N^I \text{dist}_{\mathcal{S}^2}^2(\mathbf{t}_I, \mathbf{t}) \\ &= \arg \min_{\mathbf{t} \in \mathcal{S}^2} \sum_{I=1}^n N^I \arccos^2(\mathbf{t}_I \cdot \mathbf{t}), \end{aligned} \quad (6.43)$$

taken from [San12, Eq. 29]. Solving the local minimization problem Eq. (6.43) at each integration point is documented in Appendix A.10 on page 207. These finite elements automatically inherit objectivity and path independence of the continuous formulation. This is because the interpolation scheme is constructed from a weighted (geodesic) distance measure on the corresponding manifold. This generalized distance measure is minimized and is related to the Karcher mean of the manifold. Since distances are invariant to rotations by definition, objectivity follows directly. Furthermore, due to the intrinsic nature, the interpolation always stays on the manifold and therefore this approach preserves the unit length of the director in the domain. The major drawback is the implicit definition of the interpolation, which involves a non-linear minimization

problem<sup>3</sup> at each integration point. To the author's knowledge, this interpolation scheme is applied on the Reissner-Mindlin shell for the first time in this work.

**Projection-Based Finite Elements (PBFE):** The third approach is *projection-based interpolation*, based on the works of Sprecher [Spr16] and subsequent papers, e.g. Grohs et al. [Gro19], which presents a framework for finite elements that interpolate on manifolds by closest point projection from an embedding space onto the manifold. The finite elements are constructed as in the nodal approach and then projected onto the corresponding manifold. The interpolation formula for the unit sphere reads

$$\mathbf{t}_{\text{PB}} = \frac{\sum_{I=1}^n N^I \mathbf{t}_I}{\|\sum_{I=1}^n N^I \mathbf{t}_I\|}. \quad (6.44)$$

Luckily, the closest point projection of a vector in  $\mathbb{R}^3$  onto  $\mathcal{S}^2$  has a closed form, namely the trivial normalization of the vector. This interpolation, where the vector in the embedding space is projected onto  $\mathcal{S}^2$ , was also used in [Sim89], but only for the reference director field. Furthermore, in the context of rods and  $\mathcal{SO}(3)$  the same procedure was discussed in Romero [Rom04, Ch. 4.4], which can also be interpreted as a projection-based interpolation, since it interpolates the rotation matrices in the embedding space  $\mathbb{R}^{3 \times 3}$  and then projects them back onto  $\mathcal{SO}(3)$ . A more involved version of this approach can be found in the work El-Abbasi and Meguid [EM00]. The resulting finite elements are denoted by the name *Projection-based finite elements* (PBFE).

Projection-based finite elements can be regarded as a special case of geodesic finite elements, where the distance measure for the interpolation is the one of the embedding space. For example, for the interpolation on  $\mathcal{S}^2$  the distance measure is the Euclidean distance from  $\mathbb{R}^3$ . Due to the construction of the interpolation as a distance measure, objectivity and path independence are inherited from geodesic finite elements.

Additionally, geodesic finite elements and projection-based finite elements are summarized as the group of *geometric finite elements*. Both interpolations (geodesic and projection-based) yield a *path independent* and *objective* discrete problem. The corresponding proofs can be found in [Gro19, Ch. 1.3] and [San12, Ch. 2.4, Lemma 2.5, 2.6].

Similar to the GFE definition, the nodal and the projection-based approach can be reformulated as closed-form solutions of a minimization problem. The three approaches

---

<sup>3</sup>For some problems, e.g. Cosserat rods, the solution of the minimization can be stated analytically. Therefore, in [San10] Sander deduced the same interpolation as Crisfield and Jelenić [CJ99] proposed for these rods for first-order ansatz functions.

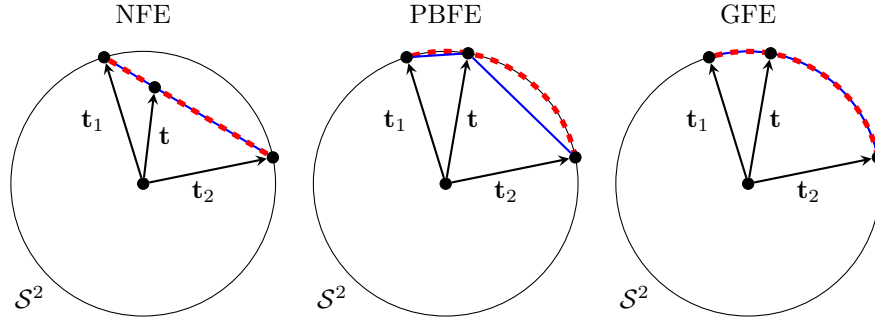


**Figure 6.4:** Graphical comparison of interpolation between two nodal directors  $\mathbf{t}_1, \mathbf{t}_2$ , using the schemes of Eq. (6.45). The blue line indicates the used distance measure and the red dashed line indicates the space in which the minimization problem is formulated, i.e. where the interpolated director lives in.

can thus be represented as

$$\begin{aligned}
 \mathbf{t}_{\text{NFE}} &= \sum_{I=1}^n N^I \mathbf{t}_I &= \arg \min_{\mathbf{t} \in \mathbb{R}^3} \sum_{I=1}^n N^I \text{dist}_{\mathbb{R}^3}^2(\mathbf{t}_I, \mathbf{t}) &= \arg \min_{\mathbf{t} \in \mathbb{R}^3} \sum_{I=1}^n N^I \|\mathbf{t}_I - \mathbf{t}\|^2, \\
 \mathbf{t}_{\text{PBFE}} &= \frac{\sum_{I=1}^n N^I \mathbf{t}_I}{\|\sum_{I=1}^n N^I \mathbf{t}_I\|} &= \arg \min_{\mathbf{t} \in \mathcal{S}^2} \sum_{I=1}^n N^I \text{dist}_{\mathbb{R}^3}^2(\mathbf{t}_I, \mathbf{t}) &= \arg \min_{\mathbf{t} \in \mathcal{S}^2} \sum_{I=1}^n N^I \|\mathbf{t}_I - \mathbf{t}\|^2, \\
 \mathbf{t}_{\text{GFE}} &= &\arg \min_{\mathbf{t} \in \mathcal{S}^2} \sum_{I=1}^n N^I \text{dist}_{\mathcal{S}^2}^2(\mathbf{t}_I, \mathbf{t}) &= \arg \min_{\mathbf{t} \in \mathcal{S}^2} \sum_{I=1}^n N^I \arccos^2(\mathbf{t}_I \cdot \mathbf{t}).
 \end{aligned} \tag{6.45}$$

These abstract definitions can be interpreted geometrically as shown in Fig. 6.4. One can see that the nodal approach in the domain violates the condition of unit length. This constraint is precisely satisfied for GFE and PBFE, because minimization occurs on the manifold. Since GFE and PBFE both precisely satisfy this constraint, they both suffer from the following issue: Consider two directors whose directions are opposite of each other. Their connecting geodesic is not unique, and the interpolation is ambiguous. This issue only occurs with extremely coarse meshes, and even then we consider it to be uncommon. Therefore, this is an interesting but theoretical issue. For the interested reader, refer to Chapter 4 of [San10]. Furthermore, GFE also uses the distance measure of the manifold and therefore it is fully intrinsic since it does not depend on a particular embedding. The hybrid nature of the projection-based approach becomes obvious, as it relies on the distance measure of the *embedding space* but the minimization is solved for values *on the manifold*. In particular, loosely speaking, PBFE inherits the simplicity of NFE and the accuracy of GFE. In contrast to nodal interpolation, projection-based interpolation, and geodesic interpolation are not exactly integrated by Gauss quadrature even for the simple case of  $N^I(\xi^1, \xi^2)$  being Lagrange polynomials. This is the case since



the interpolation formula of PBF E involves irrational fractions of the ansatz functions, whereas for GFE the dependence of  $\xi^1, \xi^2$  on the director  $\mathbf{t}$  cannot even be expressed in closed form. Nevertheless, Gauss-Legendre quadrature is used, which fits the order of the used ansatz function spaces and numerical studies reveal that increasing the number of quadrature points leaves the results practically unchanged.

In Grohs et al. [Gro19] numerical evidence is given that for the case of the unit sphere geodesic finite elements are superior to the projection-based formulation in terms of  $h$ -convergence. However, in [Gro19, Ch. 5.1] they also mention that the projection-based approach is 10 times as fast and therefore an overall superiority of PBF E can be deduced in terms of computational efficiency. As already mentioned, this is due to the implicit definition of the geodesic interpolation, which leads to a small minimization problem at each integration point, see [San15], whereas for projection-based finite elements, an explicit formula is available for the unit sphere. The implicit definition of GFE also leads to the need to use automatic differentiation for the derivatives which explains the major speed difference. This was also reported similarly in [MB22].

These interpolation rules were studied in detail in the context of the Reissner-Mindlin shell by Müller and Bischoff [MB22]. In the following, these will also be studied in the context of locking prevention techniques.



---

## Numerical Experiments

The following chapter discusses the proposed algorithm for enforcing the zero normal stress condition in the context of the Reissner-Mindlin shell model from Section 5.4. Furthermore, the numerical experiments of Müller and Bischoff [MB22] are extended by investigating the influence of the choice of director interpolation on locking prevention.

### 7.1 Point of Departure

In Müller and Bischoff [MB22], comparisons are made between three types of director interpolation: nodal-based (NFE), projection-based (PBFE), and geodesic (GFE). The results demonstrate that all three interpolation methods predict the bending behavior of the beam with varying degrees of computational efficiency. The NFE scheme is computationally efficient but less precise than the PBFE and GFE schemes, whereas the GFE scheme is more precise but computationally more expensive than PBFE. Furthermore, for higher-polynomial order, the NFE showed a deterioration in convergence order, whereas the PBFE and GFE schemes did not show such a deterioration. The authors concluded that the PBFE scheme is the most efficient and accurate scheme for the given examples. The following chapter extends and consolidates the results of Müller and Bischoff [MB22]. Therefore, the numerical experiments are not repeated but selected topics are revisited. Especially, the objectivity of the formulation is investigated in elaborate detail in Müller and Bischoff [MB22] and is therefore not investigated further in this work. Additionally, the efficiency, the robustness of the formulation, and its capability to predict complicated buckling scenarios are not investigated further, since the results of Müller and Bischoff [MB22] are sufficient to verify these claims. In Müller and Bischoff [MB22] it was also shown, that the radial return normalization of Eq. (2.57) for the unit sphere provides the best results in terms of needed load steps and outperforms the exponential map.

In contrast to the formulation from Müller and Bischoff [MB22], the formulation derived in Chapter 5 on page 91 is stress-based. Furthermore, in Müller and Bischoff [MB22] locking phenomena are excluded from the discussion. Thus, the following investigation incorporates locking prevention techniques.

The stress resultants, namely the membrane forces, moments, and shear forces, are calculated in the following by integrating the stresses through the thickness as a post-processing step. Additionally, the shown membrane strain, bending moments, and transverse shear energy fractions are calculated by the formulas given in Appendix A.9. Since the formulation at hand is stress-based, the zero normal stress condition needs to be enforced on-the-fly iteratively. The different results of using the method proposed in Section 5.4 on page 124 are investigated in the following, using an example with finite strain plasticity.

All the following numerical examples use non-uniform rational B-splines (NURBS) as ansatz functions. For linear ansatz functions, this degenerates to the usual definition of linear Lagrangian ansatz functions. Consequently, the following simulations can be interpreted as examples of isogeometric analysis (IGA) [Hug05]. For the used nomenclature, the reader is referred to Piegl and Tiller [PT95] and Hughes et al. [Hug05]. These ansatz functions are rational functions and they are defined by the control point weights and the knot vector. For weights equal to one, the rational functions degenerate to polynomials. At the element boundaries, the continuity of the ansatz functions is controlled by the knot vector. In the examples, the following shortcut describes the used ansatz functions: Ansatz functions of order  $p$  with inter-element continuity  $C^k$  are denoted by PpCk, which yields for example P2C1 for quadratic ansatz functions with  $C^1$  continuity.

## 7.2 Plastic Deformation of a Free-Form Surface

The first example is a free-form shell using a large strain plastic material model. It serves as a test for the numerical algorithms to enforce the zero normal stress condition from Section 5.4 on page 124. The large strain plastic material model is a perfect  $J_2$ -plasticity with Young's modulus  $E = 6.9e4 \text{ N mm}^{-2}$ , Poisson's ratio  $\nu = 0.3$  and yield stress  $\sigma_y = 248 \text{ N mm}^{-2}$ . The material routines are used from the material library MUESLI [Por17]. The geometry data is taken from Dornisch et al. [Dor16]. The system and boundary conditions are presented in Fig. 7.1. The problem is solved using the arc-length method. The bottom edge is simply supported and all other edges are free. At the top edge, a line load  $p_Y = \lambda(t)40 \text{ N mm}^{-1}$  in the global Y-direction is prescribed. The shell thickness is  $h = 0.5 \text{ mm}$ . The load is applied with the load factor function given in Fig. 7.2. For a pseudo time  $199 < t < 201$ , the load factor function  $\lambda(t)$  is regularized, to help the underlying arc-length method to converge at the kink at  $t = 200$ . This kink represents the

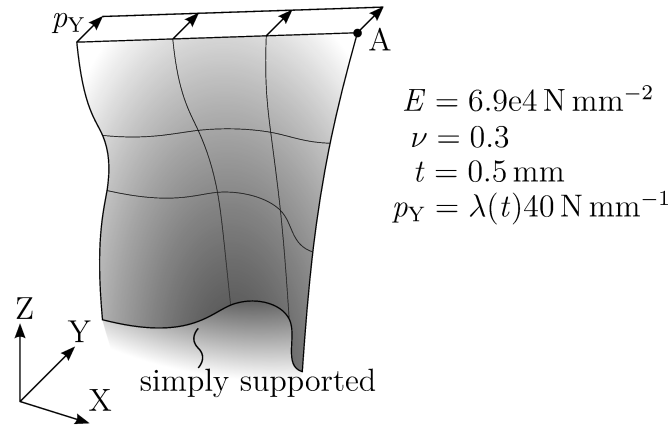


**Figure 7.1:** Structural system and boundary conditions of the free-form surface.

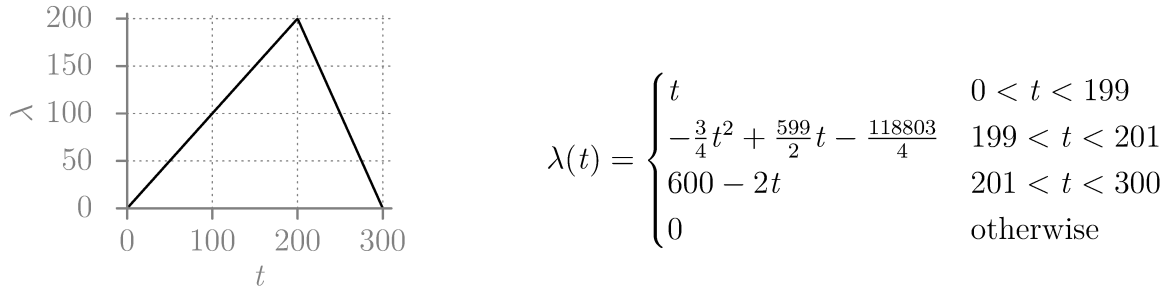


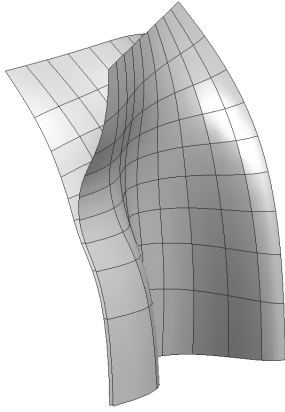
**Figure 7.2:** Graphical representation and description of the load function  $\lambda(t)$ .

start of the unloading phase. The example is calculated using the projection-based director interpolation (PBFIE) scheme with  $9 \times 9$ -P3C2 elements. In Fig. 7.3(a) the deformed midsurface after unloading is compared to the initial geometry. This indicates significant plastic deformation throughout the process, which is also underlined by Fig. 7.3(b), which shows the history of the displacement of point A in the global Y-direction. While the explicit stress state after unloading is not important for the following discussion, the example was chosen as such that the intermediate and final stress states are non-trivial.

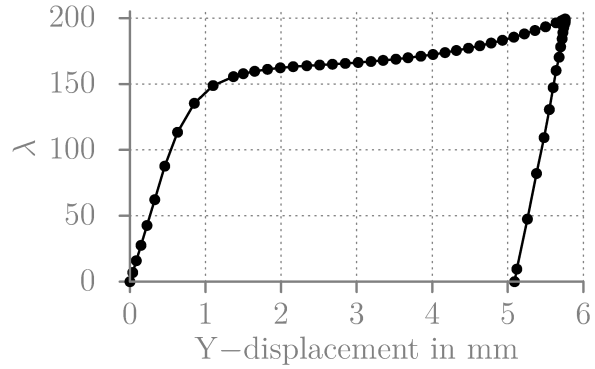
The example uses  $4 \times 4 \times 3$  Gauss quadrature points for the residual and stiffness matrix. Three integration points are used in the thickness direction. This yields in total 48 quadrature points per element, which results in 3888 quadrature points for the whole grid. The arc-length method uses 67 load steps to reach the final state. Each step is considered as converged if the residual norm fulfills the predicate:  $\|\mathbf{R}\|_2 < 1e-5$ . In total, this yields 382 Newton iterations. This leads to 1 753 488 quadrature point evaluations to calculate the residual and stiffness matrix in total. At each quadrature point, the vanishing normal stress condition is enforced using the methods from Section 5.4 on page 124.

**Table 7.1:** Average iterations necessary to solve the vanishing normal stress constraint per quadrature point. The percentage shows the improvement relative to the first-order retraction.

Elements	#Evaluations	First order		Second order		Exponential map	
		avg.	%	avg.	%	avg.	%
$9 \times 9$	1 753 488	3.1401		3.0328	3.42	3.0330	3.41
$18 \times 18$	7 853 760	3.0602		2.9316	4.20	2.9322	4.18



(a) Undeformed and deformed midsurface.



(b) Displacement of point A.

**Figure 7.3:** The undeformed midsurface and deformed midsurface after unloading are shown on the left. The undeformed surface is slightly translated in negative Y-direction for better visualization. On the right, the displacement of point A in Y-direction is shown.

The first-order retraction from literature stated in Eq. (5.127) on page 125, and second, the proposed methods, i.e., the second-order retraction from Eq. (5.137) and the exponential map from Eq. (5.136) on page 128. For each quadrature point, these methods iteratively solve the zero normal stress constraint. The constraint is applied to the  $S^{33}$  component of the second Piola-Kirchhoff stress tensor, which is usually not equal to the Cauchy stress

for small overall strain, the difference is small. The iteration is considered as converged if the vanishing stress fulfills the condition  $|S^{33}| < \max(\epsilon \|\mathbf{S}\|_2, 1e-7)$  with  $\epsilon = 1e-7$ . The number of needed iterations for each quadrature point are shown in Table 7.1. On average, the first-order retraction needs the most iterations, whereas the second-order retraction needs the least iterations. In between, the exponential map resides, but the differences here are less pronounced in comparison to the model problem from Section 5.4.3 on page 129. The exponential map needs 3.4101% less iterations and the second-order retraction needs 3.4167% less iterations, on average. Thus, the second-order retraction

is slightly better than the exponential map, but the difference is small. Table 7.1 also includes the results for a refined grid with  $18 \times 18$  elements, underlining this trend.

These results may appear insignificant at first, but taking into account the vast number of integration points, these slight improvements can significantly reduce the total computation time. This reduction is particularly crucial for large-scale simulations that employ explicit time integration schemes, where the evaluation of residual forces and material routines dominates the solution time.

The increased numerical effort for the evaluation of the complex update formulas (see Eqs. (5.136) and (5.137) on page 128) are negligible compared to performing an additional evaluation of stresses and tangent moduli. The latter, in itself, may require multiple iterations, such as a return mapping onto a yield surface, if a complex plastic material law is used. Consequently, it is better to use a complex update formula to reduce the number of iterations needed to ensure the zero normal stress constraint.

Therefore, the proposed improvements for the numerical enforcement of the vanishing normal stress constraint in the Reissner-Mindlin shell model offer significant advantages, as demonstrated by the results above. By utilizing these advancements, existing routines can be enhanced, leading to more efficient computations and reduced overall computation time. Especially, the improvements in terms of iteration counts achieved through the second-order retraction and exponential map provide benefits for implementing the zero normal stress constraint. By incorporating these advancements, both academic research codes and industry codes can enhance their computational procedures.

## 7.3 Pure Bending of Straight Beam

To compare the three director interpolation schemes denoted by the identifiers NFE (nodal finite elements), PBE (projection-based finite elements), and GFE (geodesic finite elements), consider the example of pure bending of a straight beam. The straight beam is clamped at one end and a moment load is applied at the opposite free end, see Fig. 7.4. The moment that is needed to coil the beam to a full circle is obtained as follows: Since the deformed configuration is a full circle, the geometry of the final deformed configuration is known. Consider a Saint Venant-Kirchhoff material law with the energy density

$$\psi(\mathbf{E}) = \frac{\lambda}{2} \text{tr}(\mathbf{E} : \mathbf{G}^{-1})^2 + \mu \text{tr}(\mathbf{E} : \mathbf{E}^\sharp), \quad (7.1)$$

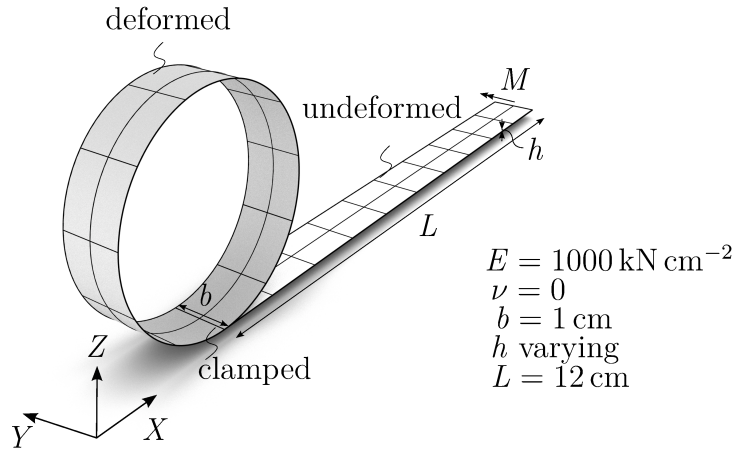


**Figure 7.4:** Deformed and undeformed midsurface configuration of the bending of a straight beam, including boundary conditions and parameters.

and the stresses

$$\mathbf{S} = \lambda \text{tr}(\mathbf{E} : \mathbf{G}^{-1}) + 2\mu \mathbf{E}^\sharp. \quad (7.2)$$

Lamé's first parameter  $\lambda$  and Lamé's second parameter  $\mu$  are related to Young's modulus  $E$  and Poisson's ratio  $\nu$  via  $\lambda = \frac{E\nu}{(1+\nu)(1-2\nu)}$  and  $\mu = \frac{E}{2(1+\nu)}$ . Since in this example Poisson's ratio is zero, Lamé's first parameter is zero and the second one simplifies to  $\mu = \frac{E}{2}$ . Moreover, no thickness change occurs, and therefore, the zero transverse normal stress condition is automatically fulfilled, see Eq. (5.119).

The same example was used in Müller and Bischoff [MB22], where the key results are summarized by the following statements:

- For linear Q1 elements, all three interpolation schemes (GFE, PBF, NFE) show practically identical convergence behavior. Omitting director normalization as done by the NFE approach is acceptable for linear elements since no difference in convergence behavior is observed.
- For higher-order elements, NFE achieves only quadratic h-convergence for the tip displacement. The NFE approach overestimates the deformation and reacts too flexible for higher-order interpolation, resulting in interpolated directors being too short, which represents an artificial thinning of the shell. PBF and GFE preserve unit length of the interpolated director and converge with higher order.
- Overall, PBF demonstrates superior efficiency compared to GFE. The GFE interpolation is superior in terms of h-convergence for higher-order interpolation, but since it needs automatic differentiation to obtain the element stiffness matrix and residual forces, it is too expensive to be competitive.



- Fewer load steps are needed in comparison to formulations found in the literature. The radial return normalization from Eq. (2.57) was shown to be superior to the exponential map from Eq. (3.21). It is possible to compute the pure bending example in a single load step, with 16 iterations (cf. [MB22]). This is in drastic contrast to the literature, where an early contribution needs 40 load steps [Ram76] or a recent contribution needs 7 load steps with 51 iterations in total [Zou20].

In summary, the discussion highlights the superiority of PBF in terms of overall efficiency and accuracy, particularly for higher-order interpolation, while NFE shows limitations in convergence and accuracy.

### 7.3.1 Analytical Solution

The boundary conditions and load are chosen such that the beam is in pure bending. The stresses can be integrated through the thickness to obtain the stress resultants, using Eq. (5.65) in a local coordinate reference frame. The local coordinate system is chosen such that the first direction is tangential and the second direction is in global Y-direction. The third direction is chosen such that it is orthogonal to the first two directions, namely in the direction of the circle's normal. Therefore, the normal force and the transverse shear force must be identically zero. From these constraints, the correct bending moment load can be derived as follows: The analytical solution has only one non-trivial deformation gradient component  $F^1_1 = 2\pi(R + \xi^3)/L$  in terms of the unknown radius  $R$  of the deformed beam. The Green-Lagrangian strain is then given by

$$E_{11} = \frac{1}{2}(F_{11}^2 - 1) = \frac{2\pi^2(R + \xi^3)^2}{L^2} - \frac{1}{2}, \quad (7.3)$$

and the second Piola-Kirchhoff stress by

$$S^{11} = 2\mu E_{11} = EE_{11} = \frac{2\pi^2(R + \xi^3)^2}{L^2} - \frac{1}{2}, \quad (7.4)$$

where  $E$  is Young's modulus. In this one-dimensional scenario, the transformation to the Cauchy stresses  $\boldsymbol{\sigma} = 1/\det \mathbf{F} \cdot \mathbf{F} \cdot \mathbf{S} \cdot \mathbf{F}^T$  simplifies to  $\sigma^{11} = F^1_1 S^{11}$ . This single Cauchy stress component is a polynomial function of the position  $\xi^3$ , namely

$$\sigma^{11} = \frac{E(4\pi^2 R^2 + 8\pi^2 R\xi^3 + 4\pi^2(\xi^3)^2 - L^2)\pi(R + \xi^3)}{L^3}, \quad (7.5)$$

which is cubic in  $\xi^3$ . The stress resultants obtained from through-the-thickness integration, defined in Eq. (5.65), of the Cauchy stress are given by

$$\begin{aligned} n^{11} &= \int_{h^-}^{h^+} \sigma^{11} d\xi^3 = \frac{E\pi Rh(4\pi^2 R^2 + \pi^2 h^2 - L^2)}{L^3}, \\ m^{11} &= \int_{h^-}^{h^+} \xi^3 \sigma^{11} d\xi^3 = \frac{EI\pi(60\pi^2 R^2 + 3\pi^2 h^2 - 5L^2)}{5L^3}, \end{aligned} \quad (7.6)$$

with  $EI = Eh^3/12$  being the bending stiffness of the shell. As stated before, from equilibrium it can be derived that  $n^{11} = 0$ , which allows the derivation of the radius  $R$  as

$$R = \frac{\sqrt{L^2 - \pi^2 h^2}}{2\pi}. \quad (7.7)$$

The radius of the final circle is shorter than  $L/(2\pi)$ , since the Saint Venant-Kirchhoff material law, coupled with the Green-Lagrange strain, is stiffer in tension than in compression. This yields higher stress at the outer surface at  $h^+$  in comparison to the inner surface at  $h^-$ . Therefore, the neutral axis is shifted towards the tension side. This yields compression at the midsurface and therefore a smaller radius.

If the derived radius from Eq. (7.7) is inserted into the bending moment  $m^{11}$ , the analytical result is,

$$m_{\text{ex}}^{11} = \frac{2EI\pi}{L} \left( 1 - \frac{6}{5} \frac{h^2 \pi^2}{L^2} \right) = M^{\text{lin}} \left( 1 - \frac{6}{5} \frac{h^2 \pi^2}{L^2} \right), \quad (7.8)$$

which is the bending moment that is needed to coil the shell to a full circle. The subscript “ex” denotes the exact solution. Here,  $M^{\text{lin}}$  denotes the bending moment that is needed to coil a beam with a linear material law to a full circle. Here, the factor  $6/5$  takes into account the non-linearity of the Green-Lagrangian strain. Since the integrand of the bending moment is of fourth order in the thickness coordinate  $\xi^3$ , the element residual and element stiffness matrices for the simulation need to be integrated with at least three-point Gauss quadrature to capture all terms. Consider the case of a very thin beam, i.e.,  $h \rightarrow 0$ , in this case, the bending moment load converges to  $M^{\text{lin}}$  and the radius  $R$  of the deformed beam converges to  $L/(2\pi)$ , which recovers the solution with a linear material law. Furthermore, we point out that this is in line with the value  $M^{\text{lin}} = 2\pi EI/L$  found in the literature [Sim90a; Büc92; Ram76].

From Eq. (7.7), the displacement and the deformed configuration can be derived as

$$\mathbf{X}(\xi^i) = \begin{bmatrix} \xi^1 \\ \xi^2 \\ -\xi^3 \end{bmatrix} \mathbf{E}_I, \quad \mathbf{x}(\xi^i) = \begin{bmatrix} \sin\left(\frac{2\pi\xi^1}{L}\right)(R + \xi^3) \\ \xi^2 \\ (-R - \xi^3)\cos\left(\frac{2\pi\xi^1}{L}\right) + R \end{bmatrix} \mathbf{E}_I. \quad (7.9)$$

Here,  $\xi^1 \in [0, L]$ ,  $\xi^2 \in [0, b]$  and  $\xi^3 \in [-h/2, h/2]$ , where the midsurface deformation  $\varphi$  can be obtained by setting  $\xi^3$  in  $\mathbf{u}(\xi^i)$  to zero.

Furthermore, the analytical solution for the potential energy from Eq. (7.1), which contains only bending energy, is given by

$$\begin{aligned} \Pi_{\text{ex}} &= \int_0^L \int_0^b \int_{h^-}^{h^+} \psi(\mathbf{E}) \, d\xi^3 \, d\xi^2 \, d\xi^1 \\ &= Ebh \frac{L^4 - \pi^2 L^2 (8R^2 + \frac{2}{3}h^2) + (16R^4 + 8R^2 h^2 + \frac{1}{5}h^4)\pi^4}{8L^3}. \end{aligned} \quad (7.10)$$

For completeness, the missing analytic results are given as

$$q_{\text{ex}}^1 = 0, \quad n_{\text{ex}}^{11} = 0, \quad \varphi_{\text{ex}}(\xi^1, \xi^2) = R \begin{bmatrix} \sin\left(\frac{2\pi\xi^1}{L}\right) - \frac{\xi^1}{R} \\ \xi^2 \\ 1 - \cos\left(\frac{2\pi\xi^1}{L}\right) \end{bmatrix} \mathbf{E}_I, \quad (7.11)$$

where the last equation is the midsurface deformation.

### 7.3.2 Exemplary Finite Element Solution

The given analytical results are used to validate and compare the interpolation schemes NFE, PBE, and GFE from Section 6.3. Thus, now the numerical results are presented and compared to the analytical solution for the example of the pure bending of a straight beam. Furthermore, locking prevention techniques are considered, namely assumed natural strains (ANS) from Appendix A.11. This is done in the following, but for a better understanding of the situation, several discrete solutions are first shown. Fig. 7.5 does not only show the midsurface but shows the three-dimensional shell body. Therefore, the thickness for these graphical purposes was chosen as  $h = 1$  cm.

The only non-zero Cauchy stress components are  $\sigma^{11}$  and  $\sigma^{13}$ , where the former is non-zero, as in the analytical solution, but the latter is also non-zero but oscillates around the analytical solution (around zero). This can be attributed to *transverse shear locking*. Refer to Braess [Bra07] for a discussion of this phenomenon. This can be seen in Fig. 7.5, where the stresses are plotted on the deformed configuration. The simulation was done

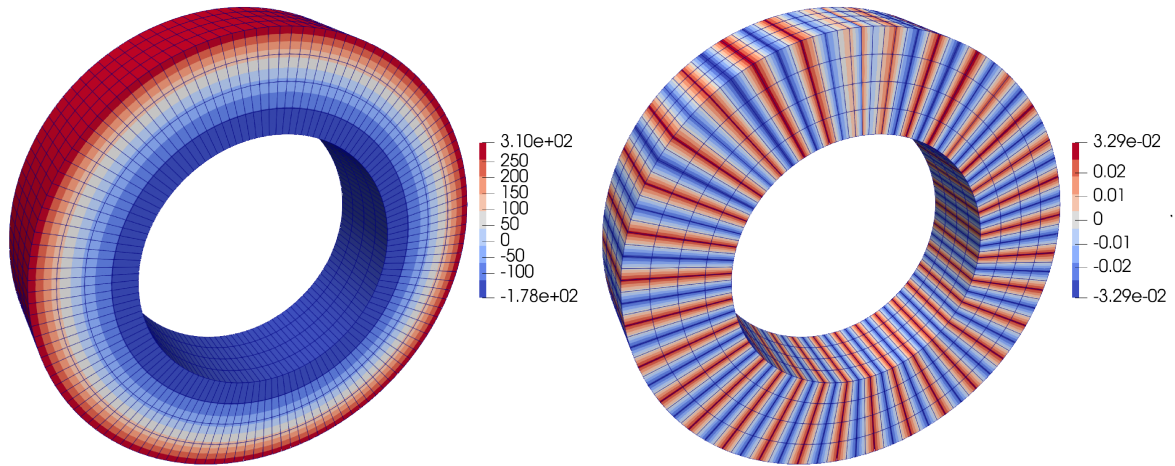


**Figure 7.5:** Stress plot of the bending of a straight beam. The Cauchy stress components  $\sigma^{11}$  (left) and  $\sigma^{13}$  (right) in  $\text{kN cm}^{-2}$  on the deformed configuration for a thickness  $h = 1 \text{ cm}$ . Images obtained from simulation data using Paraview [Ahr05]. The grid lines indicate cells, where the stress is evaluated and interpolated linearly.

with 32 elements with (P3C2)-ansatz functions in the direction, where the beam bends. In the direction, where the solution is constant, linear ansatz functions are chosen. Visibly, the displacements are converged, since the shell coils up to a full ring. Furthermore, on the left-hand side  $\sigma^{11}$  matches the theoretical maximum and minimum value, which are given by  $\sigma^{11}(h^-) = -177.7075 \text{ kN cm}^{-2}$  and  $\sigma^{11}(h^+) = 310.0044 \text{ kN cm}^{-2}$ , up to two significant digits. On the right-hand side of Fig. 7.5, the transverse shear stress is non-zero and oscillates around zero. The combination of the chosen polynomial order of the ansatz functions, number of elements, and moderate slenderness is not a challenging setup. The magnitude of these oscillations would increase by increasing the slenderness. This can also be seen if the stress resultants are considered. These are given in Fig. 7.6, depicted over the reference coordinate  $\xi^1 \in [0, L]$ . Therein, the bending moment error is shown in Fig. 7.6(a), the membrane force  $n^{11}$  in Fig. 7.6(c), and the transverse shear force  $q^1$  in Fig. 7.6(d). Furthermore, the absolute displacement error in X-direction is shown in Fig. 7.6(b). All four of them show a varying degree of oscillations around the analytical solution. These can be attributed to the transverse shear locking and membrane locking, and they are also characteristic of the problem in combination with the chosen polynomial order of the ansatz functions. Since the magnitude of the oscillations is small, their effect on the overall result quality can be considered negligible. This can be seen by comparing the analytical results with the numerical results. Since comparing against zero is not meaningful, only the relative error of the bending moment and the displacement are considered. The numerical value of the constant bending moment is  $m_{\text{ex}}^{11} = 40.0445 \text{ kN cm cm}^{-1}$ . This yields a maximum relative error  $\max(m_{\text{ex}}^{11} - m^{11})/m_{\text{ex}}^{11}$

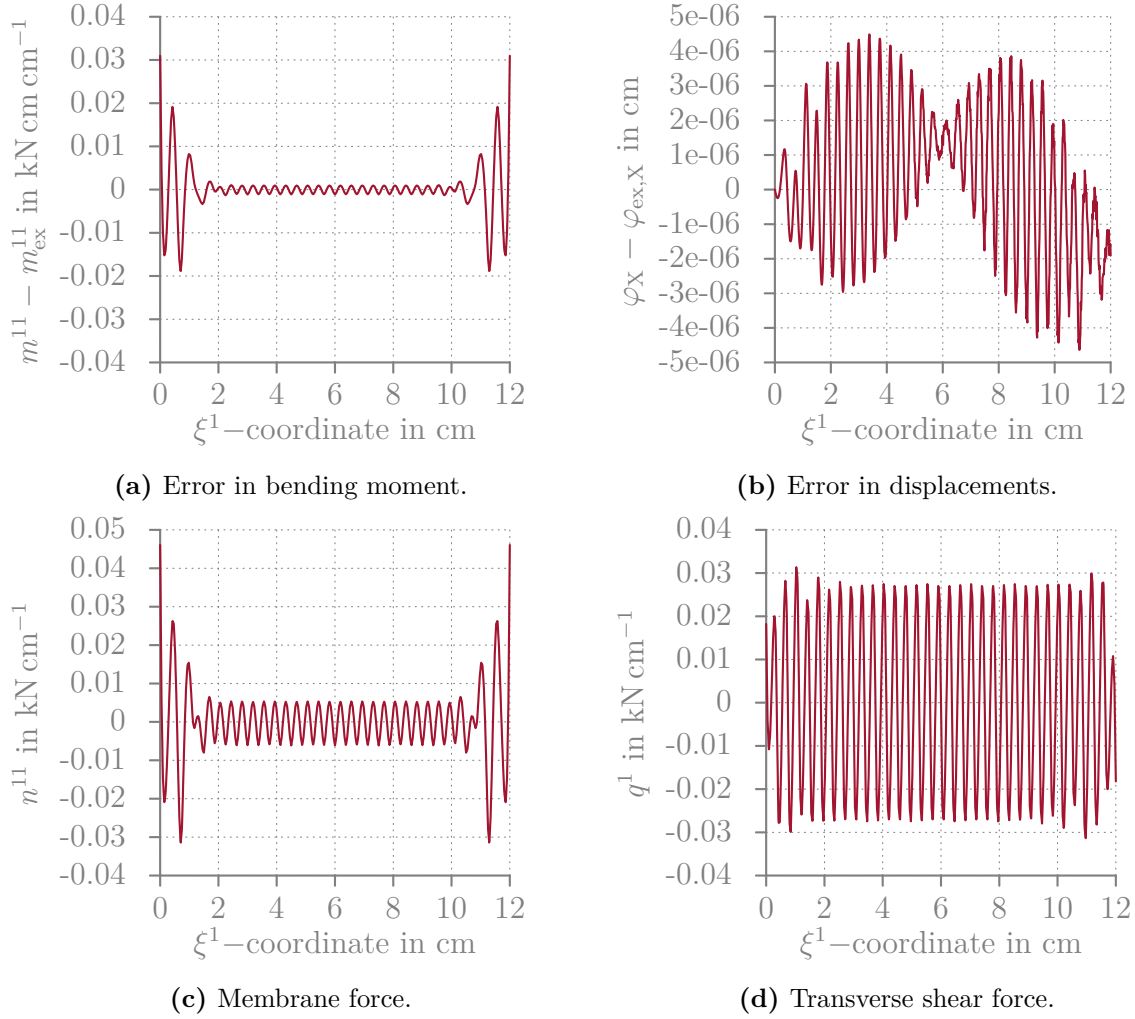


**Figure 7.6:** Stress resultants and displacement error for the pure bending with a thickness of  $h = 1$  cm. The analytical solutions of the stress resultants are  $m_{\text{ex}}^{11} = 40.0445 \text{ kN cm cm}^{-1}$ ,  $n^{11} = 0 \text{ kN cm}^{-1}$ , and  $q^1 = 0 \text{ kN cm}^{-1}$ . The analytic solution for the displacement is given by Eq. (7.11). The results are obtained with 32 elements with P3C2 and projection-based interpolation (PBFIE).

of 0.08% for the bending moment. The maximum displacement of the beam occurs at its tip with a value of exactly  $u_{\text{tip}} = 12 \text{ cm} = L$ . The maximum relative error of the displacement in X-direction is  $\max(\varphi_X - \varphi_{\text{ex},X})/12 = 1.6\text{e-}5\%$ . Consequently, the formulation is capable of reaching the analytical solution with high precision.

### 7.3.3 Q1 Elements with Assumed Natural Strain

As stated at the beginning of this section, PBFIE showed superior performance in comparison to NFE and GFE for higher-order elements, in Müller and Bischoff [MB22]. For

the Q1 element, all three formulations showed very similar results. Therefore, it was concluded that the Q1 element does not benefit from the additional numerical effort of PBE. This conclusion was made with standard Q1 elements, which suffer from transverse shear locking. If locking is eliminated, the elements show more bending, and therefore, the element directors differ more within one element. In contrast to this, when locking is present, the element directors are almost parallel, which makes the results almost independent of the chosen director interpolation scheme. Thus, the study is repeated and transverse shear locking is eliminated using the assumed natural strain (ANS) method for transverse shear. Refer to Appendix A.11 for a short description of the method. No membrane locking is present since the element's midsurface is flat.

To trigger moderate locking, the thickness is set to  $h = 0.1$  cm, resulting in a slenderness of  $L/h = 120$ . For this study, the  $L^2$  errors of the displacement and the stress resultants are considered. In Fig. 7.7, the  $L^2$  errors of the displacement and the bending moment are shown as functions of the element size  $h$ , which should not be confused with the thickness  $h$ . Therein, in black the standard formulation of the Q1 element using NFE, PBE, and GFE, is shown, which yields all the locking behavior and only reaches the correct convergence order after an initial plateau. This is the case for the displacement on the left and the bending moment on the right. In contrast to this, the versions using ANS show an earlier convergence but are accompanied by an initially unstable regime, where the iterative solution scheme does not converge or to a wrong minimizer. After this initial regime, the displacement and the bending moment converge and GFE shows the best convergence behavior for the displacement error and bending moment error. PBE and NFE are similar but PBE shows a slightly better convergence behavior for the bending moment in Fig. 7.7(b). The GFE formulation with ANS in comparison to the formulations without ANS shows partially more than three orders of magnitude smaller errors.

A similar conclusion can be drawn by investigating the errors in transverse shear forces error and membrane forces, respectively. In Fig. 7.8 the resulting errors are shown and are accompanied by the ratio of the transverse shear and the total numerical energy. The standard formulation of the Q1 element using NFE, PBE, and GFE, in black, shows severe locking and only reaches convergence after a long initial plateau. This is even more pronounced in comparison to the displacement and the bending moment since the transverse shear error and the membrane error first increase significantly. The ANS versions show a better convergence behavior, except for the initial regime.

The NFE formulation in combination with ANS shows practically no error for the shear forces in Fig. 7.8(a) or membrane forces in Fig. 7.8(b) after this initial regime. Thus, it directly reproduces the analytical solution of a pure bending problem in terms of these stress-resultants. Interestingly, PBE and GFE with ANS show the same behavior as

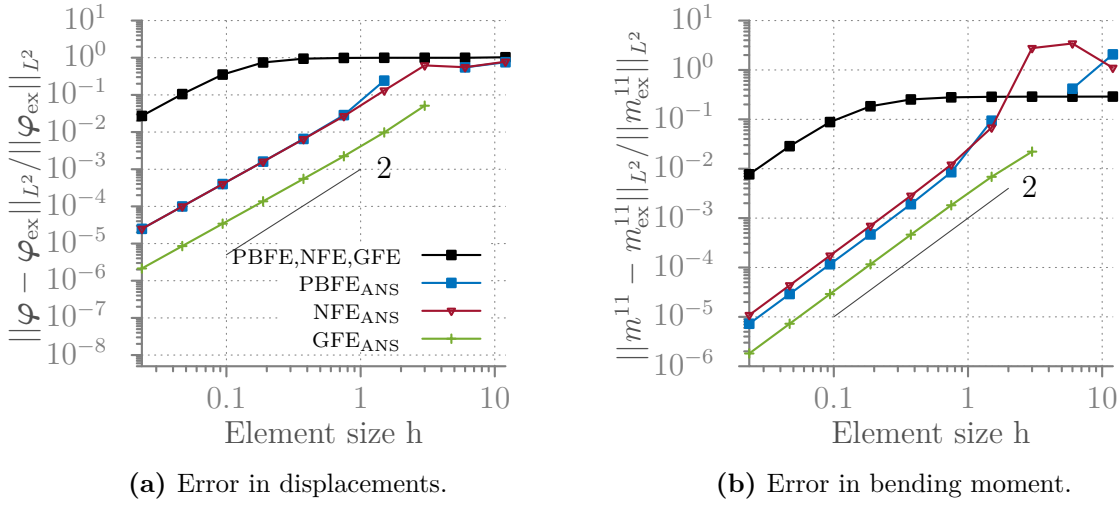
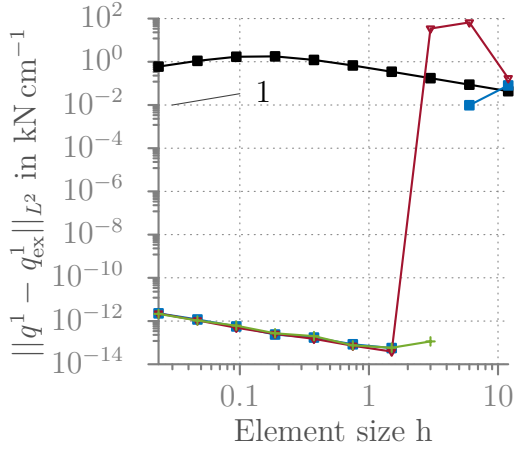


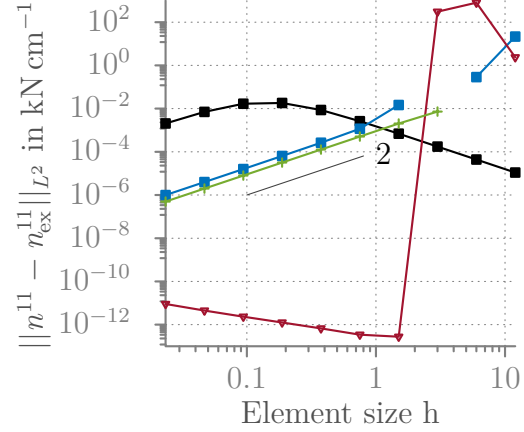
**Figure 7.7:** Illustration of displacement error (left) and bending moment error (right) for varying element sizes  $h$ . The analytical solutions  $m^{\text{II}} = 40.0445 \text{ kN cm cm}^{-1}$  and the analytic displacement is given by Eq. (7.11).

NFE, but only for the transverse shear forces in Fig. 7.8(a). The membrane forces errors for PBFE and GFE in Fig. 7.8(b) show in contrast to NFE a more typical convergence behavior, and converge to the analytical solution but do not reproduce it directly as NFE with ANS. The energy fractions are computed as stated in Appendix A.9. The bad convergence behavior of the variants without ANS is also visible in the ratio of the transverse shear energy and the total numerical energy in Fig. 7.8(c). The ratio is almost constant at one, which means that all the energy is in transverse shear. This is wrong since the analytical solution has a transverse shear energy of zero. Interestingly, the standard formulations show some slight “membrane locking behavior”, which is visible in Fig. 7.8(d) as the black line shows some increase for mesh refinement. Q1 elements are free from membrane locking, due to missing midsurface curvature and since this effect is only of magnitude  $10^{-4}$ , it could be an aftereffect of transverse shear locking. After an initially unstable area, the formulations with ANS show a ratio, where the transverse shear energy is zero and therefore reproduce the exact result directly. Considering, that PBFE and GFE exhibit non-zero errors for the membrane forces, we observe similar outcomes for the ratio of membrane energy to total energy, as depicted in Fig. 7.8(d). The convergence order of the membrane energy to total energy ratio aligns with that of the membrane error, both displaying a second-order behavior. In contrast to this, the transverse shear energy fraction in Fig. 7.8(c) shows a convergence order of two, whereas the shear error shows a convergence order of one.

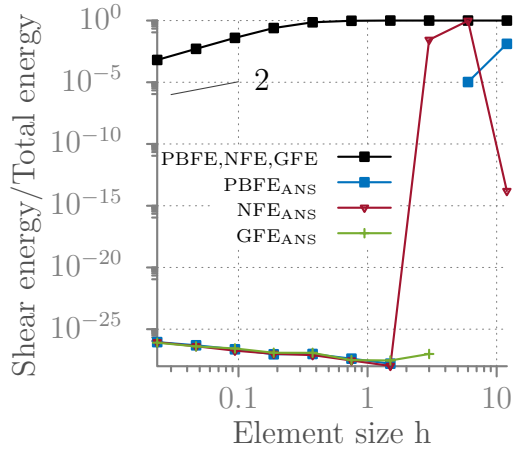
These findings lead to the following conclusion, that NFE in combination with ANS exactly predicts the zero shear forces and zero membrane forces after an initially unstable area. GFE and PBFE predict the overall displacement and the bending moment similarly



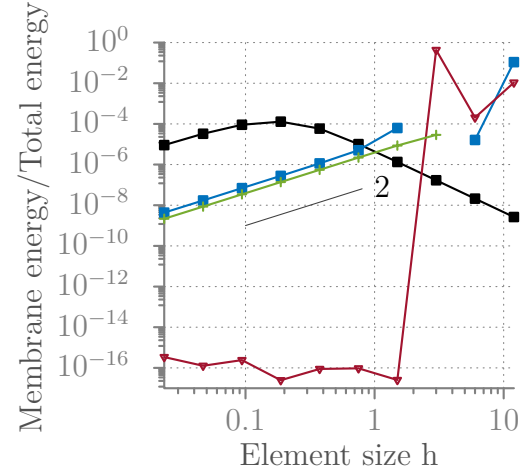
(a) Error in transverse shear forces.



(b) Error in membrane forces .



(c) Shear energy fraction.



(d) Membrane energy fraction.

**Figure 7.8:** Illustration of the shear forces error (a), the membrane forces error (b), and the corresponding energies as a fraction of the total energy (c, d) for varying element sizes  $h$ . The thickness is  $h = 0.1$  cm.

or slightly better. They are not able to reproduce a constant bending mode since they are not capable of providing constant curvature. This can be seen in Fig. 7.9, where a single linear element in bending is shown with NFE and PBFE/GFE as director interpolation, respectively. NFE provides a constant curvature on the left-hand side, since the director derivatives  $\mathbf{t}_{,1}$  are constant. In contrast to this, GFE and PBFE are not capable of providing a constant curvature, since the director derivatives  $\mathbf{t}_{,1}$  are forced to be tangential to the interpolated director, as shown on the right-hand side of Fig. 7.9. Thus, the curvature is given by  $\kappa_{11} = \mathbf{a}_1 \cdot \mathbf{t}_{,1}$ , which is only constant for NFE, and non-constant for PBFE and GFE. The same deformation pattern can be seen in the actual computation in Fig. 7.10. Therein, projection-based finite elements are used. The slight non-linearity of the bulk deformation can be seen by comparing the top and bottom



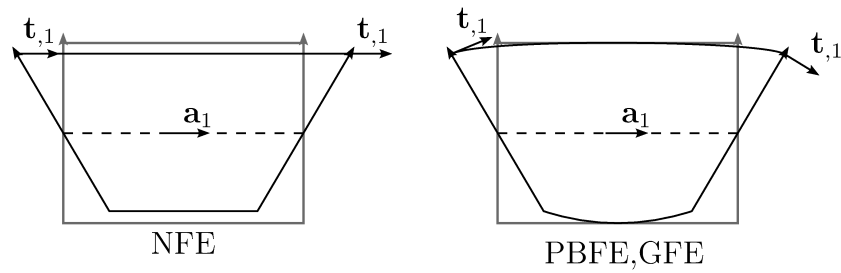


**Figure 7.9:** Pure bending configuration of an element with linear ansatz functions and NFE (left) or PBFE/GFE (right) as director interpolation.

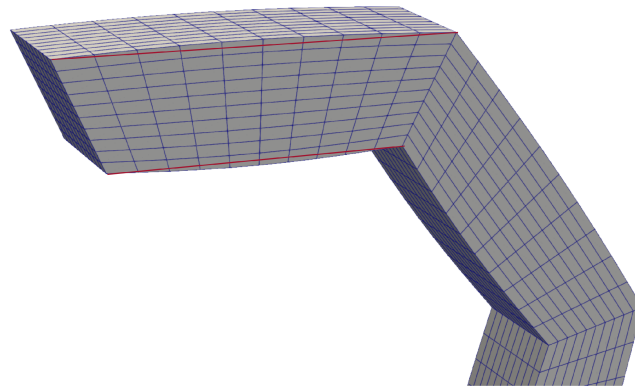


**Figure 7.10:** Illustration of a part of the deformed configuration with four elements, a thickness of 1 cm, utilizing projection-based interpolation for the director field and assumed natural strain (ANS) for transverse shear locking removal. The straight red lines depict a linear interpolation between the nodal directors. Half of the load to the full roll-up was applied. The grid lines only indicate a subsampling for plotting purposes.

surfaces with the straight red lines. Nevertheless, PBFE and GFE benefit from ANS, since they can reproduce the zero shear forces.

The following can be concluded. Since PBFE and GFE are additionally accompanied by an increase in computational cost, see Müller and Bischoff [MB22] and the improvements are quite small, NFE in combination with ANS is the best option for linear Q1 elements. Eliminating transverse shear locking is crucial for the performance of the element, even if it is accompanied by instabilities for coarse meshes, when using ANS.

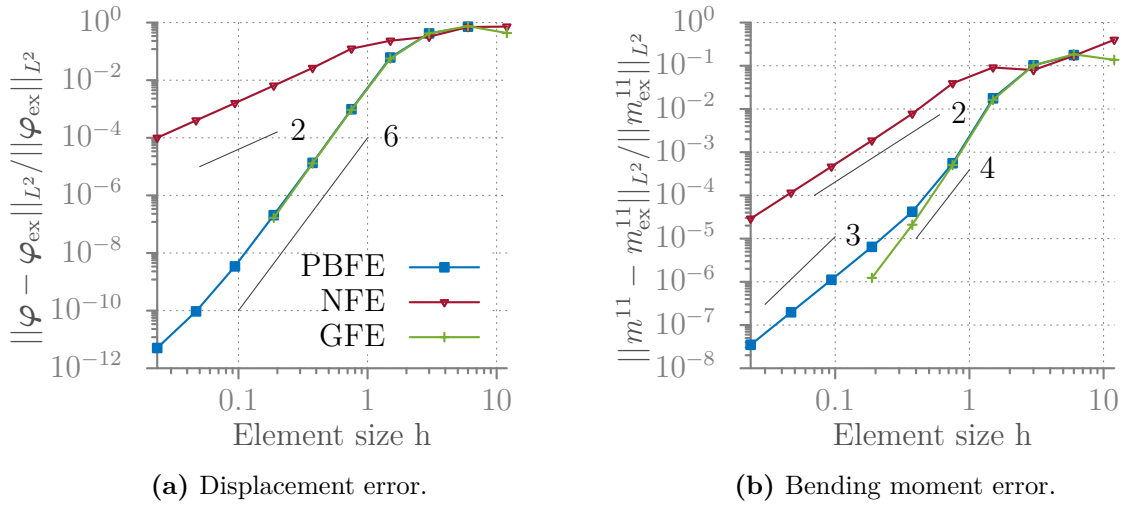


**Figure 7.11:** Illustration of displacement error (a) and bending moment error (b) for varying element sizes  $h$ . The analytical solutions  $m^{11} = 40.0445 \text{ kN cm cm}^{-1}$  and the analytic displacement is given by Eq. (7.11). The used ansatz functions are P3C2.

### 7.3.4 Higher-order NURBS Elements

In the following, the different interpolation schemes are investigated for higher-order NURBS ansatz functions. Since for curved elements, transverse shear locking and also membrane locking is present, the situation gets more complicated.

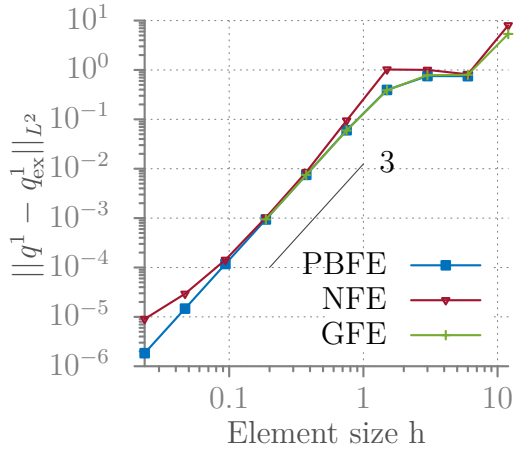
For the following investigations, the same setup as in the previous section is used. The ansatz functions are not the ones from a linear Q1 element, but they are cubic NURBS ansatz functions with  $C^2$ -continuity. Therefore, they are referred to as P3C2 elements.

The displacement error and the error of the bending moment stress resultants are shown in Fig. 7.11. The missing data points for GFE are due to numerical instabilities, for the evaluation of the geodesic interpolation. In Fig. 7.11, the different behaviors compared to linear ansatz functions become clear. As already elaborated on in Müller and Bischoff [MB22], the NFE approach suffers from a deterioration of the convergence order as seen in both Figs. 7.11(a) and 7.11(b). The error is dominated by the error of the wrong director interpolation and stays at a quadratic convergence rate. The GFE and PBFE approaches the exact solution with a convergence order between six and four for the displacement and three for the bending moment. In Fig. 7.11(b) all three director interpolations show a convergence for the bending moment between second order and fourth order. Nevertheless, NFE has a significantly higher error than the other two approaches. Furthermore, GFE provides a higher convergence order than PBFE, which is in contrast to the displacement error. The error of the shear forces and the membrane forces are shown in Figs. 7.12(a)

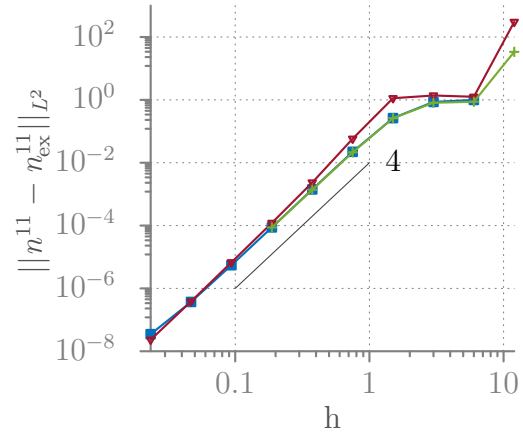
and 7.12(b), respectively. Additionally, the energy fractions of the shear energy and membrane energy of the total energy are shown in Figs. 7.12(c) and 7.12(d). The NFE approach is able to converge with the same order as PBF and GFE for the shear forces and the membrane forces. This is in contrast to the bending moment and the displacement, where the convergence order deteriorates. Therefore, the wrong director interpolation only influences the convergence order of the bending moment and the displacement. This is at least the case for the scenario at hand, where the shear forces and membrane forces should converge to zero, respectively. The convergence order is approximately three for the shear forces and four for the membrane forces. All three approaches show both transverse shear locking and membrane locking in the energy fractions, Figs. 7.12(c) and 7.12(d). This is in contrast to the linear case, where only transverse shear locking was present, due to the plane linear finite elements. The locking effect is not severe, since the energy fraction of the shear energy and membrane energy is below 0.01 % of the total energy with 16 elements. This corresponds to an element size  $h = 0.75$  cm in Figs. 7.12(c) and 7.12(d). The energy fraction in these spurious energies decreases with order six and order eight, respectively, which explains the rapid overall convergence.

### Influence of the Slenderness

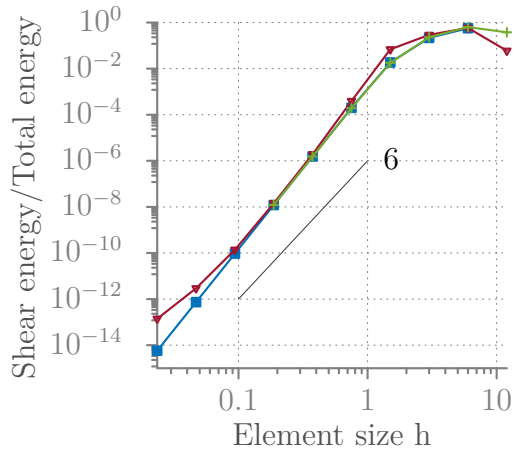
To further investigate locking elimination techniques and the behavior of the energy fractions, the PBF approach is solely used in the following. Consider a fixed discretization with 32 elements but now a varying thickness. The varying thickness is used to study the influence of the slenderness on the locking behavior. To circumvent numerical issues due to too small numbers Young's modulus is set to  $1e7$  kN cm<sup>-2</sup>. The slenderness is defined as the ratio of the length of the beam to the thickness of the beam, i.e.,  $L/h$ . To test the influence of transverse shear locking, the director field is discretized with ansatz functions one or two orders lower than the midsurface displacements. This is usually done to circumvent transverse shear locking since it balances the mismatch of the displacement field and the director field, see Braess [Bra07, Ch. VI §3., p. 311] Therefore, the midsurface displacement field is discretized with P3C2 ansatz functions, and the director field is discretized with P2C1, P2C0, or P1C0 ansatz functions, respectively. For a geometrically linear Timoshenko beam, a P2C0 discretization of the midsurface displacement field and a linear (P1C0) discretization of the director field yields a formulation free from transverse shear locking (cf. [Bra07]). In the following, the midsurface displacement is always discretized with P3C2 ansatz functions. Thus, due to the introduced geometric non-linearity and the continuity of the NURBS ansatz function, a complicated scenario is introduced and the locking behavior is not as clear as in the case of the geometrically linear Timoshenko beam.



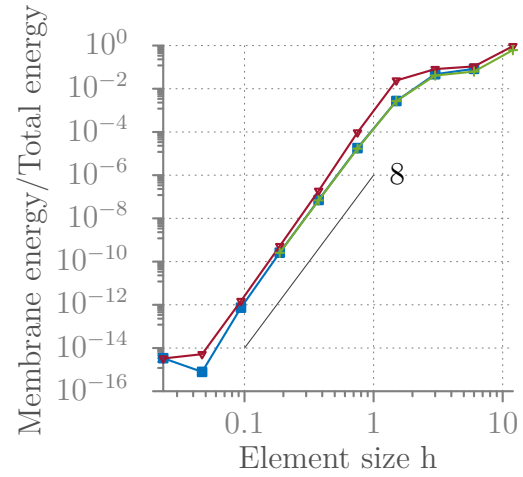
(a) Error in transverse shear forces.



(b) Error in membrane forces.



(c) Shear energy fraction.



(d) Membrane energy fraction.

**Figure 7.12:** The shear forces error (a), membrane forces error (b), and the corresponding energies are shown as a fraction of the total energy (c, d) for varying element sizes  $h$ . The thickness is  $h = 0.1$  cm. The used ansatz functions are P3C2.

In Fig. 7.13, the displacement error and the bending moment error are shown. Unfortunately, the last data point for a director interpolation P2C0 is missing, since the numerical solver did not converge, even for small load step sizes. Since the curves almost coincide this is not visible in the figure. The curves denote a midsurface displacement field that is discretized with P3C2 ansatz functions, only the varying polynomial order of the projection-based (PBF) director discretization is indicated in the figure legend. Now, instead of the element length, the slenderness is varied. This introduces an increasing locking effect for a fixed number of elements. This can be seen in Fig. 7.13(a), where the displacement error increases significantly with increasing slenderness. The magnitude of the error for the slenderness of  $1e6$  is almost in the range of bringing the beam back to the original state of a straight beam. Thus, a severe locking effect can be observed. This

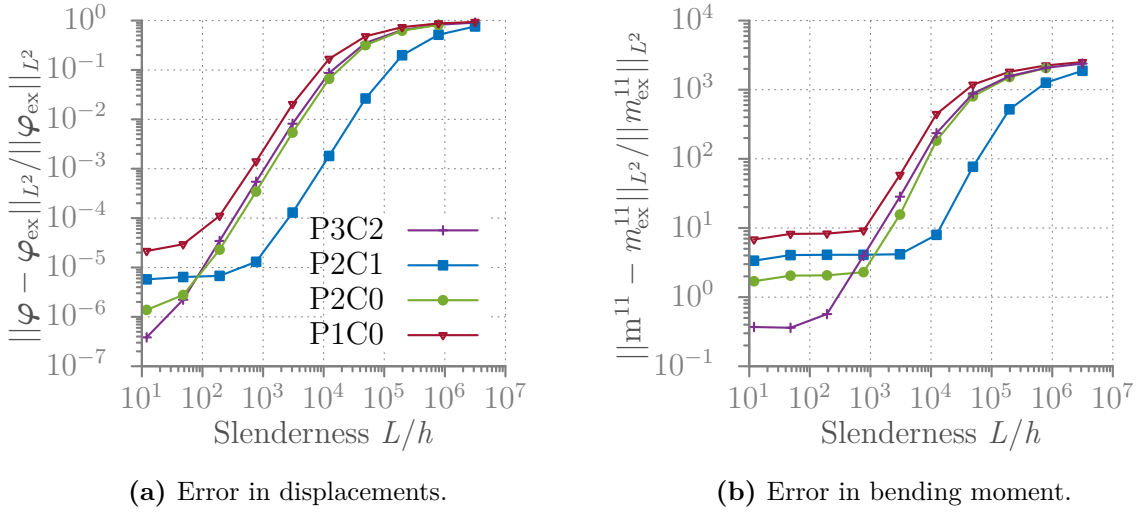
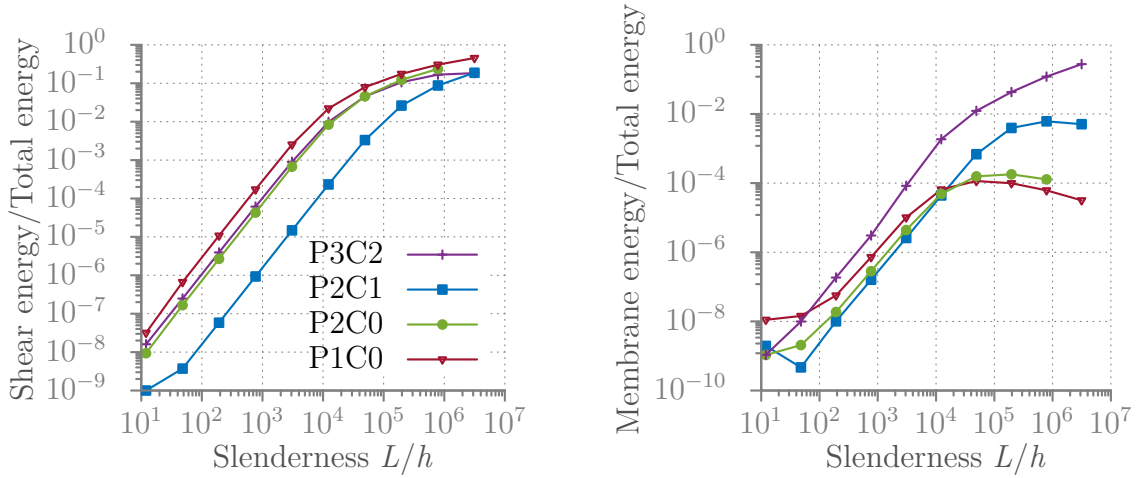


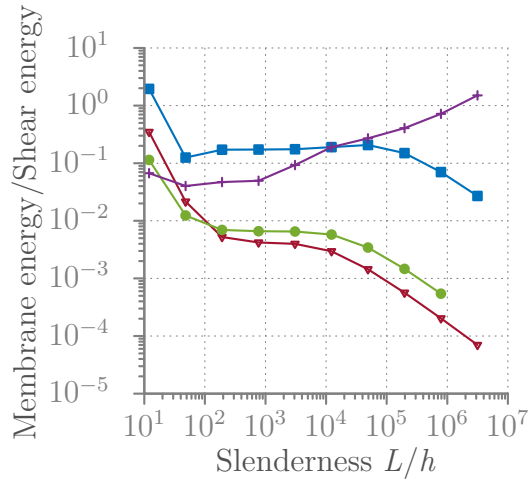
**Figure 7.13:** Error in displacements (left) and error in the bending moment (right) are shown for varying slenderness. The used ansatz functions are P3C2 for the midsurface displacements and for varying ansatz functions for the PBEF director interpolation.

is independent of the polynomial order of the director field. Nevertheless, the version where the director field is discretized with P2C1 ansatz functions shows the best results. This is true for the displacement error and for the bending moment error.

Again, the shear energy and membrane energy fractions are shown in Fig. 7.14, where also the slenderness is varied. In Fig. 7.14(a) it becomes clear that transverse shear locking can not be eliminated by interpolating the director field with lower order ansatz functions. All variants increase their energy fraction with increasing slenderness. If Fig. 7.14(b) is also considered simultaneously, it becomes clear that the membrane energy always increases for equal-order interpolation in purple (P3C2), but at some point, the lower-order variants decrease their energy fraction. Thus, for very slender structures, the total energy gets dominated by the shear energy, despite the lower-order interpolation of the director field. As a consequence, due to its significant contribution to the total energy, it dominates the bending energy, hindering the correct displacement. This can be seen in Fig. 7.14(c), where the ratio of membrane energy to shear energy is depicted. Thus, if the ratio exceeds one, the membrane energy dominates the shear energy. For increasing slenderness, this only happens for equal-order interpolation (P3C2), for lower-order interpolation, the ratio decreases. Therefore, interpolating the director field with lower-order ansatz functions does not eliminate spurious transverse shear energy contributions but it moves the dominating energy fraction from membrane energy to transverse shear energy for highly slender structures.



(a) Shear energy as a fraction of the total energy. (b) Membrane energy fraction of the total energy.



(c) Membrane energy as a fraction of the shear energy.

**Figure 7.14:** Shear and membrane energies fractions.

### 7.3.5 Conclusion

The results given in this section accommodate the result from Müller and Bischoff [MB22]. It was shown that eliminating transverse shear locking for Q1 elements does provide similar benefits for all introduced director interpolations. Especially, NFE provided the most accurate and efficient combination, since it is the only interpolation method that is capable of representing a state of constant bending. This conclusion can be used in the future to develop a more efficient formulation for Q1 elements, it could be beneficial to use NFE for the bending part, namely for the gradient of the director field, and PBEF for the shear part, namely for the director field itself, which then combines both advantages. Furthermore, it was shown that for higher-order elements, the overall

performance deteriorates, if the NFE approach is chosen. This manifests itself in a higher error for the displacement and the bending moment, but interestingly, the errors in transverse shear forces and membrane forces are not affected. Lower-order ansatzes were investigated for the director field to discuss the energy fractions between the competing locking phenomena, namely transverse shear locking and membrane locking. It was shown that for very slender structures, the membrane energy fraction decreases if the director field is interpolated with lower-order ansatz functions. This renders transverse shear locking the prevalent locking phenomenon in this particular example, although this may not be the case for other deformations with less symmetry.





---

## Summary and Outlook

The objective of this research was to improve the accuracy, efficiency, and reliability of simulation-based predictions of the mechanical behavior of thin-walled structures. In particular, existing gaps regarding Reissner-Mindlin shell formulations in the literature were filled and both theoretical and numerical aspects were improved. This progress represents an advance for the geometrically non-linear Reissner-Mindlin shell model and its formulation and contributes to the general progress in structural mechanics.

This work covers a wide range of topics. Theoretical parts are the accurate derivation of the stress resultants, balance laws for the shell, and the Reissner-Mindlin assumptions, which are studied to gain a deeper understanding of their implications. In addition, the study examines the importance of correct linearization procedures for a consistent and symmetric stiffness matrix. Due to the non-linear configuration spaces of the Reissner-Mindlin shell model, this is often controversially discussed in the literature. The properties of suitable director interpolation methods are also analyzed in detail. In addition, the influence of locking phenomena is investigated, which can significantly affect numerical performance. Functional analysis in non-linear functional spaces is examined, providing insights into their peculiarities from an engineering point of view. By addressing these different aspects, the research contributes to a better understanding of finite elements for non-linear fields. The consistent and symmetric stiffness matrix is derived by applying optimization techniques on manifolds, surpassing classical approaches that consider the unit length as a constraint through methods like introducing a Lagrange multiplier or a penalty term. This new derivation naturally leads to a five-parameter shell formulation, where five is the smallest possible number of parameters for the Reissner-Mindlin shell model.

Furthermore, the present work delves into the area of differential geometry and provides a solid mathematical basis for the shell formulation. This aspect is of particular importance

since the Reissner-Mindlin shell model is based on the unit length constraint for the director field, which has led to problems in the past. This unit length constraint is thoroughly addressed in this work, and the extensive mathematical analysis of its implications can serve as a cornerstone for future studies in the field of non-linear dynamics, particularly in the study of a non-constant, configuration-dependent, potentially unsymmetric mass matrix. Similar conclusions can be drawn for the static or dynamic analysis of three-dimensional beams, where the configuration also depends on the directional fields. Therefore, the research paves the way for further investigations in the field of structural mechanics.

A new and promising approach for the numerical implementation of the vanishing normal stress assumption has been proposed, which outperforms existing methods. This approach, which is also based on the concept of optimization on manifolds, not only leads to a more robust and efficient numerical method but can also be extended to other models with zero stress constraints. Both, a small model problem and a fully geometrically and materially non-linear shell simulation were used to validate and demonstrate the effectiveness of this approach.

Interpolation on manifolds was used to discretize the director field of the shell model in order to formulate a finite element method. Contrary to interpolation on vector spaces, for which there is a canonical option, interpolation on manifolds provides multiple alternatives. This study compared and analyzed various interpolation schemes in terms of their convergence rates and impact on locking phenomena. Linear Lagrangian interpolation and higher-order NURBS interpolation were studied by examining their finite element solutions and comparing them to an analytical solution. For linear Lagrangian interpolation, it was observed that by comparing these interpolation schemes for the director field, the standard approach, which interpolates in the embedding space, provides a superior ratio of accuracy to computational cost for the director interpolation. It has been demonstrated that, for higher-order B-spline ansatz functions, the standard approach negatively influences the convergence rate of the error of the finite element method. In contrast, it has been demonstrated that projection-based interpolation and geodesic interpolation for the director field do not show this degraded convergence rate for higher-order B-spline ansatz functions, making it the optimal choice for these ansatz spaces. This was confirmed by examining the displacement error and the bending moment error, but the standard method did not reveal any deterioration in the convergence rate for the membrane force error and the transverse shear force error. Therefore, it could be investigated in the future to use different interpolation schemes for different director quantities. For instance, the director field itself, which is required for transverse shear forces, can be interpolated using the standard interpolation, whereas the gradient of the director field, which is used for bending moments, can be discretized using the gradient resulting from the projection-based interpolation. Consequently, this would benefit from the precision

---

of projection-based interpolation and the reduced computational cost of the standard method in the appropriate locations.

The symmetry of the stiffness matrix was thoroughly investigated, leading to two important results. First, a consistent linearization process was derived for the Reissner-Mindlin shell formulation, leading to an unconditionally symmetric stiffness matrix. This is in contrast to existing approaches in the literature, where the stiffness matrix is symmetrized ad hoc or is symmetric only at equilibrium. Second, it has been shown that the symmetry of the stiffness matrix is directly derived from the use of the symmetric Riemannian Hessian, which is a more reliable alternative to the error-prone and potentially unsymmetrical second variation, which is still used in the literature. These findings also go beyond a Reissner-Mindlin shell formulation and apply to other structural models involving degrees of freedom on manifolds. Due to the consistent linearization of the tangential stiffness matrix, the derived shell formulation significantly reduces the number of required load steps in comparison to existing formulations.

The study of consistent linearization, the optimal director interpolation scheme, and the assumption of vanishing normal stress have led to the development of a novel Reissner-Mindlin shell formulation. This formulation exhibits potential improvements even for the simple case of linear Q1 elements commonly used in commercial finite element software. However, the real advantages of the proposed formulation become apparent for higher-order elements and exceed the capabilities of existing formulations.

All these findings yield a static shell formulation, where several desirable properties have been achieved. These include objectivity, the ability to accommodate unbounded magnitudes of total rotations, the satisfaction of the unit length constraint for interpolated directors, path-independent director interpolation, and avoiding any singularities due to director rotations. Moreover, the shell formulation achieves optimal convergence order, which provides superior performance compared to approaches found in the literature.

In summary, the present work addresses and deals with open issues of the non-linear Reissner-Mindlin shell model. It provides a comprehensive analysis and suggests advancements. The detailed discussions that are provided in this thesis not only provide a basis for the Reissner-Mindlin shell model but are also relevant to other structural models.



# A

---

## Appendix

### A.1 Transformation Rule of Christoffel Symbols

Consider a Riemannian manifold  $(\mathcal{M}, g)$  with a given Levi-Civita connection  $\nabla$  and metric components  $g_{ij}$ . The corresponding Christoffel symbols  $\Gamma$ , which are defined in Eq. (3.11) on page 55, transform according to

$$\begin{aligned} g^{jn}\Gamma_{ij}^k g_{kq} &= g^{jn} \frac{1}{2} g^{kl} (g_{il,i} + g_{il,j} - g_{ij,l}) g_{kq} \\ &= g^{jn} \frac{1}{2} \delta_q^l (g_{il,i} + g_{il,j} - g_{ij,l}) \\ &= g^{jn} \frac{1}{2} (g_{iq,i} + g_{iq,j} - g_{iq,l}) = -\Gamma_{iq}^n. \end{aligned} \tag{A.1}$$

Thus, we have  $g^{jn}\Gamma_{ij}^k g_{kq} = -\Gamma_{iq}^n$ .

### A.2 Divergence of a Tensor

Consider a vector field  $\xi$ . The divergence of this vector field reads in coordinates  $\theta^i$ ,

$$\xi^i_{|i} = \frac{1}{\sqrt{\det([g_{jk}]})} \frac{\partial}{\partial \theta^i} (\sqrt{\det([g_{jk}]}) \xi^i), \tag{A.2}$$

which can be derived from the contraction identity of the Christoffel symbols  $\Gamma_{kj}^k = \frac{\partial}{\partial \theta^i} \ln \sqrt{g_{jk}}$ , see also [MH94, Sec 4.27].

### A.3 Derivatives of the Projector

These derivatives are only needed for the derivation of the quantities  $\mathcal{Q}_\alpha, \mathcal{S}(\mathbf{v})$  and  $\mathcal{X}_\alpha(\mathbf{v})$ . They do not explicitly appear in the implementation.

$$\begin{aligned}
t^k &= \mathcal{P}^k(\mathbf{w}) = \frac{w^k}{\|\mathbf{w}\|}, \quad \mathbf{w} \in \mathbb{R}^3, \\
(\mathcal{P}')_l^k(\mathbf{w}) &= \frac{\partial \mathcal{P}^k}{\partial w^l} = \frac{\delta_l^k}{\|\mathbf{w}\|} - \frac{w^k w_l}{\|\mathbf{w}\|^3}, \\
&= \frac{\mathbf{I}}{\|\mathbf{w}\|} - \frac{\mathbf{w} \otimes \mathbf{w}}{\|\mathbf{w}\|^3} = \frac{\mathbf{I} - \mathbf{t} \otimes \mathbf{t}}{\|\mathbf{w}\|}, \\
(\mathcal{P}'')_{lm}^k &= \frac{\partial (\mathcal{P}')_l^k}{\partial w^m}, \\
&= \frac{1}{\|\mathbf{w}\|^2} \left[ -\delta_l^k t_m - \delta_m^k t_l - \delta_{lm} t^k + 3t^k t_l t_m \right], \\
(\mathcal{P}''')_{lmj}^k &= \frac{\partial (\mathcal{P}'')_{lm}^k}{\partial w^j} = \frac{1}{\|\mathbf{w}\|^3} \left[ -\delta_l^k \delta_{mj} - \delta_m^k \delta_{lj} - \delta_{lm} \delta_j^k, \right. \\
&\quad \left. + 3(\delta_l^k t_m t_j + \delta_m^k t_l t_j + \delta_{lm} t^k t_j), \right. \\
&\quad \left. + \delta_j^k t_m t_l + t^k \delta_{mj} t_l + t^k t_m \delta_{lj} - 15t^k t_m t_l t_j \right].
\end{aligned}$$

### A.4 Covariant Derivative for Compact Lie Groups

Let  $\mathbf{x} \in \mathcal{SO}(n)$  and  $\xi_{\mathbf{x}}, \eta_{\mathbf{x}} \in T_{\mathbf{x}}\mathcal{SO}(n)$  or another compact Lie group, respectively.

With this at hand, we can state the properties of a left-invariant metric

$$\langle \xi_{\mathbf{x}}, \eta_{\mathbf{x}} \rangle_{\mathbf{x}} = \langle \mathbf{x}^{-1} \xi_{\mathbf{x}}, \mathbf{x}^{-1} \eta_{\mathbf{x}} \rangle_{\mathbf{I}} \quad (\text{A.3})$$

where  $\mathbf{x} \in \mathcal{G}$  and  $\langle (\circ), (\circ) \rangle_{(\hat{\circ})}$  denotes the metric at the position  $(\hat{\circ})$  or respectively  $\mathbf{I}, \mathbf{x}$ . For a right-invariant metric, it needs to hold similar

$$\langle \xi_{\mathbf{x}}, \eta_{\mathbf{x}} \rangle_{\mathbf{x}} = \langle \xi_{\mathbf{x}\mathbf{x}^{-1}}, \eta_{\mathbf{x}\mathbf{x}^{-1}} \rangle_{\mathbf{I}} \quad (\text{A.4})$$

and finally, for a bi-invariant metric, it has to hold that

$$\langle \xi_{\mathbf{x}\mathbf{x}^{-1}}, \eta_{\mathbf{x}\mathbf{x}^{-1}} \rangle_{\mathbf{I}} = \langle \mathbf{x}^{-1} \xi_{\mathbf{x}}, \mathbf{x}^{-1} \eta_{\mathbf{x}} \rangle_{\mathbf{I}} \quad (\text{A.5})$$

multiplying from the right by  $\mathbf{x}$  gives

$$\langle \boldsymbol{\xi}_x, \boldsymbol{\eta}_x \rangle_{\mathbf{I}} = \langle \mathbf{x}^{-1} \boldsymbol{\xi}_x \mathbf{x}, \mathbf{x}^{-1} \boldsymbol{\eta}_x \mathbf{x} \rangle_{\mathbf{I}} \quad (\text{A.6})$$

a modified condition for a bi-invariant metric.

To obtain an expression suitable to us in the *Koszul formula*, refer to Eq. (3.10) on page 54 for a definition, we have to take the derivative of the last expression. For this we choose with the exponential map  $\exp : \mathfrak{g} \rightarrow \mathcal{G}$ , the group element  $\mathbf{x}(t) = \exp^{t\zeta_x}$  where  $\zeta_x \in \mathfrak{g}$ .

$$\langle \boldsymbol{\xi}_x, \boldsymbol{\eta}_x \rangle_{\mathbf{I}} = \langle \exp^{-t\zeta_x} \boldsymbol{\xi}_x \exp^{t\zeta_x}, \exp^{-t\zeta_x} \boldsymbol{\eta}_x \exp^{t\zeta_x} \rangle_{\mathbf{I}} \quad (\text{A.7})$$

Taking the derivative on both sides w.r.t.  $t$  and  $t = 0$  we have

$$0 = \langle -\zeta_x \boldsymbol{\xi}_x + \boldsymbol{\xi}_x \zeta_x, \boldsymbol{\eta}_x \rangle_{\mathbf{I}} + \langle \boldsymbol{\xi}_x, -\zeta_x \boldsymbol{\eta}_x + \boldsymbol{\eta}_x \zeta_x \rangle_{\mathbf{I}} \quad (\text{A.8})$$

This gives the result in terms of the Lie bracket

$$0 = \langle [\boldsymbol{\xi}_x, \zeta_x], \boldsymbol{\eta}_x \rangle + \langle \boldsymbol{\xi}_x, [\boldsymbol{\eta}_x, \zeta_x] \rangle \quad (\text{A.9})$$

where  $\mathbf{I}$  was neglected for a more compact notation.

Inserting this in the Koszul formula Eq. (3.10) on page 54 we get

$$\begin{aligned} 2\langle \nabla_{\boldsymbol{\xi}_x} \boldsymbol{\eta}_x, \zeta_x \rangle &= \langle [\boldsymbol{\xi}_x, \boldsymbol{\eta}_x], \zeta_x \rangle \\ &+ D_{\boldsymbol{\xi}_x} \langle \boldsymbol{\eta}_x, \zeta_x \rangle + D_{\boldsymbol{\eta}_x} \langle \boldsymbol{\xi}_x, \zeta_x \rangle - D_{\zeta_x} \langle \boldsymbol{\xi}_x, \boldsymbol{\eta}_x \rangle \end{aligned} \quad (\text{A.10})$$

where the second and third terms are canceled due to Eq. (A.9). Additionally, all directional derivatives vanish since the metric is left invariant and therefore  $\langle \boldsymbol{\eta}_x, \zeta_x \rangle, \langle \boldsymbol{\xi}_x, \zeta_x \rangle$  and  $\langle \boldsymbol{\xi}_x, \boldsymbol{\eta}_x \rangle$  are constant and their derivatives vanish. With this we get

$$2\langle \nabla_{\boldsymbol{\xi}_x} \boldsymbol{\eta}_x, \zeta_x \rangle = \langle [\boldsymbol{\xi}_x, \boldsymbol{\eta}_x], \zeta_x \rangle \quad (\text{A.11})$$

## A.5 The Inextensible Director Derivatives

The derivation is done using the quantities from the current shell configuration. From the director  $\mathbf{t} : \Omega \rightarrow \mathcal{S}^2$  the partial derivatives are denoted by  $\mathbf{t}_{,\alpha}$ . For the derivation of  $\mathbf{t}_{,\alpha}$  in terms of the midsurface basis  $\mathbf{a}_\alpha$ , we make the ansatz

$$\mathbf{t}_{,\alpha} = b^\mu_{\alpha} \mathbf{a}_\mu + \Gamma_{3\alpha}^3 \mathbf{t}, \quad (\text{A.12})$$

with  $b_{\beta\alpha} = \mathbf{t}_{,\beta} \cdot \mathbf{a}_\alpha$  and  $b^\mu_\alpha = a^{\mu\beta} b_{\beta\alpha}$ . Here,  $a^{\mu\beta}$  denotes the coefficients of the metric inverse of the midsurface, such that  $a_{\mu\beta} = \mathbf{a}_\alpha \cdot \mathbf{a}_\beta$ . From the inextensibility conditions  $\|\mathbf{t}\| = 1$  and  $\mathbf{t}_{,\alpha} \cdot \mathbf{t} = 0$ , it follows

$$\mathbf{t}_{,\alpha} \cdot \mathbf{t} = b^\mu_\alpha \mathbf{a}_\mu \cdot \mathbf{t} + \Gamma_{3\alpha}^3 = 0, \quad (\text{A.13})$$

which results in

$$\Gamma_{3\alpha}^3 = -b^\mu_\alpha \gamma_\mu, \quad (\text{A.14})$$

with  $\gamma_\mu = \mathbf{a}_\mu \cdot \mathbf{t}$ . Thus, Eq. (A.12) reads

$$\begin{aligned} \mathbf{t}_{,\alpha} &= b^\mu_\alpha \mathbf{a}_\mu - b^\mu_\alpha \gamma_\mu \mathbf{t}, \\ &= b^\mu_\alpha (\mathbf{a}_\mu - \gamma_\mu \mathbf{t}). \end{aligned} \quad (\text{A.15})$$

## A.6 The Shifter Tensor Components in the Midsurface Basis

The shell shifter from Eq. (5.21) on page 96 for the current configuration is defined as

$$\mathbf{z} = \delta^i_j \mathbf{g}_i \otimes \mathbf{a}^j = \mathbf{g}_i \otimes \mathbf{a}^i. \quad (\text{A.16})$$

The components of this shifter are derived in the basis  $\mathbf{a}_i \otimes \mathbf{a}^j$ , which yields a convenient geometric interpretation. The definition of the base vectors  $\mathbf{g}_\alpha = \mathbf{a}_\alpha + \xi^3 \mathbf{t}_{,\alpha}$  and  $\mathbf{g}_3 = \mathbf{a}_3 = \mathbf{t}$  is plugged in Eq. (A.16). This yields

$$\begin{aligned} \mathbf{z} &= \mathbf{g}_i \otimes \mathbf{a}^i, \\ &= (\mathbf{a}_\alpha + \xi^3 \mathbf{t}_{,\alpha}) \otimes \mathbf{a}^\alpha + \mathbf{t} \otimes \mathbf{a}^3, \\ &= \mathbf{a}_\alpha \otimes \mathbf{a}^\alpha + \xi^3 \mathbf{t}_{,\alpha} \otimes \mathbf{a}^\alpha + \mathbf{t} \otimes \mathbf{a}^3, \end{aligned} \quad (\text{A.17})$$

using the definition of the director derivatives from Appendix A.5, yields

$$\begin{aligned} \mathbf{z} &= \mathbf{a}_\alpha \otimes \mathbf{a}^\alpha + \xi^3 (b^\mu_\alpha \mathbf{a}_\mu - b^\mu_\alpha \gamma_\mu \mathbf{t}) \otimes \mathbf{a}^\alpha + \mathbf{t} \otimes \mathbf{a}^3, \\ &= \mathbf{a}_\alpha \otimes \mathbf{a}^\alpha + \xi^3 b^\mu_\alpha \mathbf{a}_\mu \otimes \mathbf{a}^\alpha - \xi^3 b^\mu_\alpha \gamma_\mu \mathbf{t} \otimes \mathbf{a}^\alpha + \mathbf{t} \otimes \mathbf{a}^3, \\ &= (\delta^\mu_\alpha + \xi^3 b^\mu_\alpha) \mathbf{a}_\mu \otimes \mathbf{a}^\alpha - \xi^3 b^\mu_\alpha \gamma_\mu \mathbf{t} \otimes \mathbf{a}^\alpha + \mathbf{t} \otimes \mathbf{a}^3, \end{aligned} \quad (\text{A.18})$$



which defines the unsymmetric shell shifter tensor components of the current configuration with  $b_{\beta\alpha} = \mathbf{t}_{,\beta} \cdot \mathbf{a}_\alpha$  and  $b^\mu_\alpha = a^{\mu\beta} b_{\beta\alpha}$ . Here,  $a^{\mu\beta}$  denotes the coefficients of the metric inverse of the midsurface, such that  $a_{\mu\beta} = \mathbf{a}_\mu \cdot \mathbf{a}_\beta$ . There are several special cases, first if the director is orthogonal to the midsurface, we have  $\gamma_\alpha = 0$  and end up with

$$\mathbf{z} = (\delta^\mu_\alpha + \xi^3 b^\mu_\alpha) \mathbf{a}_\mu \otimes \mathbf{a}^\alpha + \mathbf{t} \otimes \mathbf{a}^3, \quad (\text{A.19})$$

which is symmetric since for this case  $\mathbf{t}$  and  $\mathbf{a}^3$  are collinear and  $b_{\alpha\beta} = \mathbf{t}_{,\alpha} \cdot \mathbf{a}_\beta = b_{\beta\alpha} = \mathbf{t}_{,\beta} \cdot \mathbf{a}_\alpha$ , whereas the latter is a usual consequence of surface differential geometry. The base vector  $\mathbf{a}^3$  can be simply derived as  $\mathbf{a}^3 = (\mathbf{a}_1 \times \mathbf{a}_2) / (\mathbf{t} \cdot (\mathbf{a}_1 \times \mathbf{a}_2))$  as similarly stated in Eq. (2.104) on page 46.

The other special case is, where the curvature is zero, namely  $b^\mu_\alpha = 0$ . In this case, we have

$$\mathbf{z} = \delta^\mu_\alpha \mathbf{a}_\mu \otimes \mathbf{a}^\alpha + \mathbf{t} \otimes \mathbf{a}^3 = \mathbf{a}_i \otimes \mathbf{a}^i, \quad (\text{A.20})$$

which is simply the identity.

## A.7 The Determinant of the Shifter Tensor

From the definition of the determinant for mixed tensors Eq. (2.101) on page 45, it results that the determinant of the shifter tensor  $\det \mathbf{z}$  is merely the determinant of its component matrix  $\det([z^\mu_\alpha])$ .

In matrix notation, we have

$$z^\mu_\alpha = \begin{bmatrix} 1 + \xi^3 b^1_1 & \xi^3 b^2_1 & 0 \\ \xi^3 b^1_2 & 1 + \xi^3 b^2_2 & 0 \\ -\xi^3 (b^1_1 \gamma_1 + b^2_1 \gamma_2) & -\xi^3 (b^1_2 \gamma_1 + b^2_2 \gamma_2) & 1 \end{bmatrix}, \quad (\text{A.21})$$

therefore the determinant reads

$$\det([z^\mu_\alpha]) = 1 - 2\xi^3 H + (\xi^3)^2 K, \quad (\text{A.22})$$

where we defined the shortcuts  $K = \det([b^\mu_\alpha])$  and  $H = -(b^1_1 + b^2_2)/2$ . Note that,  $K$  and  $H$ , for the case where  $\mathbf{t}$  is the midsurface normal, exactly boil down to the usual surface definitions of *Gaussian curvature* and *mean curvature*.

## A.8 Derivation of Local Shell Angular Momentum From Local Three-Dimensional Angular Momentum

Following Simo and Fox [SF89], the three-dimensional angular momentum  $\boldsymbol{\sigma}^T = \boldsymbol{\sigma}$  can also be investigated to derive an alternative version of the angular momentum for the shell. First the angular momentum condition implies  $\boldsymbol{\sigma} : \boldsymbol{\varepsilon} = j\sigma^{ij}\varepsilon_{ijk}\mathbf{g}^k = \sigma^{ij}\mathbf{g}_i \times \mathbf{g}_j = (\boldsymbol{\sigma}\mathbf{g}^j) \times \mathbf{g}_j = \mathbf{0}$ , where  $\boldsymbol{\varepsilon}$  is the Levi-Civita tensor from Eq. (2.92) on page 43 and the identity from Eq. (2.104) on page 46 was used. Then using  $\mathbf{g}_\alpha = \mathbf{a}_\alpha + \xi^3\mathbf{t}_{,\alpha}$ ,  $\mathbf{g}_3 = \mathbf{t}$  and integration through the thickness of  $\boldsymbol{\sigma}\mathbf{g}^j \times \mathbf{g}_j$  yields

$$\begin{aligned} \int_{h^-}^{h^+} z\boldsymbol{\sigma}\mathbf{g}^j \times \mathbf{g}_j d\xi^3 &= \int_{h^-}^{h^+} z\boldsymbol{\sigma}\mathbf{g}^\alpha \times (\mathbf{a}_\alpha + \xi^3\mathbf{t}_{,\alpha}) + z\boldsymbol{\sigma}\mathbf{g}^3 \times \mathbf{t} d\xi^3 = \mathbf{0} \\ &= \int_{h^-}^{h^+} z\boldsymbol{\sigma}\mathbf{g}^\alpha \times \mathbf{a}_\alpha + z\xi^3\boldsymbol{\sigma}\mathbf{g}^\alpha \times \xi^3\mathbf{t}_{,\alpha} + z\boldsymbol{\sigma}\mathbf{g}^3 \times \mathbf{t} d\xi^3 = \mathbf{0} \\ &= \mathbf{n}^\alpha \times \mathbf{a}_\alpha + \hat{\mathbf{m}} \times \mathbf{t}_{,\alpha} + \mathbf{l} \times \mathbf{t} = \mathbf{0} \end{aligned} \quad (\text{A.23})$$

where the definition of the stress resultants from Eqs. (5.39), (5.41) and (5.42) on page 103 were inserted. If we

$$\begin{aligned} \mathbf{a}_\alpha \times (n^{\beta\alpha}\mathbf{a}_\beta + q^\alpha\mathbf{t}) + \mathbf{t}_{,\alpha} \times (\hat{m}^{\beta\alpha}\mathbf{a}_\beta + \hat{m}^{3\alpha}\mathbf{t}) + \mathbf{t} \times \mathbf{l} &= \mathbf{0}, \\ \mathbf{a}_\alpha \times (n^{\beta\alpha}\mathbf{a}_\beta + q^\alpha\mathbf{t}) + (b^\mu_\alpha(\mathbf{a}_\mu - \gamma_\mu\mathbf{t})) \times (\hat{m}^{\beta\alpha}\mathbf{a}_\beta + \hat{m}^{3\alpha}\mathbf{t}) + \mathbf{t} \times \mathbf{l} &= \mathbf{0}, \\ \mathbf{a}_\alpha \times (n^{\beta\alpha}\mathbf{a}_\beta + q^\alpha\mathbf{t}) + (b^\mu_\alpha(\mathbf{a}_\mu - \gamma_\mu\mathbf{t})) \times (\hat{m}^{\beta\alpha}\mathbf{a}_\beta + \hat{m}^{3\alpha}\mathbf{t}) + \mathbf{t} \times \mathbf{l} &= \mathbf{0}, \\ n^{\beta\alpha}\mathbf{a}_\alpha \times \mathbf{a}_\beta + (q^\alpha\mathbf{a}_\alpha - \gamma_\mu b^\mu_\alpha \hat{m}^{\beta\alpha}\mathbf{t}) \times \mathbf{a}_\beta + \hat{m}^{\beta\alpha}b^\mu_\alpha \mathbf{a}_\mu \times \mathbf{a}_\beta + \hat{m}^{3\alpha}b^\mu_\alpha \mathbf{a}_\mu \times \mathbf{t} + \mathbf{t} \times \mathbf{l} &= \mathbf{0}, \\ n^{\beta\alpha}\mathbf{a}_\alpha \times \mathbf{a}_\beta + (q^\alpha\mathbf{a}_\alpha - \gamma_\mu b^\mu_\alpha \hat{m}^{\beta\alpha}\mathbf{t}) \times \mathbf{a}_\beta - \hat{m}^{\beta\alpha}b^\mu_\alpha \mathbf{a}_\beta \times \mathbf{a}_\mu + \hat{m}^{3\alpha}b^\mu_\alpha \mathbf{a}_\mu \times \mathbf{t} + \mathbf{t} \times \mathbf{l} &= \mathbf{0}, \\ n^{\beta\alpha}\mathbf{a}_\alpha \times \mathbf{a}_\beta + (q^\alpha\mathbf{a}_\alpha - \gamma_\mu b^\mu_\alpha \hat{m}^{\beta\alpha}\mathbf{t}) \times \mathbf{a}_\beta - \hat{m}^{\alpha\mu}b^\beta_\mu \mathbf{a}_\alpha \times \mathbf{a}_\beta + \hat{m}^{3\alpha}b^\mu_\alpha \mathbf{a}_\mu \times \mathbf{t} + \mathbf{t} \times \mathbf{l} &= \mathbf{0}, \\ (n^{\beta\alpha} - \hat{m}^{\alpha\mu}b^\beta_\mu)\mathbf{a}_\alpha \times \mathbf{a}_\beta + q^\alpha\mathbf{a}_\alpha \times \mathbf{t} - \gamma_\mu b^\mu_\alpha \hat{m}^{\beta\alpha}\mathbf{t} \times \mathbf{a}_\beta + \hat{m}^{3\alpha}b^\mu_\alpha \mathbf{a}_\mu \times \mathbf{t} + \mathbf{t} \times \mathbf{l} &= \mathbf{0}, \\ (n^{\beta\alpha} - \hat{m}^{\alpha\mu}b^\beta_\mu)\mathbf{a}_\alpha \times \mathbf{a}_\beta + \mathbf{t} \times (-q^\alpha\mathbf{a}_\alpha - \gamma_\mu b^\mu_\alpha \hat{m}^{\beta\alpha}\mathbf{a}_\beta - \hat{m}^{3\alpha}b^\mu_\alpha \mathbf{a}_\mu + \mathbf{l}) &= \mathbf{0}, \\ (n^{\beta\alpha} - \hat{m}^{\alpha\mu}b^\beta_\mu)\mathbf{a}_\alpha \times \mathbf{a}_\beta + \mathbf{t} \times (-q^\alpha\mathbf{a}_\alpha - \gamma_\mu b^\mu_\beta \hat{m}^{\alpha\beta}\mathbf{a}_\alpha - \hat{m}^{3\mu}b^\alpha_\mu \mathbf{a}_\alpha + \mathbf{l}) &= \mathbf{0}, \\ (n^{\beta\alpha} - \hat{m}^{\alpha\mu}b^\beta_\mu)\mathbf{a}_\alpha \times \mathbf{a}_\beta + \mathbf{t} \times (\mathbf{l} - (q^\alpha + \gamma_\mu b^\mu_\beta \hat{m}^{\alpha\beta} + \hat{m}^{3\mu}b^\alpha_\mu)\mathbf{a}_\alpha) &= \mathbf{0}. \end{aligned} \quad (\text{A.24})$$

Using the definition of the effective stress resultants Eq. (5.52) on page 106 yields

$$\tilde{n}^{\beta\alpha}\mathbf{a}_\alpha \times \mathbf{a}_\beta + \mathbf{t} \times (\mathbf{l} - (\tilde{q}^\alpha + \hat{m}^{3\mu}b^\alpha_\mu)\mathbf{a}_\alpha) = \mathbf{0}, \quad (\text{A.25})$$

and using the definition of the components of  $\mathbf{l}$  from Table 5.2 on page 109, we have

$$\begin{aligned}
\tilde{n}^{\beta\alpha} \mathbf{a}_\alpha \times \mathbf{a}_\beta + \mathbf{t} \times [(\tilde{l}^\alpha - (\tilde{q}^\alpha + \hat{m}^{3\mu} b_\mu^\alpha)) \mathbf{a}_\alpha + l^3 \mathbf{t}] &= \mathbf{0} \\
\tilde{n}^{\beta\alpha} \mathbf{a}_\alpha \times \mathbf{a}_\beta + \mathbf{t} \times [(\tilde{l}^\alpha - \tilde{q}^\alpha) \mathbf{a}_\alpha + l^3 \mathbf{t}] &= \mathbf{0} \\
\tilde{n}^{\beta\alpha} \mathbf{a}_\alpha \times \mathbf{a}_\beta + \mathbf{t} \times \mathbf{a}_\alpha (\tilde{l}^\alpha - \tilde{q}^\alpha) + l^3 \mathbf{t} \times \mathbf{t} &= \mathbf{0}
\end{aligned} \tag{A.26}$$

## A.9 The Potential Energy Given by Midsurface Quantities

Following Bařar and Krätzig [BK13, Eq. 3.5.5], the total energy can be given in terms of the midsurface quantities. This reads

$$\begin{aligned}
\Pi_{\text{int}}^{\text{membrane}} &= \frac{1}{2} \int_{\mathcal{B}_0^C} \frac{\bar{J}}{\det \bar{\mathbf{F}}} n^{\alpha\beta} \varepsilon_{\alpha\beta} da, \\
\Pi_{\text{int}}^{\text{bending}} &= \frac{1}{2} \int_{\mathcal{B}_0^C} \frac{\bar{J}}{\det \bar{\mathbf{F}}} \left( m^{\alpha\beta} \kappa_{\alpha\beta} + k^{\alpha\beta} \rho_{\alpha\beta} \right) da, \\
\Pi_{\text{int}}^{\text{shear}} &= \frac{1}{2} \int_{\mathcal{B}_0^C} \frac{\bar{J}}{\det \bar{\mathbf{F}}} q^\alpha \gamma_\alpha da,
\end{aligned} \tag{A.27}$$

where  $\mathbf{k} = k^{\alpha\beta} \mathbf{a}_\alpha \otimes \mathbf{a}_\beta = \int_{h^-}^{h^+} z(\xi^3)^2 \mathbf{t} \times \boldsymbol{\sigma} \cdot \mathbf{g}^\alpha d\xi^3$  are the additional second-order moments not given in Bařar and Krätzig [BK13, Eq. 3.5.5]. The other stress resultants are given in Eqs. (5.48) and (5.51) and the kinematic quantities in Eq. (5.30), where the given components need to be interpreted as defined in the midsurface basis. The sum of these quantities returns the total potential energy

$$\Pi_{\text{int}} = \Pi_{\text{int}}^{\text{membrane}} + \Pi_{\text{int}}^{\text{bending}} + \Pi_{\text{int}}^{\text{shear}}, \tag{A.28}$$

which is not necessarily the same energy as given in Eq. (5.144), since Eq. (A.27) assumes that the energies can be decoupled from each other in the derivation process of a potential energy defined through a material law in midsurface quantities. For a more detailed reasoning, see Bařar and Krätzig [BK13, Sec. 3.4.3].

## A.10 Solving the Local GFE Minimization Problem

For the geodesic finite element implementation the interpolation minimization problem of Eq. (6.43) on page 170 has to be solved at every integration point. Therefore, we

reformulate Eq. (6.43) on page 170 as

$$\begin{aligned} \mathbf{t}_{\text{GFE}} &= \arg \min_{\mathbf{t} \in \mathcal{S}^2} f(\mathbf{t}), \\ f(\mathbf{t}) &= \sum_{I=1}^n N^I(\xi^\alpha) \arccos^2(\mathbf{t}_I \cdot \mathbf{t}) \\ &= \sum_{I=1}^n N^I(\xi^\alpha) \alpha^2(\mathbf{t}_I \cdot \mathbf{t}), \end{aligned} \tag{A.29}$$

where we introduced the function  $\alpha(x) = \arccos^2(x)$  for a compact notation, similar to [San12; San16b]. For the solution of Eq. (A.29), we use a Riemannian Newton-Raphson scheme as proposed in [Abs08, Table 4.1, Chapter 6.2, Chapter 6.4.1] and we use a base transformation into the tangent space using stereographic projection.

For the construction of the Riemannian gradient and Riemannian Hessian [Abs08; Abs13] we need the Euclidean gradient and Euclidean Hessian, which can be straightforwardly constructed as

$$\text{grad } \bar{f}(\mathbf{t}) = \frac{\partial \bar{f}(\mathbf{t})}{\partial \mathbf{t}} = \sum_{I=1}^n N^I(\boldsymbol{\xi}) \alpha'(\mathbf{t}_I \cdot \mathbf{t}) \mathbf{t}_I, \tag{A.30}$$

$$\text{Hess } \bar{f}(\mathbf{t}) = \frac{\partial^2 \bar{f}(\mathbf{t})}{\partial t_i \partial t_j} = \sum_{I=1}^n N^I(\boldsymbol{\xi}) \alpha''(\mathbf{t}_I \cdot \mathbf{t}) \mathbf{t}_I \otimes \mathbf{t}_I. \tag{A.31}$$

$$\tag{A.32}$$

Here,  $\bar{f} : \mathbb{R}^3 \rightarrow \mathbb{R}$  is the Euclidean extension of the function  $f : \mathcal{S}^2 \rightarrow \mathbb{R}$ . The derivatives of  $\alpha(x)$  are

$$\alpha'(x) = \frac{-2 \arccos(x)}{\sqrt{1-x^2}}, \tag{A.33}$$

$$\alpha''(x) = \frac{2}{1-x^2} - \frac{2x \arccos(x)}{(1-x^2)^{3/2}}. \tag{A.34}$$

Near  $x = 1$  these expressions are unstable, and the Taylor expansions

$$\alpha'(x) = -2 + \frac{2}{3}(x-1) + \mathcal{O}((x-1)^2), \tag{A.35}$$

$$\alpha''(x) = \frac{2}{3} - \frac{8}{15}(x-1) + \mathcal{O}((x-1)^2), \tag{A.36}$$

are used instead. We took a tolerance of  $1\text{E} - 8$  to switch between the expansion and the exact formula. In this region, the error of both Taylor expansions is within machine precision.

These Euclidean quantities are then projected onto the tangent space  $\mathbf{\Lambda}$  of the director  $\mathbf{t}$ . This matrix corresponds to the tangent space of the director at the integration point, in contrast to, e.g., Section 5.6 on page 140, where the tangent space corresponds to the nodal directors. We end up with the following equations

$$\begin{aligned}\text{grad } f(\mathbf{t})_{2 \times 1} &= \mathbf{\Lambda}^T \text{grad } \bar{f}(\mathbf{t}), \\ \text{Hess } f(\mathbf{t})_{2 \times 2} &= \mathbf{\Lambda}^T \text{Hess } \bar{f}(\mathbf{t}) \mathbf{\Lambda} - \mathbf{t}^T \text{grad } \bar{f}(\mathbf{t}) \mathbf{I}_{2 \times 2}.\end{aligned}\tag{A.37}$$

These can then be used for the Riemannian Newton-Raphson scheme

$$\begin{aligned}\Delta \mathbf{T}^k &= -\text{Hess } f(\mathbf{t}^k)^{-1} \text{grad } f(\mathbf{t}^k), \\ \Delta \mathbf{t}^k &= \mathbf{\Lambda}^k \Delta \mathbf{T}^k, \\ \mathbf{t}^{k+1} &= R_{\mathbf{t}^k}(\Delta \mathbf{t}^k),\end{aligned}\tag{A.38}$$

where  $R_{\mathbf{t}^k}(\Delta \mathbf{t}^k)$  is again one of the retractions defined in Section 2.6 on page 33. As a predictor of the GFE director, we set the projection-based director, since these interpolations are close to each other if the difference between the nodal directors is small. More formally, if the nodal directors  $\mathbf{t}_I$  are contained in a ball of radius  $h \ll 1$ , the distance of the projection-based and GFE-based director can be bounded by  $h^3$ , as done in [Spr16, Chapter 1.4.3]. Therefore, we set the first iterate in Eq. (A.38) to

$$\mathbf{t}^0 = \frac{\sum_{I=1}^n N^I \mathbf{t}_I}{\|\sum_{I=1}^n N^I \mathbf{t}_I\|}.\tag{A.39}$$

Moreover, for the strains we need the partial derivatives of the director w.r.t  $\xi^\alpha$  for the curvature terms. Following a similar reasoning as in [San12], we can recast the gradient function in Eq. (A.37), evaluated at the converged state as

$$\Phi(\mathbf{t}_I; \xi^\alpha, \mathbf{t}_{\text{GFE}}(\mathbf{t}_I; \xi^\alpha)) := \text{grad } f(\mathbf{t}) \Big|_{\mathbf{t}=\mathbf{t}_{\text{GFE}}} = \mathbf{0}.\tag{A.40}$$

Taking the total derivative, we get

$$\begin{aligned}\frac{d}{d\xi^\alpha} \Phi(\mathbf{t}_I; \xi^\alpha, \mathbf{t}_{\text{GFE}}(\mathbf{t}_I; \xi^\alpha)) &= \frac{\partial \Phi(\mathbf{t}_I; \xi^\alpha, \mathbf{t}_{\text{GFE}})}{\partial \xi^\alpha} \\ &+ \frac{\partial \Phi(\mathbf{t}_I; \xi^\alpha, \mathbf{t}_{\text{GFE}})}{\partial \mathbf{t}_{\text{GFE}}} \frac{\partial \mathbf{t}_{\text{GFE}}}{\partial \xi^\alpha} = \mathbf{0}.\end{aligned}\tag{A.41}$$

Here, we can identify several quantities and end up with

$$\frac{\partial \Phi(\mathbf{t}_I; \xi^\alpha, \mathbf{t}_{\text{GFE}})}{\partial \xi^\alpha} = \mathbf{\Lambda}^T \sum_{I=1}^n N_{,\alpha}^I(\xi^\alpha) \alpha'(\mathbf{t}_I \cdot \mathbf{t}_{\text{GFE}}) \mathbf{t}_I, \quad (\text{A.42})$$

$$\frac{\partial \Phi(\mathbf{t}_I; \xi^\alpha, \mathbf{t}_{\text{GFE}})}{\partial \mathbf{t}_{\text{GFE}}} = \text{Hess } f(\mathbf{t}_{\text{GFE}}). \quad (\text{A.43})$$

This can then be summarized as

$$\begin{aligned} \text{Hess } f(\mathbf{t}_{\text{GFE}}) \mathbf{t}_{\text{GFE},\alpha} = \\ - \mathbf{\Lambda}^T \sum_{I=1}^n N_{,\alpha}^I(\xi^\alpha) \alpha'(\mathbf{t}_I \cdot \mathbf{t}_{\text{GFE}}) \mathbf{t}_I. \end{aligned} \quad (\text{A.44})$$

This  $2 \times 2$  linear system of equations can be solved for  $\mathbf{t}_{\text{GFE},\alpha}$ . Note, that  $\mathbf{t}_{\text{GFE},\alpha}$  has only two components in the  $\mathbf{\Lambda}$  base, and therefore we need to reconstruct the three-dimensional representation with  $\mathbf{\Lambda}$ .

## A.11 Assumed Natural Strain for Transverse Shear

The usage of the assumed natural strain method (ANS) for the alleviation of locking phenomena is well-established in the literature. For the alleviation of transverse shear locking in plates and shells, the origins can be found in the works of Bathe and Dvorkin [BD85a; BD85b; BD86]. The described method therein is restricted to bi-linear Q1 elements. Extensions to bi-quadratic Q2 elements or for improving the membrane strains can be found in [HH84; HH86; PS86] whereas Park and Stanley [PS86] have coined the term *assumed natural strains*. The method can be also used for other locking phenomena, such as curvature-thickness-locking, which was done in [BR97].

Nevertheless, the following is restricted to the alleviation of transverse shear locking. The basic idea of the ANS method is to assume strains, which do not contain *spurious strains*, that would lead to locking. For transverse shear, the construction used for the assumed transverse shear strain is as follows.

1. Evaluate the transverse shear strains  $\gamma_\alpha$  at the mid-points of the element edges.
2. Interpolate the transverse shear strains  $\gamma_\alpha$  with ansatz functions  $N$ , which yield a linear strain in one direction and constant in the other.
3. Replace the transverse shear strains  $\gamma_\alpha$  with the assumed transverse shear strains  $\hat{\gamma}_\alpha$  in all quantities.

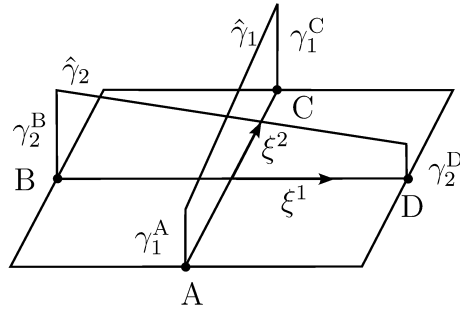


**Figure A.1:** Assumed natural strain collocation points A, B, C and D and the resulting strain functions  $\hat{\gamma}_1$  and  $\hat{\gamma}_2$ .

For a Q1 element, defined on the domain  $\Omega = [-1,1]^2$  the construction of the assumed transverse shear strain is done using the following formula

$$\begin{aligned}\hat{\gamma}_1 &= \frac{1}{2}(1 - \eta)\gamma_1^A + \frac{1}{2}(1 + \eta)\gamma_1^C, \\ \hat{\gamma}_2 &= \frac{1}{2}(1 - \xi)\gamma_2^B + \frac{1}{2}(1 + \xi)\gamma_2^D,\end{aligned}\tag{A.45}$$

which is also graphically depicted in Fig. A.1.





---

## Bibliography

- [Abr84] R. Abraham et al. *Manifolds, tensor analysis, and applications*. Vol. 37. 5. 1984, p. 86.
- [Abs08] P.-A. Absil, R. Mahony, and R. Sepulchre. *Optimization Algorithms on Matrix Manifolds*. Princeton University Press, 2008. DOI: 10.1515/9781400830244.
- [Abs13] P.-A. Absil, R. Mahony, and J. Trumpf. “An Extrinsic Look at the Riemannian Hessian”. In: *Geometric Science of Information*. Ed. by F. Nielsen and F. Barbaresco. Springer, 2013, pp. 361–368. DOI: 10.1007/978-3-642-40020-9\\_39.
- [Adl02] R. L. Adler et al. “Newton’s Method on Riemannian Manifolds and a Geometric Model for the Human Spine”. In: *IMA J Numer Anal* 22.3 (2002), pp. 359–390. DOI: 10.1093/imanum/22.3.359.
- [Ahm68] S. Ahmad, B. M. Irons, and O. C. Zienkiewicz. “Curved Thick Shell and Membrane Elements with Particular Reference to Axisymmetric Problems”. In: *Proceedings of the 2nd conference on matrix methods in structural mechanics*. 1968.
- [Ahr05] J. Ahrens et al. “ParaView: An end-user tool for large-data visualization”. In: *The visualization handbook* 717 (2005), pp. 50038–1.
- [Ant74] S. S. Antman. “Kirchhoff’s problem for nonlinearly elastic rods”. In: *Q Appl Math* 32.3 (1974), pp. 221–240.
- [Are13] P. Areias, T. Rabczuk, and D. Dias-da-Costa. “Assumed-metric spherically interpolated quadrilateral shell element”. In: *Finite Elem Anal Des* 66 (2013), pp. 53–67. DOI: 10.1016/j.finel.2012.11.006.
- [Arg78] J. Argyris, P. Dunne, and D. Scharpf. “On large displacement-small strain analysis of structures with rotational degrees of freedom”. In: *Comput Methods Appl Mech Eng* 14.3 (1978), pp. 401–451. DOI: 10.1016/0045-7825(78)90076-2.

- [Arg82] J. H. Argyris. “An excursion into large rotations”. In: *Comput Methods Appl Mech Eng* 32.1-3 (1982), pp. 85–155. DOI: 10.1016/0045-7825(82)90069-x.
- [Bau16] A. Bauer et al. “Nonlinear isogeometric spatial Bernoulli beam”. In: *Comput Methods Appl Mech Eng* 303 (2016), pp. 101–127.
- [BD85a] K.-J. Bathe and E. Dvorkin. “A formulation of general shell elements - The use of mixed interpolation of tensorial components”. In: *Proceedings of the NUMETA '85 Conference*. Swansea, 1985, pp. 551–563.
- [BD85b] K.-J. Bathe and E. Dvorkin. “A Four-Node Plate Bending Element Based on Mindlin/Reissner Theory and a Mixed Interpolation”. In: *Int J Numer Methods Eng* 21 (1985), pp. 367–383.
- [BD86] K.-J. Bathe and E. Dvorkin. “A formulation of general shell elements - the use of mixed interpolation of tensorial components”. In: *Int J Numer Methods Eng* 22 (1986), pp. 697–722.
- [Bel37] E. T. Bell. *Men of mathematics*. Simon and Schuster, 1937.
- [Bel84] T. Belytschko, J. I. Lin, and T. Chen-Shyh. “Explicit algorithms for the nonlinear dynamics of shells”. In: *Comput Methods Appl Mech Eng* 42.2 (1984), pp. 225–251. DOI: 10.1016/0045-7825(84)90026-4.
- [Bel91] B. Belhoste. *Augustin-Louis Cauchy: A Biography*. Springer New York, 1991. DOI: 10.1007/978-1-4612-2996-4. URL: <https://doi.org/10.1007/978-1-4612-2996-4>.
- [Bel92] T. Belytschko, B. L. Wong, and H.-Y. Chiang. “Advances in one-point quadrature shell elements”. In: *Comput Methods Appl Mech Eng* 96.1 (1992), pp. 93–107. DOI: 10.1016/0045-7825(92)90100-X.
- [Ben10] D. Benson et al. “Isogeometric shell analysis: the reissner–mindlin shell”. In: *Comput Methods Appl Mech Eng* 199.5-8 (2010), pp. 276–289. DOI: 10.1016/j.cma.2009.05.011.
- [Bet96] P. Betsch, F. Gruttmann, and E. Stein. “A 4-node finite shell element for the implementation of general hyperelastic 3D-elasticity at finite strains”. In: *Comput Methods Appl Mech Eng* (1996), pp. 57–79. DOI: 10.1016/0045-7825(95)00920-5.
- [Bet98] P. Betsch, A. Menzel, and E. Stein. “On the parametrization of finite rotations in computational mechanics A classification of concepts with application to smooth shells”. In: *Comput Methods Appl Mech Eng* (1998), p. 33. DOI: 10.1016/S0045-7825(97)00158-8.
- [Bio39] M. A. Biot. “Non-linear theory of elasticity and the linearized case for a body under initial stress”. In: *The London, Edinburgh, and Dublin Philosophical Magazine and Journal of Science* 27.183 (1939), pp. 468–489.

- [Bis17] M. Bischoff, E. Ramm, and J. Irslinger. “Models and Finite Elements for Thin-Walled Structures”. In: *Encyclopedia of Computational Mechanics Second Edition*. Ed. by value. John Wiley & Sons, Ltd, 2017, pp. 1–86. DOI: 10.1002/9781119176817.ecm2026.
- [Bis99] M. Bischoff. “Theorie und Numerik einer dreidimensionalen Schalenformulierung. Theory and numerics of a three-dimensional shell formulation”. Dissertation. Universität Stuttgart, 1999. DOI: 10.18419/opus-126. URL: <http://nbn-resolving.de/urn:nbn:de:bsz:93-opus-6046> (visited on 05/30/2023).
- [BJ16] P. Betsch and A. Janz. “An energy–momentum consistent method for transient simulations with mixed finite elements developed in the framework of geometrically exact shells”. In: *Int J Numer Methods Eng* 108.5 (2016), pp. 423–455.
- [BK13] Y. Başar and W. B. Krätzig. *Mechanik Der Flächentragwerke: Theorie, Berechnungsmethoden, Anwendungsbeispiele*. Springer-Verlag, 2013. DOI: 10.1007/978-3-322-93983-8.
- [Bou23] N. Boumal. *An introduction to optimization on smooth manifolds*. Cambridge University Press, 2023. DOI: 10.1017/9781009166164. URL: <https://www.nicolasboumal.net/book>.
- [BR92] N. Büchter and E. Ramm. “Shell theory versus degeneration—a comparison in large rotation finite element analysis”. In: *Int J Numer Methods Eng* 34.1 (1992), pp. 39–59. DOI: 10.1002/nme.1620340105.
- [BR97] M. Bischoff and E. Ramm. “Shear deformable shell elements for large strains and rotations”. In: *Int J Numer Methods Eng* 40.23 (Dec. 1997), pp. 4427–4449. DOI: 10.1002/(sici)1097-0207(19971215)40:23<4427::aid-nme268>3.0.co;2-9. URL: [https://doi.org/10.1002/\(sici\)1097-0207\(19971215\)40:23%3C4427::aid-nme268%3E3.0.co;2-9](https://doi.org/10.1002/(sici)1097-0207(19971215)40:23%3C4427::aid-nme268%3E3.0.co;2-9).
- [Bra07] D. Braess. *Finite elements: Theory, fast solvers, and applications in solid mechanics*. Cambridge University Press, 2007.
- [Bro12] L. Brouwer. “Über Abbildung von Mannigfaltigkeiten”. In: *Math Ann* 71 (1912), pp. 97–115. URL: <http://eudml.org/doc/158520>.
- [Bro66] W. F. J. Brown. *Magnetoelastic Interactions*. Vol. 9. Tracts in Natural Philosophy. New York: Springer-Verlag, 1966.
- [BS07] S. Brenner and R. Scott. *The mathematical theory of finite element methods*. Vol. 15. Springer Science & Business Media, 2007.
- [Büc92] N. Büchter. “Zusammenführung von Degenerationskonzept Und Schalentheorie Bei Endlichen Rotationen”. PhD thesis. Institut für Baustatik, Universität Stuttgart, 1992.

- [Cam99] D. H. van Campen. “Warner Tjardus Koiter. 16 June 1914–2 September 1997”. In: *Biographical Memoirs of Fellows of the Royal Society* 45 (1999), pp. 271–273. ISSN: 00804606. URL: <http://www.jstor.org/stable/770276> (visited on 06/15/2023).
- [Car19] S. Carroll. *Spacetime and geometry*. Cambridge University Press, 2019.
- [Cau27] A. Cauchy. *Exercices de mathématiques*. Vol. 2. De Bure Frères, 1827.
- [CC09] E. M. P. Cosserat and F. Cosserat. “Théorie des Corps déformables”. In: *Nature* 81.2072 (July 1909), pp. 67–67. ISSN: 1476-4687. DOI: 10.1038/081067a0. URL: <https://doi.org/10.1038/081067a0>.
- [CG88] A. Cardona and M. Geradin. “A beam finite element non-linear theory with finite rotations”. In: *Int J Numer Methods Eng* 26.11 (1988), pp. 2403–2438.
- [Chi44] W.-Z. Chien. “The Intrinsic Theory of Thin Shells and Plates. I. General Theory”. In: *Q Appl Math* 1.4 (1944), pp. 297–327. DOI: 10.1090/qam/9744.
- [Chr69] E. Christoffel. “Ueber die Transformation der homogenen Differentialausdrücke zweiten Grades.” ger. In: *Journal für die reine und angewandte Mathematik* 70 (1869), pp. 46–70. URL: <http://eudml.org/doc/148073>.
- [Cia02] P. G. Ciarlet. *The Finite Element Method for Elliptic Problems*. Society for Industrial and Applied Mathematics, 2002. DOI: 10.1137/1.9780898719208.
- [CJ99] M. A. Crisfield and G. Jelenić. “Objectivity of strain measures in the geometrically exact three-dimensional beam theory and its finite-element implementation”. In: *Proc Math Phys Eng Sci* 455.1983 (1999), pp. 1125–1147. DOI: 10.1098/rspa.1999.0352.
- [CN63] B. Coleman and W. Noll. “The thermodynamics of elastic materials with heat conduction and viscosity”. In: *Arch Ration Mech Anal* 13.1 (Dec. 1963), pp. 167–178. DOI: 10.1007/bf01262690. URL: <https://doi.org/10.1007/bf01262690>.
- [Cri90] M. A. Crisfield. “A Consistent Co-rotational Formulation for Non-linear, Three-dimensional, Beam-elements”. In: *Comput Methods Appl Mech Eng* 81 (1990), pp. 131–150.
- [dC92] M. P. do Carmo. *Riemannian Geometry*. Ed. by R. V. Kadison and I. M. Singer. Mathematics. Theory & Applications. Boston, Basel, Berlin: Birkhäuser, 1992.
- [Dor13] W. Dornisch, S. Klinkel, and B. Simeon. “Isogeometric reissner–mindlin shell analysis with exactly calculated director vectors”. In: *Comput Methods Appl Mech Eng* 253 (2013), pp. 491–504. DOI: 10.1016/j.cma.2012.09.010.

- [Dor16] W. Dornisch, R. Müller, and S. Klinkel. “An efficient and robust rotational formulation for isogeometric reissner–mindlin shell elements”. In: *Comput Methods Appl Mech Eng* 303 (2016), pp. 1–34. DOI: 10.1016/j.cma.2016.01.018.
- [EM00] N. El-Abbasi and S. A. Meguid. “A new shell element accounting for through-thickness deformation”. In: *Comput Methods Appl Mech Eng* 189.3 (2000), pp. 841–862. DOI: 10.1016/S0045-7825(99)00348-5.
- [Fed15] S. Federico. “Some remarks on metric and deformation”. In: *Math Mech Solids* 20.5 (2015), pp. 522–539. DOI: 10.1177/1081286513506432. eprint: <https://doi.org/10.1177/1081286513506432>. URL: <https://doi.org/10.1177/1081286513506432>.
- [Fin94] J. Finger. “Über die allgemeinsten Beziehungen zwischen den Deformationen und den zugehörigen Spannungen in aerotropen und isotropen Substanzen”. In: *Sitzber Akad Wiss Wien (2a)* 103 (1894), pp. 1073–1100.
- [Fre14] A. D. Freed. *Soft Solids*. Modeling and Simulation in Science, Engineering and Technology. Cham: Springer International Publishing, 2014. ISBN: 978-3-319-03551-2. DOI: 10.1007/978-3-319-03551-2. URL: <http://link.springer.com/10.1007/978-3-319-03551-2> (visited on 01/05/2023).
- [Gal15] B. Galerkin. “Beams and plates”. In: *Vestnik Ingenerov* 19 (1915). Series in some questions of elastic equilibrium of beams and plates (in Russian), pp. 897–908.
- [Gal90] S. Gallot, D. Hulin, and J. Lafontaine. *Riemannian Geometry*. en. 2nd ed. Universitext. Berlin ; New York: Springer-Verlag, 1990.
- [Gre48] G. Green. “On the propagation of light in crystallized media”. In: *Transactions of the Cambridge Philosophical Society* 7 (1848), p. 121. URL: <http://www.scienzadellecostruzioni.co.uk/Documenti/Green%5C%20-%5C%20On%5C%20the%5C%20propagation%5C%20of%5C%20light.pdf>.
- [Gre65] A. E. Green, P. M. Naghdi, and W. L. Wainwright. “A general theory of a Cosserat surface”. In: *Arch Ration Mech Anal* 20.4 (Jan. 1965), pp. 287–308. ISSN: 1432-0673. DOI: 10.1007/BF00253138. URL: <https://doi.org/10.1007/BF00253138>.
- [Gre71] A. E. Green, P. M. Naghdi, and M. L. Wenner. “Linear theory of Cosserat surface and elastic plates of variable thickness”. In: *Mathematical Proceedings of the Cambridge Philosophical Society* 69.1 (1971), pp. 227–254. DOI: 10.1017/S0305004100046582.

- [Gro11] P. Grohs. *Finite elements of arbitrary order and quasiinterpolation for data in Riemannian manifolds*. Tech. rep. 2011-56. Seminar for Applied Mathematics, ETH Zürich, 2011. URL: [https://www.sam.math.ethz.ch/sam%5C\\_reports/reports%5C\\_final/reports2011/2011-56.pdf](https://www.sam.math.ethz.ch/sam%5C_reports/reports%5C_final/reports2011/2011-56.pdf).
- [Gro15] P. Grohs, H. Hardering, and O. Sander. “Optimal A Priori Discretization Error Bounds for Geodesic Finite Elements”. In: *Found Comut Math* 15.6 (2015), pp. 1357–1411. DOI: 10.1007/s10208-014-9230-z.
- [Gro19] P. Grohs et al. “Projection-Based Finite Elements for Nonlinear Function Spaces”. In: *SIAM J Numer Anal* 57.1 (2019), pp. 404–428. DOI: 10.1137/18M1176798.
- [Gru00] F. Gruttmann, R. Sauer, and W. Wagner. “Theory and numerics of three-dimensional beams with elastoplastic material behaviour”. In: *Int J Numer Methods Eng* 48.12 (2000), pp. 1675–1702. DOI: 10.1002/1097-0207(20000830)48:12<1675::AID-NME957>3.0.CO;2-6.
- [Gru89] F. Gruttmann, E. Stein, and P. Wriggers. “Theory and Numerics of Thin Elastic Shells with Finite Rotations”. In: *Arch Appl Mech* 59.1 (1989), pp. 54–67. DOI: 10.1007/BF00536631.
- [GZ63] A. E. Green and W. Zerna. *Theoretical Elasticity*. Second Edition. Oxford, England: Carrendon Press, 1963, 1963. URL: [libgen.li/file.php?md5=7f4c658385e82bcb7c97790f8a4a6d0a](http://libgen.li/file.php?md5=7f4c658385e82bcb7c97790f8a4a6d0a).
- [Har15] H. Hardering. “Intrinsic Discretization Error Bounds for Geodesic Finite Elements”. PhD thesis. Mathematisches Institut, Fachbereich Mathematik und Informatik, Freie Universität Berlin, 2015. DOI: 10.17169/refubium-15367.
- [Har18] H. Hardering. “ $L^2$ -Discretization Error Bounds for Maps into Riemannian Manifolds”. en. In: *Numer Math (Heidelb)* 139.2 (2018), pp. 381–410. ISSN: 0029-599X, 0945-3245. DOI: 10.1007/s00211-017-0941-3.
- [Har21] J. Harsch, G. Capobianco, and S. R. Eugster. “Finite element formulations for constrained spatial nonlinear beam theories”. In: *Math Mech Solids* 26.12 (2021), pp. 1838–1863. DOI: 10.1177/10812865211000790.
- [Hen28] H. Hencky. “Über die Form des Elastizitätsgesetzes bei ideal elastischen Stoffen”. In: *Zeit Tech Phys* 9 (1928), pp. 215–220.
- [HH84] H. C. Huang and E. Hinton. “A nine node Lagrangian Mindlin plate element with enhanced shear interpolation”. In: *Engineering Computations* 1 (1984), pp. 369–379.

- [HH86] H. C. Huang and E. Hinton. “A new nine node degenerated shell element with enhanced membrane and shear interpolation”. In: *Int J Numer Methods Eng* 22 (1986), pp. 73–92.
- [Hil68] R. Hill. “On constitutive inequalities for simple materials–I”. In: *Journal of the Mechanics and Physics of Solids* 16.4 (1968), pp. 229–242. ISSN: 0022-5096. DOI: [https://doi.org/10.1016/0022-5096\(68\)90031-8](https://doi.org/10.1016/0022-5096(68)90031-8). URL: <https://www.sciencedirect.com/science/article/pii/0022509668900318>.
- [HL81] T. J. Hughes and W. K. Liu. “Nonlinear Finite Element Analysis of Shells: Part I. Three-Dimensional Shells”. In: *Comput Methods Appl Mech Eng* 26.3 (1981), pp. 331–362. DOI: 10.1016/0045-7825(81)90121-3.
- [Hol02] G. A. Holzapfel. “Nonlinear solid mechanics: a continuum approach for engineering science”. In: *Meccanica* 37.4 (2002), pp. 489–490.
- [HP78] T. J. Hughes and K. S. Pister. “Consistent linearization in mechanics of solids and structures”. In: *Computers & Structures* 8.3 (1978), pp. 391–397. ISSN: 0045-7949. DOI: [https://doi.org/10.1016/0045-7949\(78\)90183-9](https://doi.org/10.1016/0045-7949(78)90183-9). URL: <https://www.sciencedirect.com/science/article/pii/0045794978901839>.
- [HS20] H. Hardering and O. Sander. “Geometric Finite Elements”. en. In: *Handbook of Variational Methods for Nonlinear Geometric Data*. Ed. by P. Grohs, M. Holler, and A. Weinmann. Cham: Springer International Publishing, 2020, pp. 3–49. ISBN: 978-3-030-31351-7. DOI: 10.1007/978-3-030-31351-7\_1.
- [Hua17] W. Huang. *Introduction to Riemannian BFGS Methods*. accessed May 29, 2020. 2017. URL: [https://www.math.fsu.edu/~whuang2/pdf/SIAM%5C\\_OP17%5C\\_slides.pdf](https://www.math.fsu.edu/~whuang2/pdf/SIAM%5C_OP17%5C_slides.pdf).
- [Hug05] T. J. R. Hughes, J. A. Cottrell, and Y. Bazilevs. “Isogeometric Analysis: CAD, finite elements, NURBS, exact geometry and mesh refinement”. In: *Comput Methods Appl Mech Eng* 194.39–41 (2005), pp. 4135–4195. DOI: 10.1016/j.cma.2004.10.008.
- [Ibr95] A. Ibrahimbegović, F. Frey, and I. Kožar. “Computational aspects of vector-like parametrization of three-dimensional finite rotations”. In: *Int J Numer Methods Eng* 38.21 (1995), pp. 3653–3673. DOI: <https://doi.org/10.1002/nme.1620382107>. eprint: <https://onlinelibrary.wiley.com/doi/pdf/10.1002/nme.1620382107>. URL: <https://onlinelibrary.wiley.com/doi/abs/10.1002/nme.1620382107>.
- [IT02] A. Ibrahimbegovic and R. L. Taylor. “On the Role of Frame-Invariance in Structural Mechanics Models at finite Rotations”. In: *Comput Methods Appl Mech Eng* (2002), p. 18. DOI: 10.1016/S0045-7825(02)00442-5.

- [Jet86] P. Jetteur. “Implicit integration algorithm for elastoplasticity in plane stress analysis”. In: *Engineering Computations* 3.3 (Jan. 1986), pp. 251–253. ISSN: 0264-4401. DOI: 10.1108/eb023664. URL: <https://doi.org/10.1108/eb023664>.
- [Jeu12] B. Jeuris, R. Vandebril, and B. Vandereycken. “A Survey And Comparison Of Contemporary Algorithms For Computing The Matrix Geometric Mean”. In: *Electronic transactions on numerical analysis ETNA* 39 (Jan. 2012), pp. 379–402.
- [JM99] B. Jamtveit and P. Meakin. “Growth, dissolution and pattern formation in geosystems”. In: *Growth, Dissolution and Pattern Formation in Geosystems*. Springer, 1999, pp. 1–19.
- [JW08] J. Bonet and R. Wood. *Nonlinear Continuum Mechanics for Finite Element Analysis*. Second Edition. Cambridge University Press, Mar. 2008. DOI: 10.1017/cbo9780511755446. URL: <https://doi.org/10.1017/cbo9780511755446>.
- [KG02] S. Klinkel and S. Govindjee. “Using finite strain 3D-material models in beam and shell elements”. In: *Engineering Computations* 19.3 (2002), pp. 254–271.
- [Kie10] J. Kiendl et al. “The bending strip method for isogeometric analysis of Kirchhoff-Love shell structures comprised of multiple patches”. In: *Comput Methods Appl Mech Eng* 199 (Aug. 2010), pp. 2403–2416. DOI: 10.1016/j.cma.2010.03.029.
- [Kir50] G. Kirchhoff. “Über das Gleichgewicht und die Bewegung einer elastischen Scheibe.” In: *Journal für die reine und angewandte Mathematik (Crelles Journal)* 1850.40 (1850), pp. 51–88. DOI: doi:10.1515/crll.1850.40.51. URL: <https://doi.org/10.1515/crll.1850.40.51>.
- [Kir52] G. R. Kirchhoff. “Über die Gleichungen des Gleichgewichtes eines elastischen Körpers bei nicht unendlich kleinen Verschiebungen seiner Theile”. In: *Sitzungsberichte der Mathematisch-Naturwissenschaftlichen Classe der Kaiserlichen Akademie der Wissenschaften in Wien IX* (1852).
- [Kro95] Kronecker, Leopold. *Leopold Kronecker’s Werke*. de. Druck und Verlag von B.G. Teubner, 1895. DOI: 10.3931/E-RARA-17875. URL: <https://www.e-rara.ch/zut/doi/10.3931/e-rara-17875>.
- [Lam52] G. Lamé. *Leçons sur la théorie mathématique de l’élasticité des corps solides*. Bachelier, 1852.
- [Lee03] J. Lee. *Introduction to Smooth Manifolds*. Graduate Texts in Mathematics. Springer, 2003. ISBN: 9780387954486. URL: <https://books.google.de/books?id=eqfgZtjQceYC>.



- 
- [Lev16] M. d. T. Levi-Civita. *Nozione di parallelismo in una varietà qualunque e conseguente specificazione geometrica della curvatura riemanniana*. Dec. 1916. DOI: 10.1007/bf03014898. URL: <https://doi.org/10.1007/bf03014898>.
- [Liv19] Livermore Software Technology Corporation (LSTC). *LS-DYNA Theory Manual*. r11261 ed. 2019.
- [LL35] L. D. Landau and E. Lifshitz. “On the theory of the dispersion of magnetic permeability in ferromagnetic bodies”. In: *Phys Z Sowjet* 8 (1935), p. 153. URL: <https://cds.cern.ch/record/437299>.
- [Llo97] D. B. I. Lloyd N. Trefethen. *Numerical linear algebra*. Society for Industrial and Applied Mathematics, 1997.
- [Lon12] Q. Long, P. Burkhard Bornemann, and F. Cirak. “Shear-Flexible Subdivision Shells”. In: *Int J Numer Methods Eng* 90.13 (2012), pp. 1549–1577. DOI: 10.1002/nme.3368.
- [Lov88] A. E. H. Love. “The Small Free Vibrations and Deformation of a Thin Elastic Shell”. In: *Philos Trans R Soc London, Ser A* 179 (1888), pp. 491–546. ISSN: 02643820. URL: <http://www.jstor.org/stable/90527> (visited on 02/17/2023).
- [LS83] A. Libai and J. G. Simmonds. “Nonlinear elastic shell theory”. In: *Advances in Applied Mechanics*. Advances in applied mechanics. Elsevier, 1983, pp. 271–371.
- [Lue72] D. G. Luenberger. “The Gradient Projection Method Along Geodesics”. In: *Management Science* 18.11 (1972), pp. 620–631. DOI: 10.1287/mnsc.18.11.620. eprint: <https://doi.org/10.1287/mnsc.18.11.620>. URL: <https://doi.org/10.1287/mnsc.18.11.620>.
- [Lue73] D. G. Luenberger. *Introduction to linear and nonlinear programming*. Ed. by D. G. [ Luenberger. Reading, Mass. [u.a.]: Addison-Wesley, 1973, XII, 356 Seiten. ISBN: 0-201-04347-5.
- [MB22] A. Müller and M. Bischoff. “A Consistent Finite Element Formulation of the Geometrically Non-linear Reissner-Mindlin Shell Model”. In: *Arch Comput Methods Eng* 29.5 (Jan. 2022), pp. 3387–3434. DOI: 10.1007/s11831-021-09702-7. URL: <https://doi.org/10.1007/s11831-021-09702-7>.
- [Mei19] C. Meier, A. Popp, and W. A. Wall. “Geometrically exact finite element formulations for slender beams: Kirchhoff–Love theory versus Simo–Reissner theory”. In: *Arch Comput Methods Eng* 26.1 (2019), pp. 163–243.
- [MH94] J. Marsden and T. Hughes. *Mathematical Foundations of Elasticity*. Dover Civil and Mechanical Engineering Series. Dover, 1994. ISBN: 978-0486678658. URL: <https://books.google.de/books?id=STyKAAAQBAJ>.

- [Min51] R. Mindlin. “Influence of rotatory inertia and shear on flexural motions of isotropic, elastic plates”. In: *Journal of Applied Mechanics* (1951).
- [Mis73] C. Misner, K. Thorne, and J. Wheeler. *Gravitation*. Gravitation Teil 3. W. H. Freeman, 1973. ISBN: 9780716703440. URL: <https://books.google.de/books?id=w4Gigq3tY1kC>.
- [MS95] J. Makowski and H. Stumpf. “On the symmetry of tangent operators in nonlinear mechanics”. In: *Z Angew Math Mech* 75.3 (1995), pp. 189–198. DOI: 10.1002/zamm.19950750303.
- [Mun00] J. R. Munkres. *Topology*. Vol. 2. Prentice Hall Upper Saddle River, 2000.
- [Mün07] I. Münch. *Ein geometrisch und materiell nichtlineares Cosserat-Modell - Theorie, Numerik und Anwendungsmöglichkeiten*. de. 2007. DOI: 10.5445/IR/1000007371.
- [Nag73] P. M. Naghdi. “The Theory of Shells and Plates”. In: *Linear Theories of Elasticity and Thermoelasticity: Linear and Nonlinear Theories of Rods, Plates, and Shells*. Ed. by C. Truesdell. Berlin, Heidelberg: Springer Berlin Heidelberg, 1973, pp. 425–640. ISBN: 978-3-662-39776-3. DOI: 10.1007/978-3-662-39776-3\_5. URL: [https://doi.org/10.1007/978-3-662-39776-3\\_5](https://doi.org/10.1007/978-3-662-39776-3_5).
- [Nav21] C.-L. Navier. “Mémoire sur les lois de l’équilibre et du mouvement des corps élastiques”. In: *Mémoires de l’Acad* (1821).
- [Nee21] T. Needham. *Visual Differential Geometry and Forms: A Mathematical Drama in Five Acts*. Princeton University Press, 2021.
- [Nol55] W. Noll. “On the Continuity of the Solid and Fluid States”. In: *Indiana University Mathematics Journal* 4 (1955), pp. 3–81.
- [Oes17] B. Oesterle et al. “Hierarchic Isogeometric Large Rotation Shell Elements Including Linearized Transverse Shear Parametrization”. In: *Comput Methods Appl Mech Eng* 321 (2017), pp. 383–405. DOI: 10.1016/j.cma.2017.03.031.
- [Ogd97] R. W. Ogden. *Non-linear elastic deformations*. Mineola, N.Y: Dover Publications, 1997. 532 pp. ISBN: 978-0-486-69648-5.
- [ONe83] B. O’Neill. *Semi-Riemannian Geometry With Applications to Relativity*. ISSN. Elsevier Science, 1983. ISBN: 9780080570570. URL: <https://books.google.de/books?id=CGk1eRSjFIIC>.
- [OO84] J. Oliver and E. Onāte. “A Total Lagrangian Formulation for the Geometrically Nonlinear Analysis of Structures Using Finite Elements. Part I. Two-Dimensional Problems: Shell and Plate Structures”. In: *Int J Numer Methods Eng* 20.12 (1984), pp. 2253–2281. DOI: 10.1002/nme.1620201208.

- [Pie79a] W. Pietraszkiewicz. “Consistent second approximation to the elastic strain energy of a shell”. In: *Z Angew Math Mech* 59 (1979), pp. 206–208.
- [Pie79b] W. Pietraszkiewicz. *Finite rotations and Lagrangian description in the non-linear theory of shells*. Warsaw-Poznan: Polish Scientific Publishers, 1979.
- [Pio33] G. Piola. *La meccanica de’corpi naturalmente estesi trattata col calcolo delle variazioni*. Presso Paolo Emilio Giusti, 1833.
- [Por17] D. Portillo et al. “MUESLI - a Material UnivErSal LIbrary”. In: *Adv Eng Software* 105 (Mar. 2017), pp. 1–8. ISSN: 0965-9978. DOI: 10.1016/j.advensoft.2017.01.007. (Visited on 06/29/2023).
- [PS86] K. C. Park and G. M. Stanley. “A curved C0 shell element based on assumed natural coordinate strains”. In: *Int J Numer Methods Eng* 53 (1986), pp. 278–290.
- [PT95] L. Piegl and W. Tiller. *The NURBS Book*. Springer Berlin Heidelberg, 1995. DOI: 10.1007/978-3-642-97385-7. URL: <https://doi.org/10.1007/978-3-642-97385-7>.
- [RA02] I. Romero and F. Armero. “An objective finite element approximation of the kinematics of geometrically exact rods and its use in the formulation of an energy–momentum conserving scheme in dynamics”. In: *Int J Numer Methods Eng* 54.12 (2002), pp. 1683–1716. DOI: <https://doi.org/10.1002/nme.486>. eprint: <https://onlinelibrary.wiley.com/doi/pdf/10.1002/nme.486>. URL: <https://onlinelibrary.wiley.com/doi/abs/10.1002/nme.486>.
- [RA17] I. Romero and M. Arnold. “Computing with Rotations: Algorithms and Applications”. In: *Encyclopedia of Computational Mechanics Second Edition*. Ed. by E. Stein, R. de Borst, and T. J. R. Hughes. 2017, pp. 1–27. DOI: 10.1002/9781119176817.ecm2119.
- [Ram02] E. Ramm, E. Schunck, and H. Isler. *Heinz Isler, Schalen: Katalog zur Ausstellung*. vdf Hochschulverlag AG, 2002.
- [Ram76] E. Ramm. “Geometrisch Nichtlineare Elastostatik Und Finite Elemente”. Habilitation. University of Stuttgart, 1976.
- [Ram77] E. Ramm. “A plate/shell element for large deflections and rotations”. In: *Formulations and computational algorithms in finite element analysis* (1977), pp. 264–293.
- [Ran51] W. Rankine. “Laws of the elasticity of solid bodies”. In: *Cambridge and Dublin Mathematical Journal* 6 (1851), pp. 47–80.
- [Ran53] W. J. M. Rankine. “XVIII. On the general law of the transformation of energy”. In: *The London, Edinburgh, and Dublin Philosophical Magazine and Journal of Science* 5.30 (1853), pp. 106–117.

- [Ray15] D. Ray. *Computation of Nonlinear Structures: Extremely Large Elements for Frames, Plates and Shells*. John Wiley & Sons, 2015.
- [Rei13] K. Reich. *Die Entwicklung des Tensorkalküls: vom absoluten Differentialkalkül zur Relativitätstheorie*. Vol. 11. Springer-Verlag, 2013.
- [Rei45] E. Reissner. “The effect of transverse shear deformation on the bending of elastic plates”. In: *J Appl Mech* (1945).
- [Rep17] S. Repin. “One Hundred Years of the Galerkin Method”. In: *Comput Methods Appl Math* 17.3 (2017), pp. 351–357. DOI: doi:10.1515/cmam-2017-0013. URL: <https://doi.org/10.1515/cmam-2017-0013>.
- [Rie76] B. Riemann. *Bernhard Riemann’s gesammelte mathematische Werke und wissenschaftlicher Nachlass*. BG Teubner, 1876.
- [Rit09] W. Ritz. “Über eine neue Methode zur Lösung gewisser Variationsprobleme der mathematischen Physik.” ger. In: *Journal für die reine und angewandte Mathematik* 135 (1909), pp. 1–61. URL: <http://eudml.org/doc/149295>.
- [Rom04] I. Romero. “The Interpolation of Rotations and Its Application to Finite Element Models of Geometrically Exact Rods”. In: *Comput Mech* 34.2 (2004). DOI: 10.1007/s00466-004-0559-z.
- [Rom05] G. Romano, M. Diaco, and C. Sellitto. “Tangent Stiffness of Elastic Continua on Manifolds”. In: *Trends and Applications of Mathematics to Mechanics*. Ed. by S. Rionero and G. Romano. 2005, pp. 155–184. DOI: 10.1007/88-470-0354-7\\_14.
- [Ros60] J. B. Rosen. “The Gradient Projection Method for Nonlinear Programming. Part I. Linear Constraints”. In: *SIAM* 8.1 (1960), pp. 181–217. DOI: 10.1137/0108011.
- [Ros61] J. B. Rosen. “The Gradient Projection Method for Nonlinear Programming. Part II. Nonlinear Constraints”. In: *SIAM* 9.4 (1961), pp. 514–532. DOI: 10.1137/0109044.
- [SA92] J. C. Simo and F. Armero. “Geometrically non-linear enhanced strain mixed methods and the method of incompatible modes”. In: *Int J Numer Methods Eng* 33.7 (May 1992), pp. 1413–1449. DOI: 10.1002/nme.1620330705. URL: <https://doi.org/10.1002/nme.1620330705>.
- [San10] O. Sander. “Geodesic finite elements for Cosserat rods”. In: *Int J Numer Methods Eng* 82.13 (2010), pp. 1645–1670. DOI: 10.1002/nme.2814.
- [San12] O. Sander. “Geodesic finite elements on simplicial grids”. In: *Int J Numer Methods Eng* 92.12 (2012), pp. 999–1025. DOI: 10.1002/nme.4366.

- 
- [San15] O. Sander. “Geodesic Finite Elements of Higher Order”. In: *IMA J Numer Anal* (2015). DOI: 10.1093/imanum/drv016.
- [San16a] O. Sander. *Test Function Spaces for Geometric Finite Elements*. 2016. arXiv: 1607.07479 [math.NA].
- [San16b] O. Sander, P. Neff, and M. Bîrsan. “Numerical treatment of a geometrically nonlinear planar Cosserat shell model”. In: *Comput Mech* 57.5 (2016), pp. 817–841. DOI: 10.1007/s00466-016-1263-5.
- [SB93] S. Schoenfeld and D. Benson. “Quickly convergent integration methods for plane stress plasticity”. In: *Commun Numer Methods Eng* 9.4 (Apr. 1993), pp. 293–305. DOI: 10.1002/cnm.1640090403. URL: <https://doi.org/10.1002/cnm.1640090403>.
- [Sei73] J. Seidel. “Beitrag Zur Geometrisch Nichtlinearen Theorie Dünner Schalen Unter Annahme Kleiner Verzerrungen Und Grosser Rotationen”. PhD thesis. Institut für Baustatik, 1973.
- [Set64] B. R. Seth. *Generalized strain measure with applications to physical problems*. Ed. by A. M. and D. In: Reiner, 1964, pp. 162–172.
- [SF89] J. C. Simo and D. D. Fox. “On a stress resultant geometrically exact shell model. Part I: formulation and optimal parametrization”. In: *Comput Methods Appl Mech Eng* 72.3 (1989), pp. 267–304. DOI: 10.1016/0045-7825(89)90002-9.
- [SG88] J. C. Simo and S. Govindjee. “Exact closed-form solution of the return mapping algorithm in plane stress elasto-viscoplasticity”. In: *Engineering Computations* 5.3 (Jan. 1988), pp. 254–258. ISSN: 0264-4401. DOI: 10.1108/eb023744. URL: <https://doi.org/10.1108/eb023744>.
- [SH15] S. Sra and R. Hosseini. “Conic Geometric Optimisation on the Manifold of Positive Definite Matrices”. In: *SIAM J Optim* 25.1 (Jan. 2015), pp. 713–739. ISSN: 1052-6234, 1095-7189. DOI: 10.1137/140978168. arXiv: 1312.1039.
- [Sim85] J. C. Simo. “A finite strain beam formulation. The three-dimensional dynamic problem. Part I”. In: *Comput Methods Appl Mech Eng* 49.1 (1985), pp. 55–70. DOI: 10.1016/0045-7825(85)90050-7.
- [Sim89] J. C. Simo, D. D. Fox, and M. S. Rifai. “On a Stress Resultant Geometrically Exact Shell Model. Part II: the Linear Theory; computational Aspects”. In: *Comput Methods Appl Mech Eng* 73.1 (1989), pp. 53–92. DOI: 10.1016/0045-7825(89)90098-4.
- [Sim90a] J. C. Simo, D. D. Fox, and M. S. Rifai. “On a Stress Resultant Geometrically Exact Shell Model. Part III: Computational Aspects of the Nonlinear Theory”. In: *Comput Methods Appl Mech Eng* 79.1 (1990), pp. 21–70. DOI: 10.1016/0045-7825(90)90094-3.

- [Sim90b] J. C. Simo, M. S. Rifai, and D. D. Fox. “On a stress resultant geometrically exact shell model. Part IV: Variable thickness shells with through-the-thickness stretching”. In: *Comput Methods Appl Mech Eng* 81.1 (1990), pp. 91–126. ISSN: 0045-7825. DOI: [https://doi.org/10.1016/0045-7825\(90\)90143-A](https://doi.org/10.1016/0045-7825(90)90143-A). URL: <https://www.sciencedirect.com/science/article/pii/004578259090143A>.
- [Sim92a] J. C. Simo. “The (Symmetric) Hessian for Geometrically Nonlinear Models in Solid Mechanics: Intrinsic Definition and Geometric Interpretation”. In: *Comput Methods Appl Mech Eng* 96.2 (1992), pp. 189–200. DOI: 10.1016/0045-7825(92)90131-3.
- [Sim92b] J. C. Simo, M. S. Rifai, and D. D. Fox. “On a Stress Resultant Geometrically Exact Shell Model. Part VI: Conserving Algorithms for Non-Linear Dynamics”. In: *Int J Numer Methods Eng* 34.1 (1992), pp. 117–164. DOI: 10.1002/nme.1620340108.
- [SK92] J. C. Simo and J. G. Kennedy. “On a stress resultant geometrically exact shell model. Part V. Nonlinear plasticity: formulation and integration algorithms”. In: *Comput Methods Appl Mech Eng* 96.2 (1992), pp. 133–171. ISSN: 0045-7825. DOI: [https://doi.org/10.1016/0045-7825\(92\)90129-8](https://doi.org/10.1016/0045-7825(92)90129-8). URL: <https://www.sciencedirect.com/science/article/pii/0045782592901298>.
- [SM84] J. C. Simo and J. E. Marsden. “On the rotated stress tensor and the material version of the Doyle-Ericksen formula”. In: *Arch Ration Mech Anal* 86.3 (1984), pp. 213–231.
- [Sok56] I. S. Sokolnikoff. *Mathematical theory of elasticity*. Vol. 83. McGraw-Hill New York, 1956.
- [SP22] S. Srinivasan and N. Panda. “What is the gradient of a scalar function of a symmetric matrix?” In: *Indian J Pure Appl Math I* (Aug. 2022). DOI: 10.1007/s13226-022-00313-x. URL: <https://doi.org/10.1007/s13226-022-00313-x>.
- [Spr16] M. Sprecher. “Numerical Methods for Optimization and Variational Problems with Manifold-Valued Data”. PhD thesis. ETH Zurich, 2016. DOI: 10.3929/ethz-a-010686559.
- [ST85] J. C. Simo and R. L. Taylor. “Consistent tangent operators for rate-independent elastoplasticity”. In: *Comput Methods Appl Mech Eng* 48.1 (1985), pp. 101–118.

- [ST86] J. C. Simo and R. L. Taylor. “A return mapping algorithm for plane stress elastoplasticity”. In: *Int J Numer Methods Eng* 22.3 (1986), pp. 649–670. DOI: <https://doi.org/10.1002/nme.1620220310>. eprint: <https://onlinelibrary.wiley.com/doi/pdf/10.1002/nme.1620220310>. URL: <https://onlinelibrary.wiley.com/doi/abs/10.1002/nme.1620220310>.
- [Ste15] P. Steinmann. *Geometrical Foundations of Continuum Mechanics : An Application to First- and Second-Order Elasticity and Elasto-Plasticity*. Lecture Notes in Applied Mathematics and Mechanics. 2015. DOI: 10.1007/978-3-662-46460-1.
- [Ste99] N. Steenrod. *The topology of fibre bundles*. Vol. 44. Princeton university press, 1999.
- [Sue03] Y. Suetake, M. Iura, and S. Atluri. “Variational Formulation and Symmetric Tangent Operator for Shells with Finite Rotation Field”. In: *Comput Model Eng Sci* 4 (2003). DOI: 10.3970/cmesci.2003.004.329.
- [SV86] J. Simo and L. Vu-Quoc. “A Three-Dimensional Finite-Strain Rod Model. Part II: Computational Aspects”. In: *Comput Methods Appl Mech Eng* 58.1 (1986), pp. 79–116. DOI: 10.1016/0045-7825(86)90079-4.
- [SW03] C. Sansour and W. Wagner. “Multiplicative Updating of the Rotation Tensor in the Finite Element Analysis of Rods and Shells – a Path Independent Approach”. In: *Comput Mech* 31.1 (2003), pp. 153–162. DOI: 10.1007/s00466-002-0401-4.
- [TN04] C. Truesdell and W. Noll. *The Non-Linear Field Theories of Mechanics*. Ed. by S. S. Antman. Springer Berlin Heidelberg, 2004. DOI: 10.1007/978-3-662-10388-3. URL: <https://doi.org/10.1007/978-3-662-10388-3>.
- [TT60] C. Truesdell and R. Toupin. “The Classical Field Theories”. In: *Principles of Classical Mechanics and Field Theory / Prinzipien der Klassischen Mechanik und Feldtheorie*. Ed. by S. Flügge. Berlin, Heidelberg: Springer Berlin Heidelberg, 1960, pp. 226–858. ISBN: 978-3-642-45943-6. DOI: 10.1007/978-3-642-45943-6\_2.
- [Vis18] N. K. Vishnoi. *Geodesic Convex Optimization: Differentiation on Manifolds, Geodesics, and Convexity*. 2018. DOI: 10.48550/ARXIV.1806.06373. URL: <https://arxiv.org/abs/1806.06373>.
- [Voi98] W. Voigt. *Die fundamentalen physikalischen Eigenschaften der Krystalle in elementarer Darstellung*. de Gruyter, 1898.
- [Wal71] K.-P. Waltersdorf. “Beitrag Zur Frage Konsistenter Geometrisch Nichtlinearer Theorien Dünner Elastischer Flächentragwerke”. PhD thesis. Lehrstuhl für Massivbau, Technische Universität Hannover, 1971.

- [Wee19] O. Weeger, B. Narayanan, and M. L. Dunn. “Isogeometric shape optimization of nonlinear, curved 3D beams and beam structures”. In: *Comput Methods Appl Mech Eng* 345 (2019), pp. 26–51. ISSN: 0045-7825. DOI: <https://doi.org/10.1016/j.cma.2018.10.038>. URL: <https://www.sciencedirect.com/science/article/pii/S0045782518305425>.
- [WG93] P. Wriggers and F. Gruttmann. “Thin Shells with Finite Rotations Formulated in Biot Stresses: Theory and Finite Element Formulation”. In: *Int J Numer Methods Eng* 36.12 (1993), pp. 2049–2071. DOI: 10.1002/nme.1620361207.
- [Wri88] P. Wriggers. “Konsistente Linearisierungen in der Kontinuumsmechanik und ihre Anwendung auf die Finite-Element-Methode”. Deutsch. PhD thesis. Universität Hamburg, 1988.
- [WS85] P. Wriggers and J. C. Simo. “A note on tangent stiffness for fully nonlinear contact problems”. In: *Communications in Applied Numerical Methods* 1.5 (1985), pp. 199–203.
- [Yua20] X. Yuan et al. “Averaging Symmetric Positive-Definite Matrices”. In: *Handbook of Variational Methods for Nonlinear Geometric Data*. Ed. by P. Grohs, M. Holler, and A. Weinmann. Cham: Springer International Publishing, 2020, pp. 555–575. ISBN: 978-3-030-31351-7. DOI: 10.1007/978-3-030-31351-7\_20.
- [Zer67] W. Zerna. “Herleitung der ersten Approximation der Theorie elastischer Schalen”. In: *Abh Braunschw Wiss Ges* 19 (1967), pp. 52–71.
- [Zie14] O. Zienkiewicz, R. Taylor, and D. Fox. “Chapter 14 - A Nonlinear Geometrically Exact Shell Model”. In: *The Finite Element Method for Solid and Structural Mechanics (Seventh Edition)*. Seventh Edition. Butterworth-Heinemann, 2014, pp. 519–588. DOI: 10.1016/B978-1-85617-634-7.00014-4.
- [Zou20] Z. Zou et al. “An isogeometric Reissner–Mindlin shell element based on Bézier dual basis functions: Overcoming locking and improved coarse mesh accuracy”. In: *Computer Methods in Applied Mechanics and Engineering* 370 (2020), p. 113283.



---

## Lebenslauf

### Persönliche Angaben:

Name: Alexander Müller  
Geburtsdatum: 08.05.1992  
Geburtsort: Göppingen

### Schulische Ausbildung:

1998 – 2002 Hiltenburg-Grundschule, Bad Ditzenbach  
2002 – 2011 Michelberggymnasium, Geislingen  
07/2011 Abitur

### Universitäre Ausbildung:

10/2011 – 04/2015 Bachelorstudium Bauingenieurwesen an der Universität Stuttgart  
10/2015 – 10/2017 Masterstudium Bauingenieurwesen an der Universität Stuttgart  
10/2017 Masterprüfung  
seit 01/2018 Akademischer Mitarbeiter am Institut für Baustatik und Baudynamik der Universität Stuttgart



---

## Berichte des Instituts für Baustatik und Baudynamik der Universität Stuttgart

- 1 (1983) **P. Osterrieder:**  
Traglastberechnung von räumlichen Stabwerken bei großen Verformungen mit finiten Elementen.
- 2 (1983) **T. A. Kompfner:**  
Ein finites Elementmodell für die geometrisch und physikalisch nichtlineare Berechnung von Stahlbetonschalen.
- 3 (1983) **A. Diack:**  
Beitrag zur Stabilität diskret längsversteifter Kreiszyinderschalen unter Axialdruck.
- 4 (1984) **A. Burmeister, F.W. Bornscheuer, E. Ramm:**  
Traglasten von Kugelbehältern mit Stützen und Formabweichungen unter Innendruck und Stützenlängskraft.
- 5 (1985) **H. Stegmüller:**  
Grenzlastberechnungen flüssigkeitsgefüllter Schalen mit "degenerierten" Schalenelementen.
- 6 (1987) **A. Burmeister:**  
Dynamische Stabilität nach der Methode der finiten Elemente mit Anwendungen auf Kugelschalen.
- 7 (1987) **G. Kammler:**  
Ein finites Elementmodell zur Berechnung von Trägern und Stützen mit offenem, dünnwandigem Querschnitt unter Berücksichtigung der Interaktion zwischen globalem und lokalem Versagen.
- 8 (1988) **A. Matzenmiller:**  
Ein rationales Lösungskonzept für geometrisch und physikalisch nichtlineare Strukturberechnungen.
- 9 (1989) **D. Tao:**  
Die Technik der reduzierten Basis bei nichtlinearen finiten Element-Berechnungen.

- 10 (1989) **K. M. Weimar:**  
Ein nichtlineares Balkenelement mit Anwendung als Längssteifen axialbelasteter Kreiszyylinder.
- 11 (1990) **K.-U. Bletzinger:**  
Formoptimierung von Flächentragwerken.
- 12 (1990) **S. Kimmich:**  
Strukturoptimierung und Sensibilitätsanalyse mit finiten Elementen.
- 13 (1991) **U. Andelfinger:**  
Untersuchungen zur Zuverlässigkeit hybrid-gemischter Finiten Elemente für Flächentragwerke.
- 14 (1992) **N. Büchter:**  
Zusammenführung von Degenerationskonzept und Schalentheorie bei endlichen Rotationen.
- 15 (1992) **T. J. Hofmann:**  
Beitrag zur verfeinerten Balkentheorie.
- 16 (1994) **D. de Mesquita Roehl:**  
Zur Berechnung von großen elastoplastischen Deformationen bei Flächentragwerken und Kontinua.
- 17 (1994) **R. Reitinger:**  
Stabilität und Optimierung imperfektionsempfindlicher Tragwerke.
- 18 (1995) **R. L. M. Suanno:**  
Ein dreidimensionales Simulationsmodell für Stahlbeton mit Plastizität und Schädigung.
- 19 (1995) **M. Braun:**  
Nichtlineare Analysen von geschichteten, elastischen Flächentragwerken.
- 20 (1996) **N. Rehle:**  
Adaptive Finite Element Verfahren bei der Analyse von Flächentragwerken.

- 
- 21 (1996) **C. Haußer:**  
Effiziente Dreieckselemente für Flächentragwerke.
- 22 (1996) **D. Kuhl:**  
Stabile Zeitintegrationsalgorithmen in der nichtlinearen Elastodynamik dünnwandiger Tragwerke.
- 23 (1998) **H. Schmidts:**  
Zur effizienten Modellierung und Analyse von Hochhaustragwerken.
- 24 (1998) **H. Wang:**  
Interaktion des lokalen und globalen Stabilitätsverhaltens dünnwandiger Stäbe.
- 25 (1998) **K. Maute:**  
Topologie- und Formoptimierung von dünnwandigen Tragwerken.
- 26 (1998) **B. Maurer:**  
Karl Culmann und die graphische Statik.
- 27 (1998) **F. Cirak:**  
Adaptive Finite-Element-Methoden bei der nichtlinearen Analyse von Flächentragwerken.
- 28 (1998) **M. Trautz:**  
Zur Entwicklung von Form und Struktur historischer Gewölbe aus der Sicht der Statik.
- 29 (1999) **H. Menrath:**  
Numerische Simulation des nichtlinearen Tragverhaltens von Stahlverbundträgern.
- 30 (1999) **M. Bischoff:**  
Theorie und Numerik einer dreidimensionalen Schalenformulierung.
- 31 (1999) **W. A. Wall:**  
Fluid-Struktur-Interaktion mit stabilisierten Finiten Elementen.
- 32 (2000) **E. Kuhl:**  
Numerische Modelle für kohäsive Reibungsmaterialien.

- 33 (2001) A. Maute:**  
Fehlerkontrolle bei Finite-Element-Methoden in der linearen Struktur-  
dynamik.
- 34 (2001) S. Schwarz:**  
Sensitivitätsanalyse und Optimierung bei nichtlinearem Strukturver-  
halten.
- 35 (2001) A. Haufe:**  
Dreidimensionale Simulation bewehrter Flächentragwerke aus Beton  
mit der Plastizitätstheorie.
- 36 (2001) D. P. Mok:**  
Partitionierte Lösungsansätze in der Strukturdynamik und der Fluid-  
Struktur-Interaktion.
- 37 (2002) H. Steeb:**  
Fehlerschätzer für FE-Berechnungen bei entfestigenden Materialien.
- 38 (2002) K. Krausz:**  
Tragverhalten gemauerter Tonnengewölbe mit Stichkappen.
- 39 (2002) M. Hörmann:**  
Nichtlineare Versagensanalyse von Faserverbundstrukturen.
- 40 (2003) V. Gravemeier:**  
The Variational Multiscale Method for Laminar and Turbulent Incom-  
pressible Flow.
- 41 (2004) R. Kemmler:**  
Stabilität und große Verschiebungen in der Topologie- und Form-  
optimierung.
- 42 (2004) G. A. D’Addetta:**  
Discrete Models for Cohesive Frictional Materials.
- 43 (2004) M. Gee:**  
Effiziente Lösungsstrategien in der nichtlinearen Schalenmechanik.

- 
- 44 (2004) **T. Erhart:**  
Strategien zur numerischen Modellierung transienter Impaktvorgänge bei nichtlinearem Materialverhalten.
- 45 (2005) **M. Leukart:**  
Kombinierte anisotrope Schädigung und Plastizität bei kohäsiven Reibungsmaterialien.
- 46 (2006) **F. Huber:**  
Nichtlineare dreidimensionale Modellierung von Beton- und Stahlbetontragwerken.
- 47 (2007) **A. Lipka:**  
Verbesserter Materialeinsatz innovativer Werkstoffe durch die Topologieoptimierung.
- 48 (2007) **A. S. Hund:**  
Hierarchische Mehrskalenmodellierung des Versagens von Werkstoffen mit Mikrostruktur.
- 49 (2007) **S. Hartmann:**  
Kontaktanalyse dünnwandiger Strukturen bei großen Deformationen.
- 50 (2007) **T. M. Hettich:**  
Diskontinuierliche Modellierung zur Versagensanalyse von Verbundmaterialien.
- 51 (2007) **C. Förster:**  
Robust methods for fluid-structure interaction with stabilised finite elements.
- 52 (2009) **M. von Scheven:**  
Effiziente Algorithmen für die Fluid-Struktur-Wechselwirkung.
- 53 (2010) **J. Kato:**  
Material Optimization for Fiber Reinforced Composites applying a Damage Formulation.

- 54 (2010) C. F. Hilchenbach:**  
Optimierung von Mehrphasenstrukturen mit lokalem Schädigungsverhalten.
- 55 (2011) I. Bruss:**  
Dreidimensionale Schädigungsmodellierung heterogener Materialien.
- 56 (2012) B. J. Schneider:**  
Polygonale diskrete Elemente zur Modellierung heterogener Materialien.
- 57 (2012) R. Etlender:**  
Modellierung und Simulation der Wellenausbreitung in flexiblen hydraulischen Leitungen.
- 58 (2012) T. Cichosz:**  
Stabile und konsistente Kontaktmodellierung in Raum und Zeit.
- 59 (2013) R. Echter:**  
Isogeometric analysis of shells.
- 60 (2013) A. Tkachuk:**  
Variational methods for consistent singular and scaled mass matrices.
- 61 (2013) J. Irslinger:**  
Mechanische Grundlagen und Numerik dreidimensionaler Schalenelemente.
- 62 (2014) T. E. Pohl:**  
Adaptive Methoden zur Pfadverfolgung bei Entfestigung.
- 63 (2014) A. Sorg:**  
Adaptive diskret-kontinuierliche Modellierung von Materialien mit Mikrostruktur.
- 64 (2015) M. E. Matzen:**  
Isogeometrische Modellierung und Diskretisierung von Kontaktproblemen.



- 
- 65 (2016) V. M. Effinger:**  
Finite nichtlinear viskoelastische Modellierung offenzelliger Polymer-schäume.
- 66 (2017) C. M. Wilking:**  
Effiziente Integration und verbesserte Kontaktspannungen für duale Mortar-Formulierungen.
- 67 (2018) B. Oesterle:**  
Intrinsisch lockingfreie Schalenformulierungen.
- 68 (2018) F. Neukamm:**  
Lokalisierung und Versagen von Blechstrukturen.
- 69 (2019) A.-K. Schäuble:**  
Variationally consistent inertia templates for speed-up and customization in explicit dynamics.
- 70 (2019) T. Willerding:**  
Multiscale simulation of phase transformation in metals.
- 71 (2020) S. Roth:**  
Algorithmen zur nichtlinearen Stabilitätsanalyse dünnwandiger Strukturen.
- 72 (2020) R. Sachse:**  
Variational Motion Design for Adaptive Structures.
- 73 (2022) A. Tkachuk:**  
Parametrized variational principles in dynamics.
- 74 (2022) F. Geiger:**  
Strukturmechanische Charakterisierung von Stabtragwerken für den Entwurf adaptiver Tragwerke.
- 75 (2022) M. Benz:**  
Automatisierbare direkte Kalibrierung von Materialmodellen auf Basis digitaler Bildkorrelation.

**76 (2024) S. Bieber:**

Locking and Hourglassing in Nonlinear Finite Element Technology.





**Alexander Müller**

Dedicated to simulating thin-walled structures using the finite element method, this thesis focuses on a consistent Reissner-Mindlin shell formulation through theoretical and numerical investigations.

Emphasizing a robust mathematical foundation, particularly in differential geometry, the work explores aspects such as the derivation of stress resultants, consistent linearization, and properties of director interpolation. A pivotal outcome is a finite element formulation that outperforms existing ones, exhibiting key features like objectivity, adherence to unit length constraints, avoidance of path dependence, singularity prevention, and optimal convergence orders. Notably, the study of the consistent linearization process yields the correct tangent operator, identified as the symmetric Riemannian Hessian, serving as the stiffness matrix. This, combined with the study of the correct update of the nodal directors, contributes to the superior convergence behavior of a Newton-Raphson scheme compared to existing formulations.

Addressing the assumption of zero transverse normal stress, the thesis proposes a novel numerical treatment, using optimization on manifolds, applicable to arbitrary material models. This method shows potential applicability to other models with stress constraints.

The claim of a physically and algorithmically sound Reissner-Mindlin shell formulation is supported by results from numerical investigations. Beyond contributing to the algorithmic treatment of the Reissner-Mindlin shell model, the proposed procedures may have implications for improving the accuracy, efficiency, and reliability of numerical treatments of other structural models.